

Structure of entanglement in fracton phases of matter

Thesis by
Wilbur Shirley

In Partial Fulfillment of the Requirements for the
Degree of
Ph.D. in Physics

The logo for the California Institute of Technology (Caltech), featuring the word "Caltech" in a bold, orange, sans-serif font.

CALIFORNIA INSTITUTE OF TECHNOLOGY
Pasadena, California

2022
Defended September 23, 2021

© 2022

Wilbur Shirley

ORCID: 0000-0002-4970-1460

All rights reserved

ACKNOWLEDGEMENTS

I am deeply grateful to my advisor, Xie Chen, whose guidance and encouragement has made this thesis possible. I would like to thank my various collaborators, who have been a great source of inspiration: Kevin Slagle, Zhenghan Wang, Trithep Devakul, Juven Wang, Xiuqi Ma, Meng Cheng, Michael Levin, John McGreevy, Arpit Dua, Dominic Williamson, Xu Liu, Zijian Song, Nandagopal Manoj, Taige Wang, Tyler Ellison, Nathanan Tantivasadakarn, Yu-An Chen, Po-Shen Hsin, Chao-Ming Jian, Cenke Xu, Hao Song, and Michael Hermele. I would also like to thank my undergraduate advisors, Ryan Wilson and Brandon Anderson, for introducing me to the world of theoretical physics. Finally, I would like to acknowledge my partner Stacy Larochelle, and my parents Eric and Lena Shirley, for their love and support.

ABSTRACT

This thesis discusses recent contributions to the theory of gapped fracton phases of matter, utilizing exactly solvable Hamiltonian models as the primary tool of study. A large component of the work revolves around the notion of a foliation structure, which is a defining feature of the long-range entanglement in certain gapped fracton states. We introduce this concept, identify its presence in a handful of prominent fracton models, and explore its consequences in terms of entanglement entropy and fractional excitations. A second major theme of the thesis is the characterization of gapped fracton states via emergent gauge theories based on discrete subsystem symmetries. We introduce a variety of novel fractonic gauge theories including twisted and fermionic variants, identify their emergence in a bevy of well-known models, and classify them with the use of novel topological invariants. We also establish a link between subsystem symmetry and entanglement renormalization group flow in fractal spin liquids.

PUBLISHED CONTENT AND CONTRIBUTIONS

- [1] Trithep Devakul, Wilbur Shirley, and Juven Wang. “Strong planar subsystem symmetry-protected topological phases and their dual fracton orders”. In: *Physical Review Research* 2.1 (Mar. 2020). DOI: [10.1103/physrevresearch.2.012059](https://doi.org/10.1103/physrevresearch.2.012059). URL: <https://doi.org/10.1103%2Fphysrevresearch.2.012059>.
W.S. contributed to theoretical analysis and writing of the manuscript.
- [2] Wilbur Shirley, Kevin Slagle, and Xie Chen. “Twisted foliated fracton phases”. In: *Physical Review B* 102.11 (Sept. 2020). DOI: [10.1103/physrevb.102.115103](https://doi.org/10.1103/physrevb.102.115103). URL: <https://doi.org/10.1103%2Fphysrevb.102.115103>.
W.S. participated in conception of the project, theoretical analysis, and writing of the manuscript.
- [3] Wilbur Shirley, Kevin Slagle, and Xie Chen. “Foliated fracton order from gauging subsystem symmetries”. In: *SciPost Physics* 6.4 (Apr. 2019). DOI: [10.21468/scipostphys.6.4.041](https://doi.org/10.21468/scipostphys.6.4.041). URL: <https://doi.org/10.21468%2Fscipostphys.6.4.041>.
W.S. participated in conception of the project, theoretical analysis, and writing of the manuscript.
- [4] Wilbur Shirley, Kevin Slagle, and Xie Chen. “Foliated fracton order in the checkerboard model”. In: *Physical Review B* 99.11 (Mar. 2019). DOI: [10.1103/physrevb.99.115123](https://doi.org/10.1103/physrevb.99.115123). URL: <https://doi.org/10.1103%2Fphysrevb.99.115123>.
W.S. participated in conception of the project, theoretical analysis, and writing of the manuscript.
- [5] Wilbur Shirley, Kevin Slagle, and Xie Chen. “Fractional excitations in foliated fracton phases”. In: *Annals of Physics* 410 (Nov. 2019), p. 167922. DOI: [10.1016/j.aop.2019.167922](https://doi.org/10.1016/j.aop.2019.167922). URL: <https://doi.org/10.1016%2Fj.aop.2019.167922>.
W.S. participated in conception of the project, theoretical analysis, and writing of the manuscript.
- [6] Wilbur Shirley, Kevin Slagle, and Xie Chen. “Universal entanglement signatures of foliated fracton phases”. In: *SciPost Physics* 6.1 (Jan. 2019). DOI: [10.21468/scipostphys.6.1.015](https://doi.org/10.21468/scipostphys.6.1.015). URL: <https://doi.org/10.21468%2Fscipostphys.6.1.015>.
W.S. participated in conception of the project, theoretical analysis, and writing of the manuscript.
- [7] Taige Wang, Wilbur Shirley, and Xie Chen. “Foliated fracton order in the Majorana checkerboard model”. In: *Physical Review B* 100.8 (Aug. 2019). DOI: [10.1103/physrevb.100.085127](https://doi.org/10.1103/physrevb.100.085127). URL: <https://doi.org/10.1103%2Fphysrevb.100.085127>.

W.S. participated in conception of the project, theoretical analysis, and writing of the manuscript.

- [8] Wilbur Shirley et al. “Fracton Models on General Three-Dimensional Manifolds”. In: *Phys. Rev. X* 8 (3 Aug. 2018), p. 031051. DOI: [10.1103/PhysRevX.8.031051](https://doi.org/10.1103/PhysRevX.8.031051). URL: <https://link.aps.org/doi/10.1103/PhysRevX.8.031051>.

W.S. participated in conception of the project, theoretical analysis, and writing of the manuscript.

TABLE OF CONTENTS

<u>Acknowledgements</u>	iii
<u>Abstract</u>	iv
<u>Published Content and Contributions</u>	v
<u>Table of Contents</u>	vi
<u>Chapter I: Introduction</u>	1
<u>Chapter II: Fracton models on general three-manifolds</u>	9
<u>Chapter III: Universal entanglement signatures of foliated fracton phases</u>	37
<u>Chapter IV: Foliated fracton phases from gauging subsystem symmetries</u>	60
<u>Chapter V: Fractional excitations in foliated fracton phases</u>	91
<u>Chapter VI: Foliated fracton order in the checkerboard model</u>	137
<u>Chapter VII: Foliated fracton order in the Majorana checkerboard model</u>	158
<u>Chapter VIII: Emergent fermionic gauge theory and foliated fracton order in the Chamon model</u>	188
<u>Chapter IX: Twisted foliated fracton phases</u>	225
<u>Chapter X: Strong planar subsystem symmetry-protected topological phases and their dual fracton orders</u>	269

Chapter 1

INTRODUCTION

The characterization and classification of phases of matter is a fundamental goal of condensed matter physics. For multiple decades it was believed that the Landau theory of spontaneous symmetry breaking [5, 12] was capable of describing all equilibrium phases of matter and the phase transitions between them. However, the discovery of the fractional quantum Hall effect in 1982 [13, 26] pointed to the existence of quantum states of matter that lie outside the Landau paradigm, and the concept of topological order was conceived [30] to explain this novel phenomenon. Whereas symmetry-breaking phases of matter are characterized by long-range correlations of an order parameter, those harboring topological order are characterized by the long-range structure of entanglement in the ground state wavefunction [3].

Significant progress has been made in the understanding of gapped topological phases of matter such as the fractional quantum Hall states. Such phases are characterized by a ground state degeneracy on nontrivial spatial manifolds, as well as the existence of *fractional* quasiparticles that cannot be individually created or annihilated [11, 30]. In 2D, these excitations are *anyons* [31], quasiparticles that obey a generalized notion of particle statistics (neither Fermi nor Bose), featuring long-range interactions between pairs of anyons braiding around one another in their two-dimensional plane of existence [11]. The rigidity of such systems, owing to the existence of an energy gap above the many-body ground state, allows for a sharp classification in terms of the structure of anyonic excitations. Distinct topological orders give rise to different kinds of anyons, and the set of anyons arising in a particular topological phase form a mathematical structure known as a unitary modular tensor category [11]. The unique characteristics of topological phases, including the existence of anyons, originate microscopically due to the nontrivial structure of *long-range entanglement* (LRE) in the ground state wavefunction [3].

The study of gapped topological phases has reached a stage of relative maturity. The use of exactly solvable, commuting projector Hamiltonian models has proven to be a particularly powerful tool, starting with the introduction of the toric code in 1997 by Kitaev [10]. Although such models are not physically realistic, exact solubility

renders transparent the universal properties of a given phase of matter, for instance the exchange and braiding statistics of the anyonic quasiparticles. Therefore they are an invaluable instrument for classifying and characterizing gapped phases of matter [14].

In 2005, an exactly solvable three-dimensional spin Hamiltonian was conceived in a paper by Chamon that indelibly changed the landscape of gapped quantum phases [2]. A later work by Bravyi, Leemhuis, and Terhal [1] uncovered several fascinating properties of the Chamon model. First, they discovered that when periodic boundary conditions are imposed on the model, it harbors a ground state degeneracy that grows exponentially with linear system size. Moreover, they found that the excitations of the model are fractional, but they are not fully deconfined. Unlike ordinary particles that have freedom to move through space, the excitations of the Chamon model have intrinsic constraints on their mobility. In fact, the model harbors three distinct types of fractional excitation: *planons*, which can move within a plane, *lineons*, which can move along a line, and *fractons*, which are fundamentally immobile as individual particles. Fascinatingly, these constraints are not energetic in nature but rather arise due to the nontrivial structure of ground state entanglement. Only by destroying the phase of matter by closing the bulk gap can these constraints be overcome.

In 2011, another exactly solvable spin Hamiltonian was discovered by Haah [6] that further broadened the horizon of gapped quantum phases. This model, dubbed the Haah code, has the intriguing property that all of its fractional excitations are fractons. As a result its degenerate ground space does not admit any string-like logical operators, granting it the status of a partial self-correcting quantum memory. While individual fractons are pinned in space, fractons may move in coordination as the corners of a tetrahedron. This geometric constraint results in the striking emergence of a complex fractal geometry in the structure of fractional excitations and ground state entanglement.

These early discoveries ignited a new chapter in the study of quantum phases of matter. In the following years, a bevy of novel, exactly solvable 3D gapped Hamiltonian models were discovered [7, 9, 15, 25, 27, 28, 32] sharing the essential properties of 1) a ground state degeneracy (GSD) that scales exponentially with linear system size, 2) the existence of fractional excitations with constrained mobility, and 3) a subextensive correction to the area law of entanglement entropy that scales linearly with subregion length [8, 16, 17]. A particularly notable pair of works by Vijay, Haah, and Fu [27, 28] introduced a trio of models that sparked much interest

due to their relative simplicity — the X-cube model, the checkerboard model, and the Majorana checkerboard model. These models among others collectively represent a new kind of gapped quantum order called *fracton order*; quantum phases possessing this type of order are called *fracton phases of matter*. Broadly speaking, fracton orders can be divided into two classes depending on the nature of the quasiparticle mobility constraints [28]: Type II orders are those exhibiting an emergent fractal geometry (for instance the Haah code), whereas Type I orders are those that do not (the Chamon model for example). A decoupled stack of 2D topological orders can be regarded as the simplest, albeit somewhat trivial, kind of Type I fracton order.

Originally, fracton phases of matter were regarded as having topological order, which is reflected in the nomenclature of the early papers on the subject. This owes to the fact that they share many important properties such as long-range entanglement in the ground state, the existence of fractional excitations, and ground state degeneracy on nontrivial manifolds. However, it makes logical sense to regard topological and fracton phases of matter as distinct, unified classes under the umbrella of gapped LRE phases of matter. Topological phases of matter are those whose long wavelength, low energy properties are succinctly described by a topological quantum field theory (TQFT). On the other hand, fracton phases of matter are those whose universal properties are intrinsically intertwined with the underlying lattice geometry, and therefore do not admit a TQFT description.

A natural question to ask is how disparate fracton orders can be systematically understood within a common framework. For instance, how can we ascertain that two models belong to the same or different fracton phase? Is it possible to enumerate the different kinds of fracton phases that could exist in principle? The theory of fracton order is in its relative infancy; these models defy the conventional wisdom of many-body physics, and there is much yet to be discovered. The purpose of this thesis is to help fill the void in our knowledge of gapped fracton phases of matter. As has been discussed, the earliest known models of fracton order are exactly solvable in nature. The work described in this thesis delves into the heart of specific lattice models, uncovering properties that evade a cursory investigation and synthesizing them into a deepened understanding of the fracton order phenomenon. The contents of this thesis are as follows.

Chapter 2 explains the discovery of what we have dubbed a *foliation structure* in the paradigmatic Type I fracton model, the X-cube model. A foliation structure is a defining aspect of the pattern of long-range entanglement in a gapped ground

state. It implies the existence of local unitary transformations that *exfoliate* layers of two-dimensional topological orders from the bulk of a fracton state. These foliation layers are commensurate with the underlying lattice, forming a scaffolding of the entanglement structure. Fracton models possessing such a structure are said to have *foliated fracton order*. In the case of the X-cube model, the foliation layers lie in the three cubic lattice directions, and layers of the 2D Kitaev toric code are exfoliated from the bulk. The notion of foliation structure also provides an answer to the question of how Type I fracton models can be defined on nontrivial spatial manifolds [24].

Chapter 3 explores the structure of entanglement entropy in Type I fracton models. Previously it has been shown that the topological entanglement entropy (TEE) of such models grows linearly with the length of a given set of subregions. In this chapter we demonstrate that a number of Type I fracton orders also have a universal constant component of the entanglement entropy, which is invariant under exfoliation of 2D topological layers. We devise specific geometric configurations for computing TEE that isolate these universal entanglement signatures in various foliated fracton phases. In each case the subregion geometry is informed by the foliation structure of the fracton model, such that the TEE is invariant under exfoliation [23].

Chapter 4 discusses the notion of obtaining foliated fracton orders by gauging planar *subsystem* symmetries, which are on-site unitary symmetries that act on all the degrees of freedom within a planar subregion of a three-dimensional bulk. The main purposes of this work are to describe the most general such gauging procedure, and to explain the principle that mobility constraints of fractonic gauge charge arise from the conservation of planar subsystem symmetry [19].

Chapter 5 analyzes the structure of fractional excitations in foliated fracton phases, introducing the notion of *quotient superselection sectors* (QSS). The idea behind QSS is to regard anyons of exfoliable topological layers as trivial because they can be fully disentangled from the bulk system. Doing so defines a quotient group of the total group of superselection sectors by modding out all planon excitations, hence defining the group of QSS. For all of the foliated fracton orders we study, the group of QSS is a nontrivial finite group. The structure of QSS could serve as the starting point of a discrete mathematical structure that is analogous to unitary modular tensor categories in the study of 2D topological phases [21].

Chapters 6, 7, and 8 respectively dissect the checkerboard model, the Majorana checkerboard model, and the Chamon model. It is discovered that each of these

models possesses a foliation structure built from layers of 2D toric code, and can be described as some kind of discrete fractonic gauge theory. We argue the latter by demonstrating phase relations between each of the models and some variant of the X-cube model. In particular, we find that the checkerboard model, the Majorana checkerboard model, and the Chamon model respectively belong to the same phase as two copies of the X-cube model, the semionic X-cube model, and a novel semionic-fermionic variant of a 4-foliated X-cube model [18, 20, 29].

Chapter 9 extends the notion of foliated fracton order by introducing a pair of novel *twisted* foliated fracton phases. These models are twisted in the sense that they are obtained by gauging planar subsystem symmetries of a subsystem symmetry-protected topological state, manifesting in nontrivial exchange and braiding statistics in the gauge flux excitation sector. The result of these nontrivial statistics is that the 2D topological layers comprising the foliation structures are themselves 2D twisted gauge theories. Therefore we demonstrate that the notion of foliated fracton order generalizes beyond stabilizer codes and toric code layers [22].

Chapter 10 approaches the question of classification of Type I fracton phases by mapping it via gauge duality to the related problem of classification of subsystem symmetry-protected topological (SSPT) phases. This work achieves a partial classification of such phases in the case where all excitations of the gauged fracton order are abelian, in the process introducing a set of novel SSPT states dubbed *strong* SSPTs. We define strong SSPTs as those that cannot be obtained by stacking lower-dimensional global SPTs onto the planar subsystem symmetries of a 3D system. Upon gauging such phases are dual to novel twisted fracton phases, characterized by particular ‘global’ features of the statistical interactions within the gauge flux excitation sector [4].

References

- [1] S. Bravyi, B. Leemhuis, and B.M. Terhal. “Topological order in an exactly solvable 3D spin model”. In: *Annals of Physics* 326 (Apr. 2011), pp. 839–866. DOI: [10.1016/j.aop.2010.11.002](https://doi.org/10.1016/j.aop.2010.11.002).
- [2] Claudio Chamon. “Quantum Glassiness in Strongly Correlated Clean Systems: An Example of Topological Overprotection”. In: *Phys. Rev. Lett.* 94 (4 Jan. 2005), p. 040402. DOI: [10.1103/PhysRevLett.94.040402](https://doi.org/10.1103/PhysRevLett.94.040402). URL: <https://link.aps.org/doi/10.1103/PhysRevLett.94.040402>.
- [3] Xie Chen, Zheng-Cheng Gu, and Xiao-Gang Wen. “Local unitary transformation, long-range quantum entanglement, wave function renormalization,

- and topological order”. In: *Phys. Rev. B* 82 (15 Oct. 2010), p. 155138. DOI: [10.1103/PhysRevB.82.155138](https://doi.org/10.1103/PhysRevB.82.155138). URL: <https://link.aps.org/doi/10.1103/PhysRevB.82.155138>.
- [4] Trithep Devakul, Wilbur Shirley, and Juven Wang. “Strong planar subsystem symmetry-protected topological phases and their dual fracton orders”. In: *Physical Review Research* 2.1 (Mar. 2020). DOI: [10.1103/physrevresearch.2.012059](https://doi.org/10.1103/physrevresearch.2.012059). URL: <https://doi.org/10.1103%2Fphysrevresearch.2.012059>.
- [5] V. L. Ginzburg and L. D. Landau. “On the Theory of superconductivity”. In: *Zh. Eksp. Teor. Fiz.* 20 (1950), pp. 1064–1082.
- [6] Jeongwan Haah. “Local stabilizer codes in three dimensions without string logical operators”. In: *Phys. Rev. A* 83 (4 Apr. 2011), p. 042330. DOI: [10.1103/PhysRevA.83.042330](https://link.aps.org/doi/10.1103/PhysRevA.83.042330). URL: <https://link.aps.org/doi/10.1103/PhysRevA.83.042330>.
- [7] Gábor B. Halász, Timothy H. Hsieh, and Leon Balents. “Fracton Topological Phases from Strongly Coupled Spin Chains”. In: *arXiv:1707.02308* (July 2017). URL: <http://arxiv.org/abs/1707.02308>.
- [8] H. He et al. “Entanglement Entropy From Tensor Network States for Stabilizer Codes”. In: (Oct. 2017). arXiv: [1710.04220](https://arxiv.org/abs/1710.04220).
- [9] Timothy H. Hsieh and Gábor B. Halász. “Fractons from partons”. In: *Phys. Rev. B* 96 (16 Oct. 2017), p. 165105. DOI: [10.1103/PhysRevB.96.165105](https://link.aps.org/doi/10.1103/PhysRevB.96.165105). URL: <https://link.aps.org/doi/10.1103/PhysRevB.96.165105>.
- [10] A.Yu. Kitaev. “Fault-tolerant quantum computation by anyons”. In: *Annals of Physics* 303.1 (Jan. 2003), pp. 2–30. DOI: [10.1016/s0003-4916\(02\)00018-0](https://doi.org/10.1016/s0003-4916(02)00018-0). URL: <https://doi.org/10.1016%2Fs0003-4916%2802%2900018-0>.
- [11] Alexei Kitaev. “Anyons in an exactly solved model and beyond”. In: *Annals of Physics* 321.1 (Jan. 2006), pp. 2–111. DOI: [10.1016/j.aop.2005.10.005](https://doi.org/10.1016/j.aop.2005.10.005). URL: <https://doi.org/10.1016%2Fj.aop.2005.10.005>.
- [12] L. D. Landau. “On the theory of phase transitions”. In: *Zh. Eksp. Teor. Fiz.* 7 (1937), pp. 19–32.
- [13] R. B. Laughlin. “Anomalous Quantum Hall Effect: An Incompressible Quantum Fluid with Fractionally Charged Excitations”. In: *Phys. Rev. Lett.* 50 (18 May 1983), pp. 1395–1398. DOI: [10.1103/PhysRevLett.50.1395](https://link.aps.org/doi/10.1103/PhysRevLett.50.1395). URL: <https://link.aps.org/doi/10.1103/PhysRevLett.50.1395>.
- [14] Michael A. Levin and Xiao-Gang Wen. “String-net condensation: A physical mechanism for topological phases”. In: *Physical Review B* 71.4 (Jan. 2005). DOI: [10.1103/physrevb.71.045110](https://doi.org/10.1103/physrevb.71.045110). URL: <https://doi.org/10.1103%2Fphysrevb.71.045110>.

- [15] Han Ma et al. “Fracton topological order via coupled layers”. In: *Phys. Rev. B* 95 (24 June 2017), p. 245126. DOI: [10.1103/PhysRevB.95.245126](https://doi.org/10.1103/PhysRevB.95.245126) URL: <https://link.aps.org/doi/10.1103/PhysRevB.95.245126>.
- [16] Han Ma et al. “Topological Entanglement Entropy of Fracton Stabilizer Codes”. In: (2017). arXiv: [1710.01744](https://arxiv.org/abs/1710.01744).
- [17] Bowen Shi and Yuan-Ming Lu. “Decipher the nonlocal entanglement entropy of fracton topological orders”. In: *arXiv:1705.09300* (May 2017). URL: <http://arxiv.org/abs/1705.09300>.
- [18] Wilbur Shirley, Xu Liu, and Arpit Dua. “Emergent fermionic gauge theory and foliated fracton order in the Chamon model”. In: (2022).
- [19] Wilbur Shirley, Kevin Slagle, and Xie Chen. “Foliated fracton order from gauging subsystem symmetries”. In: *SciPost Physics* 6.4 (Apr. 2019). DOI: [10.21468/scipostphys.6.4.041](https://doi.org/10.21468/scipostphys.6.4.041) URL: <https://doi.org/10.21468/scipostphys.6.4.041>.
- [20] Wilbur Shirley, Kevin Slagle, and Xie Chen. “Foliated fracton order in the checkerboard model”. In: *Physical Review B* 99.11 (Mar. 2019). DOI: [10.1103/PhysRevB.99.115123](https://doi.org/10.1103/PhysRevB.99.115123) URL: <https://doi.org/10.1103/PhysRevB.99.115123>.
- [21] Wilbur Shirley, Kevin Slagle, and Xie Chen. “Fractional excitations in foliated fracton phases”. In: *Annals of Physics* 410 (Nov. 2019), p. 167922. DOI: [10.1016/j.aop.2019.167922](https://doi.org/10.1016/j.aop.2019.167922) URL: <https://doi.org/10.1016/j.aop.2019.167922>.
- [22] Wilbur Shirley, Kevin Slagle, and Xie Chen. “Twisted foliated fracton phases”. In: *Physical Review B* 102.11 (Sept. 2020). DOI: [10.1103/PhysRevB.102.115103](https://doi.org/10.1103/PhysRevB.102.115103) URL: <https://doi.org/10.1103/PhysRevB.102.115103>.
- [23] Wilbur Shirley, Kevin Slagle, and Xie Chen. “Universal entanglement signatures of foliated fracton phases”. In: *SciPost Physics* 6.1 (Jan. 2019). DOI: [10.21468/scipostphys.6.1.015](https://doi.org/10.21468/scipostphys.6.1.015) URL: <https://doi.org/10.21468/scipostphys.6.1.015>.
- [24] Wilbur Shirley et al. “Fracton Models on General Three-Dimensional Manifolds”. In: *Phys. Rev. X* 8 (3 Aug. 2018), p. 031051. DOI: [10.1103/PhysRevX.8.031051](https://doi.org/10.1103/PhysRevX.8.031051) URL: <https://link.aps.org/doi/10.1103/PhysRevX.8.031051>.
- [25] Kevin Slagle and Yong Baek Kim. “X-Cube Model on Generic Lattices: New Phases and Geometric Order”. In: *arXiv:1712.04511* (Dec. 2017). URL: <http://arxiv.org/abs/1712.04511>.
- [26] D. C. Tsui, H. L. Stormer, and A. C. Gossard. “Two-Dimensional Magnetotransport in the Extreme Quantum Limit”. In: *Phys. Rev. Lett.* 48 (22 May 1982), pp. 1559–1562. DOI: [10.1103/PhysRevLett.48.1559](https://doi.org/10.1103/PhysRevLett.48.1559) URL: <https://link.aps.org/doi/10.1103/PhysRevLett.48.1559>.

- [27] Sagar Vijay, Jeongwan Haah, and Liang Fu. “A new kind of topological quantum order: A dimensional hierarchy of quasiparticles built from stationary excitations”. In: *Phys. Rev. B* 92 (23 Dec. 2015), p. 235136. DOI: [10.1103/PhysRevB.92.235136](https://doi.org/10.1103/PhysRevB.92.235136). URL: <http://link.aps.org/doi/10.1103/PhysRevB.92.235136>.
- [28] Sagar Vijay, Jeongwan Haah, and Liang Fu. “Fracton topological order, generalized lattice gauge theory, and duality”. In: *Phys. Rev. B* 94 (23 Dec. 2016), p. 235157. DOI: [10.1103/PhysRevB.94.235157](https://doi.org/10.1103/PhysRevB.94.235157). URL: <https://link.aps.org/doi/10.1103/PhysRevB.94.235157>.
- [29] Taige Wang, Wilbur Shirley, and Xie Chen. “Foliated fracton order in the Majorana checkerboard model”. In: *Physical Review B* 100.8 (Aug. 2019). DOI: [10.1103/physrevb.100.085127](https://doi.org/10.1103/physrevb.100.085127). URL: <https://doi.org/10.1103/PhysRevB.100.085127>.
- [30] Xiao-Gang Wen. “Topological orders and edge excitations in fractional quantum Hall states”. In: *Advances in Physics* 44.5 (Oct. 1995), pp. 405–473. DOI: [10.1080/00018739500101566](https://doi.org/10.1080/00018739500101566). URL: <https://doi.org/10.1080/00018739500101566>.
- [31] Frank Wilczek. “Quantum Mechanics of Fractional-Spin Particles”. In: *Phys. Rev. Lett.* 49 (14 Oct. 1982), pp. 957–959. DOI: [10.1103/PhysRevLett.49.957](https://doi.org/10.1103/PhysRevLett.49.957). URL: <https://link.aps.org/doi/10.1103/PhysRevLett.49.957>.
- [32] Beni Yoshida. “Exotic topological order in fractal spin liquids”. In: *Phys. Rev. B* 88 (12 Sept. 2013), p. 125122. DOI: [10.1103/PhysRevB.88.125122](https://doi.org/10.1103/PhysRevB.88.125122). URL: <https://link.aps.org/doi/10.1103/PhysRevB.88.125122>.

FRACTON MODELS ON GENERAL THREE-MANIFOLDS

2.1 Introduction

Characterization and classification of quantum phases of matter is a fundamental problem of physics. Spectacular progress has been made in the last decade for topological phases of matter, especially those with short-range entanglement and with long-range entanglement in two spatial dimensions. Topological quantum field theory (TQFT) is the framework in which the regnant theories of these topological phases are formulated. Recently, an intriguing class of gapped Hamiltonians, referred to as fracton models in this paper, have been proposed as potential new topological phases of matter [2, 4, 12, 13, 16, 20, 22, 35-38, 42]. These models appear in three spatial dimensions and have ground states exhibiting long-range entanglement. Certain topological features [7, 15, 21, 23, 29, 30, 40] such as robust ground state degeneracy and fractional excitations rear their heads in fracton models. But these models clearly do not fit into the standard TQFT framework since their ground state degeneracies (GSD) are not topologically invariant, which is a salient feature of current TQFTs. In this paper, we investigate the nature of the underlying physics in these fracton models: topological, geometric, or something yet else?

Quantum field theory (QFT) provides powerful descriptions of many-body quantum physics. Phases of matter with intrinsic topological order can be characterized either by the existence of a low energy TQFT limit or by an anyon model that captures the algebraic structure of fractional excitations in the plane. We are thus motivated to ask whether fracton models have low energy descriptions that resemble TQFTs. (A QFT description of the X-cube model with a cut-off is proposed in [31].)

A TQFT assigns a Hilbert space $V(Y)$ to each spatial manifold Y satisfying some formal properties of a QFT; the Hilbert space $V(Y)$ is the ground state manifold. An intrinsic topological order manifests itself in the robust ground state degeneracy $V(Y)$ that depends only on the topology of the spatial manifold Y . Fracton models do not fit into this framework because their GSD

is not solely determined by the topology of the spatial manifold Y . Thus, we are interested in a modification such that the ground state manifold $V(Y, s)$ will depend not only on the topology of Y but also some extra structure s of Y analogous to a G -bundle in gauge theory or a spin structure for fermions. A condensed matter system on a closed (compact without boundary) spatial manifold Y is defined through a Hamiltonian on a lattice Δ in Y , which is a cellulation of Y mathematically. In traditional topological phases, the ground state manifold $V(Y, \Delta)$ is independent of the lattice Δ , while in fracton models, $V(Y, \Delta)$ depends on the lattice Δ in intricate ways. One hope is that for a judiciously chosen sequence of lattices Δ_i , the ground state manifolds $V(Y, \Delta_i)$ converge to a well-defined limit $V(Y, s)$, presumably infinitely dimensional, and their dependence on lattices Δ_i reduces to the well-defined structure s of Y . Then according to the structure s being regarded as topological, geometric, or something yet else, we will classify the fracton models as phases possessing such a character.

In this paper, a first step is made towards such a generalized TQFT for the X -cube model. As explained in the concluding section, we conjecture that the extra structure is a singular compact total foliation, inspired by the notion of total foliation of a 3-manifold [14]. Since a foliation of a 3-manifold is regarded as a topological structure, we suggest that the X -cube model can be considered to be a new kind of generalized topological order.

In particular, we show that the X -cube model [38], originally defined on the three-dimensional torus, can be defined on other closed 3-manifolds as well. To do so, we employ a singular compact total foliation of a 3-manifold, which partitions the manifold into three sets of transversely intersecting parallel surfaces in the complement of a (possibly empty) singular subset consisting of singular leaves. The ground state degeneracy (and its size-independent correction) depends on the topology of these leaves and the intersections of the leaves. We show that the relation between the ground state degeneracy and the foliation can be easily understood in terms of an entanglement renormalization group transformation of the X -cube model where system size can be increased or decreased by adding or removing 2D layers of toric code topological states.

The total foliation structure is well-suited for the potential construction of a continuous limit description of the phase. Additionally, we give a spherical leaf construction of the X -cube model for any 3-manifold. Remarkably, we find

that the X -cube model in the spherical leaf construction reduces to the 3D toric code model with traditional topological order of a discrete vector gauge theory.

The paper is structured as follows: In Sec. 2.2, we review the X -cube model on the 3-torus T^3 . In Sec. 2.3, 2.4, we extend the X -cube model to other closed 3-manifolds: the spherical leaf construction in Sec. 2.3 and the singular compact total foliation construction in Sec. 2.4. In Sec. 2.5, we present the entanglement renormalization procedure for the X -cube model. In Sec. 2.7 we show that these results can be generalized to the \mathbb{Z}_N version of the X -cube model.

2.2 Review of X-cube model on three-torus

The X -cube model, as first discussed in [38], is defined on a cubic lattice with qubit degrees of freedom on the edges. The Hamiltonian

$$H = - \sum_v (A_v^x + A_v^y + A_v^z) - \sum_c B_c \quad (2.1)$$

contains two types of terms: cube terms B_c which are products of the twelve Pauli X operators around a cube c , and cross terms A_v^μ which are products of the four Pauli Z operators at a vertex v in the plane normal to the μ -direction where $\mu = x, y$, or z (Fig. 2.1). These terms mutually commute and their energies can be minimized simultaneously. Moreover, they can be viewed as stabilizer generators for a quantum error-correcting stabilizer code [10] whose code space coincides with the Hamiltonian ground space. One particular ground state is given by $|\psi\rangle = \prod_c (1 + B_c) |0\rangle$, where $|0\rangle$ refers to the tensor product of the qubit state $|0\rangle$ on each edge.

Consider an $L_x \times L_y \times L_z$ cubic lattice with periodic boundary conditions. While there are $3L_x L_y L_z$ qubits in the system and $4L_x L_y L_z$ local terms in the Hamiltonian, the ground state is far from unique. In fact, the ground state degeneracy (GSD) scales linearly with the size of the system in all three directions:

$$\log_2 \text{GSD} = 2L_x + 2L_y + 2L_z - 3. \quad (2.2)$$

There are hence a large number of ‘logical operators’ that commute with all of the terms in the Hamiltonian and map one ground state to another [15, 31]. An over-complete set of X -type logical operators is given by the set of closed string-like operators W_{ij}^μ , which is a product of X operators over all

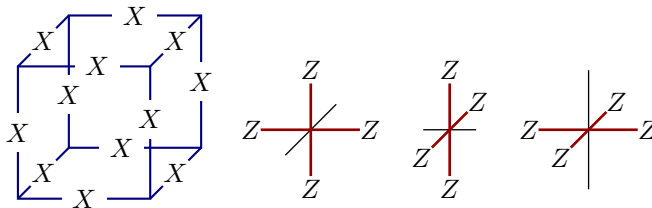


Figure 2.1: Cube and cross operators of the X-cube Hamiltonian on a cubic lattice.

μ -oriented edges with coordinates (i, j) in the plane normal to μ (see Fig. 2.2). This set is over-complete in the sense that products of the form $W_{ij}^\mu W_{il}^\mu W_{kl}^\mu W_{kj}^\mu$ are equal to a product of some B_c cube operators, and thus act trivially on the ground state manifold (here the four sets of coordinates lie at the corners of a rectangle in the plane normal to μ , as shown in Fig. 2.2). There are $L_x L_y + L_y L_z + L_z L_x - 2L_x - 2L_y - 2L_z + 3$ such relations corresponding to unique products of cube operators, thus implying Eq. (2.2). Moreover, it was found that for each ground state, the entanglement entropy of a region R satisfies an area law with subleading corrections linear in the length of R , which has a similar origin as the subextensive scaling of ground state degeneracy [15, 21].

Logical operators correspond to processes where particle anti-particle pairs are created out of the vacuum, wound around the torus, and then annihilated. Straight open string operators $W_{ij}^\mu(\mu_1, \mu_2)$ anti-commute with the vertex Hamiltonian terms at the endpoints μ_1 and μ_2 , corresponding to excitations which live on the vertices of the lattice. Here $W_{ij}^\mu(\mu_1, \mu_2)$ is defined to be the product of X operators over μ -oriented edges between $\mu = \mu_1$ and $\mu = \mu_2$ with coordinate (i, j) in the plane normal to μ (see Fig. 2.3). Conversely, acting with bent string operators introduces additional energetic costs at the corners. Therefore the particles living at the endpoints of straight open strings are energetically confined to live on a line; in this sense, they are dimension-1 particles [38]. These particles obey an unconventional fusion rule: triples of particles living along x -, y -, and z -oriented lines may annihilate into the vacuum. On the other hand, acting with a closed string operator around a rectangle creates an excitation at each corner of the rectangle. A pair of particles at adjacent corners may be viewed as a single dipole-like object which is itself a dimension-2 particle and is mobile in the plane normal to the edges

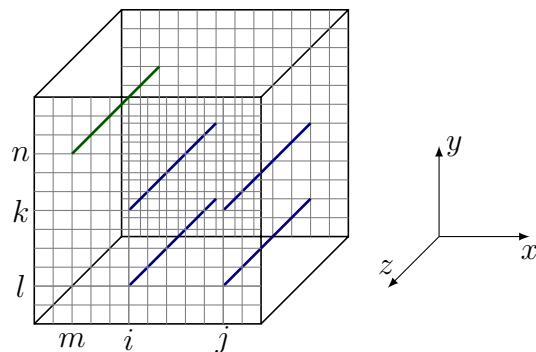


Figure 2.2: Visualization of logical operators. The green string corresponds to W_{mn}^z . The product of the four operators corresponding to the blue strings is equal to the identity, as described in the main text.

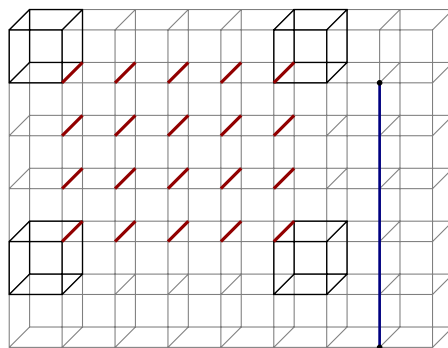


Figure 2.3: Visualization of particle creation operators. The red links correspond to a membrane geometry on the dual lattice. The product of Z operators over these edges excites the (darkened) cube operators at the corners. The product of X operators over the links comprising the straight open blue string creates excitations at its endpoints (black dots).

connecting the two corners.

In addition to these string-like operators, there are membrane-like operators which are products of Z operators over qubits corresponding to a membrane geometry on the dual lattice (see Fig. 2.3). A rectangular membrane operator anti-commutes with the cube Hamiltonian terms at its corners. A pair of adjacent corner excitations created by a rectangular membrane operator is likewise a dimension-2 dipolar particle, free to move in a plane perpendicular to its moment. A process whereby a pair of such membrane dipoles is created, separated, wound around the torus and annihilated, corresponds to a string-like Z -type logical operator.

2.3 X-cube Model on Generic Lattices

The 3D toric code model, which represents the traditional 3D \mathbb{Z}_2 gauge theory topological order, can be defined on any lattice on any manifold. For the X-cube model, however, it is not clear if this is possible. In this section, we explain how to define the X-cube model on a special class of lattices, which will enable constructions on general spatial 3-manifolds in the subsequent section.

2.3.1 Intersecting leaves

We construct a lattice by embedding a large number of transversely intersecting surfaces, referred to as leaves, into the 3-manifold M . Vertices of the resulting cellulation lie at triple intersection points of leaves, while edges lie along the intersections of pairs of leaves; a qubit is placed on each edge. We assume that the location of the leaves are generic enough such that no three leaves intersect along the same line. The cubic lattice on the 3-torus can be viewed in this way as three orthogonal stacks of toroidal leaves—the xy , yz , and xz planes of $T^3 = \mathbb{R}^3/\mathbb{Z}^3$. Unlike the cubic lattice, the general construction may result in some number of non-cubical 3-cells. Crucially, however, every vertex in this type of cellulation is locally isomorphic to a cubic lattice vertex. This fact allows the X-cube Hamiltonian to be defined as per Eq. (2.1). Similar to the cubic lattice, the three cross operators A_v^μ are products of Z operators over the four edges emanating from v in the leaf labeled by μ . The B_c operator is in general a product of X operators over all edges of the 3-cell c . The cellulation geometry ensures that the terms in the Hamiltonian are mutually commuting.

The structure of the excitation types and fusion properties carries over from the cubic lattice version of the X-cube model. However, the notion of dimension-1 and dimension-2 particles is revised in a natural way. In the general lattice construction, dimension-1 particles created at the ends of open string operators are freely mobile along the intersection lines of pairs of cellulating surfaces. Furthermore, dimension-2 particles, such as fracton dipoles, are free to move along leaves that are orthogonal to the direction of the dipole moment. In the general setting, logical operators correspond to processes where particle pairs are created, wound around the intersection circle of two surfaces, and then annihilated. Unlike the three-torus, for general manifolds these circles may be contractible.

2.3.2 Spherical leaf construction and 3+1D \mathbb{Z}_2 gauge theory

Before we turn to the notion of total foliation, we first note the existence of a somewhat anomalous lattice construction that defines an X-cube model on any 3-manifold M . We choose the leaves of the cellulation to be contractible small spheres placed randomly or periodically throughout M . As explained above, a lattice is formed by placing vertices at the intersection of three spheres and edges along the intersection of two spheres. As long as the spheres are packed closely enough that each sphere intersects with several other spheres, this construction defines a lattice in M . The X-cube Hamiltonian on this lattice generalizes Eq. (2.1), with three cross terms at each vertex v and a B_c term for each 3-cell. The operator B_c is a product of X operators over the edges of the 3-cell c .

This construction allows the X-cube model to be defined on any manifold. However, the resulting model can have fully mobile deconfined point excitations, and a constant GSD of 8 on the 3-torus. Thus we conclude that the model can exhibit conventional 3+1D \mathbb{Z}_2 gauge theory topological order rather than fracton order. We have numerically verified a GSD of 8 for a 3-torus covered with spherical leaves of radius 0.46 centered at points of an FCC lattice (see Fig. 2.4(a-b)). We used the method equivalent to the one described in Appendix B of [20]. The unit cell in this configuration contains 48 links. By enumerating the 48 links in a unit cell and inputting the complicated stabilizer Hamiltonian into the algorithm, we identify a ground state degeneracy of 8.

The 8-fold GSD can be understood by considering the string and membrane logical operators acting on the topologically protected ground space. A membrane and string operator are shown in Fig. 2.4(d-e). The membrane operator is a product of X operators on the blue edges, whereas the string operator is a product of Z operators on the red edges. These operators commute with the Hamiltonian, but anticommute with each other, and therefore describe one qubit in the degenerate ground state Hilbert space. 90 degree rotation gives the two other pairs of these operators.

The deconfined point-like charges of the model correspond to 3-cell excitations lying at the ends of open string operators (as in Fig. 2.4(b)). These particles are fully mobile because the corresponding string operators can bend without creating additional excitations. This is a surprising result, as excitations of the 3-cell operators on a cubic lattice are immobile fractons. Conversely,

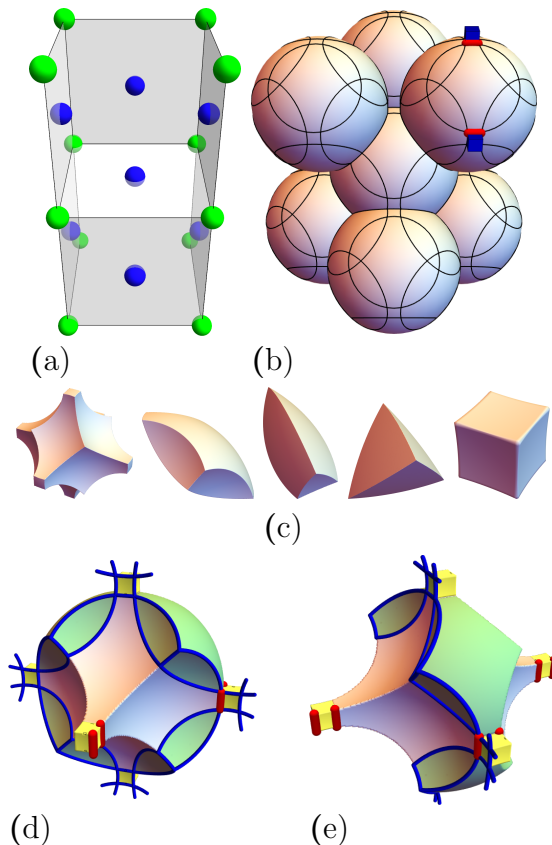


Figure 2.4: A construction with periodically placed spheres. (Sec. 2.3.2). (a-b) We place spheres of radius 0.46 on an face-centered cubic (FCC) lattice. The spheres in (b) are located at the blue points of the FCC lattice in (a). When the X-cube model is defined on the resulting lattice, the phase is equivalent to the 3D toric code. (b) The toric code charges reside on small cubes. These charges can hop e.g. between the two blue cubes via a string of Z operators on the two red edges. (c) The elementary 3-cells of the cellulation. (d-e) Membrane and string operators. The membrane operator is a product of X operators on the blue edges, whereas the string operator is a product of Z operators on the red edges.

violations of the cross operators lie along the boundary of open membrane operators (shown in blue in Fig. 2.4(d-e)). These excitations correspond to flux loops of the 3+1D \mathbb{Z}_2 gauge theory. Hence, we see that both the fractional excitations and logical operators match those of 3+1D \mathbb{Z}_2 gauge theory. Other arrangements of spheres may also result in the 3+1D \mathbb{Z}_2 gauge theory.

Thus, a different approach must be considered to construct lattices whose X-cube constructions realize fracton order. Since dimension-1 and dimension-2 particles are constrained to move within individual leaves, extended dimension-

1 and dimension-2 particles and a robust ground state degeneracy that scales subextensively with system size can be realized only in the presence of leaves that are non-locally embedded in the 3-manifold. This consideration motivates the following section.

2.4 X-cube model on general manifolds via total foliation

In this section, we consider cellulations of a 3-manifold M constructed by embedding into M three transversely intersecting stacks of parallel surfaces, which are assigned x , y , and z labels and are composed of L_x , L_y , and L_z layers, respectively. Each stack of surfaces may be viewed as a discrete sample of compact leaves of a (possibly singular)¹ two-dimensional foliation of M . (A p -dimensional foliation of a manifold M is an infinite partition of M into a collection of disjoint parallel p -dimensional submanifolds of M with infinitesimal separation. The submanifolds are referred to as leaves.) This approach is reminiscent of the mathematical notion of total foliation.² However, our construction differs in that we allow the foliations to be singular (containing leaves that are of a different dimension) but require that the leaves are compact so that the resulting lattice has a finite number of edges. The discrete foliations are required to obey the following transversality conditions, which can always be satisfied by an appropriate choice of leaves: pairs of foliating surfaces must intersect transversely (i.e. not tangentially), and triples of surfaces must intersect at points. These generalized cellulations retain a notion of continuum limit, as they can be arbitrarily refined by adding leaves to any of the three constituent foliations.

We find that the ground state degeneracy of the generalized X-cube model obeys the formula

$$\log_2 \text{GSD} = b_x L_x + b_y L_y + b_z L_z - c \quad (2.3)$$

where b_μ is the first Betti number with \mathbb{Z}_2 coefficients of the surfaces comprising the μ -oriented foliation³ and c is a constant sensitive to the topology of the intersections of the three foliations. As we will discuss in Sec.[2.5](#), the

¹In a singular foliation, leaves at singularities may differ in dimension (i.e. dimension less than two in the case of 3-manifolds).

²A total foliation of an n -dimensional manifold consists of n sets of $(n-1)$ -dimensional foliations that are transverse at every point.

³If the surfaces in the μ -oriented foliation have different Betti numbers, then one should instead multiply by the corresponding Betti number for each surface.

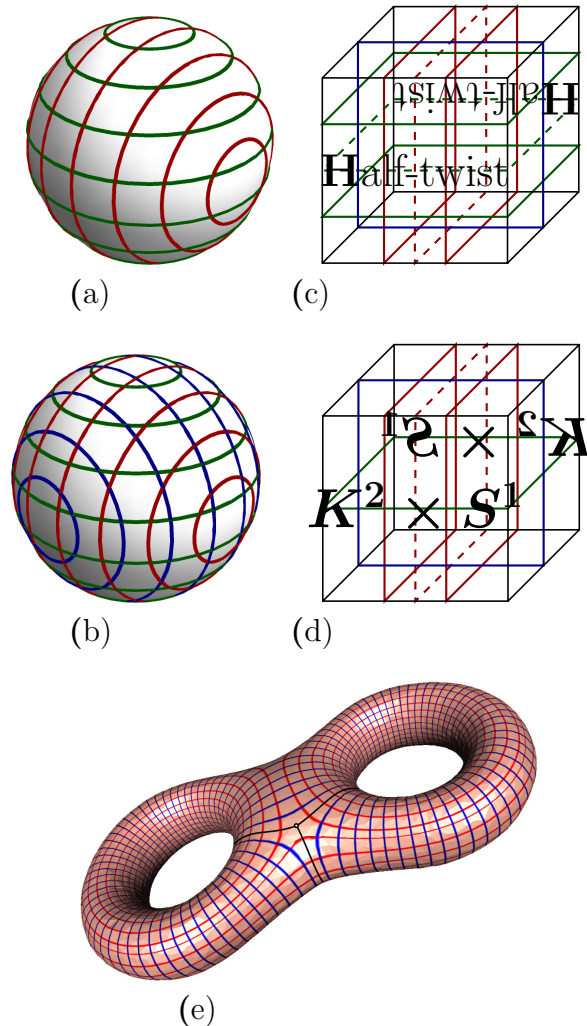


Figure 2.5: (a) A spherical cross-section of a cellulation of $S^2 \times S^1$ with $L_x = L_y = 8$. (b) The $t = 0$ equator of S^3 defined as the locus of points in \mathbb{R}^4 satisfying $x^2 + y^2 + z^2 + t^2 = 1$. In this example, S^3 is foliated by 8 spherical leaves of constant x , y , and z , which are colored red, green, and blue. Although the sphere drawn in (a) is a leaf, the sphere drawn in (b) is not a leaf; it is merely a convenient cross-section. (c) The half-twist manifold, constructed by identifying opposite faces of a cube. The front and back faces are glued after a 180° twist. The dashed red and green squares are outlines of embedded Klein bottles. The pair of solid red (or green) squares outline a single torus, as does the blue square. (d) The 3-manifold $K^2 \times S^1$, viewed as a cube with opposite faces identified; front and back faces are identified after a reflection across the vertical bisector. The pair of solid red squares outlines a single embedded torus, as do the dashed red square and solid blue square. The solid green square outlines an embedded Klein bottle. (e) Figure courtesy of [18]. A Σ_2 cross-section of a cellulation of $\Sigma_2 \times S^1$. The red and blue lines correspond to leaves of respective singular foliations. The singularities are indicated by the black lines.

3-manifold	x -leaves	y -leaves	z -leaves	\log_2 GSD	c
T^3	$L_x \times T^2$	$L_y \times T^2$	$L_z \times T^2$	$2L_x + 2L_y + 2L_z - 3$	3
$S^2 \times S^1$	$L_x \times T^2$	$L_y \times T^2$	$L_z \times S^2$	$2L_x + 2L_y - 1$ *	1
S^3	$L_x \times S^2$	$L_y \times S^2$	$L_z \times S^2$	0	0
half-twist	$L_x \times T^2$	$L_y \times T^2$	$L_z \times T^2$	$2L_x + 2L_y + 2L_z$	0
half-twist	$(L_x - 1) \times T^2 + K^2$	$L_y \times T^2$	$L_z \times T^2$	$2L_x + 2L_y + 2L_z - 2$	2
half-twist	$(L_x - 1) \times T^2 + K^2$	$(L_y - 1) \times T^2 + K^2$	$L_z \times T^2$	$2L_x + 2L_y + 2L_z - 3$	3
$K^2 \times S^1$	$L_x \times T^2$	$L_y \times T^2$	$L_z \times K^2$	$2L_x + 2L_y + 2L_z - 2$	2
$\Sigma_g \times S^1$	$L_x \times T^2$	$L_y \times T^2$	$L_z \times \Sigma_g$	$2L_x + 2L_y + 2gL_z - 3g$	$3g$

Table 2.1: A summary of the ground state degeneracy (GSD) of the X-cube model on various 3-manifolds with the foliations described in Sec. 2.4. *The logical operators with support near foliation singularities are not protected against local perturbations; see Sec. 2.4.1

presence of the first three terms can be understood in terms of an entanglement renormalization transformation which grows the system size by adding layers of toric code states, which have \log_2 GSD = b .

We stress that the degenerate ground space is sensitive to the foliation structure imposed on the 3-manifold as well as its topology, and that it is possible to endow the same 3-manifold with differing foliation structures (for example in the case of the half-twist manifold discussed below). Furthermore, we note that singularities in the foliation structure may result in partial splitting of the GSD (in the presence of local perturbations) due to the existence of logical operators with local support. This occurs, for instance in the case of $S^2 \times S^1$, in which two of the foliations have point singularities. Conversely, in the case of $\Sigma_2 \times S^1$ depicted in Fig. 2.5(e) the foliations exhibit codimension-1 singularities, but the resulting models do not contain logical operators with local support.

We now turn to some examples. The results are summarized in Table 2.1. We have numerically verified the expressions for GSD using a method equivalent to the one described in Appendix B of [20].

2.4.1 2-sphere times 1-sphere

First, consider the manifold $S^2 \times S^1$. It admits a non-singular foliation consisting of layered copies of S^2 , as well as singular foliations of tori whose projections onto S^2 latitudinally foliate the sphere with singularities at the poles. Our construction takes one stack of L_z parallel spheres and two such stacks of L_x and L_y layers of tori, respectively (see Fig. 2.5(a)). The

ground state degeneracy of the X-cube model on this lattice obeys the formula $\log_2 \text{GSD} = 2L_x + 2L_y - 1$.

It is important to note that the Wilson loops (which are a product of X operators around a red or green loop in Fig. 2.5(a)) near the foliation singularities have local support. Thus, the logical qubits corresponding to these loops are not topologically protected, and the ground state degeneracy would be partially split by local perturbations.

2.4.2 3-sphere

The 3-sphere S^3 admits latitudinal foliations with polar singularities. Viewing S^3 as a subspace of \mathbb{R}^4 defined by the equation $x^2 + y^2 + z^2 + w^2 = 1$, a leaf of an x -oriented latitudinal foliation is a 2-sphere defined by the equation $x_0^2 + y^2 + z^2 + w^2 = 1$ for fixed x_0 . Taking three such foliations in the x , y , and z directions yields a suitable cellulation of S^3 (Fig. 2.5(b)). The resulting X-cube model exhibits a unique ground state.

2.4.3 Half-twist manifold

The half-twist manifold is an orientable Euclidean 3-manifold constructed by identifying opposite faces of a cube. The y (top and bottom) and x (left and right) faces are identified in the standard way, but the z (front and back) faces are identified after a rotation of 180 degrees relative to one another. It admits a total foliation with three sets of compact toroidal leaves. A sampling of L_x , L_y , and L_z toroidal leaves corresponds to embedding a $2L_x \times 2L_y \times L_z$ cubic lattice in the original cube. The factors of 2 are due to the twist in the gluing process (see Fig. 2.5(c)). The ground state degeneracy of the X-cube model defined on this lattice is given by $\log_2 \text{GSD} = 2L_x + 2L_y + 2L_z$.

It is also possible to include one or more Klein bottles in the cellulation. Including one Klein bottle belonging to the x foliation corresponds to embedding a cubic lattice of size $2L_x - 1$ in the x direction, and changes the ground state degeneracy such that $c = 2$. Including an additional Klein bottle in the y foliation further increases c to 3. Thus the constant c is not an invariant of M , but rather is sensitive to the choice of cellulation.

2.4.4 Klein bottle times

The manifold $K^2 \times S^1$ is a simple example of a non-orientable 3-manifold, where K^2 is a Klein bottle. It admits a total foliation consisting of one set of

Klein bottle leaves and two sets of toroidal leaves. Cellulating $K^2 \times S^1$ in this fashion (with L_x , L_y , and L_z leaves) is equivalent to embedding a $2L_x \times 2L_y \times L_z$ cubic lattice into $K^2 \times S^1$. See Fig. 2.5(d) for details. As on the torus, the toric code on the Klein bottle has a fourfold ground state degeneracy. The ground state degeneracy of the X-cube model on $K^2 \times S^1$ (with this foliation) obeys $\log_2 \text{GSD} = 2L_x + 2L_y + 2L_z - 2$.

2.4.5 Genus g surface times 1-sphere

The product manifold $\Sigma_g \times S^1$ admits a natural foliation of Σ_g leaves, where Σ_g is the 2D oriented topological manifold with genus g . We can supplement this with two singular foliations of tori which intersect Σ_g slices in circles. These circles represent leaves of a *measured foliation* of Σ_g with trivalent singularities, which can be constructed for any genus by gluing together foliated pairs of pants [3]. A cross-section of a cellulation of $\Sigma_2 \times S^1$ is shown in Fig. 2.5(e). The ground state degeneracy of the X-cube model on this class of manifolds is given by $\log_2 \text{GSD} = 2gL_z + 2L_x + 2L_y - 3g$.

2.5 Entanglement renormalization for X-cube model

In this section, we introduce a procedure that transforms between X-cube ground states on coarsened or refined cellulations of a 3-manifold M . Given a cellulation composed of leaves of a triple foliation of M , the procedure allows leaves to be added or removed by adding or removing toric code states that live on the individual layers. This transformation sheds light on the structure of the ground state degeneracy in Eq. (2.3). Moreover, the procedure can be interpreted as an entanglement renormalization group (RG) transformation [34] for which the X-cube Hamiltonian is a fixed point. This interpretation motivates us to propose a definition of *type-I fracton phase* based on ground state entanglement structure (in Sec. 2.6).

2.5.1 RG transformation

To begin, we consider a transformation on an X-cube ground state $|\psi_{\text{XC}}\rangle$ that adds a single layer to one of the constituent stacks of a given 3-manifold cellulation. This new layer bisects the edges and 3-cells it intersects. Accordingly, for each edge i piercing the new layer, the qubit on this edge is split into two qubits on edges i' and j' . We then substitute $Z_i \rightarrow Z_{i'}$ and $X_i \rightarrow X_{i'}X_{j'}$ in the X-cube Hamiltonian, and add a $Z_{i'}Z_{j'}$ stabilizer to the

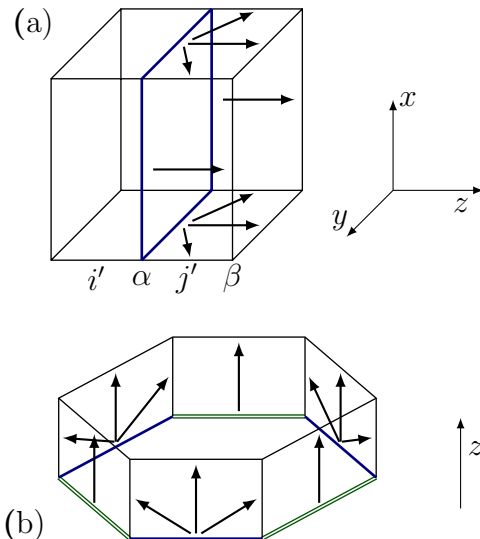


Figure 2.6: (a) Adding an xy -layer to the X-cube model on T^3 . The large cube represents a unit cell of the original X-cube model, while the bold (blue) square is an elementary plaquette of the new layer α . The original z -oriented edges are split into two by the new layer. The local unitary S is a translation-invariant composition of commuting CNOT gates; a unit cell is pictured here. Arrows point from control qubit to target qubit. (b) Action of the unitary S on the qubits of a hexagonal prism 3-cell. The lower hexagonal plaquette belongs to the new z layer α . Bold (blue) edges are transverse to the y foliation, whereas double (green) edges are transverse to the x foliation.

Hamiltonian. ⁴ The resulting ground state is labeled $|\psi_{\text{XC}}'\rangle$. Next, we take the tensor product $|\psi_{\text{XC}}'\rangle \otimes |\psi_{\text{TC}}\rangle$ of the modified X-cube ground state with a toric code ground state on the new layer, and apply a local unitary transformation S to sew the two wave functions together into a larger X-cube wave function $\widetilde{|\psi_{\text{XC}}\rangle} = S(|\psi_{\text{XC}}'\rangle \otimes |\psi_{\text{TC}}\rangle)$. This procedure can be reversed or iterated to arbitrarily change the system size.

The unitary S is a product of CNOT gates whose control qubits belong to the new layer; the precise form depends on the geometry of the cellulation. In the simplest case, the intersection of the new layer α with the two transverse foliations is isomorphic to that of one of the adjacent layers β . Suppose α and β are z leaves. The region between α and β is divided by the x and y foliations into 3-cell prisms whose base polygons have an even number of sides alternating between edges transverse to the x and y foliations. The unitary S contains

⁴More formally, the edge can be split by initializing the new qubit j' in the state $|0\rangle$ and applying a CNOT with control i' and target j' .

a CNOT gate for each edge (the control qubit) in α , whose target qubit lies on the corresponding edge in β . Additionally, for each edge transverse to the y foliation in α , there are two additional CNOT gates whose targets are the adjacent edges transverse to α (oriented in the z direction) and connected to β . The transformation for a cubic lattice is illustrated in Fig. 2.6(a) and for the edges in a hexagonal prism 3-cell in (b) CNOT acts by conjugation as:

$$\begin{aligned} ZI &\rightarrow ZI & IZ &\leftrightarrow ZZ \\ XI &\leftrightarrow XX & IX &\rightarrow IX, \end{aligned} \tag{2.4}$$

where the first and second qubits are the control and target qubits, respectively. From this follows the action of S on the generators of the stabilizer group of $|\psi_{\text{XC}}\rangle' \otimes |\psi_{\text{TC}}\rangle$, i.e. the modified X-cube Hamiltonian terms combined with toric code Hamiltonian terms on the new layer. This action is described for a cubic lattice in Fig. 2.7. The prism geometry ensures that S maps the original stabilizer generators to a set of stabilizer generators corresponding to a larger X-cube model. It follows that $|\widetilde{\psi_{\text{XC}}}\rangle$ is indeed an X-cube ground state on the enlarged lattice.

In general, the leaves adjacent to the new layer α may not have isomorphic intersections with the other foliations, in which case the local unitary S which sews α into the cellulation may take a complicated form. However, we believe that such an operator generically exists. In Appendix 2.9 we present examples of explicit transformations to add generic leaves to the total foliations of $S^2 \times S^1$ and S^3 discussed in Sec. 2.4. For the other manifolds discussed, the even-faced prism construction is sufficient to freely change the system size.

2.5.2 Ground state degeneracy

Because the toric code ground space is degenerate (on topologically non-trivial surfaces), a branching structure is present in the renormalization process. For every surface added to a cellulation, there are 2^b possible toric code ground states which can be used as inputs for the RG transformation (where b is the \mathbb{Z}_2 Betti number of the added surface); each of these choices corresponds to a different sector of X-cube ground states. Thus, the entanglement renormalization picture naturally explains the subextensive growth of the X-cube ground space described by Eq. (2.2) and (2.3): the scaling of the ground space degeneracy on a manifold M arises from the non-trivial homology of the leaves that foliate M .

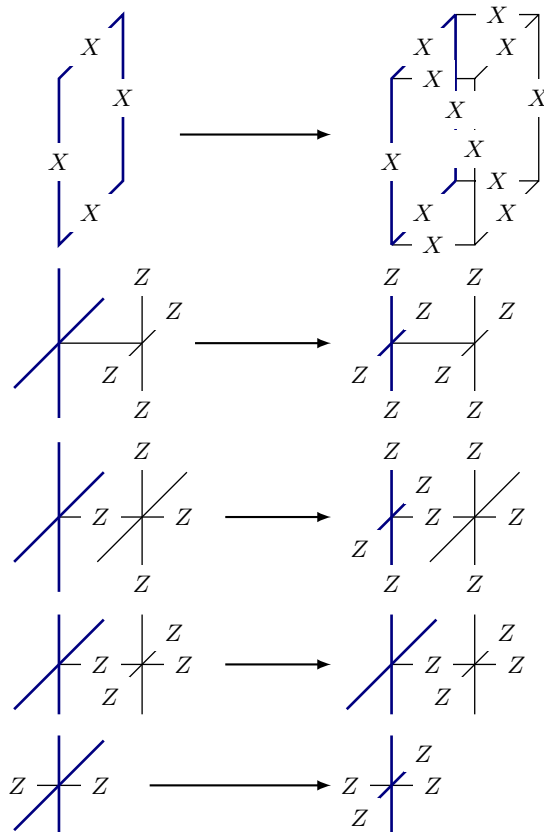


Figure 2.7: Adjoint action of S on stabilizers of $|\psi_{\text{XC}}\rangle' \otimes |\psi_{\text{TC}}\rangle$. As in Fig. 2.6, bold (blue) lines correspond to edges of the new layer. Terms not pictured are unchanged.

The constant c in Eq. (2.3) can be understood by considering the minimal cellulation (e.g. $L_x = L_y = L_z = 1$) and viewing larger systems as entanglement RG outgrowths of this seed system. (For the case of $\Sigma_g \times S^1$ and cellulations of the half-twist manifold that contain at least one Klein bottle, the minimal cellulation obtainable from disentangling toric code layers contains more than 3 leaves.) The X-cube Hilbert space can be viewed as the physical subspace of an extended Hilbert space which is a tensor product of toric code Hilbert spaces on each leaf, corresponding to two qubits per edge. X-cube ground states can be written as $|\psi_{\text{XC}}\rangle = \prod_e P_e \otimes_\ell |\psi_{\text{TC}}^\ell\rangle$, where ℓ runs over leaves, e runs over edges, $|\psi_{\text{TC}}^\ell\rangle$ is a toric code ground state on leaf ℓ , and $P_e = 1 + Z_i Z_j$ where i and j are the two qubits on edge e . The product $\prod_e P_e$ projects onto the physical subspace, and maps products of coinciding Wilson loops to the identity operator. Thus, for the seed system, c counts the redundancies in logical qubits of the minimal leaves, or in other words, the

number of leaf intersections which correspond to non-trivial first homology classes of both leaves. Thus, c is sensitive to the foliating structure on M , and in particular to the way the foliations intersect. These considerations can be used to compute the values of c shown in Table 2.1 and explain the dependence of c for the half-twist manifold on the presence or absence of Klein bottles in the cellulation, as discussed in Sec. 2.4.3

2.5.3 Relation to the Haah code

The RG transformation presented here is related to a similar transformation for the Haah code studied in [11]. The Haah code is a type-II fracton model defined on a torus with non-trivial ground-state degeneracy, fractal-like excitation structure, and no string-like logical operators. The procedure of [11] employs a local unitary transformation U to decouple the Haah code Hamiltonian H_A on a cubic lattice of size $2L$ into two Hamiltonians H_A and H_B acting separately on interlacing sublattices of size L . Similar to the Haah code, H_B is a type-II fracton model with fractal-like excitations. Conversely however, H_B admits an RG transformation in which the model on a lattice of size $2L$ is related via a local unitary transformation V to two copies of itself on interwoven size L sublattices. This information is summarized as follows:

$$\begin{aligned} UH_A(2L)U^\dagger &\cong H_A(L) + H_B(L) \\ VH_B(2L)V^\dagger &\cong H_B(L) + H_B(L), \end{aligned} \tag{2.5}$$

where $H \cong H'$ implies that H and H' have coinciding ground spaces corresponding to identical stabilizer groups. The X-cube RG transformation can be cast in the same light: H_A is the X-cube Hamiltonian, whereas H_B corresponds to three mutually perpendicular decoupled stacks of toric codes. We note that the branching structure of Eq. (2.5) indicates that X-cube ground states bear exact representations as branching MERA tensor networks [8, 9].

2.5.4 Entanglement structure

Moreover, the existence of this RG transformation underlies the entanglement structure of the X-cube ground states. Because local unitary transformations do not modify the long-range entanglement structure, the entanglement entropy of a region R can be heuristically understood as a combination of contributions from underlying toric code layers. The subleading linear correction to entanglement entropy for the X-cube model thus corresponds

to a combination of the constant topological corrections present in toric code ground states [17, 19]. Interestingly, the Haah code also exhibits subleading linear corrections to entanglement entropy [15, 21]. Whether these corrections for the Haah code can be similarly understood from the entanglement RG perspective is not clear.

2.6 Type-I fracton phases

A paradigmatic understanding of 2D quantum phases in the absence of symmetry was reached by the authors of [6]. In this framework, quantum phases are characterized by the pattern of long-range entanglement exhibited by their ground states, and correspond to unique 2D topological orders [39]. Two ground states are considered to represent the same quantum phase of matter if they are related by a generalized local unitary (gLU) transformation, which is a finite-depth quantum circuit augmented with free addition or removal of product states. System size can thus be altered by adding or removing product states and performing an appropriate local unitary transformation. In this sense, unentangled product states can be viewed as free ‘resources’ for 2D quantum phases. However, in 3D, the gLU paradigm is unsatisfactory because it over-refines the space of ground states. While conventional 3D topological orders such as discrete gauge theories represent gLU equivalence classes, exotic fracton models such as the X-cube model and the Haah code (along with simple decoupled stacks of 2D topological orders) do not represent unique equivalence classes because ground states of different system sizes are not gLU-equivalent. The gLU framework is hence inadequate in 3D as it does not allow for a notion of thermodynamic limit.

For this reason we are motivated to propose a definition of *type-I fracton phase* which incorporates the RG perspective of the X-cube model. In particular, we define a type-I fracton phase as a class of models exhibiting a thermodynamic limit whose ground state manifolds can be transformed into one another via tensor product with an arbitrary number of 2D topological ground states followed by the action of a finite-depth quantum circuit. In other words, we consider 2D topological orders as free resources for 3D fracton phases. In this sense, the X-cube model is a zero-correlation length fixed-point Hamiltonian under the entanglement RG transformation, and a representative model of a type-I fracton phase.

We note that the definition proposed here classifies decoupled stacks of 2D topological phases as trivial 3D phases. Moreover, it unifies the notions of type-I fracton order and conventional 3D topological order, where product state resources may be viewed as trivial 2D topological orders. The definition we propose is closely related to and inspired by the s -sourcery framework introduced in [33], which employs a more general notion of ‘resource’ state and proposes a classification of all long-range entangled 3D quantum matter. The X-cube model provides a new example of a phase with matrix-valued s .

2.7

The \mathbb{Z}_N version of the X-cube model, as first discussed in [31], is defined using the generalized Pauli operators $Z|p\rangle = \omega^p|p\rangle$ and $X|p\rangle = |p+1 \bmod N\rangle$, which act on dimension- N local Hilbert spaces on each edge and obey the relations $ZX = \omega XZ$ and $Z^\dagger X = \omega^{-1} X Z^\dagger$ where $\omega = e^{2\pi i/N}$. In this section, we extend the \mathbb{Z}_N model to general 3-manifolds cellulated by sets of transversely intersecting foliations, as in Sec. 2.4. To define the model it is necessary to orient each edge; reversing the orientation of an edge corresponds to inversion in \mathbb{Z}_N , given by $Z \leftrightarrow Z^\dagger$ and $X \leftrightarrow X^\dagger$. The Hamiltonian on any compact 3-manifold M takes the form

$$H = - \sum_v (A_v^x + A_v^y + A_v^z + \text{h.c.}) - \sum_c (B_c + B_c^\dagger). \quad (2.6)$$

As in the \mathbb{Z}_2 case, A_v^μ is a cross-shaped operator at vertex v whereas B_c is a product of operators over the edges of the 3-cell c . The action of A_v^μ on an edge adjacent to v is determined by the orientation and direction (x , y or z) of the edge. A_v^x acts as Z (Z^\dagger) on z -directed (y -directed) edges whose orientations point towards v , and as Z^\dagger (Z) on y -directed (z -directed) edges whose orientations point away from v , and likewise for cyclic permutations of x , y , and z . This is shown in Fig. 2.8(a) for a particular choice of orientations. On the other hand, to define the 3-cell term B_c , the vertices of c are first given an A-B bipartition. A given 3-cell c is guaranteed to be bipartite as a graph since all faces of c have edges which sequentially alternate between two directions μ and ν (due to the foliating structure of the cellulation). B_c is defined to act as X on edges oriented from A to B vertices, and as X^\dagger on edges oriented from B to A vertices (see Fig. 2.8(b)). The Hamiltonian terms mutually commute and constitute stabilizer generators for a dimension- N qudit stabilizer code.

The physics of the \mathbb{Z}_2 model generalizes in a straightforward fashion to the

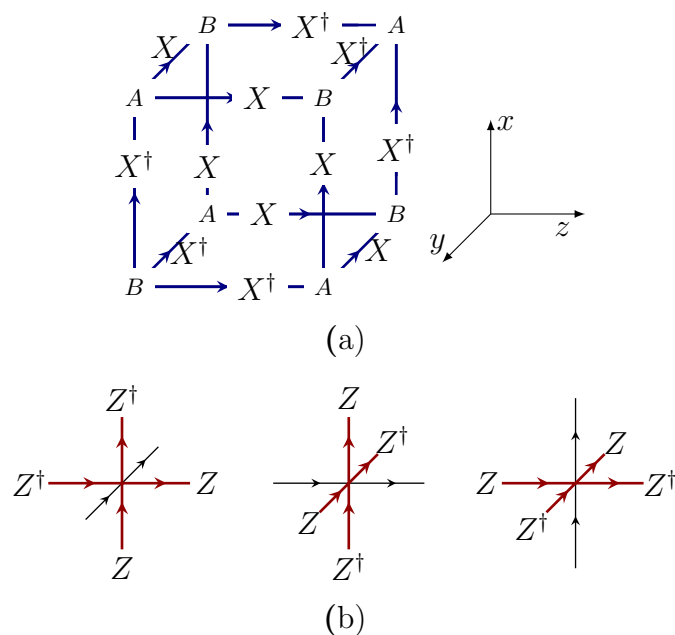


Figure 2.8: (a) Action of 3-cell operator B_c in \mathbb{Z}_N X-cube Hamiltonian on a cubic 3-cell. Vertices of the cube have been given an A-B bipartition. (b) Cross-shaped operators A_v^μ of the \mathbb{Z}_N X-cube model Hamiltonian.

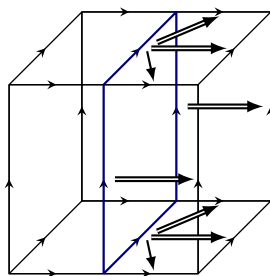


Figure 2.9: Adding a layer to the \mathbb{Z}_N X-cube model on a torus, as in Fig. 2.6. For the \mathbb{Z}_N case, S is a translation-invariant product of commuting C and C^\dagger operators; shown here is a unit cell. Arrows point from control qudit to target qudit; a single shaft indicates C whereas a double shaft corresponds to C^\dagger .

\mathbb{Z}_N setting, in which there are N species of string and membrane operators obeying respective \mathbb{Z}_N fusion rules. For prime N , the ground state degeneracy behaves identically, except that logical qubits are replaced with dimension- N logical qudits. In particular, Eq. (2.3) generalizes to the rule

$$\log_N \text{GSD} = b_x L_x + b_y L_y + b_z L_z - c \quad (2.7)$$

where b_μ is the first Betti number with \mathbb{Z}_N coefficients [1]. For composite (non-prime) N , the formula for ground state degeneracy is more complicated in general [5], since the ground space is not necessarily a tensor product of logical qudit Hilbert spaces.

In general, the scaling of the GSD can be understood in terms of an entanglement RG transformation which generalizes the discussion of Sec. 2.5. For the \mathbb{Z}_N X-cube model, generalized \mathbb{Z}_N toric code states serve as two-dimensional resource states in the procedure (each contributing b logical qudits for N prime). Such transformations exist for all of the foliations we have discussed. As in the \mathbb{Z}_2 case, to add a layer we first split the qudits on edges i intersecting the new layer into pairs of qudits i' and j' , and add $Z_{i'}^\dagger Z_{j'}$ and $Z_{i'} Z_{j'}^\dagger$ stabilizer terms to the Hamiltonian and modify it as $Z_i \rightarrow Z_{i'}$ and $X_i \rightarrow X_{i'} X_{j'}$. We then take the tensor product of the resulting \mathbb{Z}_N X-cube state with a \mathbb{Z}_N toric code state on the new layer, and apply a local unitary S . The operator S is constructed from 2-qudit gates C and C^\dagger (see Fig. 2.9 for the cubic lattice case), which are generalizations of the CNOT gate and act as $C|p, q\rangle = |p, q + p\rangle$ and $C^\dagger|p, q\rangle = |p, q - p\rangle$. The adjoint action of C is given by

$$\begin{aligned} ZI &\rightarrow ZI & IZ &\rightarrow Z^\dagger Z \\ XI &\rightarrow XX & IX &\rightarrow IX \end{aligned} \quad (2.8)$$

whereas for C^\dagger by

$$\begin{aligned} ZI &\rightarrow ZI & IZ &\rightarrow ZZ \\ XI &\rightarrow XX^\dagger & IX &\rightarrow IX. \end{aligned} \quad (2.9)$$

It can be checked that S maps the tensor product state to an enlarged \mathbb{Z}_N X-cube ground state.

2.8 Discussion

Our work on the X-cube model suggests that fracton physics could be regarded as a new kind of topological physics generalizing the traditional liquid

topological order [43, 44]. We conjecture the existence of the following X -cube TQFT.

A singular compact total foliation (SCTF) Λ of a 3-manifold M consists of singular subsets K_μ , $\mu = x, y, z$ (possibly empty) and three transversely intersecting sets of closed surfaces $\{\Lambda_x, \Lambda_y, \Lambda_z\}$ foliating the respective complements $M \setminus K_\mu$. K consists of singular leaves that are either finitely many points, a link,⁵ or some $G \times S^1$ where G is a trivalent graph. Two SCTFs $\Lambda^{(1)}$ and $\Lambda^{(2)}$ on M are considered to be equivalent if there exists a diffeomorphism f of M that sends $\Lambda^{(1)}$ to $\Lambda^{(2)}$ compatible with the singular leaves and the RG moves that define the fracton phase. We believe every orientable closed 3-manifold M has an SCTF. Given an SCTF Λ on a 3-manifold M , a finite (L_x, L_y, L_z) -version of Λ is a choice of L_x , L_y , and L_z many leaves from the three stacks $\{\Lambda_x, \Lambda_y, \Lambda_z\}$, respectively, where L_x, L_y , and L_z are natural numbers.⁶

An SCTF-TQFT will assign to each pair (M, Λ) , where Λ is an SCTF on the three manifold M , an infinite-dimensional Hilbert space $V(M, \Lambda)$ that is constructed as the limit of a sequence of finite versions of Λ . Moreover, the GSD on the finite version (L_x, L_y, L_z) depends only on the topology of M , the topology of the leaf surfaces, and the topology of the intersections of the leaves. The collection of Hilbert spaces $V(M, \Lambda)$ should satisfy some generalization of the usual TQFT axioms, and $V(M, \Lambda)$ is a representation of all diffeomorphisms of M that preserve the SCTF Λ . We will leave the construction of such an SCTF-TQFT for the X -cube model to the future.

As comparison, the authors of [32] advocate that fracton models should be regarded as representing geometric orders. Their approach was to consider how lattice geometry affects the low-energy physics and phase of matter as defined by generalized local unitary (gLU) equivalence.

It would be interesting to understand which components of this discussion generalize to other fracton models. For some of the type-I fracton models, a similar RG procedure can be identified; thus the SCTF structure may apply to these fracton models as well. On the other hand, type-II fracton models such as the Haah code do not fall within this framework. Moreover there is

⁵A link is an embedding of a finite number of circles into a 3-manifold, which may not intersect but may be linked or knotted.

⁶One could also consider 3+1D models with more or fewer than three sets of leaves.

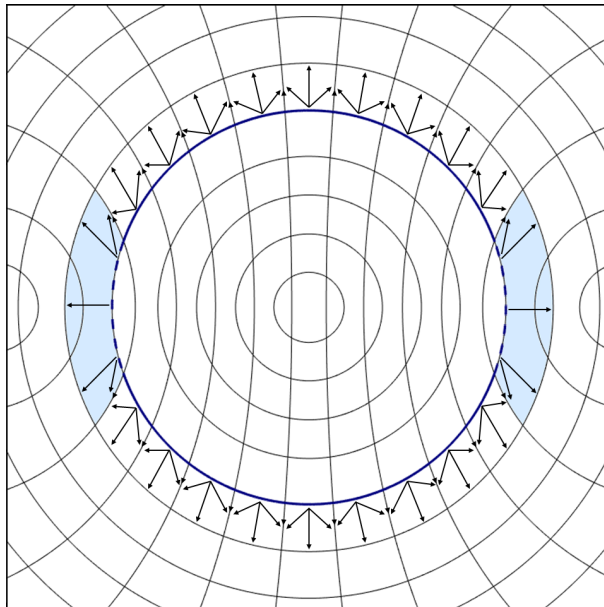


Figure 2.10: Stereographically projected spherical cross-section of the local unitary operator S , which sews the dark-blue toric code layer into the X-cube lattice, as used in the RG transformation for $S^2 \times S^1$. S is a product of CNOT gates corresponding to the arrows, which point from a control qubit to a target qubit. The arrows on the edges indicate gates that act on the edges oriented into (and out of) the plane and located at the adjacent vertices. Most of the CNOT gates are acting within cubes (depicted as curved squares above); within these cubes S is the same as in Fig. 2.6(a). The toric code plaquette operators extending out of the plane from the dashed blue lines are mapped to composite 3-cell operators on the 3-cells extending out of the plane from the shaded light-blue region.

a class of gapless $U(1)$ fracton models [24–28, 41]. It would be interesting to identify a substitute for the SCTF structure on general 3-manifolds for these related models.

2.9 Appendix: Entanglement renormalization for 3-sphere and

In this appendix we present examples of explicit transformations that add layers of toric code states to the X-cube model defined on $S^2 \times S^1$ and S^3 . In Fig. 2.10 we depict a unitary transformation that sews a toroidal layer into the cellulation of $S^2 \times S^1$ (Sec. 2.4.1).

In Fig. 2.11 we illustrate the unitary transformation S that sews a spherical layer into the cellulation of S^3 (Sec. 2.4.2). Below we list all of the gates comprising S that act on the qubits shown in Fig. 2.11(b-c): $\text{CNOT}_{1,45}$, $\text{CNOT}_{2,46}$, $\text{CNOT}_{3,47}$, $\text{CNOT}_{4,48}$, $\text{CNOT}_{5,49}$, $\text{CNOT}_{6,50}$, $\text{CNOT}_{7,51}$, $\text{CNOT}_{8,52}$,

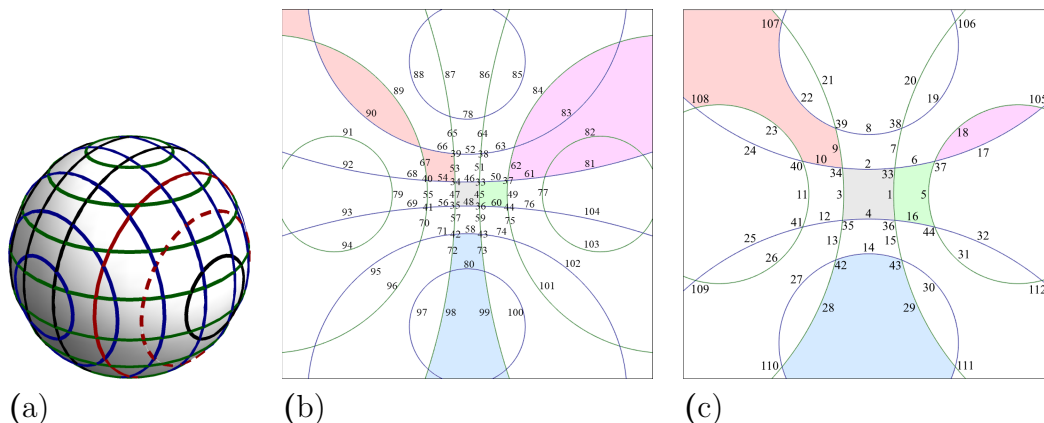


Figure 2.11: (a) The equatorial cross-section of S^3 from Fig. 2.5(b). We emphasize that the sphere drawn in (a) is not a leaf; it is merely a convenient cross-section. (b-c) Stereographic projections of spherical leaves embedded in S^3 . (b) and (c) intersect the equator (i.e. the spherical cross-section shown in (a)) at the solid and dashed red lines in (a), respectively. The green and blue lines represent links of the cellulation lying along the respective red-colored leaves in (a). The numbered vertices correspond to links that connect the two leaves, and thus share an index in (b) and (c). The unitary S sews a toric code state (on the dashed red leaf) into the X-cube model on S^3 . S consists of a product of CNOT gates, and maps toric code plaquette operators on the dashed red layer to composite 3-cell operators lying between the two leaves. Some of the faces of these composite operators have been shaded in the figures as example. Plaquettes in (b) and (c) with corresponding colors indicate faces that belong to the same composite 3-cell.

CNOT_{9,53}, CNOT_{10,54}, CNOT_{11,55}, CNOT_{12,56}, CNOT_{13,57}, CNOT_{14,58}, CNOT_{15,59},
 CNOT_{16,60}, CNOT_{17,61}, CNOT_{17,81}, CNOT_{18,62}, CNOT_{18,84}, CNOT_{19,63}, CNOT_{19,83},
 CNOT_{20,64}, CNOT_{20,86}, CNOT_{21,65}, CNOT_{21,87}, CNOT_{22,66}, CNOT_{22,90}, CNOT_{23,67},
 CNOT_{23,89}, CNOT_{24,68}, CNOT_{24,92}, CNOT_{25,69}, CNOT_{25,93}, CNOT_{26,70}, CNOT_{26,96},
 CNOT_{27,71}, CNOT_{27,95}, CNOT_{28,72}, CNOT_{28,98}, CNOT_{29,73}, CNOT_{29,99}, CNOT_{30,74},
 CNOT_{30,102}, CNOT_{31,75}, CNOT_{31,101}, CNOT_{32,76}, CNOT_{32,104}, CNOT_{1,33}, CNOT_{1,36},
 CNOT_{3,34}, CNOT_{3,35}, CNOT_{5,37}, CNOT_{5,44}, CNOT_{7,33}, CNOT_{7,38}, CNOT_{9,34}, CNOT_{9,39},
 CNOT_{11,40}, CNOT_{11,41}, CNOT_{13,35}, CNOT_{13,42}, CNOT_{15,36}, CNOT_{15,43}, CNOT_{18,37},
 CNOT_{18,105}, CNOT_{20,38}, CNOT_{20,106}, CNOT_{21,39}, CNOT_{21,107}, CNOT_{23,40}, CNOT_{23,108},
 CNOT_{26,41}, CNOT_{26,109}, CNOT_{28,42}, CNOT_{28,110}, CNOT_{29,43}, CNOT_{29,111}, CNOT_{31,44},
 and CNOT_{31,112}.

References

- [1] The n^{th} Betti number with \mathbb{Z}_p coefficients of a manifold M is defined to be the rank of the n^{th} homology group $H_n(M, \mathbb{Z}_p)$ over \mathbb{Z}_p . For the case of

connected orientable surfaces, the first Betti number with \mathbb{Z}_p coefficients is equal to twice the genus.

- [2] S. Bravyi, B. Leemhuis, and B.M. Terhal. “Topological order in an exactly solvable 3D spin model”. In: *Annals of Physics* 326 (Apr. 2011), pp. 839–866. DOI: [10.1016/j.aop.2010.11.002](https://doi.org/10.1016/j.aop.2010.11.002).
- [3] Andrew Casson and Steven Bleiler. *Automorphisms of Surfaces after Nielsen and Thurston*. Cambridge University Press, 1988. ISBN: 0521349850, 9780521349857.
- [4] Claudio Chamon. “Quantum Glassiness in Strongly Correlated Clean Systems: An Example of Topological Overprotection”. In: *Phys. Rev. Lett.* 94 (4 Jan. 2005), p. 040402. DOI: [10.1103/PhysRevLett.94.040402](https://doi.org/10.1103/PhysRevLett.94.040402). URL: <https://link.aps.org/doi/10.1103/PhysRevLett.94.040402>.
- [5] A. P. O. Chan, J. C. Y. Teo, and S. Ryu. “Topological phases on non-orientable surfaces: twisting by parity symmetry”. In: *New Journal of Physics* 18.3, 035005 (Mar. 2016), p. 035005. DOI: [10.1088/1367-2630/18/3/035005](https://doi.org/10.1088/1367-2630/18/3/035005).
- [6] Xie Chen, Zheng-Cheng Gu, and Xiao-Gang Wen. “Local unitary transformation, long-range quantum entanglement, wave function renormalization, and topological order”. In: *Phys. Rev. B* 82 (15 Oct. 2010), p. 155138. DOI: [10.1103/PhysRevB.82.155138](https://doi.org/10.1103/PhysRevB.82.155138). URL: <https://link.aps.org/doi/10.1103/PhysRevB.82.155138>.
- [7] Trithep Devakul, S. A. Parameswaran, and S. L. Sondhi. “Correlation function diagnostics for type-I fracton phases”. In: *arXiv:1709.10071* (Sept. 2017). URL: <http://arxiv.org/abs/1709.10071>
- [8] G. Evenbly and G. Vidal. “Class of Highly Entangled Many-Body States that can be Efficiently Simulated”. In: *Phys. Rev. Lett.* 112 (24 June 2014), p. 240502. DOI: [10.1103/PhysRevLett.112.240502](https://doi.org/10.1103/PhysRevLett.112.240502). URL: <https://link.aps.org/doi/10.1103/PhysRevLett.112.240502>.
- [9] G. Evenbly and G. Vidal. “Scaling of entanglement entropy in the (branching) multiscale entanglement renormalization ansatz”. In: *Phys. Rev. B* 89 (23 June 2014), p. 235113. DOI: [10.1103/PhysRevB.89.235113](https://doi.org/10.1103/PhysRevB.89.235113). URL: <https://link.aps.org/doi/10.1103/PhysRevB.89.235113>.
- [10] Daniel Gottesman. “Stabilizer Codes and Quantum Error Correction”. In: *arXiv:quant-ph/9705052* (May 1997). URL: <http://arxiv.org/abs/quant-ph/9705052>.
- [11] Jeongwan Haah. “Bifurcation in entanglement renormalization group flow of a gapped spin model”. In: *Phys. Rev. B* 89 (7 Feb. 2014), p. 075119. DOI: [10.1103/PhysRevB.89.075119](https://doi.org/10.1103/PhysRevB.89.075119). URL: <https://link.aps.org/doi/10.1103/PhysRevB.89.075119>.

- [12] Jeongwan Haah. “Local stabilizer codes in three dimensions without string logical operators”. In: *Phys. Rev. A* 83 (4 Apr. 2011), p. 042330. DOI: [10.1103/PhysRevA.83.042330](https://doi.org/10.1103/PhysRevA.83.042330). URL: <https://link.aps.org/doi/10.1103/PhysRevA.83.042330>.
- [13] Gábor B. Halász, Timothy H. Hsieh, and Leon Balents. “Fracton Topological Phases from Strongly Coupled Spin Chains”. In: *arXiv:1707.02308* (July 2017). URL: <http://arxiv.org/abs/1707.02308>.
- [14] Detlef Hardorp. *All Compact Orientable Three Dimensional Manifolds Admit Total Foliations*. American Mathematical Soc., 1980. ISBN: 978-0-8218-2233-3.
- [15] H. He et al. “Entanglement Entropy From Tensor Network States for Stabilizer Codes”. In: (Oct. 2017). arXiv: [1710.04220](https://arxiv.org/abs/1710.04220).
- [16] Timothy H. Hsieh and Gábor B. Halász. “Fractons from partons”. In: *Phys. Rev. B* 96 (16 Oct. 2017), p. 165105. DOI: [10.1103/PhysRevB.96.165105](https://doi.org/10.1103/PhysRevB.96.165105). URL: <https://link.aps.org/doi/10.1103/PhysRevB.96.165105>.
- [17] Alexei Kitaev and John Preskill. “Topological entanglement entropy”. In: *Phys. Rev. Lett.* 96 (2006), p. 110404. DOI: [10.1103/PhysRevLett.96.110404](https://doi.org/10.1103/PhysRevLett.96.110404).
- [18] Na Lei et al. “Quadrilateral and hexahedral mesh generation based on surface foliation theory”. In: *Computer Methods in Applied Mechanics and Engineering* 316.Supplement C (2017). Special Issue on Isogeometric Analysis: Progress and Challenges, pp. 758–781. ISSN: 0045-7825. DOI: [10.1016/j.cma.2016.09.044](https://doi.org/10.1016/j.cma.2016.09.044). URL: <http://www.sciencedirect.com/science/article/pii/S0045782516312762>.
- [19] M. Levin and X.-G. Wen. “Detecting Topological Order in a Ground State Wave Function”. In: *Phys. Rev. Lett.* 96.11, 110405 (Mar. 2006), p. 110405. DOI: [10.1103/PhysRevLett.96.110405](https://doi.org/10.1103/PhysRevLett.96.110405).
- [20] Han Ma et al. “Fracton topological order via coupled layers”. In: *Phys. Rev. B* 95 (24 June 2017), p. 245126. DOI: [10.1103/PhysRevB.95.245126](https://doi.org/10.1103/PhysRevB.95.245126). URL: <https://link.aps.org/doi/10.1103/PhysRevB.95.245126>.
- [21] Han Ma et al. “Topological Entanglement Entropy of Fracton Stabilizer Codes”. In: (2017). arXiv: [1710.01744](https://arxiv.org/abs/1710.01744).
- [22] Olga Petrova and Nicolas Regnault. “A simple anisotropic three-dimensional quantum spin liquid with fracton topological order”. In: *arXiv:1709.10094* (Sept. 2017). URL: <http://arxiv.org/abs/1709.10094>.

- [23] Abhinav Prem, Jeongwan Haah, and Rahul Nandkishore. “Glassy quantum dynamics in translation invariant fracton models”. In: *Phys. Rev. B* 95 (15 Apr. 2017), p. 155133. DOI: [10.1103/PhysRevB.95.155133](https://doi.org/10.1103/PhysRevB.95.155133). URL: <https://link.aps.org/doi/10.1103/PhysRevB.95.155133>.
- [24] Michael Pretko. “Generalized electromagnetism of subdimensional particles: A spin liquid story”. In: *Phys. Rev. B* 96 (3 July 2017), p. 035119. DOI: [10.1103/PhysRevB.96.035119](https://doi.org/10.1103/PhysRevB.96.035119). URL: <https://link.aps.org/doi/10.1103/PhysRevB.96.035119>.
- [25] Michael Pretko. “Higher-Spin Witten Effect and 2d Chiral Fracton Phases”. In: *arXiv:1707.03838* (July 2017). URL: <http://arxiv.org/abs/1707.03838>
- [26] Michael Pretko. “Subdimensional particle structure of higher rank $U(1)$ spin liquids”. In: *Phys. Rev. B* 95 (11 Mar. 2017), p. 115139. DOI: [10.1103/PhysRevB.95.115139](https://doi.org/10.1103/PhysRevB.95.115139). URL: <https://link.aps.org/doi/10.1103/PhysRevB.95.115139>.
- [27] Michael Pretko and Leo Radzihovsky. “Fracton-Elasticity Duality”. In: *arXiv:1711.11044* (Nov. 2017). URL: <http://arxiv.org/abs/1711.11044>.
- [28] Alex Rasmussen, Yi-Zhuang You, and Cenke Xu. “Stable Gapless Bose Liquid Phases without Any Symmetry”. In: *arXiv:1601.08235* (Jan. 2016). URL: <http://arxiv.org/abs/1601.08235> (visited on 02/02/2016).
- [29] A. T. Schmitz et al. “Recoverable Information and Emergent Conservation Laws in Fracton Stabilizer Codes”. In: *arXiv:1712.02375* (Dec. 2017). URL: <http://arxiv.org/abs/1712.02375>.
- [30] Bowen Shi and Yuan-Ming Lu. “Decipher the nonlocal entanglement entropy of fracton topological orders”. In: *arXiv:1705.09300* (May 2017). URL: <http://arxiv.org/abs/1705.09300>.
- [31] Kevin Slagle and Yong Baek Kim. “Quantum field theory of X-cube fracton topological order and robust degeneracy from geometry”. In: *Phys. Rev. B* 96 (19 Nov. 2017), p. 195139. DOI: [10.1103/PhysRevB.96.195139](https://doi.org/10.1103/PhysRevB.96.195139). URL: <https://link.aps.org/doi/10.1103/PhysRevB.96.195139>.
- [32] Kevin Slagle and Yong Baek Kim. “X-Cube Model on Generic Lattices: New Phases and Geometric Order”. In: *arXiv:1712.04511* (Dec. 2017). URL: <http://arxiv.org/abs/1712.04511>.
- [33] Brian Swingle and John McGreevy. “Renormalization group constructions of topological quantum liquids and beyond”. In: *Phys. Rev. B* 93 (4 Jan. 2016), p. 045127. DOI: [10.1103/PhysRevB.93.045127](https://doi.org/10.1103/PhysRevB.93.045127). URL: <https://link.aps.org/doi/10.1103/PhysRevB.93.045127>.

- [34] G. Vidal. “Entanglement Renormalization”. In: *Phys. Rev. Lett.* 99.22 (2007), p. 220405. DOI: [10.1103/PhysRevLett.99.220405](https://doi.org/10.1103/PhysRevLett.99.220405).
- [35] S. Vijay. “Isotropic Layer Construction and Phase Diagram for Fracton Topological Phases”. In: (Jan. 2017). arXiv: [1701.00762](https://arxiv.org/abs/1701.00762).
- [36] Sagar Vijay and Liang Fu. “A Generalization of Non-Abelian Anyons in Three Dimensions”. In: *arXiv:1706.07070* (June 2017). URL: <http://arxiv.org/abs/1706.07070>.
- [37] Sagar Vijay, Jeongwan Haah, and Liang Fu. “A new kind of topological quantum order: A dimensional hierarchy of quasiparticles built from stationary excitations”. In: *Phys. Rev. B* 92 (23 Dec. 2015), p. 235136. DOI: [10.1103/PhysRevB.92.235136](https://doi.org/10.1103/PhysRevB.92.235136). URL: <http://link.aps.org/doi/10.1103/PhysRevB.92.235136>.
- [38] Sagar Vijay, Jeongwan Haah, and Liang Fu. “Fracton topological order, generalized lattice gauge theory, and duality”. In: *Phys. Rev. B* 94 (23 Dec. 2016), p. 235157. DOI: [10.1103/PhysRevB.94.235157](https://doi.org/10.1103/PhysRevB.94.235157). URL: <https://link.aps.org/doi/10.1103/PhysRevB.94.235157>.
- [39] Xiao-Gang Wen. “A theory of 2+1D bosonic topological orders”. In: *National Science Review* 3.1 (2016), pp. 68–106. DOI: [10.1093/nsr/nwv077](https://doi.org/10.1093/nsr/nwv077). URL: <http://dx.doi.org/10.1093/nsr/nwv077>.
- [40] Dominic J. Williamson. “Fractal symmetries: Ungauging the cubic code”. In: *Phys. Rev. B* 94 (15 Oct. 2016), p. 155128. DOI: [10.1103/PhysRevB.94.155128](https://doi.org/10.1103/PhysRevB.94.155128). URL: <https://link.aps.org/doi/10.1103/PhysRevB.94.155128>.
- [41] Cenke Xu. “Gapless bosonic excitation without symmetry breaking: An algebraic spin liquid with soft gravitons”. In: *Phys. Rev. B* 74 (22 Dec. 2006), p. 224433. DOI: [10.1103/PhysRevB.74.224433](https://doi.org/10.1103/PhysRevB.74.224433). URL: <http://link.aps.org/doi/10.1103/PhysRevB.74.224433>.
- [42] Beni Yoshida. “Exotic topological order in fractal spin liquids”. In: *Phys. Rev. B* 88 (12 Sept. 2013), p. 125122. DOI: [10.1103/PhysRevB.88.125122](https://doi.org/10.1103/PhysRevB.88.125122). URL: <https://link.aps.org/doi/10.1103/PhysRevB.88.125122>.
- [43] B. Zeng et al. “Quantum Information Meets Quantum Matter – From Quantum Entanglement to Topological Phase in Many-Body Systems”. In: (Aug. 2015). arXiv: [1508.02595](https://arxiv.org/abs/1508.02595)
- [44] Bei Zeng and Xiao-Gang Wen. “Gapped quantum liquids and topological order, stochastic local transformations and emergence of unitarity”. In: *Phys. Rev. B* 91 (12 Mar. 2015), p. 125121. DOI: [10.1103/PhysRevB.91.125121](https://doi.org/10.1103/PhysRevB.91.125121). URL: <https://link.aps.org/doi/10.1103/PhysRevB.91.125121>.

UNIVERSAL ENTANGLEMENT SIGNATURES IN FOLIATED FRACTON PHASES

3.1 Introduction

Fracton models, a collection of gapped three-dimensional lattice models [1, 5, 14, 15, 18, 26, 28, 41, 43–47, 53], are known to exhibit a range of exotic properties [2, 7, 17, 27, 29, 37, 38, 42, 50, 54]. First, they harbor a ground state degeneracy (GSD) that is stable against arbitrary local perturbations and increases exponentially with linear system size. More strikingly, fracton models contain quasi-particle excitations whose motion is restricted to a sub-dimensional manifold (a plane or a line) or which cannot move individually at all [1, 14, 46]. Due to these constraints on quasi-particle mobility, the models have unusually slow dynamics even in the absence of disorder [2, 29]. Furthermore, for the ground states of these models, the entanglement entropy of a region in the bulk contains a term that scales linearly with the size of the region, in addition to the dominant area law term which scales quadratically [17, 27, 38].

Among these properties, which ones are universal characteristics of fracton topological phases? This is an important question because the study of fracton phases thus far has been mostly focused on specific exactly solvable models. Once we move away from the exactly solvable points, we want to know which sets of properties remain and are indicative of the underlying fracton order. Moreover, given two generic interacting many-body models, we want to be able to determine whether or not they belong to the same fracton phase by comparing their universal properties.

For conventional (gapped) topological phases in 2D and 3D, such as fractional quantum Hall systems and discrete gauge theories, an understanding of the universal properties is more or less complete. These properties include the fractional quasi-particle content and their self- and mutual braiding statistics [20], the (finite) ground state degeneracy as a function of the topology of the spatial manifold [48, 49], the perimeter scaling law of Wilson loop operators in the ground state [51], the topological entanglement entropy [12, 21, 22] etc.

At the same time, it is also clear that some properties of specific models are merely accidental and are not universal to the phase. Such accidental properties include—assuming there is no extra symmetry requirement on the models—a uniform Berry curvature in quantum Hall systems, the fact that electric and magnetic charges have the same energy in discrete gauge theories, an expectation value of unity for Wilson loops in the ground state, etc.

Fracton models lie beyond the conventional framework of gapped topological phases, which is made clear by the fact that their ground state degeneracy increases with system size. To extend the idea of universality to fracton models, we must first define the notion of a fracton phase. In [40], we generalized the notion of gapped topological phases to encompass fractons by allowing the addition of gapped two-dimensional resource layers when smoothly evolving between two three-dimensional gapped models. According to this definition, a stack of decoupled layers of 2D topological orders belongs to a trivial phase whereas the X-cube model belongs to a non-trivial phase [40]. It can be shown that the kagome lattice X-cube model [43], the checkerboard model [47], and the 3D toric code model (with trivial foliation structure) belong to non-trivial phases according to this definition as well. Due to the deep connection of this definition with the foliation structure of the underlying spatial manifold, we will refer to such phases as *foliated fracton phases*.

In accordance with this definition, in this paper we identify certain universal properties of these phases that remain invariant as one moves throughout each phase. We propose a multi-partite entanglement quantity (Fig. 3.3) calculated from the ground state wave function, generalizing the proposal of topological entanglement entropy [12, 21, 22] to characterize conventional topological orders. We argue for the universality of this quantity and show that it attains positive constant value (Table 3.1) in non-trivial phases that contain the X-cube model [47] on cubic and stacked-kagome lattices [43], the checkerboard model [47], the Chamon model [5], and the 3D toric code model [4] respectively. The multi-partite entanglement quantity we design is in general non-topological in the sense that its value can change if the shape of the regions involved changes in an arbitrary way. However it does remain invariant provided it follows the foliation structure of the fracton model, which can be determined from simpler entanglement quantities calculated from the ground state wave function.

The paper is structured as follows. In Sec. [3.2](#) we review the definition of foliated fracton phases and explain its motivation and applicability. Based on this definition, in Sec. [3.3](#) we state the criteria that must be satisfied by an entanglement quantity in order to be universal. In Sec. [3.4](#) we present a scheme for calculating such a quantity and the calculation results for a handful of relevant models. We conclude with a discussion of open questions in section Sec. [3.5](#)

3.2 Foliated fracton phases

Foliated fracton phases are defined in [\[40\]](#) as follows: *Two gapped three dimensional Hamiltonians H_1 and H_2 are in the same **foliated fracton phase** if by adding layers of two-dimensional gapped Hamiltonians H_1^{2D} to H_1 , and layers of (potentially different) two-dimensional gapped Hamiltonians H_2^{2D} to H_2 , it is possible to adiabatically evolve from $H_1 + H_1^{2D}$ to $H_2 + H_2^{2D}$ without closing the gap^{[1](#)}*

Written as a formula, we have

$$\text{Foliated fracton phase: } H_1 + H_1^{2D} \xleftrightarrow{\text{Adiabatic evolution}} H_2 + H_2^{2D} \quad (3.1)$$

Here, adiabatic evolution refers to a smooth deformation of the Hamiltonian that preserves the energy gap, i.e. an evolution that does not pass through a critical point or an intervening gapless phase. Equivalently, because we are considering gapped systems, this relation can be stated in terms of the ground space. Denote by GS_1 and GS_2 the gapped ground spaces of H_1 and H_2 , and GS_1^{2D} and GS_2^{2D} the gapped ground spaces of layers of 2D Hamiltonians. Then H_1 and H_2 are in the same foliated fracton phase if $GS_1 \otimes GS_1^{2D}$ and $GS_2 \otimes GS_2^{2D}$ can be mapped into each other through finite depth local unitary transformations. [\[1\]](#)

$$\text{Foliated fracton phase: } GS_1 \otimes GS_1^{2D} \xleftrightarrow[\text{unitary transformation}]{\text{Finite depth local}} GS_2 \otimes GS_2^{2D} \quad (3.2)$$

That is, although the finite depth local unitary acts on the entire Hilbert space, it must map ground states $GS_1 \otimes GS_1^{2D}$ into ground states $GS_2 \otimes GS_2^{2D}$.

In comparison, the conventional definition of gapped phases only allows the addition of decoupled degrees of freedom in the form of a product state in

¹Before performing the adiabatic evolution (or local unitary transformations), we have the freedom to match locality and identify local degrees of freedom in the two models.

the process of adiabatic evolution. That is, the conventional definition can be expressed as:

$$\text{Conventional gapped phase: } H_1 + H_1^{0D} \xleftrightarrow{\text{Adiabatic evolution}} H_2 + H_2^{0D} \quad (3.3)$$

where H_1^{0D} and H_2^{0D} are Hamiltonians with direct product ground states. In terms of the ground space, the definition is given as

$$\text{Conventional gapped phase: } GS_1 \otimes GS_1^{0D} \xleftrightarrow[\text{unitary transformation}]{\text{Finite depth local}} GS_2 \otimes GS_2^{0D} \quad (3.4)$$

where G_1^{0D} and G_2^{0D} are non-degenerate (one-dimensional as a Hilbert space) spaces spanned by respective product states. GS_1 and GS_2 are said to be connected by a ‘generalized local unitary’ (gLU) transformation [6].

A major difference between these two definitions of phases of matter is that systems in the same conventional gapped phase always have the same GSD while systems in the same foliated fracton phase can have varying ground state degeneracy owing to the additional 2D layers. This simple observation is the chief motivation to propose this new definition as it is known that the GSD of fracton models can change with system size.

In [40], we showed that the X-cube model belongs to such a foliated fracton phase. The X-cube model is actually the fixed point of the phase that remains invariant under the renormalization group transformation: the X-cube model defined on a $L_x \times L_y \times L_z$ cubic lattice can be mapped to the X-cube model defined on a $L_x \times L_y \times (L_z + 1)$ cubic lattice by adding a layer of the 2D toric code in the xy plane and applying local unitary transformations to sew this new layer into the original X-cube model. Similar procedures can be applied to increase the system size in the x and y directions as well. Therefore, the foliation structure of the X-cube model is composed of layers in the xy , yz and zx planes. Such a foliation structure provides a natural explanation for the linear scaling of the entanglement entropy and the logarithm of the GSD in the X-cube model. Similar RG transformations and foliation structures can be identified [39] in the kagome X-cube model [43] and the checkerboard model [47].

On the other hand, not all fracton models are captured by this notion of foliated fracton phase. Type-II fracton models such as the Haah code are evidently not encompassed by this definition as they do not contain two

dimensional quasi-particles that can move freely in a plane. How to generalize these definitions to describe such fractal spin liquids remains an open question.

3.3 Signatures of long-range entanglement

Given the definition of foliated fracton phases, we can now pose the question of what universal properties characterize such phases and represent the corresponding foliated fracton order. In other words, we aim to identify properties of fracton models that remain invariant not only under smooth deformations of the Hamiltonian, but also under the addition or removal of gapped 2D layers.

As a first consideration, one can ask whether the ground state degeneracy (GSD) on a 3D torus plays such a role. In a conventional topological phase, the finite GSD (as a function of spatial topology) is indeed a universal quantity. Conversely, for foliated fracton phases, the GSD is no longer constant, but instead increases exponentially with linear system size and takes the generic form

$$\log \text{GSD} = aL + b. \quad (3.5)$$

This scaling form loses meaning in systems lacking a regular lattice structure (e.g. a general triangulation), for which it is not obvious how to measure L . Therefore, the GSD cannot serve as a universal quantity in the most general case. When translation symmetry is preserved, the constant b is an invariant of the phase while a does not have an absolute meaning as it can be arbitrarily changed by changing the unit of length. In the presence of translation invariance, b can potentially be used to distinguish between different foliated fracton phases, although it only applies when the system exists on a three-torus and depends sensitively on the periodic boundary conditions.

We note that one aspect is in need of clarification: in Ref. [40], we discussed the scaling of the GSD (in the form of Eq. 3.5) of the X-cube model on various spatial 3-manifolds, and how its dependence can be interpreted as a consequence of the topology of the foliating leaves and the topology of their intersections. This discussion applies to the fixed point models studied in Ref. [40]. Away from the fixed point, however, both constants a and b may lose their meaning: a becomes ill-defined due to the arbitrariness in choosing the unit of length, whereas b is not well-defined due to the existence of ‘small’

logical operators near singularities which do not have an infinite size in an infinite system²

Alternatively, we aim to identify universal quantities that do not depend on boundary conditions or translation invariance. For conventional topological phases, the topological entanglement entropy [12, 21, 22] is known to be such a quantity, and can be calculated from a local region in a ground state wave function. In this paper, we seek to characterize foliated fracton phases using a similar quantity. In the following subsections, we first briefly review the notion of topological entanglement entropy and then specify explicit criteria that must be satisfied by an entanglement quantity in order to universally characterize foliated fracton order. In section 3.4, we present such a quantity.

3.3.1 Review of topological entanglement entropy

Recall that the entanglement entropy of a state $|\psi\rangle$ with respect to a region R is defined as the von Neumann entropy

$$S_R = -\text{tr}(\rho_R \log \rho_R) \quad (3.6)$$

of the reduced density operator $\rho_R = \text{tr}_{\bar{R}} |\psi\rangle\langle\psi|$ where the subsystem \bar{R} , the complement of R , has been traced out. Because the model Hamiltonians we discuss are Z_2 stabilizer codes, it is convenient to take logarithms with respect to base 2 throughout the paper. For ground states of gapped 2D systems, the entanglement entropy takes the generic form

$$S_R = \alpha L - c\gamma + \dots, \quad (3.7)$$

where L is the length of the boundary ∂R , c is the number of connected components of ∂R , α is a non-universal constant, and the region R is assumed to have a smooth boundary relative to the correlation length of the system [8, 16]. (The ellipsis represents contributions that vanish when L is large and ∂R is smooth.) Whereas the dominant area law term is sensitive to the microscopic details of the model, the topological contribution $-c\gamma$ is a universal feature of generic topologically ordered ground states, and is referred to as the topological entanglement entropy. Here $\gamma = \log \mathcal{D}$ where \mathcal{D} is the total quantum dimension of the 2D topological order [21, 22]. For non-chiral orders, the origin of this term has a simple interpretation in terms of the string-net condensate picture

²These ‘small’ logical operators occur in, for example, the foliation of $S^2 \times S^1$ considered in [40].

[23] of 2D topological ground state wavefunctions: the net topological charge of all strings crossing a component of ∂R must be trivial, resulting in non-local correlations that correspondingly reduce the entropy of entanglement [22].

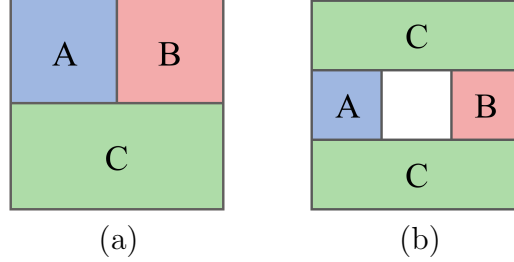


Figure 3.1: (a) Square $I(A; B; C)$ and (b) annular $I(A; B|C)$ schemes to isolate topological entanglement entropy in 2D.

It is possible to isolate the topological entanglement entropy $-\gamma$ by taking additive combinations of entanglement entropies of varying regions suitably chosen to cancel the area law terms as well as local contributions that may arise from sharp corners in the boundary of a region [21, 22]. Two such schemes for extracting the topological term are depicted in Fig. 3.1. In each, three compact regions (A , B , and C) with partially shared boundary are carved out of the planar medium. For the square scheme (Fig. 3.1(a)), the quantum tripartite information

$$I(A; B; C) \equiv S_A + S_B + S_C - S_{AB} - S_{BC} - S_{AC} + S_{ABC} \quad (3.8)$$

is used. AB denotes the composite of regions A and B . Each region's entropy contributes a single $-\gamma$ term, so in total $I(A; B; C) = -\gamma$ [21]. In the annular scheme (Fig. 3.1(b)), the tripartite information reduces to the simpler expression for the quantum conditional mutual information

$$I(A; B|C) \equiv S_{AC} + S_{BC} - S_C - S_{ABC}. \quad (3.9)$$

Since the boundaries of regions C and ABC each have two components, it follows that $I(A; B|C) = 2\gamma$ [21, 22]. Crucially, these entanglement quantities remain unchanged under generalized local unitary (gLU) transformations (Eq. 3.4) of the ground state. In this sense, they represent universal signatures of the long-range entanglement structure of 2D topological orders, and can be used to detect the order present in generic ground state wavefunctions away from the RG fixed-point. Moreover, these quantities are topological invariants;

i.e. they depend solely on the connectivity of the regions and not on their geometry.

For ground states of gapped phases in 3D, the entanglement entropy of a region R takes the generic form

$$S_R = \alpha A + \beta L + \gamma + \dots, \quad (3.10)$$

where in addition to the area law term αA (α is a non-universal constant and A is the area of the boundary ∂R), a subleading correction, βL , linear in the length L of the region may be present [13, 55]. The constant term γ contains both universal corrections as well as non-universal local contributions due to the curvature of ∂R (manifesting in a correction proportional to χ , the Euler characteristic of ∂R) [10, 12]. For conventional gapped topological phases in 3D, the linear corrections vanish, and suitable generalizations of the 2D ABC schemes serve as entanglement signatures of the topological order [4, 12].

3.3.2 Subleading linear corrections and foliation structure

Conversely, for foliated fracton phases (as well as simple decoupled stacks of 2D topological orders) the subleading linear corrections can not be ignored. Previous work has employed similar schemes (Fig. 3.2) to isolate these linear contributions from the dominant area law term [27, 38].

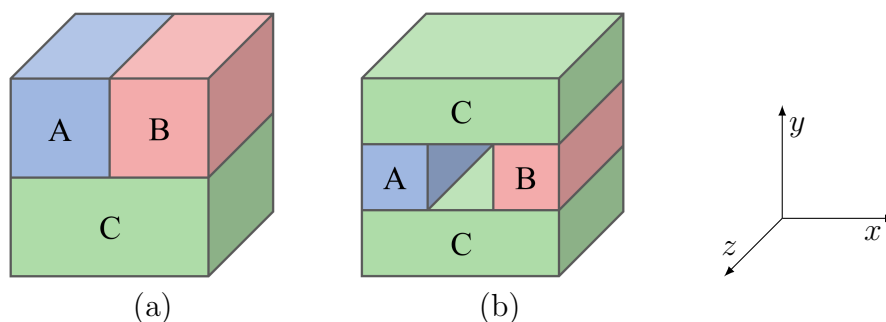


Figure 3.2: (a) 3D cube $I(A; B; C)$ and (b) solid torus $I(A; B|C)$ schemes. In both cases the regions are contained within an overall cube of side length L .

The results of these prescriptions are elucidated by the underlying foliation structure of the fracton models; the surviving linear quantity is an additive combination of topological entanglement entropies from the individual foliating layers. For example, applying the cube and solid torus schemes (Fig. 3.2) to the X-cube model yields the quantities $I(A; B; C) = -L$ and $I(A; B|C) = 2L + 1$,

respectively [27]. The linear components arise from the toric code foliating layers parallel to the xy plane, which intersect the cube and solid torus schemes in the respective 2D square and annular schemes (Fig. 3.1), and thus contribute -1 and 2 per unit length to these quantities respectively (as the total quantum dimension of the toric code topological order is $\mathcal{D} = 2$). The foliation perspective of fracton phases therefore suggests that the linear term in entanglement entropy is itself a non-universal feature of specific models, as it absorbs the topological entanglement entropies of added layers of 2D topological orders. Thus, we argue that these sub-extensive entanglement quantities are not universal. (The constant component, excluding the curvature contribution, is not universal either, which was pointed out in [27].)

These schemes can, however, be used to diagnose the underlying foliation structure. Consider a model with underlying foliations labelled $i = 1, 2, \dots, n$, where foliation i is composed of parallel leaves with separation $1/|F_i|$ and orthogonal to the vector F_i . Each leaf is composed of a 2D topological order with topological entanglement entropy $\gamma_i = \log \mathcal{D}_i$. Then consider a tripartite cube scheme (Fig. 3.2(a)) described by a vector L . For this scheme the overall cube has side length $|L|$, and the front face is normal to L . Then

$$I(A; B; C) = - \sum_i \gamma_i |L \cdot F_i| + O(1). \quad (3.11)$$

Due to the non-linearity of this expression, the orientations of the underlying foliations can be deduced by considering several such tripartite cubic schemes with varying overall orientation.

For instance, consider the X-cube model. As discussed, a cubic scheme of size L with the front face oriented normal to the x , y , or z direction will result in a tripartite information of $I(A; B; C) = -L$. However, rotating the regions such that the front face of the cube is normal to the $(1, 1, 1)$ direction yields $I(A; B; C) \sim -L\sqrt{3}$. These results are consistent with a foliation structure aligned parallel to the xy , yz , and xz planes. (In order to rule out all other possible foliation structures, schemes with additional orientations would have to be examined in order to check consistency.) Conversely, for the X-cube model on the stacked kagome lattice, there are four underlying foliations. The stacked kagome lattice is built out of a stacked triangular Bravais lattice with basis vectors \hat{x} , \hat{z} , and $\alpha = (1/2, \sqrt{3}/2, 0)$. A cube scheme with the front face normal to the z direction yields $I(A; B; C) = -L$, whereas schemes with the

front face parallel to the planes spanned by \hat{z} and \hat{x} , \hat{z} and α , or \hat{z} and $\alpha - \hat{x}$ will each yield $I(A; B; C) \sim -2L/\sqrt{3}$.

3.3.3 Criteria for universal entanglement quantity

In pursuit of universal characteristics, we are motivated to take an additional step and identify an entanglement quantity I that satisfies the following criteria:

1. All area law and local contributions to I cancel.
2. All contributions to I from the foliating layers must cancel. (This would otherwise result in contributions that scale linearly with subsystem size.)
3. I attains non-zero value for non-trivial foliated fracton phases (including conventional topological phases).

We note that the first and second criteria together are equivalent to demanding that I vanishes for arbitrary product states as well as simple decoupled stacks of 2D topological states. Thus, in accordance with the definition of foliated fracton phases discussed in the previous section, these criteria merely codify the requirement of a universal quantity that it is invariant under gLU transformations augmented with the free addition or removal of 2D topological resource states.

3.4 Universal schemes for foliated fracton phases

In this section we introduce a family of novel entanglement schemes with the above criteria in mind, and apply these prescriptions to a handful of stabilizer code models, revealing universal signatures of foliated fracton order.

3.4.1 Wireframe schemes

These prescriptions employ a set of regions whose union forms a solid wireframe region which is aligned with the foliating layers and supports closed branching string operators in the shape of the wireframe. The quantities considered are the quantum conditional mutual information $I(A; B|C)$ and the quantum conditional four-partite information $I(A; B; C; D|E)$ for choices of regions depicted in Fig. 3.3. By definition, $I(A; B; C; D|E) = I(A; B; C; D) - I(A; B; C; D; E)$ where $I(A; B; C; D)$ and $I(A; B; C; D; E)$ are

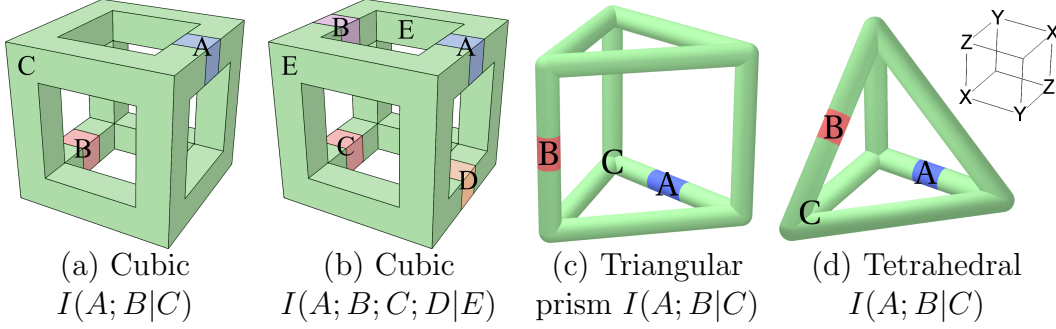


Figure 3.3: (a) Cubic $I(A; B|C)$, (b) cubic $I(A; B; C; D|E)$, (c) triangular prism $I(A; B|C)$, and (d) tetrahedral $I(A; B|C)$ entanglement schemes for foliated fracton phases. (d) Stabilizer for the Chamon model defined on a cubic lattice with one qubit per vertex (inset).

the quantum four-partite and five-partite information respectively. Explicitly,

$$\begin{aligned}
 I(A; B; C; D|E) \equiv & -S_E + S_{AE} + S_{BE} + S_{CE} + S_{DE} \\
 & - S_{ABE} - S_{BCE} - S_{CDE} - S_{ACE} - S_{BDE} - S_{ADE} \quad (3.12) \\
 & + S_{ABCE} + S_{ABDE} + S_{ACDE} + S_{BCDE} - S_{ABCDE}.
 \end{aligned}$$

$I(A; B|C)$ is defined in (3.9). Following the arguments of Refs. [21, 22], these schemes directly cancel the area law and local contributions of each boundary region. As discussed in the previous section, to ensure the cancellation of the subleading linear corrections, it is sufficient to guarantee that no foliating layer contributes a non-zero topological entropy. Each of our schemes is designed such that no layer intersects all regions of the scheme, ensuring that the contributions of each foliating layer, to the quantities $I(A; B|C)$ and $I(A; B; C; D|E)$, vanish. These quantities thus capture a universal feature of the long-range entanglement structure.

We have computed their values numerically for the stabilizer code models listed using the methods introduced in [9]. (Details of these computations are contained in Appendix 3.6; a review of the models considered is contained in Appendix 3.7.) The results are summarized in Table 3.1. As can be seen, the tetrahedral and triangular-prism schemes yield non-zero values only for the Chamon model and the stacked kagome X-cube model respectively, owing to their unique foliation structures.

For the 3D toric code, these values can be understood in terms of the string condensate picture of the ground state wavefunction. Given a region

	Cubic $I(A; B C)$	Cubic $I(A; B; C; D E)$	Triangular prism $I(A; B C)$	Tetrahedral $I(A; B C)$
2D toric code stack	0	0	0	0
3D toric code	0	1	0	0
X-cube model	1	1	0	0
Kagome X-cube [†]	1	1	1	0
Checkerboard model	2	2	0	0
Chamon model [‡]	1	1	0	1

Table 3.1: Entanglement quantities for the wireframe schemes discussed (Fig. 3.3). Logarithms (in Eq. (3.6)) are calculated in base 2. Models are reviewed in Appendix 3.7. [†]In order to attain a non-zero value for the kagome lattice X-cube model [43], the regions must be slanted in accordance with the foliation structures so that the wireframe actually forms a parallelepiped (see Fig. 3.4(c)). [‡]Here we have modified the Chamon model so that it is defined on a cubic lattice with one qubit per vertex. The lone stabilizer term is depicted in Fig. 3.3(d).

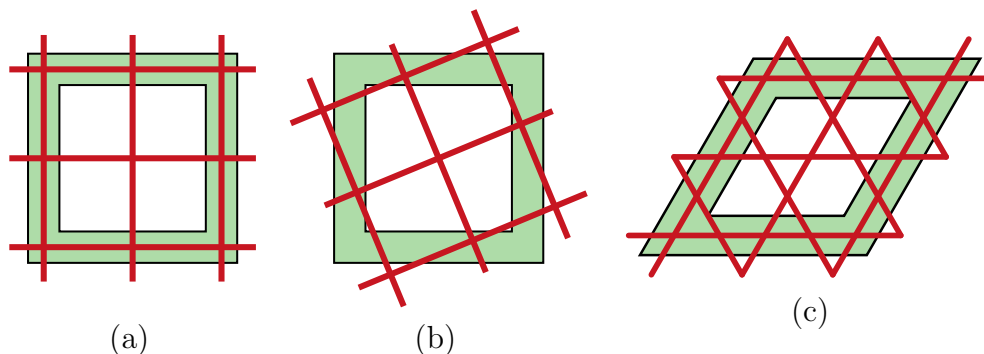


Figure 3.4: A side-view of the cubic entanglement regions (green) from Fig. 3.3(a-b) for different possible orientations with respect to the foliating layers (red). (a) Proper alignment on a cubic lattice, yielding the values Table 3.1. (b) Improper alignment, for which entanglement quantities $I(A; B|C) = I(A; B; C; D|E) = 0$. (c) Top-down view of a properly aligned solid wireframe on a stacked-kagome lattice, which yields $I(A; B|C) = I(A; B; C; D|E) = 1$ for the kagome X-cube model [43] as per Table 3.1.

R , each component of ∂R must be pierced by an even number of strings, which decreases the Schmidt number of the reduced density operator ρ_R by 1 and thus contributes -1 to S_R per boundary component. The three-region wireframe schemes each contain four positive and four negative topological contributions, and hence $I(A; B|C)$ vanishes, whereas in the five-region scheme $I(A; B; C; D|E) = 1$ due to nine positive contributions and eight negative contributions.

Intriguingly, for the foliated fracton models, this relation no longer holds, implying that the universal contribution to the entanglement entropy of a region is not simply proportional to the number of boundary components. Moreover, we find that $I(A; B|C)$ and $I(A; B; C; D|E)$ are not invariants of the region topology, but rather depend intimately on their geometry; for example, simply rotating the overall figures such that the wireframes do not align with the axes of the foliation structure causes both quantities to vanish for all of the foliated fracton models considered (see Fig. 3.4). However, the quantities are invariant under changes in the overall size and thickness of the wireframe as well as generic ‘small’ deformations of the regions.

3.4.2 Lower bounds on conditional mutual information

The existence of closed branching string operators supported by the solid wireframe shape can be used to establish a lower bound on the conditional mutual information $I(A; B|C)$ via the methods introduced in [38]. These bounds are saturated by the values reported in Table 3.1. In particular, given the existence of unitary operators U_i , U_i^{def} , and W_i (for $i = 1, \dots, n$) that satisfy the following conditions:

$$\begin{aligned} U_i &\subset \overline{AC} & U_i |\psi\rangle &= U_i^{\text{def}} |\psi\rangle & U_i W_i &= -W_i U_i \\ U_i^{\text{def}} &\subset \overline{BC} & W_i |\psi\rangle &= |\psi\rangle & U_i W_j &= W_j U_i \text{ if } i \neq j \\ W_i &\subset ABC, \end{aligned} \quad (3.13)$$

where $|\psi\rangle$ is a ground state of the model and $U_i \subset \overline{AC}$ indicates that U_i has support in \overline{AC} , the following inequality is satisfied [38]:

$$I(A; B|C) \geq n. \quad (3.14)$$

For the fracton models considered under our schemes, W_i can be chosen to be a closed branching string operator in the shape of the wireframe, piercing

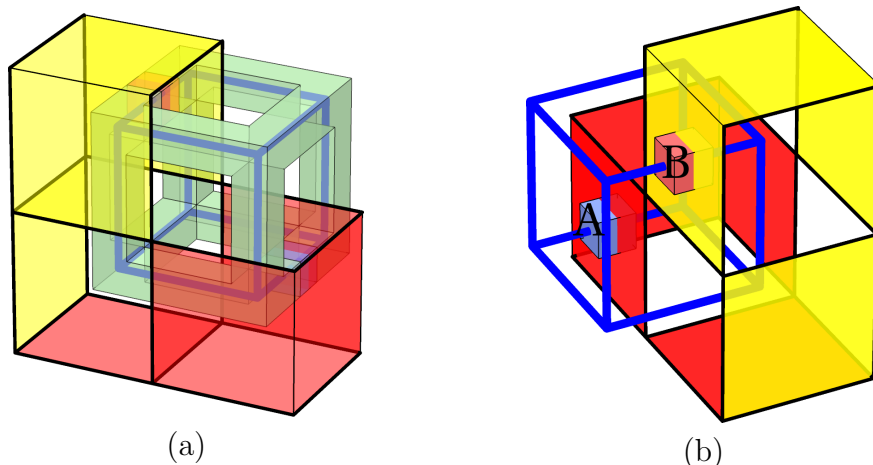


Figure 3.5: Operators satisfying the conditions of Eq. (3.13) which can be used to bound $I(A; B|C)$ for the cubic scheme depicted in Fig. 3.3(a). (a) For the X-cube model (Fig. 3.7(c)), $I(A; B|C) \geq 1$ is obtained by taking W_1 to be a product of X operators along the blue lines, and U_1 and U_1^{def} to be products of Z operators over all links that penetrate the red and yellow regions, respectively. For the checkerboard model (Fig. 3.7(d)), $I(A; B|C) \geq 2$ can be obtained by taking W_1 (W_2) to be a product of X (Z) operators along the blue lines, and U_1 and U_1^{def} (U_2 and U_2^{def}) to be products of Z (X) operators over the red and yellow surfaces, respectively. $I(A; B|C) \geq 1$ can similarly be obtained for the Chamon model (Fig. 3.7(e)) using a tetrahedral-shaped geometry, but each operator will contain a mix of X , Y , and Z Pauli operators. (b) Another view with subsystem C (green) hidden for clarity.

open membrane operators U_i and U_i^{def} , which create fractonic excitations in identical locations. As an example, in Fig. 3.5 we depict unitary operators that apply to the cubic entanglement scheme for the X-cube, checkerboard, and Chamon models.

3.5 Discussion

In this paper, we have identified multi-partite entanglement quantities that represent universal signatures of zero-temperature foliated fracton order, and thus characterize the corresponding foliated fracton phases. These schemes are borne of the observation that layers of 2D topological orders serve as resources in the RG transformations for certain fracton models. These layers constitute an underlying foliation structure which is, by design, invisible to the entanglement quantities we consider. The non-zero values they attain for the X-cube, kagome lattice X-cube, and checkerboard models are a manifestation of the non-trivial long-range entanglement structure present in the ground

states of these exotic phases of matter. Nonetheless, an understanding of the universal properties of these phases is still far from complete. Whereas for conventional topological orders a complete picture of universal characteristics is described in terms of quasiparticle sectors and their braiding statistics, elegantly packaged in the framework of topological quantum field theory (TQFT), it remains unclear which set of properties fully characterize foliated fracton orders, and what mathematical framework underlies the classification of these phases.

On the other hand, the related fractal spin liquids, i.e. type-II fracton models, remain largely enigmatic. To begin with, it is not clear in what sense these models even represent phases of matter. What is apparent is that, like conventional topological orders and foliated fracton orders, the ground states of fractal spin liquids exhibit highly non-trivial patterns of long-range entanglement. It remains an open question whether the entanglement structure present in these models can be captured by similar universal quantities. The foliated fracton models are also related (via Higgs and partial confinement mechanisms [3, 24]) to higher-rank $U(1)$ gauge theories with fractonic charge excitations [11, 25, 30–32, 34–36, 52]. The entanglement structure of these gapless models [33] is another potentially interesting avenue of future research.

3.6 Appendix: Numerical calculations

In this appendix, we briefly discuss details of the numerical calculations used to obtain the results of Table 3.1. Each model considered is a stabilizer code model, i.e. the Hamiltonians are sums of products of Pauli matrices where each term commutes with all other terms and has eigenvalue -1 in the ground state. For this class of exactly solvable models, entanglement entropies can be computed numerically (in polynomial time with subsystem size) using the methods introduced in [9]. Fig. 3.6 illustrates the lattice geometries that realize the entanglement subsystems in Fig. 3.3. For the toric code and X-cube models, multiple edges are grouped together appropriately to form unit cells.

As discussed in the main text, it is crucial that the subsystems are aligned with the foliating layers (see Fig. 3.4). For the X-cube and checkerboard models, the foliating layers are the xy , xz , and yz planes; therefore the cubic entanglement

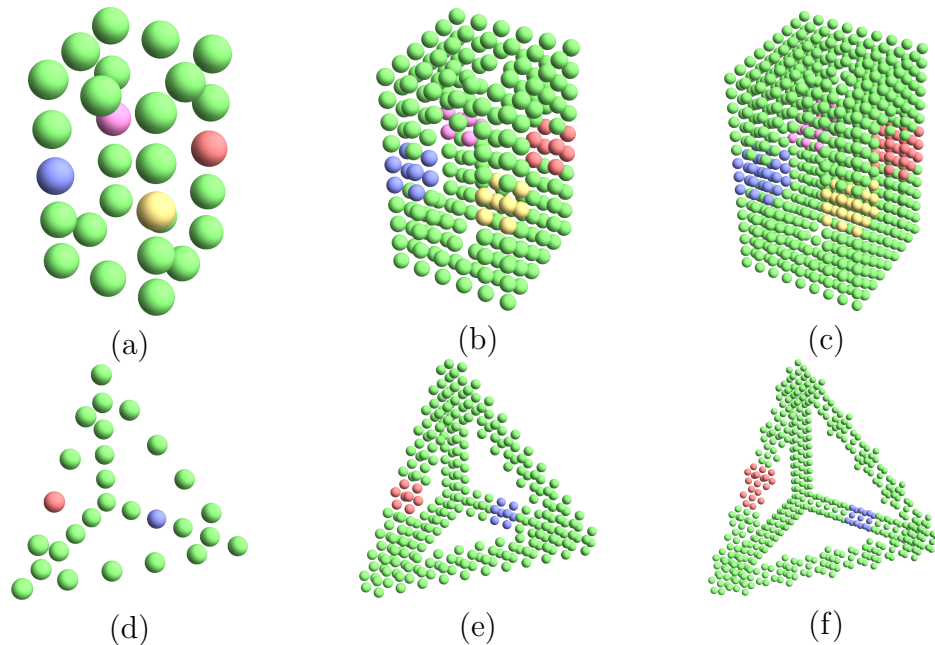


Figure 3.6: Geometries used to check Table 3.1 on a computer. Each point represents a unit cell of the lattice model that is included in the subsystem of the given color. (a-c) Lattice implementations of the cubic $I(A; B; C; D|E)$ scheme for three different sizes of subregions. The cubic and triangular-prism $I(A; B|C)$ scheme implementations are similar. (d-f) Lattice implementations of the tetrahedral $I(A; B|C)$ scheme. Since we used stabilizer models, no entry in Table 3.1 depended on the subsystem sizes.

schemes must be aligned with these axes (as per Fig. 3.4(a-b)). For the X-cube model on the stacked kagome lattice, the cubic wireframe must be tilted so that it is actually a parallelepiped in order to yield a non-zero value (see Fig. 3.4(c)), and similarly the triangular prism must be aligned with the underlying stacked triangular Bravais lattice. For the Chamon model, it is actually convenient to redefine the model on a cubic lattice (as in Fig. 3.3(d)). For liquid topological models, such as the 3D toric code, there is no (non-trivial) foliation structure and thus the orientation of the subsystems does not matter.

3.7 Appendix: Model Hamiltonians

This appendix contains a review of the models discussed in the paper. Each of these models is a qubit stabilizer code, meaning that the Hamiltonian is composed of mutually commuting products of Pauli operators.

The 2D toric code, originally introduced in [19], is defined on a square lattice

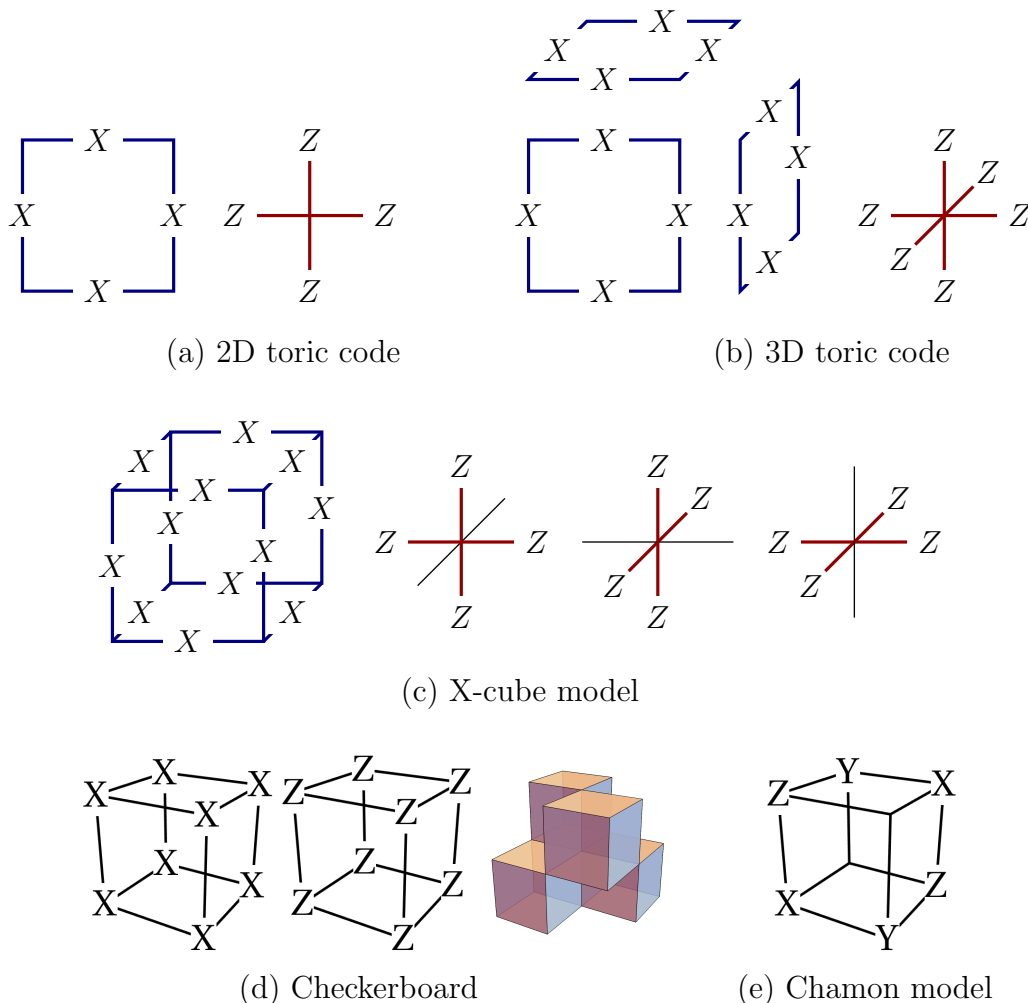


Figure 3.7: Hamiltonian terms for the stabilizer code models discussed.

with one qubit per edge, and has Hamiltonian

$$H = - \sum_v A_v - \sum_p B_p \quad (3.15)$$

where v runs over all vertices and p runs over all elementary plaquettes, A_v is a product of Pauli Z operators over the edges adjacent to v , and B_p is a product of Pauli X operators over the edges of p (see Fig. 3.7(a)). As a natural generalization, the 3D toric code has one qubit degree of freedom on each edge of a cubic lattice. The Hamiltonian is defined similarly, except there are three orientations of plaquettes, and the A_v term is modified to a six-spin interaction (as shown in Fig. 3.7(b)).

The X-cube model is likewise defined on a cubic lattice with one qubit per

edge. The Hamiltonian takes the form

$$H = - \sum_v (A_v^{xy} + A_v^{yz} + A_v^{zx}) - \sum_c B_c \quad (3.16)$$

where v runs over vertices and c runs over elementary cubes. Here A_v^{xy} is a product of Z operators over the edges adjacent to v in the x and y directions, whereas B_c is a product of X operators over all edges of c (see Fig. 3.7(c)). As discussed in [43], it is possible to generalize the X-cube model to a stacked kagome lattice (as well as other lattice geometries), again with one qubit per edge. As each vertex of the stacked kagome lattice is locally isomorphic to a cubic lattice vertex, in the generalized model there remain three vertex terms which are fourfold products of Z operators. However, the cube terms are replaced by generalized 3-cell terms for each elementary volume of the lattice (triangular and hexagonal prisms), which are likewise products of X operators over all edges of the 3-cell.

Finally, the checkerboard and Chamon models are both defined on a cubic lattice with one qubit per vertex. For the checkerboard model, the elementary cubes are divided into 3D checkerboard A - B sublattices. The Hamiltonian is composed of two terms for each cube in the A sublattice: the first is a product of Pauli X operators over all vertices of the cube, whereas the second is a product of Pauli Z operators over all vertices of the cube (see Fig. 3.7(d)). For the Chamon model, there is one stabilizer term per unit cell, as depicted in Fig. 3.7(e)

References

- [1] S. Bravyi, B. Leemhuis, and B.M. Terhal. “Topological order in an exactly solvable 3D spin model”. In: *Annals of Physics* 326 (Apr. 2011), pp. 839–866. DOI: [10.1016/j.aop.2010.11.002](https://doi.org/10.1016/j.aop.2010.11.002).
- [2] Sergey Bravyi and Jeongwan Haah. “Energy Landscape of 3D Spin Hamiltonians with Topological Order”. In: *Phys. Rev. Lett.* 107 (15 Oct. 2011), p. 150504. DOI: [10.1103/PhysRevLett.107.150504](https://doi.org/10.1103/PhysRevLett.107.150504). URL: <https://link.aps.org/doi/10.1103/PhysRevLett.107.150504>.
- [3] Daniel Bulmash and Maissam Barkeshli. “The Higgs Mechanism in Higher-Rank Symmetric $U(1)$ Gauge Theories”. In: (Feb. 2018). eprint: [1802.10099](https://arxiv.org/abs/1802.10099). URL: <https://arxiv.org/abs/1802.10099>.
- [4] Claudio Castelnovo and Claudio Chamon. “Topological order in a three-dimensional toric code at finite temperature”. In: *Phys. Rev. B* 78 (15

- Oct. 2008), p. 155120. DOI: [10.1103/PhysRevB.78.155120](https://doi.org/10.1103/PhysRevB.78.155120). URL: <https://link.aps.org/doi/10.1103/PhysRevB.78.155120>.
- [5] Claudio Chamon. “Quantum Glassiness in Strongly Correlated Clean Systems: An Example of Topological Overprotection”. In: *Phys. Rev. Lett.* 94 (4 Jan. 2005), p. 040402. DOI: [10.1103/PhysRevLett.94.040402](https://doi.org/10.1103/PhysRevLett.94.040402). URL: <https://link.aps.org/doi/10.1103/PhysRevLett.94.040402>.
- [6] Xie Chen, Zheng-Cheng Gu, and Xiao-Gang Wen. “Local unitary transformation, long-range quantum entanglement, wave function renormalization, and topological order”. In: *Phys. Rev. B* 82 (15 Oct. 2010), p. 155138. DOI: [10.1103/PhysRevB.82.155138](https://doi.org/10.1103/PhysRevB.82.155138). URL: <https://link.aps.org/doi/10.1103/PhysRevB.82.155138>.
- [7] Trithep Devakul, S. A. Parameswaran, and S. L. Sondhi. “Correlation function diagnostics for type-I fracton phases”. In: *Phys. Rev. B* 97 (4 Jan. 2018), p. 041110. DOI: [10.1103/PhysRevB.97.041110](https://doi.org/10.1103/PhysRevB.97.041110). URL: <https://link.aps.org/doi/10.1103/PhysRevB.97.041110>.
- [8] J. Eisert, M. Cramer, and M. B. Plenio. “Area laws for the entanglement entropy - a review”. In: *Rev. Mod. Phys.* 82 (2010), pp. 277–306. DOI: [10.1103/RevModPhys.82.277](https://doi.org/10.1103/RevModPhys.82.277). arXiv: [0808.3773 \[quant-ph\]](https://arxiv.org/abs/0808.3773).
- [9] David Fattal et al. “Entanglement in the stabilizer formalism”. In: (June 2004). eprint: [quant-ph/0406168](https://arxiv.org/abs/quant-ph/0406168). URL: <http://arxiv.org/abs/quant-ph/0406168>.
- [10] Eduardo Fradkin and Joel E. Moore. “Entanglement entropy of 2D conformal quantum critical points: hearing the shape of a quantum drum”. In: *Phys. Rev. Lett.* 97 (2006), p. 050404. DOI: [10.1103/PhysRevLett.97.050404](https://doi.org/10.1103/PhysRevLett.97.050404). arXiv: [cond-mat/0605683 \[cond-mat.str-el\]](https://arxiv.org/abs/cond-mat/0605683).
- [11] Andrey Gromov. “Fractional Topological Elasticity and Fracton Order”. In: (Dec. 2017). eprint: [1712.06600](https://arxiv.org/abs/1712.06600). URL: <http://arxiv.org/abs/1712.06600>.
- [12] Tarun Grover, Ari M. Turner, and Ashvin Vishwanath. “Entanglement entropy of gapped phases and topological order in three dimensions”. In: *Phys. Rev. B* 84 (19 Nov. 2011), p. 195120. DOI: [10.1103/PhysRevB.84.195120](https://doi.org/10.1103/PhysRevB.84.195120). URL: <https://link.aps.org/doi/10.1103/PhysRevB.84.195120>.
- [13] Tarun Grover, Ari M. Turner, and Ashvin Vishwanath. “Entanglement entropy of gapped phases and topological order in three dimensions”. In: *Phys. Rev. B* 84 (19 Nov. 2011), p. 195120. DOI: [10.1103/PhysRevB.84.195120](https://doi.org/10.1103/PhysRevB.84.195120). URL: <https://link.aps.org/doi/10.1103/PhysRevB.84.195120>.

- [14] Jeongwan Haah. “Local stabilizer codes in three dimensions without string logical operators”. In: *Phys. Rev. A* 83 (4 Apr. 2011), p. 042330. DOI: [10.1103/PhysRevA.83.042330](https://doi.org/10.1103/PhysRevA.83.042330). URL: <https://link.aps.org/doi/10.1103/PhysRevA.83.042330>.
- [15] Gábor B. Halász, Timothy H. Hsieh, and Leon Balents. “Fracton Topological Phases from Strongly Coupled Spin Chains”. In: *Phys. Rev. Lett.* 119 (25 Dec. 2017), p. 257202. DOI: [10.1103/PhysRevLett.119.257202](https://doi.org/10.1103/PhysRevLett.119.257202). URL: <https://link.aps.org/doi/10.1103/PhysRevLett.119.257202>.
- [16] Alioscia Hamma, Radu Ionicioiu, and Paolo Zanardi. “Ground state entanglement and geometric entropy in the Kitaev model”. In: *Physics Letters A* 337.1 (2005), pp. 22–28. ISSN: 0375-9601. DOI: [10.1016/j.physleta.2005.01.060](https://doi.org/10.1016/j.physleta.2005.01.060). URL: <http://www.sciencedirect.com/science/article/pii/S0375960105001544>.
- [17] Huan He et al. “Entanglement entropy from tensor network states for stabilizer codes”. In: *Phys. Rev. B* 97 (12 Mar. 2018), p. 125102. DOI: [10.1103/PhysRevB.97.125102](https://doi.org/10.1103/PhysRevB.97.125102). URL: <https://link.aps.org/doi/10.1103/PhysRevB.97.125102>.
- [18] Timothy H. Hsieh and Gábor B. Halász. “Fractons from partons”. In: *Phys. Rev. B* 96 (16 Oct. 2017), p. 165105. DOI: [10.1103/PhysRevB.96.165105](https://doi.org/10.1103/PhysRevB.96.165105). URL: <https://link.aps.org/doi/10.1103/PhysRevB.96.165105>.
- [19] A. Yu. Kitaev. “Fault tolerant quantum computation by anyons”. In: *Annals Phys.* 303 (2003), pp. 2–30. DOI: [10.1016/S0003-4916\(02\)00018-0](https://doi.org/10.1016/S0003-4916(02)00018-0). arXiv: [quant-ph/9707021](https://arxiv.org/abs/quant-ph/9707021) [quant-ph].
- [20] Alexei Kitaev. “Anyons in an exactly solved model and beyond”. In: *Annals of Physics* 321.1 (2006). January Special Issue, pp. 2–111. ISSN: 0003-4916. DOI: [10.1016/j.aop.2005.10.005](https://doi.org/10.1016/j.aop.2005.10.005). URL: <http://www.sciencedirect.com/science/article/pii/S0003491605002381>.
- [21] Alexei Kitaev and John Preskill. “Topological entanglement entropy”. In: *Phys. Rev. Lett.* 96 (2006), p. 110404. DOI: [10.1103/PhysRevLett.96.110404](https://doi.org/10.1103/PhysRevLett.96.110404).
- [22] M. Levin and X.-G. Wen. “Detecting Topological Order in a Ground State Wave Function”. In: *Phys. Rev. Lett.* 96.11, 110405 (Mar. 2006), p. 110405. DOI: [10.1103/PhysRevLett.96.110405](https://doi.org/10.1103/PhysRevLett.96.110405).
- [23] Michael A. Levin and Xiao-Gang Wen. “String-net condensation: A physical mechanism for topological phases”. In: *Phys. Rev. B* 71 (4 Jan. 2005), p. 045110. DOI: [10.1103/PhysRevB.71.045110](https://doi.org/10.1103/PhysRevB.71.045110). URL: <https://link.aps.org/doi/10.1103/PhysRevB.71.045110>.

- [24] Han Ma, Michael Hermele, and Xie Chen. “Fracton topological order from Higgs and partial confinement mechanisms of rank-two gauge theory”. In: (Feb. 2018). eprint: [1802.10108](https://arxiv.org/abs/1802.10108), URL: <https://arxiv.org/abs/1802.10108>.
- [25] Han Ma and Michael Pretko. “Higher Rank Deconfined Quantum Criticality and the Exciton Bose Condensate”. In: (Mar. 2018). eprint: [1803.04980](http://arxiv.org/abs/1803.04980), URL: <http://arxiv.org/abs/1803.04980>.
- [26] Han Ma et al. “Fracton topological order via coupled layers”. In: *Phys. Rev. B* 95 (24 June 2017), p. 245126. DOI: [10.1103/PhysRevB.95.245126](https://doi.org/10.1103/PhysRevB.95.245126), URL: <https://link.aps.org/doi/10.1103/PhysRevB.95.245126>.
- [27] Han Ma et al. “Topological Entanglement Entropy of Fracton Stabilizer Codes”. In: (2017). arXiv: [1710.01744](https://arxiv.org/abs/1710.01744).
- [28] O. Petrova and N. Regnault. “Simple anisotropic three-dimensional quantum spin liquid with fractonlike topological order”. In: *Phys. Rev. B* 96 (22 Dec. 2017), p. 224429. DOI: [10.1103/PhysRevB.96.224429](https://doi.org/10.1103/PhysRevB.96.224429), URL: <https://link.aps.org/doi/10.1103/PhysRevB.96.224429>.
- [29] Abhinav Prem, Jeongwan Haah, and Rahul Nandkishore. “Glassy quantum dynamics in translation invariant fracton models”. In: *Phys. Rev. B* 95 (15 Apr. 2017), p. 155133. DOI: [10.1103/PhysRevB.95.155133](https://doi.org/10.1103/PhysRevB.95.155133), URL: <https://link.aps.org/doi/10.1103/PhysRevB.95.155133>.
- [30] Michael Pretko. “Emergent gravity of fractons: Mach’s principle revisited”. In: *Phys. Rev. D* 96 (2 July 2017), p. 024051. DOI: [10.1103/PhysRevD.96.024051](https://doi.org/10.1103/PhysRevD.96.024051), URL: <https://link.aps.org/doi/10.1103/PhysRevD.96.024051>.
- [31] Michael Pretko. “Generalized electromagnetism of subdimensional particles: A spin liquid story”. In: *Phys. Rev. B* 96 (3 July 2017), p. 035119. DOI: [10.1103/PhysRevB.96.035119](https://doi.org/10.1103/PhysRevB.96.035119), URL: <https://link.aps.org/doi/10.1103/PhysRevB.96.035119>.
- [32] Michael Pretko. “Higher-spin Witten effect and two-dimensional fracton phases”. In: *Phys. Rev. B* 96 (12 Sept. 2017), p. 125151. DOI: [10.1103/PhysRevB.96.125151](https://doi.org/10.1103/PhysRevB.96.125151), URL: <https://link.aps.org/doi/10.1103/PhysRevB.96.125151>.
- [33] Michael Pretko. “On the Entanglement Entropy of Maxwell Theory: A Condensed Matter Perspective”. In: (Jan. 2018). eprint: [1801.01158](https://arxiv.org/abs/1801.01158), URL: <http://arxiv.org/abs/1801.01158>.
- [34] Michael Pretko. “Subdimensional particle structure of higher rank $U(1)$ spin liquids”. In: *Phys. Rev. B* 95 (11 Mar. 2017), p. 115139. DOI: [10.1103/PhysRevB.95.115139](https://doi.org/10.1103/PhysRevB.95.115139), URL: <https://link.aps.org/doi/10.1103/PhysRevB.95.115139>.

- [35] Michael Pretko and Leo Radzihovsky. “Fracton-Elasticity Duality”. In: (Nov. 2017). eprint: [1711.11044](https://arxiv.org/abs/1711.11044). URL: <http://arxiv.org/abs/1711.11044>.
- [36] Alex Rasmussen, Yi-Zhuang You, and Cenke Xu. “Stable Gapless Bose Liquid Phases without Any Symmetry”. In: (Jan. 2016). arXiv: [1601.08235](https://arxiv.org/abs/1601.08235) [[cond-mat](#)]. URL: <http://arxiv.org/abs/1601.08235> (visited on 02/02/2016).
- [37] A. T. Schmitz et al. “Recoverable Information and Emergent Conservation Laws in Fracton Stabilizer Codes”. In: (Dec. 2017). eprint: [1712.02375](https://arxiv.org/abs/1712.02375). URL: <http://arxiv.org/abs/1712.02375>.
- [38] Bowen Shi and Yuan-Ming Lu. “Decipher the nonlocal entanglement entropy of fracton topological orders”. In: (May 2017). eprint: [1705.09300](https://arxiv.org/abs/1705.09300). URL: <http://arxiv.org/abs/1705.09300>.
- [39] Wilbur Shirley, Kevin Slagle, and Xie Chen. in progress. 2018.
- [40] Wilbur Shirley et al. “Fracton Models on General Three-Dimensional Manifolds”. In: (2017). arXiv: [1712.05892](https://arxiv.org/abs/1712.05892) [[cond-mat.str-el](#)]. URL: <http://arxiv.org/abs/1712.05892>.
- [41] Kevin Slagle and Yong Baek Kim. “Fracton topological order from nearest-neighbor two-spin interactions and dualities”. In: *Phys. Rev. B* 96 (16 Oct. 2017), p. 165106. DOI: [10.1103/PhysRevB.96.165106](https://doi.org/10.1103/PhysRevB.96.165106). URL: <https://link.aps.org/doi/10.1103/PhysRevB.96.165106>.
- [42] Kevin Slagle and Yong Baek Kim. “Quantum field theory of X-cube fracton topological order and robust degeneracy from geometry”. In: *Phys. Rev. B* 96 (19 Nov. 2017), p. 195139. DOI: [10.1103/PhysRevB.96.195139](https://doi.org/10.1103/PhysRevB.96.195139). URL: <https://link.aps.org/doi/10.1103/PhysRevB.96.195139>.
- [43] Kevin Slagle and Yong Baek Kim. “X-Cube Model on Generic Lattices: New Phases and Geometric Order”. In: (Dec. 2017). eprint: [1712.04511](https://arxiv.org/abs/1712.04511). URL: <http://arxiv.org/abs/1712.04511>.
- [44] S. Vijay. “Isotropic Layer Construction and Phase Diagram for Fracton Topological Phases”. In: (Jan. 2017). arXiv: [1701.00762](https://arxiv.org/abs/1701.00762).
- [45] Sagar Vijay and Liang Fu. “A Generalization of Non-Abelian Anyons in Three Dimensions”. In: (June 2017). eprint: [1706.07070](https://arxiv.org/abs/1706.07070). URL: <http://arxiv.org/abs/1706.07070>.
- [46] Sagar Vijay, Jeongwan Haah, and Liang Fu. “A new kind of topological quantum order: A dimensional hierarchy of quasiparticles built from stationary excitations”. In: *Phys. Rev. B* 92 (23 Dec. 2015), p. 235136. DOI: [10.1103/PhysRevB.92.235136](https://doi.org/10.1103/PhysRevB.92.235136). URL: <http://link.aps.org/doi/10.1103/PhysRevB.92.235136>.

- [47] Sagar Vijay, Jeongwan Haah, and Liang Fu. “Fracton topological order, generalized lattice gauge theory, and duality”. In: *Phys. Rev. B* 94 (23 Dec. 2016), p. 235157. DOI: [10.1103/PhysRevB.94.235157](https://doi.org/10.1103/PhysRevB.94.235157). URL: <https://link.aps.org/doi/10.1103/PhysRevB.94.235157>.
- [48] X. G. Wen. “TOPOLOGICAL ORDERS IN RIGID STATES”. In: *International Journal of Modern Physics B* 04.02 (1990), pp. 239–271. DOI: [10.1142/S0217979290000139](https://doi.org/10.1142/S0217979290000139).
- [49] X. G. Wen and Q. Niu. “Ground-state degeneracy of the fractional quantum Hall states in the presence of a random potential and on high-genus Riemann surfaces”. In: *Phys. Rev. B* 41 (13 May 1990), pp. 9377–9396. DOI: [10.1103/PhysRevB.41.9377](https://doi.org/10.1103/PhysRevB.41.9377). URL: <https://link.aps.org/doi/10.1103/PhysRevB.41.9377>.
- [50] Dominic J. Williamson. “Fractal symmetries: Ungauging the cubic code”. In: *Phys. Rev. B* 94 (15 Oct. 2016), p. 155128. DOI: [10.1103/PhysRevB.94.155128](https://doi.org/10.1103/PhysRevB.94.155128). URL: <https://link.aps.org/doi/10.1103/PhysRevB.94.155128>.
- [51] Kenneth G. Wilson. “Confinement of quarks”. In: *Phys. Rev. D* 10 (8 Oct. 1974), pp. 2445–2459. DOI: [10.1103/PhysRevD.10.2445](https://doi.org/10.1103/PhysRevD.10.2445). URL: <https://link.aps.org/doi/10.1103/PhysRevD.10.2445>.
- [52] Cenke Xu. “Gapless bosonic excitation without symmetry breaking: An algebraic spin liquid with soft gravitons”. In: *Phys. Rev. B* 74 (22 Dec. 2006), p. 224433. DOI: [10.1103/PhysRevB.74.224433](https://doi.org/10.1103/PhysRevB.74.224433). URL: <http://link.aps.org/doi/10.1103/PhysRevB.74.224433>.
- [53] Beni Yoshida. “Exotic topological order in fractal spin liquids”. In: *Phys. Rev. B* 88 (12 Sept. 2013), p. 125122. DOI: [10.1103/PhysRevB.88.125122](https://doi.org/10.1103/PhysRevB.88.125122). URL: <https://link.aps.org/doi/10.1103/PhysRevB.88.125122>.
- [54] Yizhi You et al. “Subsystem symmetry protected topological order”. In: (Mar. 2018). eprint: [1803.02369](https://arxiv.org/abs/1803.02369). URL: <http://arxiv.org/abs/1803.02369>.
- [55] Yunqin Zheng et al. “Structure of the Entanglement Entropy of (3+1)D Gapped Phases of Matter”. In: (Oct. 2017). eprint: [1710.01747](https://arxiv.org/abs/1710.01747). URL: <http://arxiv.org/abs/1710.01747>.

FOLIATED FRACTON ORDER FROM GAUGING SUBSYSTEM SYMMETRIES

4.1 Introduction

Gauging is a powerful tool in the study of gapped quantum phases with global symmetry. When gauging the global symmetry of a system, gauge fields corresponding to the symmetry group are added to the system so that the global symmetry can be enhanced to a local symmetry. It is useful to consider such a procedure because different phases under global symmetry map into different phases of the gauge theory. Symmetric (e.g. paramagnetic) phases map into deconfined gauge theories while symmetry breaking phases map into a Higgsed gauge theory. Different symmetry protected topological (SPT)/symmetry enriched topological (SET) phases map into different deconfined gauge theories with different statistics among the gauge fluxes (see, e.g., Refs. [15, 18]).

Recently, it has been realized that a similar gauging procedure can be applied to systems with subsystem symmetries as well [8, 17, 46, 50, 51, 54, 55]. Subsystem symmetries are symmetries with generators that act non-trivially only on a sub-manifold of the system. After gauging, the system is mapped to a model with ‘fracton order’ [1, 2, 4, 6, 7, 9, 11–14, 21–23, 25–28, 36–39, 42–44, 47–50, 53]. This relation has been demonstrated for various classical/quantum spin models, stabilizer codes, domain-frame condensate models, etc. In this paper, we summarize and make explicit the general gauging procedure. That is, we describe explicitly a systematic procedure for gauging models with subsystem symmetries which can be applied to any local quantum model with such symmetry. In particular, the gauge fields are added at the center of ‘minimal’ coupling terms which are not on-site symmetric and which generate all other non-on-site-symmetric coupling terms. A modified Hamiltonian can then be written with enhanced local symmetry and with dynamical terms for the gauge field, which defines the gauge theory. We focus on abelian symmetry groups only in this paper.

The next key question is: what is the relation between the ungauged order

under subsystem symmetry and the gauged fracton order? To address this question, we study the mapping between ungauged and gauged phases (several of these examples have been studied in the previous literature [8, 17, 46, 50, 51, 54, 55]) and propose a way to interpret the correspondence. In 2D and 3D, gauging linear subsystem symmetries (which act on 1D lines) maps paramagnetic (trivially symmetric) phases and symmetry breaking phases into one another, while subsystem symmetry protected topological (SPT) phases [54] may map into themselves. This is similar to the case of global symmetries in 1D, where paramagnets are mapped into symmetry breaking phases, and SPT phases can map into SPTs. In 3D, gauging planar subsystem symmetries leads to foliated fracton order, as defined in Refs. [38, 39]. In particular, symmetry charges that transform under planar symmetries in one, two or three directions map directly to planon, lineon and fracton charge excitations, which are restricted to move only in a plane, along a line, or which cannot move at all. The restricted motion of the charge excitations in the fracton model hence originates from the requirement to preserve subsystem symmetries in the ungauged model. By counting the species of symmetry charges in the ungauged model, we can make direct connection to the foliated fracton order after gauging. For example, it was shown in Ref. [50] that gauging the (paramagnet phase of) the plaquette Ising model and the tetrahedral Ising model results in the X-cube and the checkerboard model respectively. By counting symmetry charges, we can see that the checkerboard model should be equivalent to two copies of the X-cube model. We present the mapping between the two in Ref. [40] and in section 4.4, we explain how counting symmetry charges leads to the same conclusion.

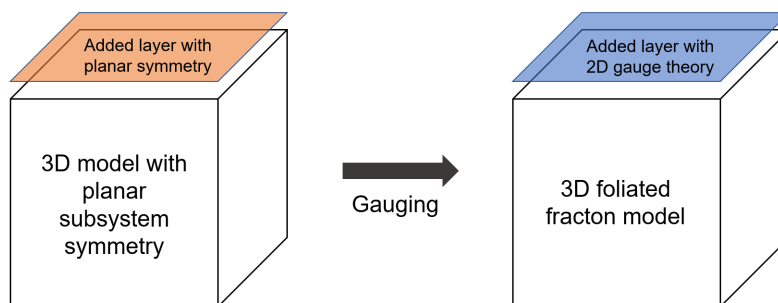


Figure 4.1: Correspondence of foliation structure in 3D systems with planar subsystem symmetry and 3D foliated fracton models.

Given the analogous foliation (or layered) structure in 3D models with planar

subsystem symmetry and 3D foliated fracton phases, there is a natural correspondence. As shown in Fig. 4.1, for 3D models with planar subsystem symmetry, to increase the system size by one lattice spacing in the direction of one set of planar subsystem symmetries, it is necessary to add degrees of freedom (DOFs) on an entire plane and increase the number of generators of subsystem symmetries by one. The added planar subsystem symmetry acts as a global symmetry on the added plane. On the other hand, as we discussed in Ref. 38, 39, for 3D foliated fracton phases, to increase the system size by one lattice spacing along one of the foliation axes, it is necessary to add a layer containing a gapped 2D topological state as a resource. Thus, it is natural that subsystem symmetric states gauge into foliated fracton models since the added layer gauges into a deconfined 2D gauge theory with gapped topological order.

The paper is organized as follows: In section 4.2 we briefly review the procedure of gauging global symmetries using as an example the 2D paramagnetic state. Section 4.3 then discusses the generalized gauging procedure that can be applied to systems with subsystem symmetries in a systematic way. Multiple examples (including examples that have appeared in the previous literature) are discussed to show how the procedure works in different situations. Section 4.4 studies the correspondence between phases with subsystem symmetries and the phases of their gauged theories through multiple examples and the result is summarized in Table 4.1 in section 4.5

4.2 Review: Gauging global symmetry

First, we give a brief review of the procedure for gauging global symmetries (for more careful discussions see, e.g., Refs. 16, 18). We consider the simplest example: the transverse field Ising model with global Z_2 symmetry, coupled to a Z_2 gauge field. The Hamiltonian takes the simple form of

$$H = -J_x \sum_v \sigma_v^x - J_z \sum_{\langle vw \rangle} \sigma_v^z \sigma_w^z \quad (4.1)$$

where the σ 's are Pauli matrices on each lattice site (blue dots in Fig. 4.2) and $\langle vw \rangle$ denotes nearest neighbor pairs. The system has a global Z_2 symmetry of $U = \prod_v \sigma_v^x$. To couple the model to a Z_2 gauge field, we introduce gauge field degrees of freedom τ on each link of the lattice (green dots in Fig. 4.2). τ^x corresponds to (the exponential e^{iE} of) the ‘electric field’ of the gauge field and τ^z corresponds to (the exponential of) the ‘vector potential’ of the gauge

field. The local symmetry, or the Gauss's law, is given by $A_v = \sigma_v^x \prod_{e \ni v} \tau_e^x$ where the product is over all edges e with v as one end point.

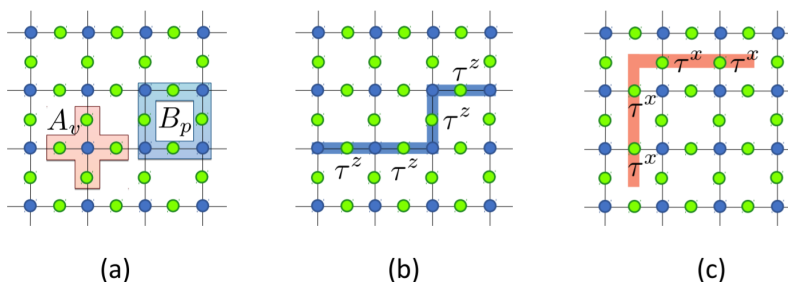


Figure 4.2: Gauging global Z_2 symmetry in 2D. (a) Vertex $A_v = \sigma_v^x \prod_{e \ni v} \tau_e^x$ and plaquette $B_p = \prod_{e \in p} \tau_e^z$ terms that appear in Eq. (4.2). (b-c) String operators.

Next, we couple H to the gauge fields such that the new Hamiltonian is invariant under the local symmetry transformations A_v . The transverse field terms σ_i^x are already invariant under the local symmetries, so we do not need to modify them and simply include them in the new Hamiltonian. The Ising coupling terms $\sigma_i^z \sigma_j^z$ need to be replaced with $\sigma_i^z \tau_{ij}^z \sigma_j^z$ in order to be gauge invariant (i.e. commute with the A_v term). Besides that we add the vertex term $A_v = \sigma_v^x \prod_{e \ni v} \tau_e^x$ at every vertex v to enforce gauge symmetry (Gauss's law) and $B_p = \prod_{e \in p} \tau_e^z$, where the product is over all edges around a plaquette p , to enforce the zero flux constraint on every plaquette. The total Hamiltonian then reads

$$H_g = -J_x \sum_v \sigma_v^x - J_z \sum_{\langle vw \rangle} \sigma_v^z \tau_{vw}^z \sigma_w^z - J_v \sum_v \sigma_v^x \prod_{e \ni v} \tau_e^x - J_p \sum_p \prod_{e \in p} \tau_e^z. \quad (4.2)$$

When $J_z = 0$, the Ising model H is in the symmetric paramagnetic phase. After gauging, it maps to the deconfined phase of the Z_2 gauge theory. This can be seen by noticing that when the energy of the $\sum_v \sigma_v^x$ term is minimized, the gauged Hamiltonian reduces to

$$H_{\text{TC}} = -J_v \sum_v \prod_{e \ni v} \tau_e^x - J_p \sum_p \prod_{e \in p} \tau_e^z \quad (4.3)$$

which is exactly the toric code Hamiltonian representing the deconfined phase of the Z_2 gauge theory. The low energy excitations include a bosonic gauge flux, which corresponds to the violation of one $\prod_{e \in p} \tau_e^z$ term, and a bosonic gauge charge, which corresponds to the violation of one $\prod_{e \ni v} \tau_e^x$ term. These

two excitations can be created with string operators shown in Fig. 4.2b-c. They braid with each other with a phase factor of -1 , which is the Aharonov-Bohm phase factor in the Z_2 case.

When $J_x = 0$, the Ising model H is in the symmetry breaking ferromagnetic phase. After gauging, it maps to the Higgsed phase which lacks non-trivial topological order. This can be seen by noticing that when $J_x = 0$, H_g has a unique ground state and no fractional excitations.

This gauging procedure can be applied to any local quantum Hamiltonian on any lattice satisfying a global symmetry G by introducing gauge fields on the links of the lattice, enforcing gauge symmetry (Gauss's law), modifying interaction terms to be gauge invariant, and finally including a flux term for the gauge field. By doing so, we obtain a gauge theory of group G . The properties of the gauge theory can be determined from the ungauged model in the following ways:

1. If the symmetry is spontaneously broken in the ungauged model, then the gauge theory is Higgsed with trivial topological order.
2. Otherwise, the deconfined gauge charge comes from the symmetry charge. The deconfined charges are either bosonic or fermionic, depending on whether the symmetry charges in the ungauged model are bosonic or fermionic.
3. The deconfined gauge flux comes from the symmetry flux, except it is dynamical. The statistics of the gauge flux depends on the particular order (SPT/SET) of the ungauged model. Some interesting examples include: gauging the Z_2 fermion parity symmetry in the 2D chiral $p + ip$ superconductor results in a non-abelian flux; also, gauging the 2D bosonic SPT with Z_2 symmetry results in a semionic flux.
4. The braiding statistics between a gauge charge and a gauge flux is independent of the original order; it is given by the Aharonov-Bohm phase factor, which is determined by the symmetry group. For example, in a Z_N gauge theory, the phase factor between an elementary charge and an elementary flux is $e^{i2\pi/N}$.
5. In 1D, gauge theories are not topologically ordered. Symmetry breaking and trivial SPT phases map into each other upon gauging. Non-trivial

SPT phases can map to themselves upon gauging. (We briefly review the gauging of 1D phases in appendix [4.6](#).)

4.3 Gauging subsystem symmetry: general procedure

How do we gauge models with subsystem symmetries? The simplest example of a system with subsystem symmetry is an Ising paramagnet on a cubic lattice (corresponding to the plaquette Ising model in Ref. [\[50\]](#)). Consider a cubic lattice with spin 1/2 degrees of freedom at each lattice site (blue dots in Fig. [4.3](#)). The Hamiltonian is simply given by $H = \sum_v \sigma_v^x$. This Hamiltonian is invariant under planar subsystem symmetries

$$U_n^{XY} = \prod_{v \in P_n^{XY}} \sigma_v^x \quad U_n^{YZ} = \prod_{v \in P_n^{YZ}} \sigma_v^x \quad U_n^{ZX} = \prod_{v \in P_n^{ZX}} \sigma_v^x. \quad (4.4)$$

where P_n^{XY} labels the XY plane with Z direction coordinate n and similarly for P_n^{YZ} and P_n^{ZX} . Throughout this paper, we use X, Y, Z to label spatial directions and x, y, z to label spin directions.

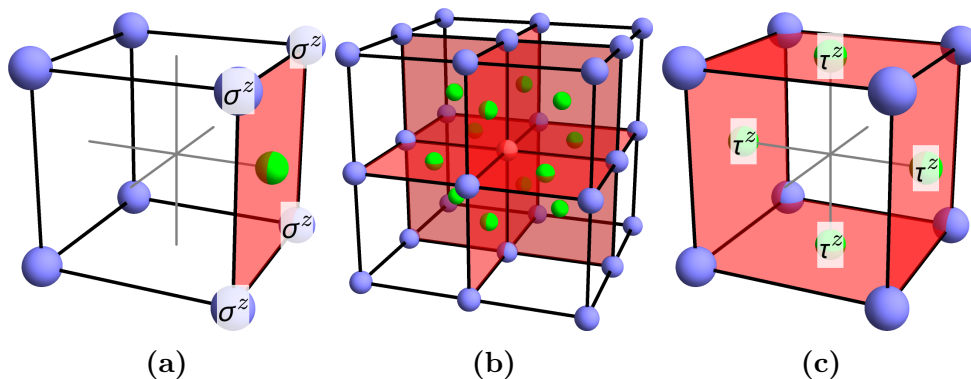


Figure 4.3: Gauging planar symmetry on a cubic lattice. (a) The minimal symmetric coupling term: a product of four σ^z around a plaquette (of the cubic lattice of blue spheres). A gauge field τ (green sphere) is therefore placed at the center of the plaquette, and all other plaquettes. The gray lines form the dual lattice. (b) The red vertex is involved in the twelve minimal coupling terms highlighted by red squares. The gauge symmetry term is a product of a σ^x at the red sphere and twelve τ^x on the green spheres. (c) The product of four minimal coupling terms around the four blue plaquettes is the identity. The corresponding flux term is a product of four τ^z on the green spheres.

This model (with additional plaquette terms) was originally considered in Ref. [\[50\]](#); however, we are not including the Ising coupling term here for simplicity of discussion. To gauge it, Ref. [\[50\]](#) proposed to add a gauge degree

of freedom τ at each face-center of the cubic lattice (green dots in Fig. [4.3](#)). The gauge symmetry is then given by

$$A_v = \sigma_v^x \prod_{f \ni v} \tau_f^x \quad (4.5)$$

which is the product of a symmetry charge σ_v^x at a site v and the (twelve) electric gauge fields τ_f^x on the neighboring faces f . The gauge flux terms, which are minimal pure vector potential terms that satisfy the gauge symmetry, now involve the product of four τ^z 's as shown in Fig. [4.3](#). The gauged Hamiltonian takes the form

$$H_g = - \sum_v \sigma_v^x - \sum_v A_v - \sum_c (B_c^{XY} + B_c^{YZ} + B_c^{ZX}) \quad (4.6)$$

Since the symmetry charges are fixed by the transverse field σ^x (in the ground state), the zero temperature phase of the gauged Hamiltonian becomes equivalent to that of the X-cube model [50](#).

However, for generic systems with subsystem symmetry the degrees of freedom may be located at different places in the lattice and may transform under the subsystem symmetry in different ways. For example, in Ref. [50](#), an example was discussed where the ungauged model contains DOFs at the vertices *and* at the face centers of a cubic lattice, where the subsystem symmetry acts on planes with integer and half integer coordinates (in units of the cubic lattice constant). Ref. [55](#) discussed an example where the DOFs lives both at the vertices and body centers; the ones at vertices transform under subsystem symmetry in one direction only. For a generic configuration of lattice structure and DOFs, where should the gauge fields be added and how should the gauge symmetry of the gauged model be defined?

4.3.1 General procedure

We will now outline a gauging procedure that is consistent with the gauging procedure for global symmetry [16](#), [18](#) and various previous works for gauging subsystem symmetries. The input to the procedure is a lattice of degrees of freedom (in a Hilbert space), a set of symmetry operators, and a model $H = \sum h$ that is symmetric under the symmetry. We will focus on abelian groups only in this paper.

Suppose that the on-site symmetry charge at each site is measured by σ_v^x (in

general the charge does not have to be a Z_2 charge, although we use the σ notation without loss of generality). The procedure is as follows:

1. Find the minimum coupling terms c that a) are not on-site symmetric; b) are a tensor product of operators carrying elementary symmetry charges at each site; and which, c) together with on-site symmetric terms, can be composed into any coupling term satisfying the symmetry. (Note that these minimum coupling terms are not necessarily included in the Hamiltonian; they are used only to locate the gauge degree of freedom in the next step.)
2. Assign a gauge degree of freedom τ_c at the center of each minimum coupling term. (τ_c^x can be thought of as the exponential e^{iE} of the electric field E , while τ_c^z is the exponential of the vector potential. τ can be a general gauge field, not just a Z_2 one.)
3. The gauge symmetry is given by $A_v = \sigma_v^x \prod_{c \ni v} \tau_c^x$, where the product is over all minimum coupling terms c that contain v .
4. All symmetric coupling terms h can then be made into gauge symmetric terms h_g by multiplying each minimal coupling factor in h by a τ_c^z .
5. The minimum coupling terms will usually not be independent of each other. Or sometimes, gauge fields are added for non-minimum coupling terms as well. In such cases, we then find independent minimum sets \mathcal{C} of coupling terms $c \in \mathcal{C}$ whose product is either the identity or a product of on-site symmetric terms σ^x .^[1] Correspondingly, the product $B_{\mathcal{C}} = \prod_{c \in \mathcal{C}} \tau_c^z$ becomes the flux term of the gauge field if it is a local term.

In this way, we can gauge a model $H = \sum h$ with global or subsystem symmetry into a gauge theory $H_g = \sum h' - \sum_v A_v - \sum_{\mathcal{C}} B_{\mathcal{C}}$. Let us consider some examples to see how this works.

¹Products of on-site symmetric terms can result for example when choices of minimal couplings terms contain σ^x .

4.3.2 Example: global symmetry

For global symmetry, the minimum symmetric coupling term is a nearest neighbor two-body term of the form $O_i O'_j$ where O_i carries charge e and O'_j carries charge $-e$. Other symmetric coupling terms, including non-nearest-neighbor two-body terms and multi-body terms, can all be constructed as composites of the nearest-neighbor two-body terms and on-site symmetric terms. Therefore, the gauge DOFs are assigned to each link of the lattice. The gauge symmetry term involves one lattice site and all the emanating links. The set of two-body terms around the same plaquette combine into on-site symmetric terms; therefore we have one flux term per plaquette. This is exactly the gauging procedure we reviewed in Sec. 4.2. Changing the lattice structure corresponds to choosing a different set of minimum coupling terms, which does not affect the nature of the gauge theory obtained.

4.3.3 Example: 3D planar symmetry on a cubic lattice

For the subsystem symmetry example discussed above (DOFs at vertices of cubic lattice, transforming under planar symmetry in three directions), the minimum symmetric coupling term is the four-body plaquette term $\prod_{v \in p} \sigma_v^z$, as shown in Fig. 4.3a. All other symmetric coupling terms can be obtained as composites of such plaquette terms and on-site symmetric terms. Therefore, as suggested in Ref. 50, we can add one gauge field per plaquette. Each vertex is involved in 12 minimum coupling terms; therefore the gauge symmetry term is a product of one σ^x and twelve τ^x (Fig. 4.3b). Four minimum coupling terms around the same cube combine into identity as shown in Fig. 4.3c; therefore we have the corresponding flux terms. This is exactly the gauging procedure we reviewed at the beginning of this section [Sec. 4.3].

4.3.4 Example: 3D planar symmetry on a FCC lattice

Consider the situation corresponding to the tetrahedral Ising model discussed in Ref. 50, as shown in Fig. 4.4. Besides the DOF σ_v at vertices of the cubic lattice, there are DOF σ_f at the faces of the cubic lattice. Subsystem symmetry acts on each XY , YZ and ZX direction plane either with integer

or half integer coordinates.:

$$\begin{aligned}
U_n^{XY} &= \prod_{v,f \in P_n^{XY}} \sigma_v^x \sigma_f^x, \\
U_n^{YZ} &= \prod_{v,f \in P_n^{YZ}} \sigma_v^x \sigma_f^x, \\
U_n^{ZX} &= \prod_{v,f \in P_n^{ZX}} \sigma_v^x \sigma_f^x, \\
U_{n+1/2}^{XY} &= \prod_{f \in P_{n+1/2}^{XY}} \sigma_f^x, \\
U_{n+1/2}^{YZ} &= \prod_{f \in P_{n+1/2}^{YZ}} \sigma_f^x, \\
U_{n+1/2}^{ZX} &= \prod_{f \in P_n^{ZX}} \sigma_f^x.
\end{aligned} \tag{4.7}$$

The minimum coupling terms, as shown in Fig. 4.4a, are the tetrahedral terms involving one σ_v^z and three σ_f^z 's. All other symmetric coupling terms, including four-body terms of σ_v^z 's and four-body terms of σ_f^z , can all be constructed from this minimum coupling term. Therefore, as discuss in Ref. 50, one gauge DOF τ is to be assigned to each tetrahedron. The gauge symmetry terms are the product of one σ^x together with the eight τ^x 's in the surrounding tetrahedrons (Fig. 4.4b). The product of the same eight tetrahedron minimum coupling terms also happens to be the identity; therefore, we have the product of eight τ^z 's as the flux term (Fig. 4.4b). If the σ DOF are all polarized by $-\sigma^x$, the gauged model becomes exactly the same as the checkerboard model.

4.3.5 Example: 3D planar symmetry on a BCC lattice

Now consider the situation described in Ref. 55, where there is one DOF σ_0 at each cube center and three DOFs $\sigma_a, \sigma_b, \sigma_c$ at each vertex, as shown in Fig. 4.5. σ_0 transforms under subsystem planar symmetries in all three directions while $\sigma_a, \sigma_b,$ and σ_c transform only under symmetries in $XY, YZ,$ and ZX planes, respectively. An XY -plane subsystem symmetry generator is a product of all σ_0^x in a particular XY plane ($P_{m+1/2}^{XY}$) with Z coordinate $m + 1/2$ and all σ_a^x in the two neighboring XY planes (P_m^{XY} and P_{m+1}^{XY}) with Z coordinate m and $m + 1$:

$$U_{m+1/2}^{XY} = \prod_{i \in P_{m+1/2}^{XY}} \sigma_{0,i}^x \prod_{j \in P_m^{XY}} \sigma_{a,j}^x \prod_{k \in P_{m+1}^{XY}} \sigma_{a,k}^x \tag{4.8}$$

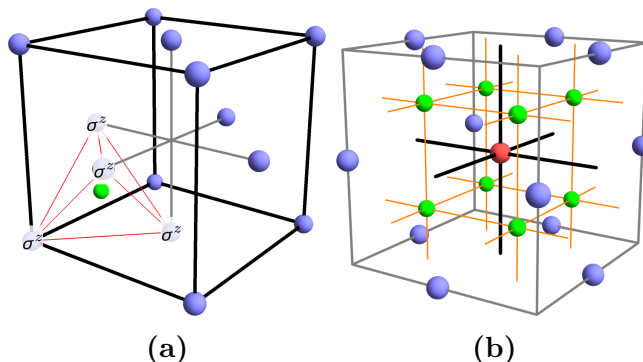


Figure 4.4: Gauging planar symmetry on FCC lattice. (a) A minimal symmetric coupling term: a product of four σ^z at the corners of the red tetrahedron. A gauge field τ (green sphere) is placed at the center of tetrahedron. Within the above cube, there are eight tetrahedra (one for each corner of the cube) and gauge fields. The gray lines form the dual lattice. (b) The red vertex is involved in the eight minimal coupling tetrahedron terms centered at the green spheres. The gauge symmetry term is thus a product of a σ^x at the red sphere and eight τ^x on the green spheres. The product of the eight minimal coupling tetrahedron terms is the identity. The corresponding flux term is a product of eight τ^z on the green spheres.

U^{YZ} and U^{ZX} are defined in similar ways. The minimum coupling terms are the triangular terms shown in Fig. 4.5a. All other symmetric coupling terms can be composed from these minimum coupling terms. Therefore, to gauge the model, we need to assign one gauge DOF τ per triangle. The gauge symmetry terms are then the product of one σ_0^x with 24 τ^x 's around it (Fig. 4.5b), and the product of one σ_a^x (or σ_b^x , σ_c^x) with four τ^x 's around it (Fig. 4.5c). The product of four triangular coupling terms is the identity, therefore we have the product of the corresponding four τ^z 's as the flux term (Fig. 4.5d). This is the minimum gauging scheme for such a distribution of symmetry charges.

We could add gauge fields corresponding to non-minimum coupling terms as well. This is what was done in Ref. 55, where a gauge field is added for each four-body plaquette coupling term of the σ_0 's. Since this four-body term can be obtained by composing two triangular terms, this results in one more type of gauge flux term corresponding to the product of the τ^z associated with these three coupling terms (one plaquette and two triangular terms).

4.3.6 Example: 3D scalar charge tensor gauge theory

The previous examples have considered gauging various gapped qubit models with planar symmetries. However, the gauging procedure in Sec. 4.3.1 can

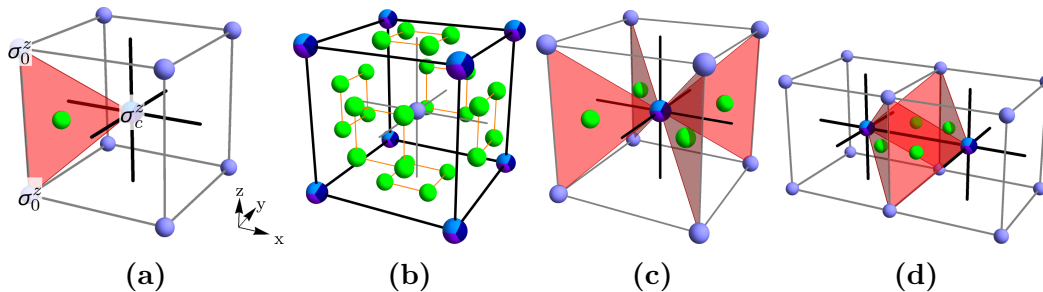


Figure 4.5: Gauging planar symmetry on BCC lattice. (a) A minimal symmetric coupling term: a product of two σ_0^z and one σ_c^z . The black lines form the cubic lattice, while the gray lines form the dual lattice. There are 12 minimal coupling terms within the shown dual-lattice cube: one for each gray edge of the cube. For the other terms, the σ_c^z at the center becomes a σ_a^z or σ_b^z when the two σ_0^z are displaced in the x or y direction, respectively. (b) The body-center is involved in 4×6 minimal coupling terms, which are centered at the green spheres, which lie on the faces of the black cube. (The orange lines are guides for the eye.) The gauge symmetry term is therefore a product of a σ^x at the center and $24 \tau^x$ on the green spheres. (c) The σ_c^z operator in the center is involved in 4 minimal coupling terms (highlighted in red). The gauge symmetry term is therefore a product of a σ_c^x at the center and four τ^x on the green spheres. (d) The product of the four minimal coupling triangular terms is the identity. The corresponding flux term is a product of four τ^z on the four green spheres.

also be used to obtain the gapless $U(1)$ tensor gauge theory models [10, 20, 24, 29, 35, 52], which also have fractons, lineons, and planons. In this case, the gauging procedure is very closely related to the Higgs mechanisms discussed in [5, 19]. In these $U(1)$ models, one can gauge a disordered field theory that has various kinds of global charge conservation laws. Similar to the previously discussed models, the conservation laws for the $U(1)$ models also result in mobility restrictions [33].

As an example, in this section we will consider gauging the following matter Hamiltonian

$$H = \int \pi^2 + \sum_{ab} (\partial_a \partial_b \phi)^2 \quad (4.9)$$

which has a global symmetry that results in a conserved dipole moment

$$P^a = \int x^a \pi \quad (4.10)$$

since $[H, P^a] = 0$, where ϕ and π are conjugate fields: $[\phi(x), \pi(x')] = i \delta^3(x - x')$. In this section, Latin letters $a, b, i, j = 1, 2, 3$ denote spatial indices. Repeated indices are implicitly summed.

We will now follow the general gauging procedure. For clarity, we will number the steps to match those in Sec. [4.3.1](#).

1) The minimal coupling operators that respect the symmetry are

$$\partial_a \partial_b \phi \tag{4.11}$$

That is, $[\partial_a \partial_b \phi, P^c] = 0$, and all other local terms that commute with P^a can be written as a polynomial in $\partial_a \partial_b \phi$ and π .

2) Since the minimal coupling operator is a symmetric tensor, we introduce a symmetric tensor gauge field A_{ab} , which is conjugate to an electric field E^{ab} : $[A_{ab}(x), E^{ij}(x')] = -\frac{i}{2}(\delta_a^i \delta_b^j + \delta_a^j \delta_b^i) \delta^3(x - x')$.

3) The gauge symmetry at x is $\pi(x)$ minus an electric field in place of every minimal coupling term that contains $\phi(x)$. The resulting expression can be calculated as follows

$$\pi(x) + i \int_{x'} [\partial_a \partial_b \phi(x), \pi(x')] E^{ab}(x') = \pi(x) - \partial_a \partial_b E^{ab}(x). \tag{4.12}$$

4) The minimal coupling term can be made gauge symmetric by coupling it to a gauge field: $\partial_a \partial_b \phi \rightarrow \partial_a \partial_b \phi - A_{ab}$.

5) We now need to find linear combinations of the minimal coupling terms $\partial_a \partial_b \phi$ that result in zero. Equivalently, we want to find linear combinations of derivatives of A_{ab} that are invariant under the replacement $A_{ab} \rightarrow A_{ab} + \partial_a \partial_b \lambda$, which is often referred to as a gauge transformation. Thus, we want to find the smallest possible basis of gauge invariant operators, which is given by the magnetic tensor $B_j^i = \epsilon^{iab} \partial_a A_{bj}$ [33](#).

Therefore, gauging the matter Hamiltonian [Eq. [\(4.9\)](#)] results in the following gauged Hamiltonian

$$H = \int \pi^2 + \sum_{ab} (\partial_a \partial_b \phi - A_{ab})^2 + (\pi - \partial_a \partial_b E^{ab})^2 + \sum_{ij} (\epsilon^{iab} \partial_a A_{bj})^2 + \sum_{ab} (E^{ab})^2 \tag{4.13}$$

$(E^{ab})^2$ is added at the end since the above model is a gapless gauge theory. Traditionally, the $(\pi - \partial_a \partial_b E^{ab})^2$ is not explicitly written, but is instead imposed as a gauge constraint or is considered irrelevant (under RG) at long length scales.

4.4 Correspondence before and after gauging

Using the general gauging procedure, in this section we are going to explore the correspondence between models with subsystem symmetry (before gauging) and the gauged model with foliated fracton order, which we refer to as the ‘gauging correspondence’ in the following.

In Ref. [41], we proposed to characterize fractional excitations in foliated fracton phases using the notion of *quotient superselection sectors* (QSS). In particular, two fractional excitations are considered as equivalent (i.e. they belong to the same QSS class) if they differ only by local excitation and planons – a fractional excitation that moves in a 2D plane. Among the foliated fracton phases that we have studied, there are two types of QSS: 1) fracton sectors where the fractional excitation is fully immobile as an individual quasiparticle, and 2) lineon sectors where the excitation can only move along a straight line.

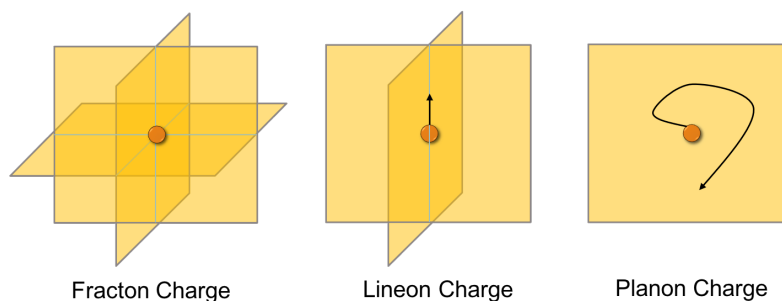


Figure 4.6: Symmetry charges transforming under planar symmetries in three, two, one directions are fractons (cannot move), lineons (can move only along a line), and planons (can move only in a plane) respectively.

In terms of the gauging correspondence, it is easy to see how the fracton/lineon QSS can emerge after gauging subsystem symmetries. Before gauging, if a symmetry charge transforms under planar subsystem symmetries in three directions, then to preserve subsystem symmetry, this charge cannot move freely in any direction. It is pinned at the intersection point of the three planes, as shown in Fig. 4.6, and such fracton symmetry charges have to be created four at a time. Upon gauging, they become the fracton gauge charges. If a symmetry charge transforms under planar symmetries in two directions, then this charge can move but only along the intersection line of the two planes. Such lineon symmetry charges become the lineon gauge charge upon gauging. Finally, if a symmetry charge transforms under planar symmetries in one direction only, then this charge can move along the plane.

Such planon symmetry charges become the planon gauge charge upon gauging. Composites of fracton charges can become lineon or planon charges. For example, composing two fracton charges in the same plane and displaced by a diagonal direction results in a lineon charge because the composite carries nontrivial symmetry charge in the two orthogonal planes only. By analyzing how the symmetry charges and their composites transform under subsystem symmetry, we can see how the gauging correspondence emerges. Let us see how this works through the following examples.

4.4.1 3D paramagnet with planar symmetry in one direction

We start with a simple and almost trivial case where the subsystem symmetry acts only in XY planes. Consider again the cubic lattice with DOF at vertices and the paramagnetic model $H = -\sum_v \sigma_v^x$. The subsystem symmetry is given by

$$U_m^{XY} = \prod_{v \in P_m^{XY}} \sigma_v^x \quad (4.14)$$

Upon gauging, this model should naturally map to a stack of 2D (untwisted) deconfined gauge theories in the XY plane. The symmetry charges become the planon gauge charges in each 2D layer. The gauged theory is a trivial foliated fracton phase. Of course, this result does not depend sensitively on the lattice structure or details of the Hamiltonian, as long as the planar symmetries are preserved.

4.4.2 3D paramagnet with planar symmetry in two directions

A less trivial example is the 3D paramagnet $H = -\sum_v \sigma_v^x$ with two sets of planar symmetries

$$U_m^{XZ} = \prod_{v \in P_m^{XZ}} \sigma_v^x, \quad U_n^{YZ} = \prod_{v \in P_n^{YZ}} \sigma_v^x \quad (4.15)$$

Each symmetry charge transforms under planar symmetries in two directions and hence becomes a lineon gauge charge upon gauging. The combination of two symmetry charges separated in the X or Y directions transform under planar symmetry in one direction only and hence is a planon. The combination of two symmetry charges separated in the Z direction does not transform under subsystem symmetry at all and hence is not a fractional excitation. Therefore, in the gauged theory, we expect only one lineon QSS in the charge sector.

This can be seen explicitly by applying the gauging procedure described in section 4.3. The two minimum coupling terms are 1) four σ^z 's around a plaquette in the same XY plane (Fig. 4.7a), and 2) two σ^z 's along the Z axis (Fig. 4.7b). Correspondingly, gauge fields are placed in each XY plane plaquette and on each link in the Z direction. The gauge symmetry term involves the product of one σ_v^x , four τ_{XY}^x 's and two τ_Z^x 's, as shown in Fig. 4.7c. The product of two plaquette coupling terms and four link coupling terms is identity, giving rise to the flux term as shown in Fig. 4.7d. The gauge charge, which corresponds to the violation of the gauge symmetry term, is a lineon that moves in the Z direction. It turns out that the flux excitation is also a lineon that moves in the Z direction. This is the anisotropic model introduced in Ref. 41.

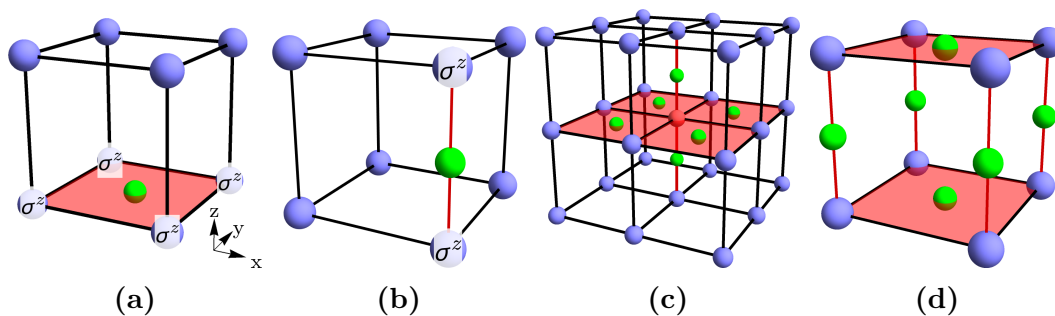


Figure 4.7: Gauging planar symmetry in XZ and YZ directions only. (a-b) Minimal coupling terms. (c) The red vertex term in the center is included in four plaquette minimal coupling terms (red plaquettes) and two Z -axis terms (red edges). Therefore, the gauge symmetry term is a product of a σ^x at the center (red sphere) and six τ^x at the green spheres. (d) The flux term is a product of six τ^z at the green spheres.

4.4.3 3D paramagnet with planar symmetry in three directions

Now let us consider the case where the planar subsystem symmetries lie along three directions. We have discussed the gauging procedure of three different cases (with different distributions of symmetry charges) in section 4.3. Now we will examine how the symmetry charge becomes a gauge charge through the gauging process and how the corresponding foliated fracton order emerges after gauging.

4.4.3.1 Cubic lattice

In the case discussed in section [4.3.3](#), where symmetry charges live at the vertices of a 3D cubic lattice and transform under planar symmetries in all three directions, each symmetry charge is a fracton and cannot move (since the charge is conserved on every plane). If two symmetry charges separated in the X , Y or Z direction are combined, then the composite transforms under planar symmetry in one direction only and hence is a planon. Therefore, upon gauging, the gauge charge sector of the gauge theory should contain only one quotient superselection sector – a fracton QSS. This is indeed the case for the corresponding gauge theory of X-cube model. As discussed in Ref. [\[41\]](#), the X-cube model contains three elementary QSSs: one fracton QSS and two lineon QSS. The one fracton QSS is the gauge charge sector of the gauge theory while the two lineon QSSs are the gauge flux sector of the gauge theory.

4.4.3.2 Cubic lattice: dual model

In fact, the X-cube model can be obtained through gauging a different model. Consider a 3D cubic lattice with two DOFs σ_r and σ_b (red and blue) at each lattice site. The red σ_r transform under planar symmetry in XY and YZ directions; the blue σ_b transform under planar symmetry in YZ and ZX directions; and their composite at each lattice site transforms under planar symmetry in ZX and XY directions. That is, the symmetries act as

$$U_m^{XY} = \prod_{v \in P_m^{XY}} \sigma_{v,r}^x, \quad U_m^{YZ} = \prod_{v \in P_m^{YZ}} \sigma_{v,r}^x \sigma_{v,b}^x, \quad U_n^{ZX} = \prod_{v \in P_n^{ZX}} \sigma_{v,b}^x. \quad (4.16)$$

The minimum coupling terms are two-body terms $\sigma_{v,r}^z \sigma_{v+\hat{y},r}^z$ in the Y direction, two-body terms $\sigma_{v,b}^z \sigma_{v+\hat{z},b}^z$ in the Z direction, and four-body terms $\sigma_{v,r}^z \sigma_{v,b}^z \sigma_{v+\hat{x},r}^z \sigma_{v+\hat{x},b}^z$ in the X direction, as shown in Fig. [4.8a](#). Therefore, according to the general procedure, a gauge field is added to each link of the cubic lattice. The gauge symmetry term is the product of $\sigma_{v,r}^x$ ($\sigma_{v,b}^x$) with four τ^x on neighboring links in the XY plane (ZX plane), as shown in Fig. [4.8b-c](#). The combination of twelve minimum coupling terms around a cube is identity, therefore the flux term is the product of twelve τ^z around a cube as shown in Fig. [4.8d](#).

If the σ spins are all polarized by Hamiltonian $H = -\sum_v (\sigma_{v,r}^x + \sigma_{v,b}^x)$, then the gauged model is exactly the X-cube model, but as the electromagnetic

dual of the previous case. The symmetry charges transform under two planar symmetries, and therefore gauge into two independent lineon gauge charges (that move in the Y and Z directions). Their combination is a lineon charge that transforms under the XY and XZ planar symmetries and therefore moves only in the X direction. If two red charges separated in the X , Y , or Z directions are combined, then they form either a planon or a local excitation, and similarly for the blue charges. Therefore, the gauge charge sector contains two independent lineon QSSs. The gauge flux in this case makes up the fracton QSS.

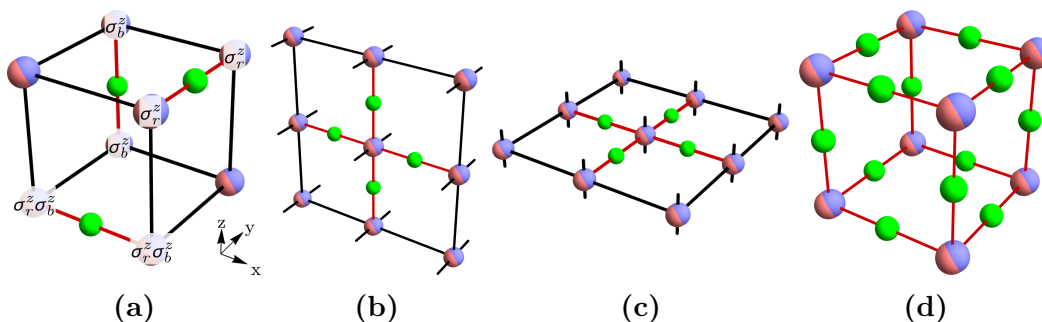


Figure 4.8: Gauging planar symmetry on the cubic lattice with lineon charges. (a) The three minimal coupling terms, which are each a product of σ^z operators across one of the red links. (b) A σ_b^z operator at the center is included in four minimal coupling terms on the red links. The corresponding gauge symmetry term is a product of a σ_b^x at the center and τ^x operators on the green spheres. (c) Same as (b), but for σ_r^z . (d) The flux term is a product of τ^z on the twelve green spheres.

4.4.3.3 FCC lattice

In the second case discussed in section [4.3.4](#), symmetry charges live both at vertices and face centers and transform under planar symmetry in all three directions. Again, each symmetry charge (both the vertex and face-center charges) is a fracton and cannot move. The combination of two vertex charges separated in X , Y , or Z directions transforms under planar symmetry in one direction only, and hence is a planon. Therefore, the vertex charge alone makes one fracton QSS after gauging. The combination of a vertex charge and a face-center charge separated by half of a face diagonal transforms under two planar symmetries and are hence lineons. Similarly, the combination of two face-center charges separated by half of a face diagonal (out of the plane of the face) are also lineons. Taking into account neutral excitations

– excitations carrying no symmetry charges – involving one vertex charge and three face-center charges, we can see that there are all together two independent lineon sectors. Therefore, upon gauging, the charge sector should contain one independent fracton QSS and two independent lineon QSSs. This corresponds exactly to the combination of the original and dual cubic lattice examples discussed above. Therefore, the gauged theory – the checkerboard model [50] – should be equivalent to two copies of X-cube model combined in a electromagnetic dual way. This is exactly what we show in Ref. [40].

4.4.3.4 BCC lattice

Now we come to the case discussed in section [4.3.5] where symmetry charges at cube center transform in three directions while symmetry charges at vertices transform in one direction only. The vertex charges are planon charges so they can be omitted when counting QSSs. The cube center charge is a fracton. Two fracton charges separated in the X , Y or Z direction combine into a planon. Therefore, upon gauging, the gauge charge sector contains only one fracton QSS. If the ungauged Hamiltonian is in the trivial phase (given for example by $H = -\sum_i \sigma_{0,i}^x - \sum_j \sigma_{a,j}^x - \sum_k \sigma_{b,k}^x - \sum_l \sigma_{c,l}^x$), then the gauged model would belong to the same foliated fracton phase as the X-cube model.

In Ref. [55], a twisted version of the ungauged Hamiltonian is discussed. Upon gauging, the charge sector remains the same, while the flux sector may have different statistics compared to the X-cube model. Ref. [55] discussed the difference in statistics in terms of the self rotation of lineons. In Ref. [41], we show that this difference can be removed if 2D layers of twisted gauge theories are added to the 3D fracton model. Therefore, the gauged model has the same foliated fracton order as the X-cube model. Correspondingly, the difference between the twisted and non-twisted versions of the ungauged Hamiltonian can be removed by adding 2D layers of twisted SPTs. Therefore, the twisted ungauged model is equivalent to a ‘weak SSPT’, i.e. a stack of 2D SPTs, as defined in Ref. [54].

4.4.4 3D paramagnet with planar symmetry in 4 directions

It is also possible to construct a paramagnet in which every DOF transforms under a planar subsystem symmetry in 4 different directions. The model is constructed as follows: first, a lattice is constructed out of a fourfold foliation

structure. To be precise, given four stacks of parallel planes such that no four planes intersect at a single point, a natural cellulation structure is defined in which each elementary 3-cell is a polyhedron bounded by these planes. Then, a σ DOF is placed in each 3-cell. The planar subsystem symmetries act on all 3-cells *between* neighboring parallel planes. The minimal symmetric coupling terms are the four-body terms $\prod_{v \in p} \sigma_v^z$ with a σ^z operator on each of the four 3-cells adjacent to a given edge (which is along the intersection between two planes). In the dual cellulation (or lattice), this edge is dual to a quadrilateral plaquette p , and the 3-cells are dual to vertices v . Upon gauging, the subsystem symmetric paramagnet defined on this type of lattice yields a generalized X-cube model as discussed in [44]. For example, using this type of construction, one can obtain the stacked kagome lattice X-cube model.

4.4.5 3D symmetry breaking state with planar symmetry

In all previous examples, for the ungauged model, we considered the simplest symmetric Hamiltonian of the form $H = -\sum_v \sigma_v^x$ where the ground state is symmetric under all subsystem symmetries. For global symmetry, it is known that when the matter field undergoes spontaneous symmetry breaking, the gauge field is Higgsed and the gauge theory become non-topological. For subsystem symmetry, a similar Higgs mechanism applies, as first discussed in Ref. [50]. Let us repeat the exercise and see how Higgsing occurs in the cubic lattice example of section [4.3.3]

The minimum Ising coupling term that can be added to the system is the plaquette term involving four σ^z 's (Fig. [4.3a]). To make the term gauge invariant, we attach a τ^z term in the middle of the plaquette. The total gauged Hamiltonian hence takes the form

$$H_g = -\sum_p \tau_p^z \prod_{v \in p} \sigma_v^z - \sum_v A_v - \sum_c (B_c^{XY} + B_c^{YZ} + B_c^{ZX}) \quad (4.17)$$

The B_c terms are actually redundant for determining ground state because they can be composed out of the plaquette terms. Therefore, the Hamiltonian can be simplified into

$$H_g = -\sum_p \tau_p^z \prod_{v \in p} \sigma_v^z - \sum_v \sigma_v^x \prod_{v \in p} \tau_p^x \quad (4.18)$$

This is a cluster state [3] Hamiltonian where the σ and τ DOFs are connected through face diagonals. It has a unique ground state, and hence no topological or fracton order.

4.4.6 2D paramagnet/symmetry breaking state with linear symmetry

It is possible for 2D systems to have linear subsystem symmetries. As we will see, gauging 2D systems with linear subsystem symmetries bears great similarity to gauging global symmetries in 1D. In particular, in both cases, trivial paramagnet and symmetry breaking phases are dual to each other through gauging. Consider a 2D square lattice with a σ DOF at each vertex. The subsystem symmetries acts along each row L_m^X and each column L_n^Y of the square lattice:

$$U_m^X = \prod_{v \in L_m^X} \sigma_v^x, \quad U_n^Y = \prod_{v \in L_n^Y} \sigma_v^x. \quad (4.19)$$

The minimum coupling term satisfying these symmetries is a product of four σ^z around a plaquette. Consider the ungauged Hamiltonian

$$H = -B_x \sum_v \sigma_v^x - J \sum_p \prod_{v \in p} \sigma_v^z \quad (4.20)$$

To gauge this model, we place one gauge DOF τ_p on each plaquette so that the gauge symmetry is given by $A_v = \sigma_v^x \prod_{p \ni v} \tau_p^x$. No local flux term satisfies all of the gauge symmetries; the only allowed flux terms are products along an entire row or a column:

$$B_{m,m+1}^X = \prod_{p \in L_{m,m+1}^X} \tau_p^z, \quad B_{n,n+1}^Y = \prod_{p \in L_{n,n+1}^Y} \tau_p^z. \quad (4.21)$$

Thus, the flux terms become subsystem symmetries of the gauged theory.

The Hamiltonian after gauging takes the form

$$H_g = -B_x \sum_v \sigma_v^x - J \sum_p \tau_p^z \prod_{v \in p} \sigma_v^z - J_v \sum_v \sigma_v^x \prod_{v \in p} \tau_p^x. \quad (4.22)$$

When $B_x = 0$, corresponding to the symmetry breaking phase before gauging, the gauged model is

$$H_g = -J \sum_p \tau_p^z \prod_{v \in p} \sigma_v^z - J_v \sum_v \sigma_v^x \prod_{v \in p} \tau_p^x \quad (4.23)$$

which is a 2D cluster state model with unique ground state that is symmetric under the subsystem symmetries B^X and B^Y . Moreover, this state can be mapped to a symmetric product state through a symmetric local unitary

transformation, indicating that it is equivalent to a trivial paramagnet. The symmetric local unitary is given by

$$V = \prod_v \left(\prod_{v \in p} C_v X_p \right) \prod_v H_v \prod_v \left(\prod_{v \in p} C_v X_p \right) \quad (4.24)$$

where $C_v X_p = \frac{1}{2}(1 + \sigma_v^z) \otimes \tau_p^0 + \frac{1}{2}(1 - \sigma_v^z) \otimes \tau_p^x$ is the controlled- X operation from a vertex spin to its neighboring gauge field and the Hadamard operator $H = \begin{pmatrix} 1 & 1 \\ 1 & -1 \end{pmatrix}$ maps between σ^x and σ^z .

When $J = 0$, corresponding to the trivial paramagnet phase before gauging, the gauged model is

$$H_g = -B_x \sum_v \sigma_v^x - J_v \sum_v \sigma_v^x \prod_{v \in p} \tau_p^x \quad (4.25)$$

which can be reduced to

$$H_g = -J_v \sum_v \prod_{v \in p} \tau_p^x \quad (4.26)$$

if the $-B_x \sigma_v^x$ terms are all satisfied. This corresponds to the symmetry breaking phase of the gauge field under subsystem symmetries B^X and B^Y .

4.4.7 2D linear symmetry protected topological model

We now discuss an example of a 2D model with linear SSPT order, which is self-dual under gauging the subsystem symmetries. The system contains a σ DOF at each vertex of two interlocking square lattices labelled α and β . The linear symmetries act on all spins in a given row or column of either the α or β lattice. Explicitly, the symmetry generators are

$$U_m^{X,\alpha} = \prod_{v \in L_m^{X,\alpha}} \sigma_v^x, \quad U_n^{Y,\alpha} = \prod_{v \in L_n^{Y,\alpha}} \sigma_v^x, \quad U_p^{X,\beta} = \prod_{v \in L_p^{X,\beta}} \sigma_v^x, \quad U_q^{Y,\beta} = \prod_{v \in L_q^{Y,\beta}} \sigma_v^x. \quad (4.27)$$

As discussed in [\[54\]](#), the 2D cluster state model is a strong SSPT, which exhibits a protected edge degeneracy that grows exponentially with the length of the boundary. The Hamiltonian (also shown in [Fig. 4.9](#)) is

$$H = - \sum_{a \in \alpha} \sigma_{i(a)}^z \sigma_{j(a)}^z \sigma_{k(a)}^z \sigma_{l(a)}^z \sigma_a^x - \sum_{b \in \beta} \sigma_{i(b)}^z \sigma_{j(b)}^z \sigma_{k(b)}^z \sigma_{l(b)}^z \sigma_b^x, \quad (4.28)$$

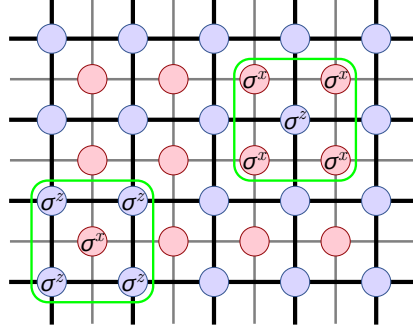


Figure 4.9: The 2D cluster state model. The two stabilizer terms in Eq. (4.28) are circled in green above. The black and gray lattices are the α and β lattices. After gauging, gauge fields τ are placed on both the red and blue vertices.

where $i(a)$, $j(a)$, $k(a)$, and $l(a)$ refer to the four β lattice vertices neighboring vertex a , and vice versa for $i(b)$, $j(b)$, $k(b)$, and $l(b)$.

The minimal coupling terms satisfying the subsystem symmetry are the four-body terms around each elementary plaquette of either the α or β lattice. Thus, to gauge the model, gauge fields τ_v are placed at every vertex v of both the α and β lattices (on top of each matter DOF), as shown in Fig. 4.9. The gauge symmetries then take the form $A_v = \sigma_v^x \tau_{i(v)}^x \tau_{j(v)}^x \tau_{k(v)}^x \tau_{l(v)}^x$. As in the previous example, there are no local gauge-symmetric flux operators; the only allowed flux terms act along an entire row or column:

$$B_m^{X,\alpha} = \prod_{v \in L_m^{X,\alpha}} \tau_v^z, \quad B_n^{X,\beta} = \prod_{v \in L_n^{X,\beta}} \tau_v^z, \quad B_p^{Y,\alpha} = \prod_{v \in L_p^{Y,\alpha}} \tau_v^z, \quad B_q^{Y,\beta} = \prod_{v \in L_q^{Y,\beta}} \tau_v^z. \quad (4.29)$$

These operators correspond to symmetry generators of the gauge theory.

Upon gauging the Hamiltonian takes the form

$$H_g = - \sum_{a \in \alpha} \tau_a^z \sigma_{i(a)}^z \sigma_{j(a)}^z \sigma_{k(a)}^z \sigma_{l(a)}^z \sigma_a^x - \sum_{b \in \beta} \tau_b^z \sigma_{i(b)}^z \sigma_{j(b)}^z \sigma_{k(b)}^z \sigma_{l(b)}^z \sigma_b^x - J_v \sum_{v \in \alpha, \beta} A_v. \quad (4.30)$$

This gauged model is actually a linear SSPT and is dual to the original SSPT. To see this, note that the matter DOFs can be decoupled from the gauge DOFs via the symmetric local unitary operator

$$V = \prod_{v \in \alpha, \beta} C_{\sigma_v} X_{\tau_{i(v)}} C_{\sigma_v} X_{\tau_{j(v)}} C_{\sigma_v} X_{\tau_{k(v)}} C_{\sigma_v} X_{\tau_{l(v)}}, \quad (4.31)$$

where as before, $C_\sigma V_\tau$ is the controlled- X gate from the vertex spin σ to an adjacent gauge field τ . Then

$$VH_gV^\dagger \cong - \sum_{a \in \alpha} \tau_{i(a)}^x \tau_{j(a)}^x \tau_{k(a)}^x \tau_{l(a)}^x \tau_a^z - \sum_{b \in \beta} \tau_{i(b)}^x \tau_{j(b)}^x \tau_{k(b)}^x \tau_{l(b)}^x \tau_b^z - \sum_{v \in \alpha, \beta} \sigma_v^x, \quad (4.32)$$

which is a 2D cluster state model residing on the gauge DOFs. Here the relation $H \cong H'$ indicates that H and H' have coinciding ground spaces and thus represent the same gapped phase.

4.4.8 3D models with linear subsystem symmetry

It is also possible for 3D systems to have linear subsystem symmetries. For example, suppose a system has a σ DOF at every vertex of a cubic lattice and symmetries which act along lines of spins along the X , Y , or Z direction. In this case, the minimal coupling terms that commute with the symmetries are eight-body terms $\prod_{v \in c} \sigma_v^z$ involving the 8 qubits at the corners of a cube c . Therefore, to gauge such models, gauge fields are placed at the centers of each cube.

The correspondence before and after gauging of linear subsystem symmetries in 3D bears similarities to the case of linear symmetries in 2D and global symmetries in 1D. For instance, the cubic Ising Hamiltonian

$$H = - \sum_v \sigma_v^x - \lambda \sum_c \prod_{v \in c} \sigma_v^z \quad (4.33)$$

is self-dual under gauging: the weak-coupling paramagnetic phase maps into the strong-coupling subsystem symmetry breaking phase and vice versa. Furthermore, the linear SSPT given by the the 3D cluster state Hamiltonian [\[54\]](#) is self-dual under gauging, in analogy with the 2D cluster state linear SSPT and the 1D cluster state global SPT.

4.5 Discussion

The gauging correspondence revealed in the previous examples is summarized in the table below. Fracton charges are acted upon by planar symmetry in three directions, whereas lineon charges are acted upon by planar symmetry in two directions. The fracton and lineon charges in the table are counted up to the attachment of planon charges, which are acted upon by planar symmetry in one direction only.

Therefore, by counting the types of symmetry charges before gauging, we can determine the gauge charge and correspondingly gauge flux quotient

	Before Gauging	After Gauging
Planar symmetry in 3D	One fracton charge	X-cube with lineon flux
	Lineon charges in X, Y, Z directions	X-cube with fracton flux
	One lineon charge in Z direction	Anisotropic model with lineon flux
Linear symmetry in 2D/3D	Trivial paramagnet	Symmetry breaking
	Symmetry breaking	Trivial paramagnet
	Non-trivial SSPT	Non-trivial SSPT

Table 4.1: Correspondence between phases with subsystem symmetries and gauge theory phases. The X-cube and anisotropic model listed refer to the corresponding foliated fracton phase, not to the specific model.

superselection sectors in the gauge theory. A highly interesting and open question is whether there are non-trivial SPT phases with planar subsystem symmetry in 3D. The model discussed in Ref. [55] we now know to be equivalent to a weak SSPT. Hence upon gauging, it gives the same foliated fracton order as the X-cube model [41]. For a truly non-trivial SSPT, upon gauging, we expect the gauge charge and gauge flux to correspond to the same quotient superselection sectors while the gauge flux has non-trivial statistics compared to the X-cube model.

4.6 Appendix: Gauging global symmetry in 1D systems

In this section, we review the process of gauging 1D symmetric, symmetry breaking and SPT phases and see how symmetric and symmetry breaking phases map into each other upon gauging while SPT phases can map into themselves.

Consider the 1D transverse field Ising model with Hamiltonian

$$H = -B_x \sum_i \sigma_i^x - J \sum_i \sigma_i^z \sigma_{i+1}^z \quad (4.34)$$

and global symmetry $U = \prod_i \sigma_i^x$. To gauge the model, we put gauge fields τ on every link. The gauge symmetry term is $A_i = \tau_{i-1,i}^x \sigma_i^x \tau_{i,i+1}^x$. The only flux term that satisfies all the gauge symmetries is a global term $B = \prod_i \tau_{i,i+1}^z$. Therefore, the flux term effectively becomes a Z_2 global symmetry of the gauged model.

Coupling H to the gauge field, we obtain the gauged Hamiltonian

$$H_g = -B_x \sum_i \sigma_i^x - J \sum_i \sigma_i^z \tau_{i,i+1}^z \sigma_{i+1}^z - J_v \sum_i \tau_{i-1,i}^x \sigma_i^x \tau_{i,i+1}^x \quad (4.35)$$

When $J = 0$, in the ground state, all the σ spins are polarized in the X direction and the gauge fields couple effectively through $\tau_{i-1,i}^x \tau_{i,i+1}^x$. With respect to the effective global symmetry of $B = \prod_i \tau_{i,i+1}^z$, the gauge field ground state spontaneously breaks the symmetry.

On the other hand, if $B_x = 0$, the Hamiltonian becomes a 1D cluster state [3] model with unique ground state which is symmetric under the global $B = \prod_i \tau_{i,i+1}^z$ symmetry.

Now let us discuss an SPT example. Consider the 1D cluster state model

$$H = - \sum_i h_{2i-1}^o - \sum_i h_{2i}^e = - \sum_i \sigma_{2i-2}^z \sigma_{2i-1}^x \sigma_{2i}^z - \sum_i \sigma_{2i-1}^z \sigma_{2i}^x \sigma_{2i+1}^z. \quad (4.36)$$

This model has a global $Z_2 \times Z_2$ symmetry generated by

$$g_1 = \prod_i \sigma_{2i}^x, \quad g_2 = \prod_i \sigma_{2i-1}^x \quad (4.37)$$

and the model has symmetry protected topological order under this symmetry [45].

To gauge the $Z_2 \times Z_2$ symmetry, we put gauge fields τ between neighboring gauge charges. That is, we place one gauge DOF per site. The ones on the even sites are gauge fields of g_2 . The ones on the odd sites are gauge fields of g_1 . The Gauss law terms are

$$c_{2i} = \tau_{2i-1}^x \sigma_{2i}^x \tau_{2i+1}^x, \quad c_{2i+1} = \tau_{2i}^x \sigma_{2i+1}^x \tau_{2i+2}^x. \quad (4.38)$$

The flux terms, which are pure gauge terms that satisfy the Gauss law, are

$$f_1 = \prod_i \tau_{2i-1}^z, \quad f_2 = \prod_i \tau_{2i}^z. \quad (4.39)$$

They become the global $Z_2 \times Z_2$ symmetry of the gauged model.

To make the original Hamiltonian terms gauge invariant, we modify them to be

$$h_{2i-1}^o = \sigma_{2i-2}^z \sigma_{2i-1}^x \tau_{2i-1}^z \sigma_{2i}^z, \quad h_{2i}^e = \sigma_{2i-1}^z \sigma_{2i}^x \tau_{2i}^z \sigma_{2i+1}^z. \quad (4.40)$$

Now the total Hamiltonian is

$$H_g = - \sum_i \left(\tau_{2i-1}^x \sigma_{2i}^x \tau_{2i+1}^x + \tau_{2i}^x \sigma_{2i+1}^x \tau_{2i+2}^x + \sigma_{2i-2}^z \sigma_{2i-1}^x \tau_{2i-1}^z \sigma_{2i}^z + \sigma_{2i-1}^z \sigma_{2i}^x \tau_{2i}^z \sigma_{2i+1}^z \right) \quad (4.41)$$

All the terms commute, are independent, and are symmetric under the global symmetry. Therefore, on a closed ring, the ground state is unique. On an open chain, the terms

$$\sigma_1^x \tau_2^x, \tau_{2N-1}^x \sigma_{2N}^x \quad (4.42)$$

no longer commute with the symmetry and need to be removed, leaving a two fold degeneracy at the edge as the symmetry protected edge state.

References

- [1] S. Bravyi, B. Leemhuis, and B.M. Terhal. “Topological order in an exactly solvable 3D spin model”. In: *Annals of Physics* 326 (Apr. 2011), pp. 839–866. DOI: [10.1016/j.aop.2010.11.002](https://doi.org/10.1016/j.aop.2010.11.002).
- [2] Sergey Bravyi and Jeongwan Haah. “Energy Landscape of 3D Spin Hamiltonians with Topological Order”. In: *Phys. Rev. Lett.* 107 (15 Oct. 2011), p. 150504. DOI: [10.1103/PhysRevLett.107.150504](https://doi.org/10.1103/PhysRevLett.107.150504).
- [3] Hans J. Briegel and Robert Raussendorf. “Persistent Entanglement in Arrays of Interacting Particles”. In: *Phys. Rev. Lett.* 86 (5 Jan. 2001), pp. 910–913. DOI: [10.1103/PhysRevLett.86.910](https://doi.org/10.1103/PhysRevLett.86.910) URL: <https://link.aps.org/doi/10.1103/PhysRevLett.86.910>.
- [4] D. Bulmash and M. Barkeshli. “Generalized $U(1)$ Gauge Field Theories and Fractal Dynamics”. In: *ArXiv e-prints* (June 2018). arXiv: [1806.01855](https://arxiv.org/abs/1806.01855) [[cond-mat.str-el](https://arxiv.org/abs/1806.01855)].
- [5] Daniel Bulmash and Maissam Barkeshli. “Higgs mechanism in higher-rank symmetric $U(1)$ gauge theories”. In: *Phys. Rev. B* 97 (23 June 2018), p. 235112. DOI: [10.1103/PhysRevB.97.235112](https://doi.org/10.1103/PhysRevB.97.235112) URL: <https://link.aps.org/doi/10.1103/PhysRevB.97.235112>.
- [6] Claudio Chamon. “Quantum Glassiness in Strongly Correlated Clean Systems: An Example of Topological Overprotection”. In: *Phys. Rev. Lett.* 94 (4 Jan. 2005), p. 040402. DOI: [10.1103/PhysRevLett.94.040402](https://doi.org/10.1103/PhysRevLett.94.040402).
- [7] T. Devakul and D. J. Williamson. “Universal quantum computation using fractal symmetry-protected cluster phases”. In: *ArXiv e-prints* (June 2018). arXiv: [1806.04663](https://arxiv.org/abs/1806.04663) [[quant-ph](https://arxiv.org/abs/1806.04663)].
- [8] T. Devakul et al. “Fractal Symmetric Phases of Matter”. In: *ArXiv e-prints* (May 2018). arXiv: [1805.04097](https://arxiv.org/abs/1805.04097) [[cond-mat.str-el](https://arxiv.org/abs/1805.04097)].
- [9] Trithep Devakul, S. A. Parameswaran, and S. L. Sondhi. “Correlation function diagnostics for type-I fracton phases”. In: *Phys. Rev. B* 97 (4 Jan. 2018), p. 041110. DOI: [10.1103/PhysRevB.97.041110](https://doi.org/10.1103/PhysRevB.97.041110).
- [10] A. Gromov. “Fractional Topological Elasticity and Fracton Order”. In: *ArXiv e-prints* (Dec. 2017). arXiv: [1712.06600](https://arxiv.org/abs/1712.06600) [[cond-mat.str-el](https://arxiv.org/abs/1712.06600)].

- [11] Jeongwan Haah. “Local stabilizer codes in three dimensions without string logical operators”. In: *Phys. Rev. A* 83 (4 Apr. 2011), p. 042330. DOI: [10.1103/PhysRevA.83.042330](https://doi.org/10.1103/PhysRevA.83.042330).
- [12] Gábor B. Halász, Timothy H. Hsieh, and Leon Balents. “Fracton Topological Phases from Strongly Coupled Spin Chains”. In: *Phys. Rev. Lett.* 119 (25 Dec. 2017), p. 257202. DOI: [10.1103/PhysRevLett.119.257202](https://doi.org/10.1103/PhysRevLett.119.257202).
- [13] Huan He et al. “Entanglement entropy from tensor network states for stabilizer codes”. In: *Phys. Rev. B* 97 (12 Mar. 2018), p. 125102. DOI: [10.1103/PhysRevB.97.125102](https://doi.org/10.1103/PhysRevB.97.125102).
- [14] Timothy H. Hsieh and Gábor B. Halász. “Fractons from partons”. In: *Phys. Rev. B* 96 (16 Oct. 2017), p. 165105. DOI: [10.1103/PhysRevB.96.165105](https://doi.org/10.1103/PhysRevB.96.165105).
- [15] Alexei Kitaev. “Anyons in an exactly solved model and beyond”. In: *Annals of Physics* 321.1 (2006). January Special Issue, pp. 2–111. ISSN: 0003-4916. DOI: [10.1016/j.aop.2005.10.005](https://doi.org/10.1016/j.aop.2005.10.005).
- [16] John B. Kogut. “An introduction to lattice gauge theory and spin systems”. In: *Rev. Mod. Phys.* 51 (4 Oct. 1979), pp. 659–713. DOI: [10.1103/RevModPhys.51.659](https://doi.org/10.1103/RevModPhys.51.659). URL: <https://link.aps.org/doi/10.1103/RevModPhys.51.659>.
- [17] A. Kubica and B. Yoshida. “Ungauging quantum error-correcting codes”. In: *ArXiv e-prints* (May 2018). arXiv: [1805.01836 \[quant-ph\]](https://arxiv.org/abs/1805.01836).
- [18] Michael Levin and Zheng-Cheng Gu. “Braiding statistics approach to symmetry-protected topological phases”. In: *Phys. Rev. B* 86 (11 Sept. 2012), p. 115109. DOI: [10.1103/PhysRevB.86.115109](https://doi.org/10.1103/PhysRevB.86.115109). URL: <https://link.aps.org/doi/10.1103/PhysRevB.86.115109>.
- [19] H. Ma, M. Hermele, and X. Chen. “Fracton topological order from Higgs and partial confinement mechanisms of rank-two gauge theory”. In: *ArXiv e-prints* (Feb. 2018). arXiv: [1802.10108 \[cond-mat.str-el\]](https://arxiv.org/abs/1802.10108).
- [20] H. Ma and M. Pretko. “Higher Rank Deconfined Quantum Criticality and the Exciton Bose Condensate”. In: *ArXiv e-prints* (Mar. 2018). arXiv: [1803.04980 \[cond-mat.str-el\]](https://arxiv.org/abs/1803.04980).
- [21] Han Ma et al. “Fracton topological order via coupled layers”. In: *Phys. Rev. B* 95 (24 June 2017), p. 245126. DOI: [10.1103/PhysRevB.95.245126](https://doi.org/10.1103/PhysRevB.95.245126).
- [22] Han Ma et al. “Topological entanglement entropy of fracton stabilizer codes”. In: *Phys. Rev. B* 97 (12 Mar. 2018), p. 125101. DOI: [10.1103/PhysRevB.97.125101](https://doi.org/10.1103/PhysRevB.97.125101).
- [23] R. M. Nandkishore and M. Hermele. “Fractons”. In: *ArXiv e-prints* (Mar. 2018). arXiv: [1803.11196 \[cond-mat.str-el\]](https://arxiv.org/abs/1803.11196).

- [24] Shriya Pai and Michael Pretko. “Fractonic line excitations: An inroad from three-dimensional elasticity theory”. In: *Phys. Rev. B* 97 (23 June 2018), p. 235102. DOI: [10.1103/PhysRevB.97.235102](https://doi.org/10.1103/PhysRevB.97.235102). URL: <https://link.aps.org/doi/10.1103/PhysRevB.97.235102>.
- [25] O. Petrova and N. Regnault. “Simple anisotropic three-dimensional quantum spin liquid with fractonlike topological order”. In: *Phys. Rev. B* 96 (22 Dec. 2017), p. 224429. DOI: [10.1103/PhysRevB.96.224429](https://doi.org/10.1103/PhysRevB.96.224429).
- [26] A. Prem et al. “Cage-Net Fracton Models”. In: *ArXiv e-prints* (June 2018). arXiv: [1806.04687 \[cond-mat.str-el\]](https://arxiv.org/abs/1806.04687).
- [27] A. Prem et al. “Pinch Point Singularities of Tensor Spin Liquids”. In: *ArXiv e-prints* (June 2018). arXiv: [1806.04148 \[cond-mat.str-el\]](https://arxiv.org/abs/1806.04148).
- [28] Abhinav Prem, Jeongwan Haah, and Rahul Nandkishore. “Glassy quantum dynamics in translation invariant fracton models”. In: *Phys. Rev. B* 95 (15 Apr. 2017), p. 155133. DOI: [10.1103/PhysRevB.95.155133](https://doi.org/10.1103/PhysRevB.95.155133).
- [29] Abhinav Prem, Michael Pretko, and Rahul M. Nandkishore. “Emergent phases of fractonic matter”. In: *Phys. Rev. B* 97 (8 Feb. 2018), p. 085116. DOI: [10.1103/PhysRevB.97.085116](https://doi.org/10.1103/PhysRevB.97.085116). URL: <https://link.aps.org/doi/10.1103/PhysRevB.97.085116>.
- [30] Michael Pretko. “Emergent gravity of fractons: Mach’s principle revisited”. In: *Phys. Rev. D* 96 (2 July 2017), p. 024051. DOI: [10.1103/PhysRevD.96.024051](https://doi.org/10.1103/PhysRevD.96.024051).
- [31] Michael Pretko. “Generalized electromagnetism of subdimensional particles: A spin liquid story”. In: *Phys. Rev. B* 96 (3 July 2017), p. 035119. DOI: [10.1103/PhysRevB.96.035119](https://doi.org/10.1103/PhysRevB.96.035119).
- [32] Michael Pretko. “Higher-spin Witten effect and two-dimensional fracton phases”. In: *Phys. Rev. B* 96 (12 Sept. 2017), p. 125151. DOI: [10.1103/PhysRevB.96.125151](https://doi.org/10.1103/PhysRevB.96.125151).
- [33] Michael Pretko. “Subdimensional particle structure of higher rank $U(1)$ spin liquids”. In: *Phys. Rev. B* 95 (11 Mar. 2017), p. 115139. DOI: [10.1103/PhysRevB.95.115139](https://doi.org/10.1103/PhysRevB.95.115139).
- [34] Michael Pretko and Leo Radzihovsky. “Fracton-Elasticity Duality”. In: *Phys. Rev. Lett.* 120 (19 May 2018), p. 195301. DOI: [10.1103/PhysRevLett.120.195301](https://doi.org/10.1103/PhysRevLett.120.195301).
- [35] A. Rasmussen, Y.-Z. You, and C. Xu. “Stable Gapless Bose Liquid Phases without any Symmetry”. In: *ArXiv e-prints* (Jan. 2016). arXiv: [1601.08235 \[cond-mat.str-el\]](https://arxiv.org/abs/1601.08235).

- [36] A. T. Schmitz et al. “Recoverable information and emergent conservation laws in fracton stabilizer codes”. In: *Phys. Rev. B* 97 (13 Apr. 2018), p. 134426. DOI: [10.1103/PhysRevB.97.134426](https://doi.org/10.1103/PhysRevB.97.134426). URL: <https://link.aps.org/doi/10.1103/PhysRevB.97.134426>.
- [37] Bowen Shi and Yuan-Ming Lu. “Deciphering the nonlocal entanglement entropy of fracton topological orders”. In: *Phys. Rev. B* 97 (14 Apr. 2018), p. 144106. DOI: [10.1103/PhysRevB.97.144106](https://doi.org/10.1103/PhysRevB.97.144106).
- [38] W. Shirley, K. Slagle, and X. Chen. “Universal entanglement signatures of foliated fracton phases”. In: *ArXiv e-prints* (Mar. 2018). arXiv: [1803.10426](https://arxiv.org/abs/1803.10426) [[cond-mat.str-el](https://arxiv.org/abs/1803.10426)].
- [39] W. Shirley et al. “Fracton Models on General Three-Dimensional Manifolds”. In: *ArXiv e-prints* (Dec. 2017). arXiv: [1712.05892](https://arxiv.org/abs/1712.05892) [[cond-mat.str-el](https://arxiv.org/abs/1712.05892)].
- [40] Wilbur Shirley, Kevin Slagle, and Xie Chen. “Foliated fracton order in the checkerboard model”. In: (2018). to appear soon.
- [41] Wilbur Shirley, Kevin Slagle, and Xie Chen. “Fractional excitations in foliated fracton phases”. In: (2018). to appear soon.
- [42] Kevin Slagle and Yong Baek Kim. “Fracton topological order from nearest-neighbor two-spin interactions and dualities”. In: *Phys. Rev. B* 96 (16 Oct. 2017), p. 165106. DOI: [10.1103/PhysRevB.96.165106](https://doi.org/10.1103/PhysRevB.96.165106).
- [43] Kevin Slagle and Yong Baek Kim. “Quantum field theory of X-cube fracton topological order and robust degeneracy from geometry”. In: *Phys. Rev. B* 96 (19 Nov. 2017), p. 195139. DOI: [10.1103/PhysRevB.96.195139](https://doi.org/10.1103/PhysRevB.96.195139).
- [44] Kevin Slagle and Yong Baek Kim. “X-cube model on generic lattices: Fracton phases and geometric order”. In: *Phys. Rev. B* 97 (16 Apr. 2018), p. 165106. DOI: [10.1103/PhysRevB.97.165106](https://doi.org/10.1103/PhysRevB.97.165106).
- [45] W. Son, L. Amico, and V. Vedral. “Topological order in 1D Cluster state protected by symmetry”. In: *Quantum Information Processing* 11.6 (Dec. 2012), pp. 1961–1968. ISSN: 1573-1332. DOI: [10.1007/s11128-011-0346-7](https://doi.org/10.1007/s11128-011-0346-7). URL: <https://doi.org/10.1007/s11128-011-0346-7>.
- [46] H. Song et al. “Twisted Fracton Models in Three Dimensions”. In: *ArXiv e-prints* (May 2018). arXiv: [1805.06899](https://arxiv.org/abs/1805.06899) [[cond-mat.str-el](https://arxiv.org/abs/1805.06899)].
- [47] S. Vijay. “Isotropic Layer Construction and Phase Diagram for Fracton Topological Phases”. In: *ArXiv e-prints* (Jan. 2017). arXiv: [1701.00762](https://arxiv.org/abs/1701.00762) [[cond-mat.str-el](https://arxiv.org/abs/1701.00762)].
- [48] S. Vijay and L. Fu. “A Generalization of Non-Abelian Anyons in Three Dimensions”. In: *ArXiv e-prints* (June 2017). arXiv: [1706.07070](https://arxiv.org/abs/1706.07070) [[cond-mat.str-el](https://arxiv.org/abs/1706.07070)].

- [49] Sagar Vijay, Jeongwan Haah, and Liang Fu. “A new kind of topological quantum order: A dimensional hierarchy of quasiparticles built from stationary excitations”. In: *Phys. Rev. B* 92 (23 Dec. 2015), p. 235136. DOI: [10.1103/PhysRevB.92.235136](https://doi.org/10.1103/PhysRevB.92.235136).
- [50] Sagar Vijay, Jeongwan Haah, and Liang Fu. “Fracton topological order, generalized lattice gauge theory, and duality”. In: *Phys. Rev. B* 94 (23 Dec. 2016), p. 235157. DOI: [10.1103/PhysRevB.94.235157](https://doi.org/10.1103/PhysRevB.94.235157).
- [51] Dominic J. Williamson. “Fractal symmetries: Ungauging the cubic code”. In: *Phys. Rev. B* 94 (15 Oct. 2016), p. 155128. DOI: [10.1103/PhysRevB.94.155128](https://doi.org/10.1103/PhysRevB.94.155128).
- [52] Cenke Xu. “Gapless bosonic excitation without symmetry breaking: An algebraic spin liquid with soft gravitons”. In: *Phys. Rev. B* 74 (22 Dec. 2006), p. 224433. DOI: [10.1103/PhysRevB.74.224433](https://doi.org/10.1103/PhysRevB.74.224433).
- [53] Beni Yoshida. “Exotic topological order in fractal spin liquids”. In: *Phys. Rev. B* 88 (12 Sept. 2013), p. 125122. DOI: [10.1103/PhysRevB.88.125122](https://doi.org/10.1103/PhysRevB.88.125122).
- [54] Y. You et al. “Subsystem symmetry protected topological order”. In: *ArXiv e-prints* (Mar. 2018). arXiv: [1803.02369](https://arxiv.org/abs/1803.02369) [[cond-mat.str-el](#)].
- [55] Y. You et al. “Symmetric Fracton Matter: Twisted and Enriched”. In: *ArXiv e-prints* (May 2018). arXiv: [1805.09800](https://arxiv.org/abs/1805.09800) [[cond-mat.str-el](#)].

FRACTIONAL EXCITATIONS IN FOLIATED FRACTON PHASES

5.1 Introduction

Gapped topological phases are characterized by their fractional excitations and the universal braiding statistics amongst them. For example, the $\nu = 1/3$ fractional quantum Hall state contains $e/3$ fractional charges; exchanging two fractional charges results in a phase factor of $\pi/3$ [1, 53]. In two-dimensional gapped topological phases, possible sets of fractional excitations and their fusion rules and braiding statistics are captured by the mathematical framework of unitary modular tensor categories [17]. In three spatial dimensions (3D), there are loop-like excitations in addition to point-like excitations. For example, a discrete gauge theory in 3D contains both point-like gauge charges and loop-like gauge fluxes; the exchange of gauge charges, the braiding of a gauge charge around a gauge flux, and the three-loop braiding of (linked) gauge fluxes [16, 49, 51] give rise to universal statistics. In general, it is expected that the set of fractional excitations together with their exchange and braiding statistics provide a complete characterization of the underlying topological order. In other words, if two gapped systems have the same fractional excitations, then they belong to the same topological phase and can be deformed into one another without undergoing a phase transition.

The recent discovery of *fracton* models [2, 4, 6, 9, 12, 13, 15, 21, 23, 25, 26, 39, 41–48, 56, 58] introduces new possibilities [3, 8, 10, 14, 18, 22, 27, 28, 36–38, 54, 57] and at the same time poses new challenges to this means of characterization. It was found that in these 3D gapped lattice models, point-like excitations have restricted motion (whereas point-like excitations of topological phases can move freely throughout the entire 3D space). Some excitations, which we will refer to as *lineons*, can only move along a line; others, which we call *planons*, can only move within a plane; the so-called *fractons* are fully immobile as individual particles – however they may move in coordination as the corners of an expanding or shrinking rectangle or tetrahedron. The excitations are *fractional* in the sense that they cannot be individually created

or destroyed by local operations. (We do not assume any global symmetry in these models and are not using the word ‘fractional’ in the sense that the excitations carry fractional symmetry representations such as fractional charge or spin).

It is not obvious how to properly describe these excitations. Point-like excitations in conventional topological phases are grouped into superselection sectors: two excitations belong to the same superselection sector if they can be mapped into each other via local operations [17]. If we utilize the same notion to describe fractional excitations in fracton phases, the number of superselection sectors is unbounded and grows exponentially with the total system size. Moreover, due to the restricted mobility of the excitations, it is not clear what constitutes a universal quasiparticle ‘braiding’ process. Given such difficulties, it is not clear how to use fractional excitations to characterize and compare the non-trivial orders in different fracton models.

In this paper, we introduce a way of characterizing fractional excitations and their statistics for a sub-class of fracton phases – the ‘foliated fracton phases’ which we defined in Ref. [39] and Ref. [38]. We observed that a large class of fracton models contain a foliation structure – the system size can be increased by adding two dimensional topological layers and smoothly fusing them in – such that their non-trivial properties can in large part be attributed to these underlying layers.¹ Such properties include the sub-extensive scaling of the logarithm of the ground state degeneracy with system size (linear in the length of the system), and a sub-leading correction to the area law term in the ground state entanglement entropy of a region that scales linearly with the diameter of the region. To unmask the intrinsic 3D nature of the order in these models, we consider models that differ by gapped 2D layers to be equivalent. That is, we define two gapped fracton models to be in the same foliated fracton phase if they can be smoothly deformed into one another (without closing the energy gap to excited states) upon the addition of gapped 2D layers. This definition subsequently points to the natural way to properly describe fractional excitations in foliated fracton phases – by *modding out* the planons.

More specifically, we generalize the notion of superselection sectors to that of *quotient superselection sectors* (QSS) so that two point-like excitations are

¹Gapless $U(1)$ fracton models [5, 11, 19, 20, 24, 29, 35, 55] and type-II fracton models (for which excitations are created at corners of fractal operators) [12, 56] are not foliated fracton phases, and will not be considered in this work.

considered as equivalent not only if they can be related by local operations, but also if they can be related by attaching a planon (i.e. an excitation that can only move in two dimensions). Under this generalized notion of equivalence, the number of sectors becomes finite, which greatly simplifies the counting. Correspondingly, when we subsequently define quasiparticle statistics using interferometric detection, we only consider processes which are indifferent to the attachment of planons.

This way of describing fractional excitations provides a powerful tool for comparing foliated fracton order in different models. In particular, we show that the X-cube model [48] and the semionic X-cube model [21] have the same fractional excitations and statistics according to this definition, despite the fact that their statistics appear very different prior to taking the quotient. This suggests that these two models may have the same foliated fracton order and indeed we present an exact mapping from one to another that involves the addition of 2D topological layers to each model.

This paper is organized as follows: in section [5.2] we briefly review the X-cube model, in particular its fractional excitations and foliation structure. Section [5.3] defines the quotient superselection sectors (QSS) and the subsequent section [5.4] discusses a way of characterizing their statistics using interferometric detection. Both sections use the X-cube model as an example to explain the idea. In section [5.5] several other fracton models are studied, including a novel anisotropic lineon model in section [5.5.7]. Their fractional excitation content is found to belong to several classes, as summarized in the table in the concluding section [5.8]. The explicit mapping between the semionic X-cube model to the X-cube model is given in section [5.6]. In section [5.7] we briefly extend the discussion to encompass loop excitations of 3D topological orders.

5.2 The X-cube model

In this section we briefly review the X-cube model, its hierarchy of subdimensional fractional excitations, and the RG transformation for the model which utilizes 2D toric code layers as resource states. As originally discussed in [48], the model is defined on a cubic lattice with a qubit degree of freedom placed on each lattice link. The Hamiltonian is a frustration-free

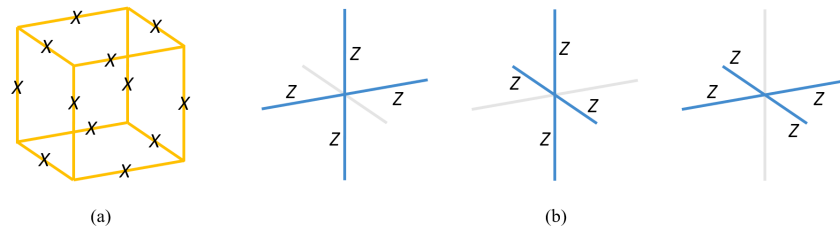


Figure 5.1: (a) Cube and (b) cross terms of the X-cube Hamiltonian.

sum of mutually commuting operators (shown in Fig. 5.1):

$$H = - \sum_v (A_v^{xy} + A_v^{xz} + A_v^{yz}) - \sum_c B_c, \quad (5.1)$$

where the first sum is overall vertices v of the lattice, and the second sum is over all elementary cubes c . The vertex term A_v^{xy} is equal to a product of Pauli Z operators over the four links emanating adjacent to v within the xy plane (and likewise for A_v^{xz} and A_v^{yz}). Conversely, the cube term B_c is equal to a product of Pauli X operators over the twelve edges of the cube c . The ground state wavefunction under open boundary conditions may be written as

$$|\psi_0\rangle = \prod_c (1 + B_c) |0\rangle \quad (5.2)$$

where $|0\rangle$ is the simultaneous +1 eigenstate of the Pauli Z operators on all links. It can be helpful to conceptualize this wavefunction as a condensate of extended objects with rectangular prism geometry.

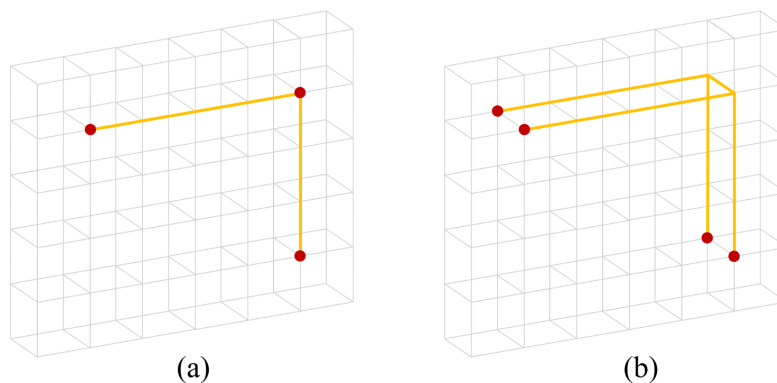


Figure 5.2: (a) A rigid string operators in the X-cube model. Lineons, represented as red dots, are created at the endpoints and corner. (b) A flexible string operator. Lineon dipoles, which are free to move in a 2D plane, are created at the endpoints.

The fractional excitations of the model can be naturally grouped into ‘electric’ and ‘magnetic’ sectors, whose quasiparticles are violations of the cross and cube terms respectively. The electric sector contains three types of lineons (1D particles), which are created at the ends of open *rigid* string operators and move in the x , y , or z direction (as shown in Fig. 5.2(a)). These objects obey a triple fusion rule, in which three lineons moving in different directions may collectively annihilate to the vacuum if they meet at a point. Moreover, pairs of adjacent lineons may be viewed as dipolar objects which are themselves fractional planon excitations (2D particles). For example, a pair of lineons mobile in the x direction and separated in the z direction may move within the xy plane via the action of *flexible* string operators (see Fig. 5.2(b)). On the other hand, the magnetic sector hosts fracton excitations which occur at the corners of open membrane operators. These membrane operators are most naturally thought of in the dual lattice picture in which qubits are attached to elementary plaquettes of the lattice, which are grouped together to form membranes (as shown in Fig. 5.3(a)). Pairs of fractons created at adjacent corners of a membrane operator may be viewed as dipolar planons in their own right, which become mobile within a plane via the action of thin membrane operators which we will call *ribbon* operators (see Fig. 5.3(b)). These ribbon operators along with the flexible string operators can be thought of as 2D string operators which create planons out of the vacuum at their endpoints.

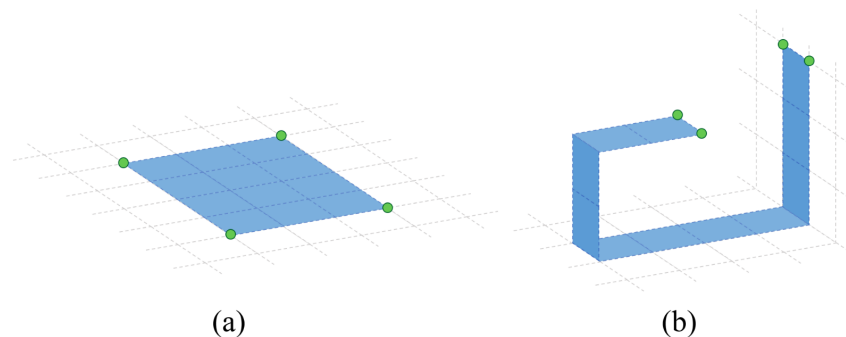


Figure 5.3: (a) A membrane operator. It resides on the plaquettes of the dual lattice, whose edges are depicted as dashed lines. Fractons, represented as green dots, are created at the corners. b) A ribbon operator, which is a type of membrane operator. The fracton dipoles created at its endpoints are free to move in a 2D plane.

The X-cube model has vanishing correlation length, and is actually a fixed point model under a renormalization group (RG) procedure which refines or

coarsens the underlying lattice by sewing and un-sewing toric code layers into the system via quantum circuits of finite depth [39]. The elementary transformation disentangles a single toric code layer from an $L_x \times L_y \times L_z$ size X-cube model to yield a reduced X-cube model on a lattice of dimensions $L_x \times L_y \times (L_z - 1)$. This is realized as a finite depth quantum circuit S which satisfies

$$SH_{\text{XC}}S^\dagger \cong H'_{\text{XC}} + H_{\text{TC}} + H_0, \quad (5.3)$$

where H_{XC} is the original X-cube Hamiltonian, H'_{XC} is the reduced X-cube Hamiltonian, H_{TC} is the Hamiltonian of the decoupled toric code layer, and H_0 is a trivial Hamiltonian corresponding to ancillary product state degrees of freedom. Here the relation $H \cong H'$ indicates that H and H' have coinciding ground spaces and thus correspond to the same phase of matter. The unitary operator S can be written as the composition $S = S_1S_2$. Here S_1 and S_2 are commuting tensor products of controlled-NOT 2-qubit gates and are depicted graphically in Fig. 5.4.

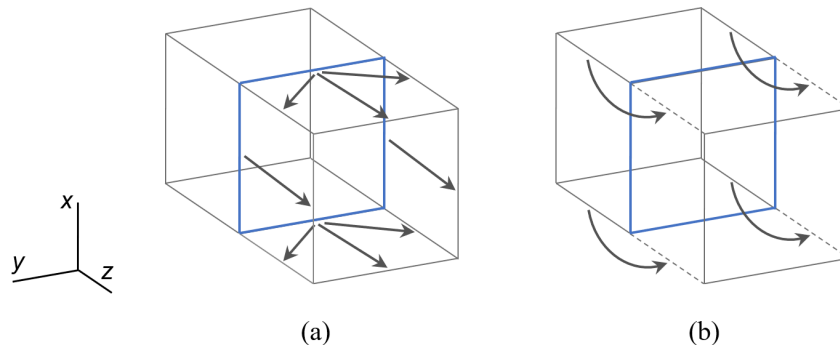


Figure 5.4: A graphical representation of the unitary operators (a) S_1 and (b) S_2 . In this figure only a single unit cell is depicted, although S_1 and S_2 act uniformly along an xy plane. The finite depth quantum circuit $S = S_1S_2$ disentangles the blue xy layer from the bulk X-cube system. The qubits represented by dashed edges in (b) are decoupled ancilla qubits stabilized by H_0 of Eq. (5.3).

5.3 Quotient superselection sectors

5.3.1 Review: superselection sectors

Before defining the notion of *quotient superselection sectors*, we will begin by reviewing the notion of ordinary *superselection sectors*, which correspond to the elementary quasiparticle types of a topological phase. First, let us carve a small, ball-shaped region \mathcal{R} out of a three-dimensional gapped bulk. Suppose

that the medium is of infinite spatial extent, and consider the set of all excited states $|\psi_s\rangle$ that are locally indistinguishable from the ground state outside of \mathcal{R} , but may contain excitations within \mathcal{R} . An ordinary *superselection sector* is a universality class of such states which are related to one another via local unitary operators. To be precise, two normalized states $|\psi_p\rangle$ and $|\psi_q\rangle$ are said to belong to the same superselection sector if there exists a local unitary operator U with support in \mathcal{R} such that $|\psi_p\rangle = U|\psi_q\rangle$. The superselection sector may be subsequently viewed as the subspace spanned by all such equivalent excited states.

Actually, because the system has been posited to have infinite spatial extent, this heuristic discussion does not have a solid footing since there are ambiguities when comparing wavefunctions of infinite extent. However, it can be made rigorous by imagining that we take a finite macroscopic sample \mathcal{M} of the system surrounding \mathcal{R} , and map wavefunctions into the space of density matrices on the subsystem \mathcal{M} . An arbitrary wavefunction $|\psi\rangle$ corresponds to the reduced density matrix $\rho = \text{tr}_{\overline{\mathcal{M}}}|\psi\rangle\langle\psi|$, where the degrees of freedom outside \mathcal{M} have been traced out. Two density matrices ρ_p and ρ_q are then considered equivalent if there is a unitary U such that $\rho_p = U\rho_qU^\dagger$. The use of density matrices is implicit in the definitions that follow; however we will omit mention of them as to do otherwise would obfuscate the physical intuition, and in all cases it is a straightforward task to make the definitions rigorous by incorporating their use.

The *vacuum* sector consists of states containing only local excitations, whereas the non-trivial sectors correspond to fractional excitations of the medium, which cannot be annihilated via local processes. For conventional 3D topological orders, there are a finite number of superselection sectors, corresponding to the point-like topological charges of the phase which are created at the endpoints of open Wilson strings. For example, for a 3+1D discrete gauge theory based on a finite group G , the superselection sectors (for a ball-shaped region) correspond to irreducible representations of G . Conversely, for foliated fracton phases, the fundamental constraints on quasiparticle mobility give rise to an exponential growth of the number of superselection sectors as the diameter of the region \mathcal{R} is increased, corresponding to an infinite number of fractional excitation types. However, as we will see, by ‘modding out’ the fractional excitations that correspond to

anyonic quasiparticles of the underlying foliation layers, i.e. the *planon* sectors of the phase, the resulting *quotient superselection sectors* are finite in number and independent of the size of \mathcal{R} .

5.3.2 Definition: Quotient superselection sectors

The RG picture of foliated fracton phases, in which layers of 2D topological orders can be systematically disentangled from the rest of the system, can be used to make the intuition mentioned above precise. For simplicity, consider a state $|\psi_\rho\rangle$ containing only a single planon, labeled ρ , in region \mathcal{R} , whose plane of mobility is denoted by \mathcal{P} . The planon can be ‘disentangled’ from the rest of the system via an RG transformation, i.e. a finite depth quantum circuit V such that $V|\psi_\rho\rangle = |\psi'_0\rangle \otimes |\psi_\alpha^{2D}\rangle$. Here $|\psi'_0\rangle$ is the ground state of a modified system with inhomogeneities in the vicinity of \mathcal{P} , and $|\psi_\alpha^{2D}\rangle$ is an excited state of a 2D topologically ordered phase living in plane \mathcal{P} , containing an anyonic excitation α in the region $\mathcal{R} \cap \mathcal{P}$ ^[2]. The planon ρ can thus be thought of as a fractional excitation belonging to layer \mathcal{P} of the underlying foliation structure.

It is instructive to understand how the disentangling of planons can be achieved in the X-cube model. As discussed, there are two types of planons in the X-cube model: fracton dipoles, and lineon dipoles. Consider a path γ , with endpoints, lying along the direct lattice edges in the $z = z_0$ plane. Denote by $W_\varepsilon(\gamma)$ a flexible string operator lying alongside γ adjacent to the $z = z_0$ plane, for example as shown in Fig. 5.5. $W_\varepsilon(\gamma)$ creates lineon dipoles at its endpoints, which are elementary in the sense that they are separated by a single lattice spacing in the z direction. Likewise, consider a ribbon λ composed of dual lattice plaquettes which are dual to x and y links in the $z = z_0$ plane, and let $W_\mu(\lambda)$ denote the membrane operator corresponding to λ , which creates elementary fracton dipoles (i.e. pairs of fractons separated by a single lattice spacing) at its endpoints (see Fig. 5.5). Now consider the action of the operator S , introduced in the discussion of the X-cube RG transformation in the previous section, which disentangles a toric code layer along $z = z_0$ from the rest of the system. It can be seen that

$$SW_\varepsilon(\gamma)S^\dagger = W_\varepsilon(\gamma) \quad (5.4)$$

$$SW_\mu(\lambda)S^\dagger = W_m(\lambda) \quad (5.5)$$

²The local unitary V , viewed as a quantum circuit, has a minimum depth which scales with the spatial extent of ρ . For instance, in the case of a dipolar planon composed of two fractons, the depth scales as the distance between the fractons.

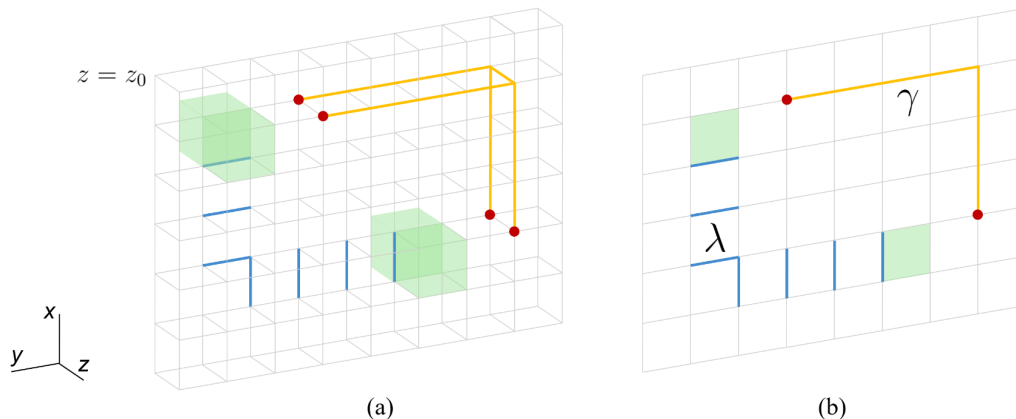


Figure 5.5: (a) A flexible string operator $W_\epsilon(\gamma)$ and a ribbon operator $W_\mu(\lambda)$ of the X-cube model, which are mapped under conjugation by the finite-depth circuit S to (b) electric and magnetic string operators $W_e(\gamma)$ and $W_m(\lambda)$ acting on a decoupled toric code layer lying along the $z = z_0$ plane, which is the back plane pictured in (a). These operators are respectively defined as tensor products of Pauli X operators over the yellow edges and Pauli Z operators over the blue edges. γ and λ are paths on the direct and dual lattices respectively of the $z = z_0$ plane. The red dots represent X-cube lineons in (a) and \mathbb{Z}_2 charges in (b). Conversely, the shaded green cubes in (a) represent fractons, whereas the green squares in (b) represent \mathbb{Z}_2 fluxes.

where $W_e(\gamma)$ is an open electric string operator along the path γ , residing in the disentangled toric code layer along the $z = z_0$ plane, and likewise $W_m(\lambda)$ is an open magnetic string operator in the toric code layer which lies along λ (the dual lattice plaquettes comprising λ become dual lattice links when restricted to the planar square lattice). $W_e(\gamma)$ creates \mathbb{Z}_2 charges at the endpoints of γ whereas $W_m(\lambda)$ creates \mathbb{Z}_2 fluxes at the endpoints of λ . From Eq. (5.4) it follows that $S|\psi_\epsilon\rangle = |\psi'_0\rangle \otimes |\psi_e^{\text{TC}}\rangle$ where $|\psi'_0\rangle$ is the ground state of the reduced X-cube Hamiltonian H'_{XC} , and $|\psi_\epsilon\rangle$ and $|\psi_e^{\text{TC}}\rangle$ are excited states of the (original) X-cube and toric code Hamiltonians respectively containing an elementary lineon dipole and a \mathbb{Z}_2 gauge charge. Similarly, $S|\psi_\mu\rangle = |\psi'_0\rangle \otimes |\psi_m^{\text{TC}}\rangle$. The above discussion addresses elementary dipoles of lineons and fractons. For dipolar planons which a larger spatial extent, similar disentangling circuits can be constructed; however, the depth of the circuit scales linearly with the length of the dipole.

With this motivation in mind, we define two (normalized) excited states $|\psi_p\rangle$ and $|\psi_q\rangle$ to belong to the same *quotient superselection sector* (QSS) if there

exists a unitary operator U with support in \mathcal{R} and a finite depth quantum circuit V that satisfy

$$\begin{aligned} U |\psi'_p\rangle &= |\psi'_q\rangle \\ V |\psi_p\rangle &= |\psi'_p\rangle \otimes |\psi_{\alpha_1}^{2D}\rangle \otimes \cdots \otimes |\psi_{\alpha_n}^{2D}\rangle \\ V |\psi_q\rangle &= |\psi'_q\rangle \otimes |\psi_{\beta_1}^{2D}\rangle \otimes \cdots \otimes |\psi_{\beta_n}^{2D}\rangle, \end{aligned} \quad (5.6)$$

where $|\psi'_p\rangle$ and $|\psi'_q\rangle$ are modified excited states, and $|\psi_{\alpha_i}^{2D}\rangle$ and $|\psi_{\beta_i}^{2D}\rangle$ are 2D topologically ordered states living along plane \mathcal{P}_i and respectively harboring (possibly vacuous) anyonic excitations α_i and β_i in the region $\mathcal{R} \cap \mathcal{P}_i$. The operator V naturally decomposes into a product, $V = \prod_i V_i$, where V_i are operators that subsequently disentangle 2D layers along \mathcal{P}_i . According to this definition, it immediately follows that superselection sectors containing only planons belong to the vacuum quotient sector, since the planons can be mapped into a $|\psi^{2D}\rangle$ state, as exemplified in Fig. 5.5. In this sense, the planon sectors are factored out, and the resulting quotient sectors may be viewed as fractional quasiparticle species *modulo* anyons of the underlying foliation layers. Factoring out the planons in this manner consistently results in a finite set \mathcal{A} of QSS. If a quasiparticle state belongs to a particular quotient sector $a \in \mathcal{A}$, let us say that such an excitation carries *quotient charge* a . States within a given sector may be viewed as belonging to a Hilbert space \mathcal{H}_a .

In foliated fracton models, the above definition is equivalent to a more transparent formulation which more closely parallels the definition of ordinary superselection sectors. A *planon creation operator* W_ρ is a unitary operator that has planar support and creates a planon ρ at its endpoint in region \mathcal{R} , and extends to spatial infinity at the other end. Then, two states $|\psi_p\rangle$ and $|\psi_q\rangle$ are defined to represent the same quotient superselection sector if there exist planon creation operators W_{ρ_j} ($j = 1, \dots, m$) and a local unitary operator U such that

$$\left(U \prod_j W_{\rho_j} \right) |\psi_p\rangle = |\psi_q\rangle. \quad (5.7)$$

In other words, an equivalence relation on excited states is imposed which affords the freedom to arbitrarily create and annihilate planons, in addition to local excitations, within \mathcal{R} .

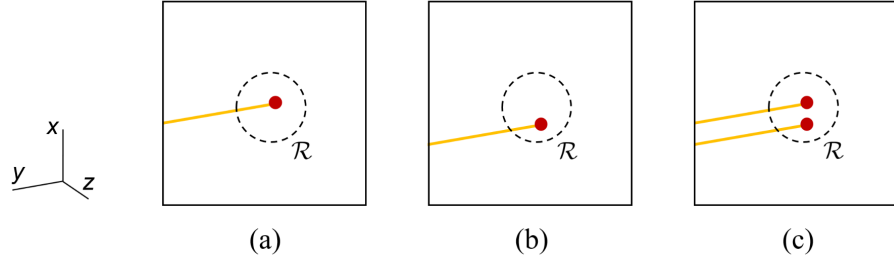


Figure 5.6: (a, b) Representative states of the ℓ_y quotient superselection sector of the X-cube model. These states are the result of acting on the ground state with the yellow rigid string operators, which create lineons at their endpoints (red dots) in \mathcal{R} . (c) A state containing a planon free to move in a yz plane. The flexible string operator that creates this planon is an effective hopping operator between the lineon states in (a) and (b).

5.3.3 Example: X-cube model

As an example, let us apply this definition to the X-cube model. First consider the lineon excitations of the model, which can move within a straight line via the action of rigid string segment (unitary) operators. The key observation is that lineon dipoles, where the dipolar axis is normal to the direction of mobility, are themselves fractional planon excitations. Thus, the action of the flexible string operators that create these dipolar planons can effectively translate lineon excitations parallel to their dipolar axes (see Fig. 5.6 for an example). However, there are no such operators capable of transmuting say, an x direction lineon into a y direction lineon. Similarly, the planon creation operators that create fracton dipoles (of any axial orientation x , y , or z), i.e. half-open ribbon operators, are effective hopping operators for individual fractons. Moreover, since these operators nucleate fracton dipoles out of the vacuum, only the total fracton parity of a given state is relevant in determining the quotient superselection sector to which that state belongs. Likewise, only the parities of the number of x , y , and z direction lineons come into play. However, due to the triple lineon fusion rule, one of these parities is actually redundant; hence, there are a total of 8 quotient sectors for the X-cube model. Let us label the quotient superselection sector with odd fracton parity and even lineon parities as f , and the sector with odd parity of direction- σ lineons ($\sigma = x, y, z$) and all other parities even as ℓ_σ . Note that due to the triple fusion rule, the sector ℓ_z corresponds also to odd parity of x and y direction lineons and even parity of fractons and z direction lineons. Finally, sectors

with odd fracton parity, odd parity of σ direction lineons, and even parity of the other two types of lineons will be labeled $l_\sigma f$. The 8 quotient sectors in \mathcal{A} are thus the vacuum sector 1, the fracton sector f , the lineon sectors $l_x, l_y,$ and l_z , and the composite sectors $l_x f, l_y f, l_z f$. In Fig. 5.7 we have illustrated representative states of each quotient sector.

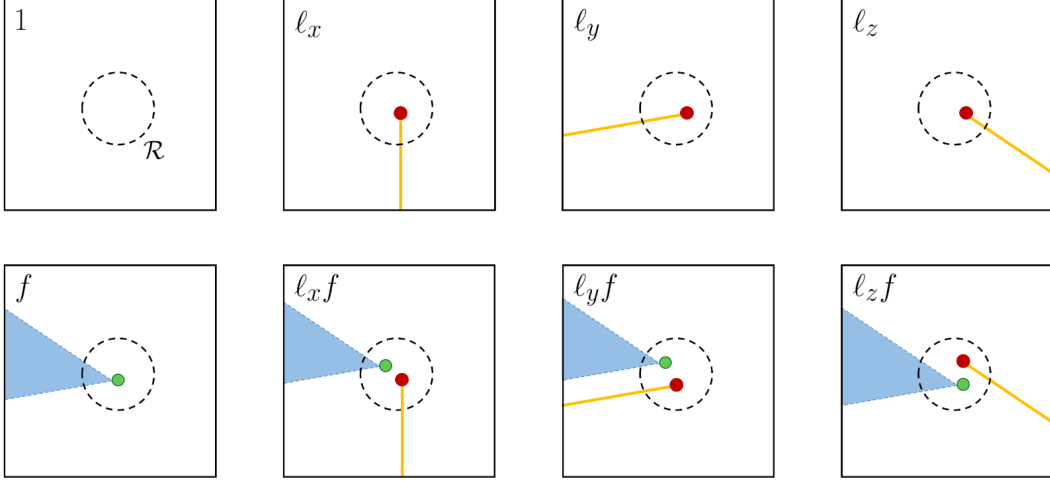


Figure 5.7: The 8 quotient superselection sectors of the X-cube model. The $l_x,$ $l_y,$ and l_z lineons (red) are created by string operators (orange) along the $x,$ $y,$ and z direction, respectively. The fracton (green) is created by a membrane operator (blue).

The set of quotient superselection sectors for abelian phases has a natural abelian group structure in which the group multiplication corresponds to fusion of quotient sectors, and the vacuum sector represents the identity. To make this precise, we can consider two nearby non-overlapping regions \mathcal{R}_1 and \mathcal{R}_2 which are encompassed by a larger region \mathcal{R} . Suppose \mathcal{R}_1 contains excitations of total quotient charge a , and \mathcal{R}_2 of total quotient charge b . Then a and b fuse into c , written as $a \times b = c$, if the encompassing region \mathcal{R} has total quotient charge c . For the X-cube model, the non-trivial fusion rules are $a \times a = 1$ for all $a \in \mathcal{A}$, secondly $l_\sigma \times f = l_\sigma f$ (where $\sigma = x, y, z$), and finally $l_x \times l_y \times l_z = 1$. Hence the fusion group is $\mathbb{Z}_2 \times \mathbb{Z}_2 \times \mathbb{Z}_2$ with generators $l_x, l_y,$ and f .

5.4 Quasiparticle statistics

In this section, we develop a notion of interferometric detection of quotient superselection sectors, which will serve as the foliated fracton phase analog of quasiparticle braiding statistics in abelian topological phases. The basic idea is to consider equivalence classes of operators which interferometrically detect

the presence of excitations in a given quotient sector via Aharonov-Bohm-like phases. Whereas for 2D topological phases, these operators correspond to processes in which one quasiparticle is wound around another, for foliated fracton phases these interferometry operators lack any sort of topological interpretation. Instead, as we will see, they have a geometric character that is inherited from the geometry of the foliation structure.

5.4.1 Interferometric detection

As discussed above, each quotient superselection sector $a \in \mathcal{A}$ corresponds to a subspace \mathcal{H}_a of states containing fractional excitations of quotient charge a within a fixed region \mathcal{R} . To formulate a notion of universal quasiparticle statistics for foliated fracton phases, we consider the set \mathcal{O} of *interferometric operators*, which are defined with reference to the region \mathcal{R} . An *interferometric operator* is a local unitary operator O that (1) commutes with the Hamiltonian, (2) has compact support in $\overline{\mathcal{R}}$, the complement of \mathcal{R} , (3) acts as a pure phase $e^{i\theta_a(O)}$ within each subspace \mathcal{H}_a ($O|a\rangle = e^{i\theta_a(O)}|a\rangle$ for all $|a\rangle \in \mathcal{H}_a$), and (4) acts as the identity on the ground state ($O|\psi_0\rangle = |\psi_0\rangle$). We note that condition (3) strongly restricts the set of interferometric operators, because states in a given subspace \mathcal{H}_a may differ by the presence of planons in \mathcal{R} ; hence interferometric operators must be indifferent to these excitations. Condition (4) merely specifies the overall phase of operators in \mathcal{O} .

The set \mathcal{O} may be naturally partitioned into a finite set of classes \mathcal{O}_i ($i \in I$ where I is a finite set), according to equivalence of the statistical phase angles $\theta_a(O)$. That is, if $\theta_a(O) = \theta_{ai}$ for all $a \in \mathcal{A}$, then $O \in \mathcal{O}_i \subset \mathcal{O}$, where the θ_{ai} have been introduced as statistical angles which depend only on the interferometry class i and the quotient sector a .

These phase factors are the foliated fracton analog of long-range Aharonov-Bohm interactions in abelian 2D topological orders. They arise due to the non-trivial commutation relations between interferometric operators O and operators W_a which create fractional excitations of quotient charge a out of the vacuum: $OW_a = e^{i\theta_{ai}}W_aO$ for all $O \in \mathcal{O}_i$ and W_a such that $W_a|\psi_0\rangle \in \mathcal{H}_a$. (More precisely, these operators bring excitations of quotient charge a from spatial infinity to the region \mathcal{R} .) The statistical phase angles θ_{ai} are well-defined for generic gapped models, and robust under adiabatic deformation of the Hamiltonian. They are thus universal quantities which

partially characterize the foliated fracton phase surrounding a generic model. We note that the set I naturally forms an abelian group with the trivial class as the identity element, and the addition operation coming from operator composition. The maps $i \mapsto e^{i\theta_{ai}}$ are homomorphisms from $I \rightarrow U(1)$.

It is interesting to note that in all the models we have considered, the interferometric operators can be thought of as processes in which a dipolar planon of macroscopic dipole length is braided in a 2D plane around the region \mathcal{R} . Moreover, we find in all cases that the number of interferometric classes is equal to the number of QSS. Thus, it is natural to arrange the statistical phases in matrix form: $S_{ai} = e^{i\theta_{ai}}$. In fact, the resulting S matrix is a direct generalization of the topological S matrix in the theory of 2D topological orders, in the sense that the equivalent definitions applied to 2D topological phases yield the topological S matrix. However, the S matrix for foliated fracton phases differs from the topological S matrix in that there is no inherent symmetry between the row and column indices, whereas for the topological S matrix both indices correspond to anyon species and it generically holds that $S_{ab} = S_{ba}^*$.

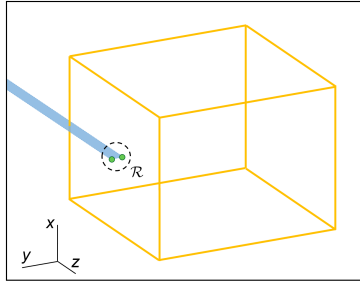


Figure 5.8: An example of a wireframe operator O (defined as the tensor product of Pauli X operators along the yellow edges) which violates condition (3) discussed in the main text. This operator anti-commutes with the blue ribbon operator pictured, which creates a planon (i.e. a fracton dipole) in region \mathcal{R} . Hence O acts as $+1$ on some states and -1 on other states in the trivial quotient superselection sector, and so $O \notin \mathcal{O}$.

5.4.2 Example: X-cube model

Let us continue to consider the X-cube model as a primary example. First, we need to determine the set of interferometric operators \mathcal{O} with reference to a particular region \mathcal{R} of an X-cube system. Since the X-cube Hamiltonian is a stabilizer code, the algebra of observables that commute with the Hamiltonian

is generated by the Hamiltonian terms themselves. Of the operators that commute with H and have compact support in $\overline{\mathcal{R}}$, condition (3) further restricts this set, because a rigid string operator lying in a plane that intersects \mathcal{R} will anti-commute with certain ribbon operators that create fracton dipoles in \mathcal{R} . An example of an operator which satisfies conditions (1) and (2) but not (3) is shown in Fig. 5.8. It can then be seen by careful inspection that the set \mathcal{O} contains 8 inequivalent classes of interferometric operators (including the trivial class).

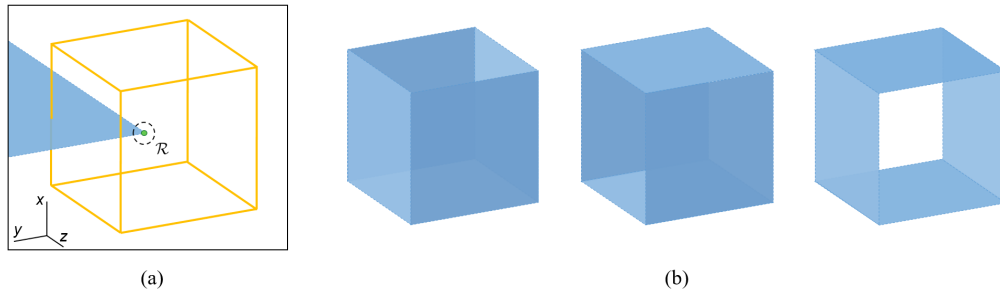


Figure 5.9: (a) An example of a wireframe interferometric operator belonging to the F class, defined as the product of Pauli X operators over the yellow edges. The region \mathcal{R} is located at the center of the wireframe. This operator detects the presence of a fracton (green dot) due to the anti-commutation relation with the blue membrane operator. (b) Cylindrical membrane operators representing, from left to right, the X , Y and Z interferometry classes, of which only 2 are independent. In each case \mathcal{R} resides at the center of the prism.

The first non-trivial class, denoted by the label F , contains wireframe string operators that measure the fracton parity in region \mathcal{R} , and are insensitive to the presence of lineons. An example is shown in Fig. 5.9(a). In other words, $\theta_{f,F} = \theta_{\ell_x f,F} = \theta_{\ell_y f,F} = \theta_{\ell_z f,F} = \pi$, whereas the remaining phase factors are trivial. The $e^{i\pi}$ phase factors arise due to the anti-commutation relation between these wireframe operators and the membrane operators that create fractons in \mathcal{R} at their corners. Conversely, the next three non-trivial classes, denoted by the labels X , Y , and Z , detect lineon parity and are insensitive to the fracton sector. They obey the relation $\mathcal{O}_X \mathcal{O}_Y \mathcal{O}_Z = \mathcal{O}_1$. The X class contains large membrane operators with cylindrical topology which wrap around \mathcal{R} around the x axis, and likewise for the Y and Z classes. These membrane operators anti-commute with the half-open rigid string operators that create lineons of quotient charge ℓ_y and ℓ_z in \mathcal{R} , while commuting with

those that create lineons of charge ℓ_x . Therefore, $\theta_{\ell_y, X} = \theta_{\ell_z, X} = \pi$ whereas $\theta_{\ell_x, X} = 1$, and similarly for the fracton-lineon composite sectors (and likewise for cyclic permutations of the indices). Examples of these cylindrical operators are shown in Fig. 5.9(b). It is instructive to note that the four interferometric classes indexed by X , Y , Z , and F , respectively detect violations of the A_v^{yz} , A_v^{xz} , A_v^{xy} , and B_c terms of the X-cube Hamiltonian in Eq. (5.1) (or rather, odd numbers of violations). The remaining three classes, given the labels XF , YF , and ZF , contain compositions of operators in the other classes. The group structure on the classes of interferometric operators for the X-cube model is therefore $\mathbb{Z}_2 \times \mathbb{Z}_2 \times \mathbb{Z}_2$ with generators X , Y , and F . The statistics are summarized in the following S matrix, in which the rows correspond to QSS in the order $\{1, \ell_x, \ell_y, \ell_z, f, \ell_x f, \ell_y f, \ell_z f\}$, and the columns correspond to interferometric classes in the order $\{1, X, Y, Z, F, XF, YF, ZF\}$:

$$S = \begin{pmatrix} 1 & 1 & 1 & 1 & 1 & 1 & 1 & 1 \\ 1 & 1 & -1 & -1 & 1 & 1 & -1 & -1 \\ 1 & -1 & 1 & -1 & 1 & -1 & 1 & -1 \\ 1 & -1 & -1 & 1 & 1 & -1 & -1 & 1 \\ 1 & 1 & 1 & 1 & -1 & -1 & -1 & -1 \\ 1 & 1 & -1 & -1 & -1 & -1 & 1 & 1 \\ 1 & -1 & 1 & -1 & -1 & 1 & -1 & 1 \\ 1 & -1 & -1 & 1 & -1 & 1 & 1 & -1 \end{pmatrix}. \quad (5.8)$$

5.5 More examples

In this section we examine the quotient superselection sectors, fusion rules, and classes of interferometric operators and statistical phases for a handful of exactly solvable models, which may be viewed as RG fixed point representatives of corresponding foliated fracton phases. In Sec. 5.5.7 we introduce a novel anisotropic foliated fracton model which exhibits fractional lineon and planon excitations but no fractons.

5.5.1 Stack of 2D topological orders

A simple decoupled stack of 2D topological orders, viewed as a 3D model, belongs to the trivial foliated fracton phase according to the definition proposed in Ref. [39]. This is reflected in the structure of excitations in such models: since all fractional excitations are anyons of the constituent layers, there is only one quotient superselection sector, that of the vacuum.

5.5.2 Semionic X-cube model

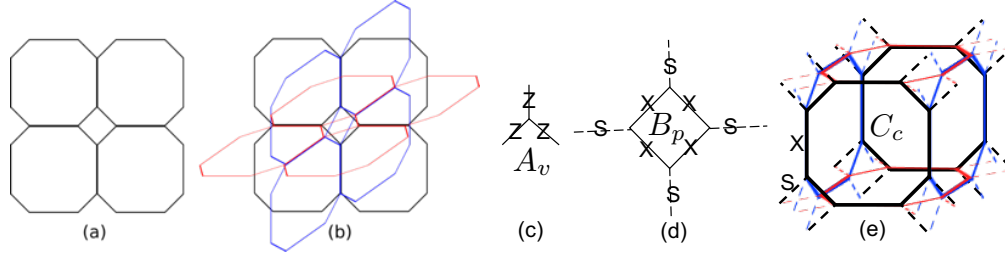


Figure 5.10: (a) A trivalent 2D lattice obtained by decorating a 2D square lattice with diamond plaquettes at each vertex. (b) Stacks of such trivalent lattices in the xy , yz , and zx planes; the edges in x , y and z directions overlap in pairs. (c) The vertex term, (d) the diamond plaquette term, and (e) the cube term of the semionic X-cube Hamiltonian. Here, X and Z are Pauli operators and $S = \text{diag}(1, i)$. In the cube term (e), there is one X on each qubit on the solid edges and one S on each qubit on the dashed edges. For clarity, we only draw one of each.

The semionic X-cube model was discussed in Ref. [21] as a semionic generalization of the original X-cube model. The model is defined on a variation of the cubic lattice which can be obtained as the union of three stacks of 2D decorated square lattices parallel to the xy , yz and zx planes (Fig. 5.10(b)). In each 2D plane, a small diamond shape is added at each vertex of the square lattice so that in the new lattice each vertex has degree three (Fig. 5.10(a)). The Hamiltonian contains three types of terms: a vertex term A_v at each of the trivalent vertices in the xy , yz and zx planes as shown in Fig. 5.10(c), a plaquette term B_p at each diamond plaquette in the planes as shown in Fig. 5.10(d) and a cube term C_c at each cubic cell as shown in Fig. 5.10(e)

$$H_1 = - \sum_v A_v^{(1)} - \sum_p B_p^{(1)} - \sum_c C_c^{(1)}. \quad (5.9)$$

For comparison, we can also define the X-cube model on the decorated lattice:

$$H_0 = - \sum_v A_v^{(0)} - \sum_p B_p^{(0)} - \sum_c C_c^{(0)} \quad (5.10)$$

The Hamiltonian also takes the form shown in Fig. 5.10(c-e) but differs from H_1 in that the operator S is absent from the dashed lines. As explained in Ref. [21], the X-cube and semionic X-cube model on the decorated lattice can be obtained by taking toric code or double semion layers respectively

in each xy , yz and zx plane and coupling them together. The A_v and B_p terms come directly from the vertex and plaquette terms of the toric code and double semion models. The C_c term is a combination of six plaquette terms on neighboring planes.

The quotient superselection sectors and the S matrix of the X-cube model on the decorated lattice is the same as those on the original cubic lattice. To see this, we note that on the decorated lattice, violations of the A_v and C_c terms correspond to the lineon and fracton excitations as before while violations of the B_p term are a new type of planon. Interferometric operators take the same form as before (wireframe, cylinder and their composition) except for the decoration at each vertex. There are still eight quotient superselection sectors and eight interferometric operators which give rise to the same S matrix as in Eq. 5.8.

Similarly, the semionic X-cube model on the decorated cubic lattice has eight quotient superselection sectors generated by a fracton and two lineons as discussed in Ref. 21. To detect these sectors interferometrically, we can use a wireframe shaped operator which is a composition of all C_c operators inside the wireframe. There are also cylinder shaped interferometric operators and they take the same form as in the X-cube model. Direct calculation shows that the S matrix of the semionic X-cube model is the same as that of the X-cube model (Eq. 5.8).

5.5.3 Stacked kagome lattice X-cube model

As discussed in Ref. 43, it is possible to define the X-cube model on generalized lattices which arise as the triple intersection points of three or more stacks of parallel planes. This class includes the stacked kagome lattice, which is formed from 4 underlying stacks. These stacks are normal to the $(0, 1, 0)$, $(\sqrt{3}/2, 1/2, 0)$, $(-\sqrt{3}/2, 1/2, 0)$, and $(0, 0, 1)$ directions respectively. The fourth stack, whose layers are parallel to the xy plane, contains embedded 2D kagome lattices. Actually, these stacks represent an underlying foliation structure whose leaves correspond to 2D toric code layers; hence the stacked kagome X-cube model constitutes a foliated fracton model composed of 4 foliations. As in the normal X-cube model, qubits are placed on each edge of the lattice, and the Hamiltonian takes the form

$$H = - \sum_v (A_v^1 + A_v^2 + A_v^3) - \sum_c B_c. \quad (5.11)$$

In this case, v runs over all vertices, and the operators A_v^i are tensor products of Pauli Z operators over four coplanar edges adjacent to v , one for each of the 3 foliating planes containing v . Here, c indexes the elementary 3-cells of the lattice, which are all either triangular or hexagonal prisms, and B_c is a tensor product of Pauli X operators over the edges of c .

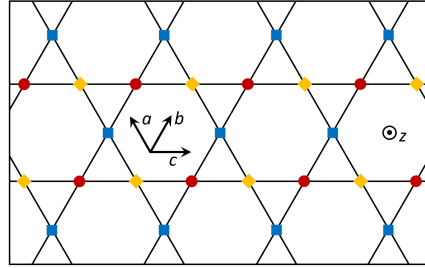


Figure 5.11: The three sublattices of the kagome lattice, indicated by red circles, blue squares, and yellow diamonds. In the stacked kagome X-cube model, there are three types of z -direction (out of the plane) lineons, corresponding to the three sublattices.

The excitation structure of the stacked kagome X-cube model is quite similar in spirit to that of the original X-cube model: violations of the vertex Hamiltonian terms are lineons, whereas violations of the 3-cell terms are fractons. However, there are four possible directions of mobility for lineons: $a = (-1/2, \sqrt{3}/2, 0)$, $b = (1/2, \sqrt{3}/2, 0)$, $c = (1, 0, 0)$ and $\hat{z} = (0, 0, 1)$. (The first 3 directions lie within the 2D kagome layers, whereas the fourth is normal to them). In all cases, the lineons are mobile along the line of intersection of two of the underlying foliation leaves. Pairs of a , b , or c direction lineons separated along the z axis or within the xy plane constitute fractional planon excitations. Thus the lineons mobile in each of these 3 directions constitute their own quotient superselection sectors, which we will label ℓ_a , ℓ_b , and ℓ_c . On the other hand, the z direction lineons can be divided into three sublattices as shown in Fig. 5.11 lineon dipoles may be free to move in a 2D plane only if the two lineons belong to the same sublattice. Thus, each of these three types of z direction lineons represents a quotient superselection sector as well, labeled ℓ_R , ℓ_Y , and ℓ_B . However, due to the triple fusion rules, each of these quotient sectors is the result of fusion of two of the sectors ℓ_a , ℓ_b , and ℓ_c . In

particular, the fusion rules are

$$\begin{aligned}\ell_R &= \ell_b \times \ell_c \\ \ell_Y &= \ell_a \times \ell_c \\ \ell_B &= \ell_a \times \ell_b.\end{aligned}$$

Therefore, there are only 3 independent lineon quotient sectors. The last non-trivial lineon QSS is given by the fusion result $\ell_a \times \ell_b \times \ell_c$.

As in the cubic lattice X-cube model, dipoles of adjacent fractons are themselves planons, and thus all fractons belong to the same quotient superselection sector. In total there are therefore $2^4 = 16$ quotient superselection sectors in the stacked kagome X-cube model. The group of interferometric operators that detect these sectors are generated by a class F of wireframe operators which detects fractons, as well as 3 independent classes of membrane operators A , B , and C which detect the presence of lineons. These operators are membrane-like in the sense that they have support along the surface of a polyhedron, which can be chosen to be a hexagonal (or triangular) prism (see Fig. 5.12). The remaining classes of membrane operators are $AB = A \times B$, $BC = B \times C$, $AC = A \times C$, and $Z = A \times B \times C$.

Since the fracton and lineon sectors are independent of each other in this model, it is instructive to construct an abbreviated \tilde{S} matrix which contains the interferometric statistics between the lineon QSS and membrane operators alone. Indexing the rows in the order $\{1, \ell_a, \ell_b, \ell_c, \ell_a \times \ell_b \times \ell_c, \ell_R, \ell_Y, \ell_B\}$ and the columns in the order $\{1, A, B, C, Z, BC, AC, AB\}$, this matrix takes the form

$$\tilde{S} = \begin{pmatrix} 1 & 1 & 1 & 1 & 1 & 1 & 1 & 1 \\ 1 & -1 & 1 & 1 & -1 & 1 & -1 & -1 \\ 1 & 1 & -1 & 1 & -1 & -1 & 1 & -1 \\ 1 & 1 & 1 & -1 & -1 & -1 & -1 & 1 \\ 1 & -1 & -1 & -1 & -1 & 1 & 1 & 1 \\ 1 & 1 & -1 & -1 & 1 & 1 & -1 & -1 \\ 1 & -1 & 1 & -1 & 1 & -1 & 1 & -1 \\ 1 & -1 & -1 & 1 & 1 & -1 & -1 & 1 \end{pmatrix}. \quad (5.12)$$

The full S matrix including the fracton QSS and wireframe interferometric operators then takes the form

$$S = \begin{pmatrix} 1 & 1 \\ 1 & -1 \end{pmatrix} \otimes \tilde{S}. \quad (5.13)$$

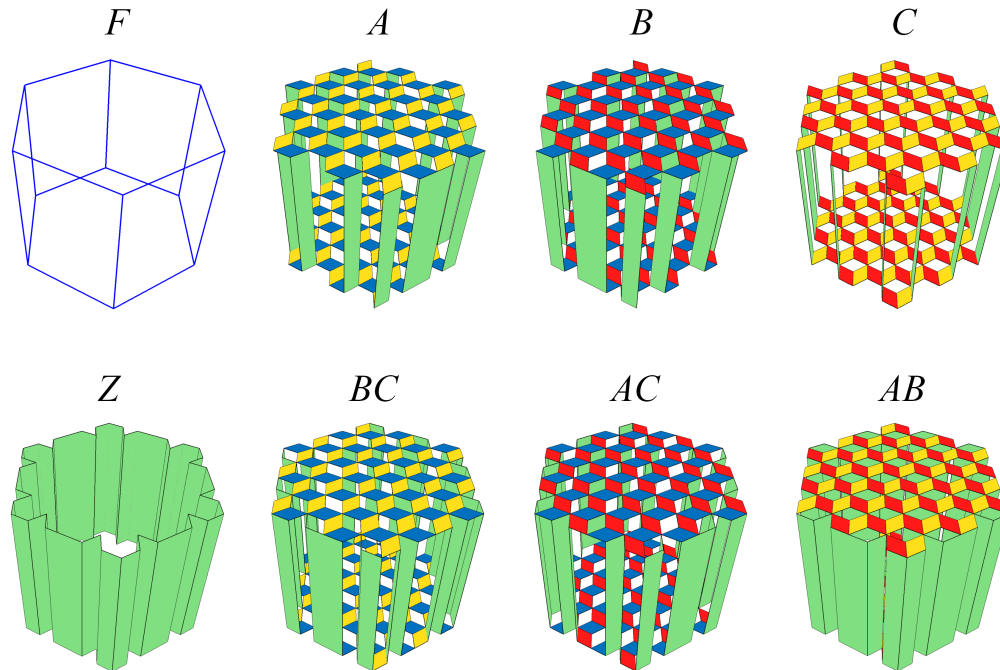


Figure 5.12: Representative operators of the interferometric classes in the stacked kagome X-cube model. The top left figure depicts a wireframe operator which is a tensor product of Pauli X operators over the qubits along the edges. The remaining figures depict membrane operators which are tensor products of Pauli Z operators over the dual lattice plaquettes drawn in the figures. These operators may also be chosen to be in the shape of a triangular prism.

5.5.4 Hyperkagome lattice X-cube model

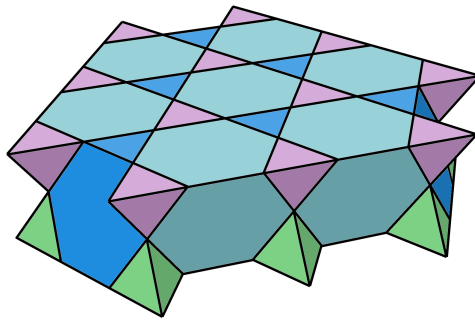


Figure 5.13: The hyperkagome lattice. The elementary 3-cells are small tetrahedra (green and purple) and large truncated tetrahedra (turquoise and blue).

Using an analogous construction to the previous example, it is possible to define a version of the X-cube model where the qubits reside on the edges of a hyperkagome lattice (also known as a quarter cubic honeycomb lattice).

The hyperkagome lattice arises as the set of triple intersection points of planes belonging to the 4 discrete foliations defined by the equations $-x + y + z = k$, $+x - y + z = k$, $+x + y - z = k$, and $+x + y + z = k + 1/2$ for all $k \in \mathbb{Z}$. The Hamiltonian for this version of the X-cube model takes the same form as in Eq. (5.11); for the hyperkagome lattice, the elementary 3-cells consist of small tetrahedra and large truncated tetrahedra, as shown in Fig. 5.13.

In this geometry, there are 6 species of lineons which move along the $a = (1, 1, 0)$, $b = (1, 0, 1)$, $c = (0, 1, -1)$, $d = (1, -1, 0)$, $e = (1, 0, -1)$, and $f = (0, 1, 1)$ directions, corresponding to lines of intersection of the foliating planes (see Fig. 5.14(a)). As in the other X-cube models, pairs of lineons moving in the same direction may combine to form dipolar planon excitations. Thus, all lineons mobile in the σ direction belong to a single quotient superselection sector ℓ_σ . Moreover, there are four triple fusion rules:

$$\begin{aligned} \ell_a \times \ell_b \times \ell_f &= 1 \\ \ell_b \times \ell_c \times \ell_d &= 1 \\ \ell_a \times \ell_c \times \ell_e &= 1 \\ \ell_d \times \ell_e \times \ell_f &= 1. \end{aligned}$$

Therefore, there are exactly 3 independent lineon quotient sectors, which can be chosen to be, for instance, a , b , and c . The fusion result $\ell_a \times \ell_b \times \ell_c$ constitutes a 7th non-trivial lineon sector. On the other hand, there is just a single fracton sector f since neighboring fractons combine to form planons as in the cubic and stacked kagome lattice X-cube models. Hence there are a total of $2^4 = 16$ QSS.

As in the stacked kagome X-cube model, in the hyperkagome X-cube model there is one class of wireframe interferometric operators which detects fracton parity, and 3 classes of independent membrane operators which are sensitive to the lineon content of the region \mathcal{R} . The membrane operators can be chosen to have support over the surface of a rhombic dodecahedron which is aligned with the Wigner-Seitz cell of the underlying fcc Bravais lattice (itself a rhombic dodecahedron). They can be constructed in the following way. First, note that the cross-shaped Hamiltonian terms correspond to intersections of pairs of lines of lineon mobility, and may be divided into 12 groups and labeled according to the directions of these two lines. For example, if vertex v lies at the intersection

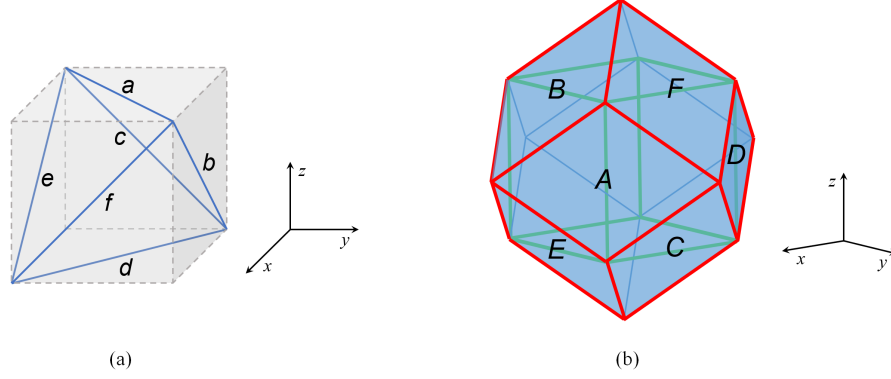


Figure 5.14: (a) The six possible directions of mobility of lineons in the hyperkagome X-cube model. (b) A rhombic dodecahedron. Each face of the dodecahedron is normal to one of the 6 directions of lineon mobility.

of lines oriented in the a , c , and e directions, then the vertex terms associated with v are A_v^{ac} , A_v^{ce} , and A_v^{ae} .

The membrane operators are then constructed as a product of vertex terms within a large rhombic dodecahedral region \mathcal{D} . The microscopic region \mathcal{R} lies at the center of this dodecahedron. In particular, we define

$$O_{ABC} = \prod_{v \in \mathcal{D}} A_v^{ab} A_v^{bc} A_v^{ac} \quad (5.14)$$

and likewise for O_{AEF} , O_{BDF} , and O_{CDE} . Moreover,

$$\begin{aligned} O_{BCEF} &= O_{ABC} O_{AEF} \\ O_{ACDF} &= O_{ABC} O_{BDF} \\ O_{ABDE} &= O_{ABC} O_{CDE}. \end{aligned}$$

A rigid string operator that creates a lineon in region \mathcal{R} must pierce the center of one of the 12 faces of \mathcal{D} (see Fig. 5.14b). The interferometric operators are constructed such that they anti-commute with rigid string operators passing through some, but not all of these faces. For instance, the operator O_{ABC} anti-commutes with rigid string operators oriented in the a , b , and c directions. Thus, the abbreviated \tilde{S} matrix, which contains the statistics of the lineon QSS and membrane interferometry operators, with respect to the bases $\{1, l_a, l_b, l_c, l_a \times l_b \times l_c, l_d, l_e, l_f\}$ and

$\{1, AEF, BDF, CDE, ABC, BCEF, ACDF, ABDE\}$, takes the form

$$\tilde{S} = \begin{pmatrix} 1 & 1 & 1 & 1 & 1 & 1 & 1 & 1 \\ 1 & -1 & 1 & 1 & -1 & 1 & -1 & -1 \\ 1 & 1 & -1 & 1 & -1 & -1 & 1 & -1 \\ 1 & 1 & 1 & -1 & -1 & -1 & -1 & 1 \\ 1 & -1 & -1 & -1 & -1 & 1 & 1 & 1 \\ 1 & 1 & -1 & -1 & 1 & 1 & -1 & -1 \\ 1 & -1 & 1 & -1 & 1 & -1 & 1 & -1 \\ 1 & -1 & -1 & 1 & 1 & -1 & -1 & 1 \end{pmatrix}. \quad (5.15)$$

and the full S matrix is given by

$$S = \begin{pmatrix} 1 & 1 \\ 1 & -1 \end{pmatrix} \otimes \tilde{S}. \quad (5.16)$$

Interestingly, the QSS and quasiparticle statistics of the hyperkagome and stacked kagome X-cube models have identical algebraic structure; the models differ only in the geometry of their foliation structures.

5.5.5 \mathbb{Z}_N X-cube model

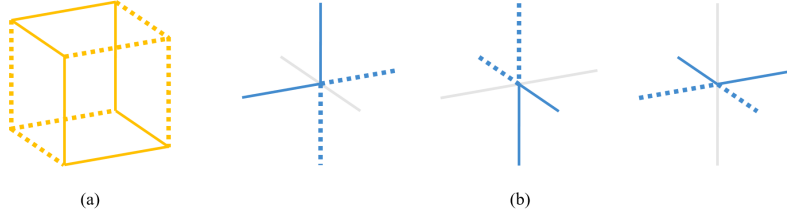


Figure 5.15: (a) Cube term B_c of the \mathbb{Z}_N X-cube Hamiltonian, defined as the tensor product of generalized Z operators over the solid yellow edges and Z^\dagger operators over the dotted yellow edges. (b) Cross stabilizers A_v^{xy} , A_v^{xz} , and A_v^{yz} . They act as generalized X on the solid blue edges and X^\dagger on the dotted blue edges.

The X-cube model is also readily generalized to a family of abelian rotor models, in which each edge of a cubic lattice contains a \mathbb{Z}_N rotor degree of freedom spanned by basis states $|0\rangle, \dots, |N-1\rangle$. The Hamiltonian is defined in terms of clock and shift operators X and Z which act as $Z|m\rangle = \omega^m|m\rangle$ and $X|m\rangle = |m+1 \bmod N\rangle$, where $\omega = e^{2\pi i/N}$, and satisfy the commutation relations $ZX = \omega XZ$ and $Z^\dagger X = \omega^{-1} XZ^\dagger$. The Hamiltonian takes the form

$$H = - \sum_v (A_v^{xy} + A_v^{yz} + A_v^{xz} + \text{h.c.}) - \sum_c (B_c + B_c^\dagger) \quad (5.17)$$

where per usual v and c run over the vertices and elementary cubes of the lattice, respectively. The operators A_v^{xy} , A_v^{yz} , A_v^{xz} , and B_c are depicted in Fig. 5.15.

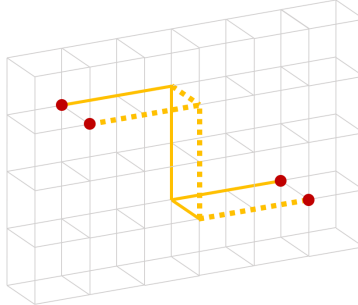


Figure 5.16: A flexible string operator for the \mathbb{Z}_N X-cube model. It is defined as the tensor product of generalized Z operators over the solid yellow edges and Z^\dagger operators over the dotted yellow edges, and creates pairs of lineons, represented as red dots, at its endpoints.

Like the original \mathbb{Z}_2 version, the \mathbb{Z}_N X-cube Hamiltonian is exactly solvable, and exhibits lineon excitations created at the endpoints of rigid string operators, and fracton excitations created at the corners of membrane operators. However, in the rotor model these excitations obey \mathbb{Z}_N fusion rules, and the lineons obey generalized triple fusion rules. Moreover, pairs of adjacent fractons form composite dipolar planons free to move in a 2D plane, as do pairs of adjacent lineons (for example, see Fig. 5.16). As a result, the quotient superselection sectors for the \mathbb{Z}_N X-cube model represent the group $\mathbb{Z}_N \times \mathbb{Z}_N \times \mathbb{Z}_N$, with generators ℓ_x , ℓ_y , and f . The classes of interferometric operators likewise form the group $\mathbb{Z}_N \times \mathbb{Z}_N \times \mathbb{Z}_N$, with generators X , Y , and F , where X and Y are cylindrical membrane operators along the x and y -axes, and F is a rigid wireframe operator. The precise form of the interferometric operators can be computed as a composition of Hamiltonian terms within a region encompassing \mathcal{R} . They exhibit the non-trivial statistical phases $S_{\ell_x, Y} = S_{\ell_y, X} = S_{f, F} = \omega$.

5.5.6 Checkerboard model

The checkerboard model, as introduced in Ref. 48, is a stabilizer code model defined on a cubic lattice with one qubit degree of freedom per site. The elementary cubes of the lattice are bipartitioned into A - B checkerboard

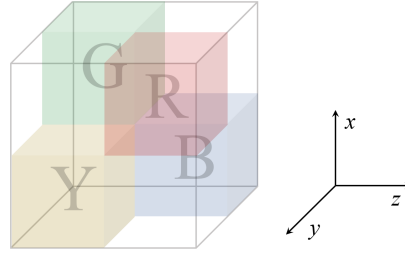


Figure 5.17: The A checkerboard sublattice is further subdivided into R , G , B , and Y sublattices.

sublattices, and the Hamiltonian is defined as follows:

$$H = - \sum_{c \in A} X_c - \sum_{c \in A} Z_c \quad (5.18)$$

where $c \in A$ denotes the set of all cubes in sublattice A . The stabilizer generator X_c (Z_c) is a product of Pauli X (Z) operators over the vertices of cube c .

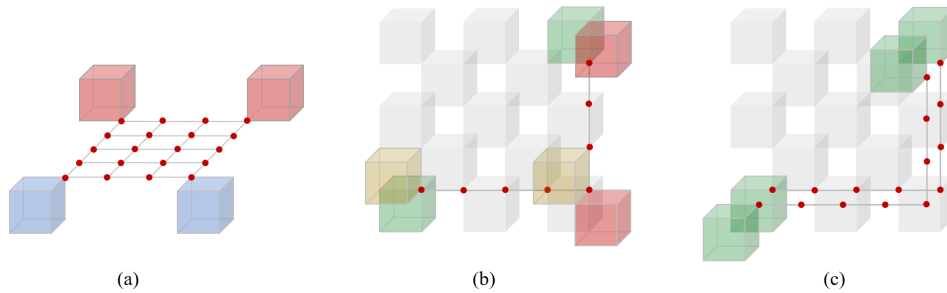


Figure 5.18: Examples of (a) fracton excitations at the corners of membrane operators, (b) lineon excitations at the endpoints and corners of rigid string operators, and (c) planon excitations at the ends of flexible string operators in the checkerboard model. In all cases, the operators are products of Pauli X or Z over the red qubits.

To analyze the structure of fractional excitations in the model, it is convenient to regard a $2 \times 2 \times 2$ box as the elementary unit cell of the system, and to further subdivide the A sublattice into R , G , B , and Y sublattices, as pictured in Fig. 5.17. The model exhibits an ‘electric-magnetic’ duality realized by Hadamard rotation which greatly simplifies the analysis. Let us first focus on the elementary electric excitations, which correspond to violations of individual Z_c cube operators. They are immobile fractons that can only be created at the corners of membrane operators. Pairs of neighboring (i.e. sharing an edge)

fracton excitations in differing sublattices (e.g. R and G) are free to move along a line, and are thus lineons, whereas pairs of neighboring fractons in the same sublattice are planons with mobility in a 2D plane (see Fig. 5.18). Consequently, all the electric fractons in a single sublattice belong to the same QSS. However, fractons residing in different sublattices correspond to distinct quotient sectors, which are given labels f_R^Z , f_G^Z , f_B^Z , and f_Y^Z . Finally, because a composite of four adjacent electric fractons, one in each of the R , G , B , and Y sublattices, is a local excitation (created by the action of a Pauli X operator on a single qubit), each of these sectors is the result of fusion of the other three. In other words,

$$f_R^Z \times f_G^Z \times f_B^Z \times f_Y^Z = 1. \quad (5.19)$$

Therefore, the electric excitations comprise 3 independent QSS. Likewise, there are 3 independent quotient sectors corresponding to magnetic quasiparticles, for a total of $2^6 = 64$ quotient sectors.

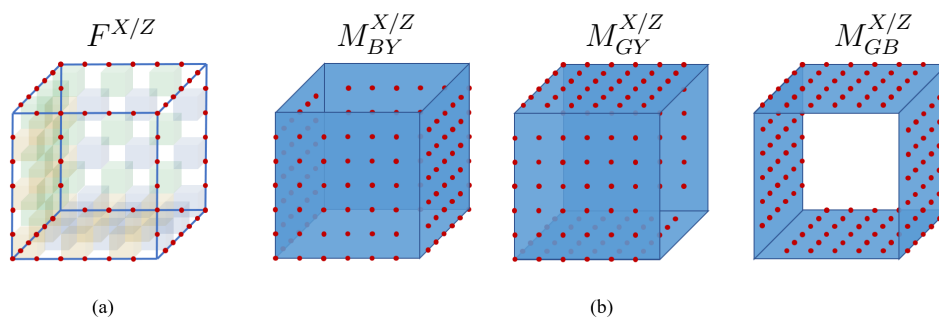


Figure 5.19: Examples of (a) a wireframe operator and (b) membrane operators in the checkerboard model. The operators are tensor products of Pauli X or Z over the red qubits. Shaded cubes belong to the A sublattice.

Due to the self-duality, the interferometric operators of the checkerboard model may also be split according to whether they detect electric or magnetic excitations. Like the X-cube model, the checkerboard model has wireframe operators which correspond to processes in which lineons travel along the edges of the wireframe and fuse into the vacuum at the corners, as well as cylindrical membrane operators wrapping around one of three coordinate axes (for instance, as shown in Fig. 5.19). The operators are tensor products of Pauli X or Z over the red qubits. The wireframe operators can be obtained as a product of all the X_c or Z_c cube operators inside the wireframe and are labeled as F^X or F^Z , respectively. The membrane operators can be obtained as

a product of all the cube operators in every other layer inside the overall cube. Depending on the orientation of the membrane operators, we label them as M_{BY}^X , M_{GY}^X , and M_{GB}^X or as M_{BY}^Z , M_{GY}^Z , and M_{GB}^Z . The superscript denotes whether it is a tensor product of Pauli X or Z , and the subscript specifies which layers of cubes; for instance, M_{BY}^Z is a product of Z_c over all B and Y cubes.

The structure of fractional excitations of the checkerboard model is *identical* to that of two copies of the X-cube model. In other words, there is a mapping between quotient superselection sectors and interferometric operators of the two models which preserves the fusion rules and quasiparticle statistics, suggesting that the two models represent the same foliated fracton phase. In a separate work, we show that these models are in fact equivalent up to a generalized local unitary transformation [40]. The correspondence between non-trivial QSS and interferometric operators (IO) of the checkerboard model and two copies of the X-cube model is as follows:

Checkerboard QSS	QSS of 2 X-cube	Checkerboard IO	IO of 2 X-cube
f_R^Z	f^2	F^Z	F^2
f_G^Z	$\ell_x^1 \times f^2$	M_{BY}^Z	X^1
f_Y^Z	$\ell_y^1 \times f^2$	M_{GB}^Z	Y^1
f_B^Z	$\ell_z^1 \times f^2$	M_{GY}^Z	Z^1
$f_R^Z \times f_G^Z$	ℓ_x^1	$F^Z M_{BY}^Z$	$F^2 X^1$
$f_R^Z \times f_Y^Z$	ℓ_y^1	$F^Z M_{GB}^Z$	$F^2 Y^1$
$f_R^Z \times f_B^Z$	ℓ_z^1	$F^Z M_{GY}^Z$	$F^2 Z^1$
f_R^X	f^1	F^X	F^1
f_G^X	$\ell_x^2 \times f^1$	M_{BY}^X	X^2
f_Y^X	$\ell_y^2 \times f^1$	M_{GB}^X	Y^2
f_B^X	$\ell_z^2 \times f^1$	M_{GY}^X	Z^2
$f_R^X \times f_G^X$	ℓ_x^2	$F^X M_{BY}^X$	$F^1 X^2$
$f_R^X \times f_Y^X$	ℓ_y^2	$F^X M_{GB}^X$	$F^1 Y^2$
$f_R^X \times f_B^X$	ℓ_z^2	$F^X M_{GY}^X$	$F^1 Z^2$

The superscripts in the X-cube columns indicate whether the sector or operator corresponds to the first or second X-cube copy. Note that there is an ambiguity

in the correspondence due to the four-fold permutation symmetry of the R , G , B , and Y sublattices; for example, we could have chosen f^2 (f^1) to correspond to f_G^Z (f_G^X) instead of f_R^Z (f_R^X), in which case R and G would be swapped in the above table.

5.5.7 An anisotropic model with lineons and planons

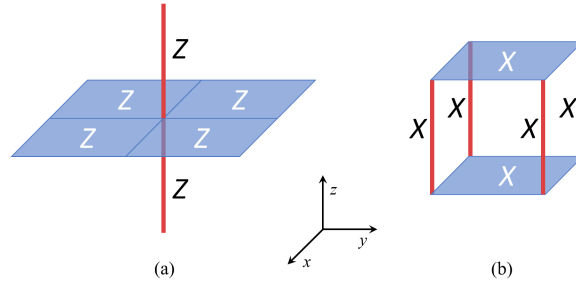


Figure 5.20: The Hamiltonian terms of the anisotropic model. Qubits lie on the red edges and blue plaquettes.

In this section we discuss a novel stabilizer code Hamiltonian. In fact, it arises as a particular example of the polynomial formalism for translation-invariant stabilizer codes developed by Yoshida in Ref. [56]. The model is defined on a cubic lattice, with one qubit attached to each z -oriented link and one qubit attached to each xy plaquette. The Hamiltonian takes the simple form

$$H_{\text{aniso}} = - \sum_v A_v - \sum_c B_c \quad (5.20)$$

where v runs over all vertices of the lattice, and c runs over all elementary cubes. Here A_v is defined as the product of Pauli Z operators over the 4 plaquettes and 2 links adjacent to v , whereas B_c is a product of Pauli X operators over the 2 plaquettes and 4 links surrounding c (as shown in Fig. [5.20]). The model exhibits a self-duality realized by duality of the underlying lattice composed with Hadamard rotation. It represents a foliated fracton phase with 2 foliations composed of toric code layers along the xz and yz planes. A fixed-point RG transformation for the model is discussed in Appendix [5.9]. The model also admits a simple field theory description which is derived in Appendix [5.10].

There are two varieties of fractional excitations in this model: ‘electric’ lineons, and ‘magnetic’ lineons. The electric quasiparticles are created at the corners of membrane operators, which are tensor products of Pauli X operators over the

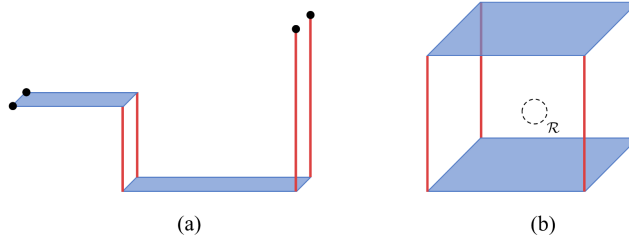


Figure 5.21: (a) An open ribbon operator given by the tensor product of Pauli X operators over the pictured qubits. Individual black dots represent lineons; the dipolar composites are planons. (b) An interferometric operator for the anisotropic model belonging to the M class, given by the product of X operators over the pictured qubits. The microscopic region R lies at the center of the prism.

plaquettes in a region of a single xy plane, and also at the ends of rigid string operators, which are tensor products of X operators over the edges along a line segment oriented in the z direction. These particles are individually only free to move in the z direction, and are hence lineons. However, pairs of adjacent lineons are free to move in a 2D plane via the action of *ribbon* operators, and are thus fractional planon excitations in their own right. Therefore, all electric lineon excitations belong to the same quotient superselection sector, which we label as e . An example of such a ribbon operator is depicted in Fig. 5.21(a).

Analogously, the magnetic excitations are created at the corners of membrane operators and the ends of string operators which are defined on the *dual* lattice and are tensor products of Pauli Z operators. These quasiparticles are likewise z direction lineons, and pair to form dipolar planons. Thus the magnetic lineons represent a second non-trivial quotient superselection sector, labeled m . Finally, the composite of an electric and a magnetic lineon is a ‘dyonic’ lineon which represents a non-trivial quotient sector labeled by ϵ . The quotient sectors obey the simple fusion rules $e \times e = m \times m = 1$, and $e \times m = \epsilon$.

The interferometric operators of this model correspond to compositions of Hamiltonian terms within some macroscopic region. Products of the cube terms, denoted as the class M since such operators correspond to tunneling processes of magnetic lineons, detect the parity of electric lineons, whereas products of the vertex terms, denoted E , detect the parity of magnetic lineons. An example of an interferometric operator belonging to the M class is shown in Fig. 5.21(b). Composite operators belonging to the class Σ detect both types

of lineons. The S matrix, with respect to bases $\{1, e, m, \epsilon\}$ and $\{1, E, M, \Sigma\}$, is as follows:

$$S = \begin{pmatrix} 1 & 1 & 1 & 1 \\ 1 & 1 & -1 & -1 \\ 1 & -1 & 1 & -1 \\ 1 & -1 & -1 & 1 \end{pmatrix}. \quad (5.21)$$

5.6 Mapping the semionic X-cube model to the X-cube model

As discussed in section [5.5.2](#) the semionic X-cube model has the same quotient superselection sectors and interferometric statistics as the X-cube model, indicating that they may belong to the same foliated fracton phase. In this section, we show that this is indeed the case by presenting an explicit mapping between the two. Note that, as discussed in Ref. [\[21\]](#), the two models appear to be very different because in the X-cube model string operators of lineons always commute with each other, while in the semionic X-cube model string operators of lineons may anti-commute with each other (if they lie in orthogonal directions and intersect one another). However, as we see below, this difference is merely superficial and can be removed by considering the general equivalence relation used to define foliated fracton phases. In fact, to map between the two models, we must first add stacks of 2D double semion layers in the xy , yz , and zx planes to both models before applying local unitary transformations. In the presence of such layers, the two models become equivalent. One way to see this equivalence is to realize that with these layers, we can bind the 2D semions from the layers to the lineons in the model, hence changing the string operators of the lineons from commuting to anti-commuting or vice versa. Therefore, in the presence of the double semion layers, the two models are no longer distinct.

The mapping goes as follows. We add to the decorated cubic lattice three stacks of double semion layers in the xy , yz , and zx planes, as shown in Fig. [5.22\(a\)](#). The double semion models are defined on decorated square lattices as shown in Fig. [5.10\(a\)](#). With this addition, the two models take the form

$$H'_n = - \sum_v A_v - \sum_p B_p^{(n)} - \sum_c C_c^{(n)} - \sum_L \left(\sum_{s \in L} A_s + \sum_{d \in L} B_d^{(1)} + \sum_{o \in L} B_o^{(1)} \right), \quad (5.22)$$

where $n = 0$ for the X-cube model and $n = 1$ for the semionic X-cube model.

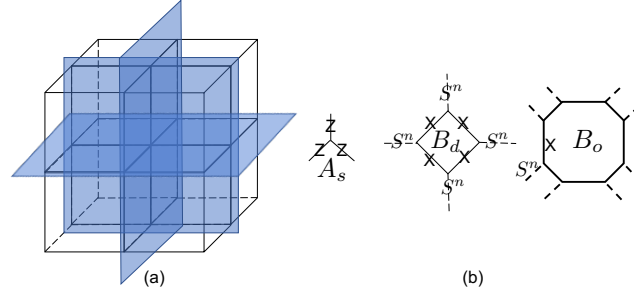


Figure 5.22: (a) Inserting stacks of double semion layers (blue planes) along the xy , yz and zx planes into the X-cube and semionic X-cube models. The layers overlap with the xy , yz , and zx planes of the decorated cubic lattice. For clarity, the decoration (which is shown in Fig. 5.10) in the cubic lattice is not shown and only one layer is shown for each stack. (b) The vertex and plaquette Hamiltonian terms of the 2D toric code model ($n = 0$) and 2D double semion model ($n = 1$) on the decorated square lattice. In the B_o term, there is one X operator on each solid edge and one S^n operator on each dashed edge. For clarity, only two of these operators in the right-most figure are shown.

The A_v , $B_p^{(n)}$, $C_c^{(n)}$ terms are given in Fig. 5.10(c-e). The A_s (vertex), $B_d^{(1)}$ (diamond plaquette), $B_o^{(1)}$ (octagon plaquette) terms belong to each double semion layer labeled by L and take the form as shown in Fig. 5.22(b). The difference between the two models lies in the B_p , C_c terms while all other terms are the same. Each B_p term overlaps with one $B_d^{(1)}$ term in the double semion layers while each side surface of the C_c term overlaps with one $B_o^{(1)}$ term in these layers. Therefore, to map between the two models, it suffices to show that the combination of the B_p , $B_d^{(1)}$ terms and the combination of the C_c , $B_o^{(1)}$ terms can be mapped from one model to the other without affecting the other terms.

To establish this mapping, first we consider a 2D problem of mapping from one 2D toric code model plus one 2D double semion model to two copies of the 2D double semion model. The Hamiltonian of the first system is given by

$$H_a = \sum_{s_1 \in L_1} A_{s_1} + \sum_{d_1 \in L_1} B_{d_1}^{(0)} + \sum_{o_1 \in L_1} B_{o_1}^{(0)} + \sum_{s_2 \in L_2} A_{s_2} + \sum_{d_2 \in L_2} B_{d_2}^{(1)} + \sum_{o_2 \in L_2} B_{o_2}^{(1)}. \quad (5.23)$$

Here L_1 and L_2 are two separate layers. The Hamiltonian for the second system is given by

$$H_b = \sum_{s_1 \in L_1} A_{s_1} + \sum_{d_1 \in L_1} B_{d_1}^{(1)} + \sum_{o_1 \in L_1} B_{o_1}^{(1)} + \sum_{s_2 \in L_2} A_{s_2} + \sum_{d_2 \in L_2} B_{d_2}^{(1)} + \sum_{o_2 \in L_2} B_{o_2}^{(1)}. \quad (5.24)$$

It is possible to map between these two models with local unitary transformations because they have the same topological order. This can be seen by observing that both models represent $\mathbb{Z}_2 \times \mathbb{Z}_2$ gauge theories containing two independent gauge charges c_1, c_2 and two independent gauge fluxes f_1, f_2 . The statistics of the two models are similar in the following ways:

$$\begin{aligned} t_{c_1} = 1, & & t_{c_2} = 1, & & s_{c_1 f_1} = -1, & & s_{c_2, f_2} = -1, \\ s_{c_1, c_2} = 1, & & s_{f_1, f_2} = 1, & & s_{c_1, f_2} = 1, & & s_{c_2, f_1} = 1 \end{aligned} \quad (5.25)$$

where t denotes topological spin, and s denotes the braiding statistics. The two models are different in the topological spin for the two fluxes. In model a :

$$t_{f_1} = 1, \quad t_{f_2} = i \quad (5.26)$$

In model b :

$$t_{f_1} = i, \quad t_{f_2} = i \quad (5.27)$$

But this difference is only superficial because we can reorganize the quasiparticles of model a so that they have the same statistics as model b . In particular, if we redefine the quasiparticles in model a as

$$c'_1 = c_1, \quad c'_2 = c_1 c_2, \quad f'_1 = c_1 f_1 c_2 f_2, \quad f'_2 = f_2, \quad (5.28)$$

then they have the same statistics as model b . Therefore, there exists a local unitary transformation mapping the ground state of model a to the ground state of model b . At the same time, it maps c_1 in model a to c_1 in model b , $c_1 c_2$ to c_2 , $c_1 f_1 c_2 f_2$ to f_1 , f_2 to f_2 . Correspondingly, it maps the Hamiltonian terms, which are also loop operators of the quasiparticles, as follows

$$\begin{aligned} A_{s_1} &\rightarrow A_{s_1}, & A_{s_1} A_{s_2} &\rightarrow A_{s_2}, & B_{d_1}^{(0)} B_{d_2}^{(1)} &\rightarrow B_{d_1}^{(1)}, \\ B_{d_2}^{(1)} &\rightarrow B_{d_2}^{(1)}, & B_{o_1}^{(0)} B_{o_2}^{(1)} &\rightarrow B_{o_1}^{(1)}, & B_{o_2}^{(1)} &\rightarrow B_{o_2}^{(1)} \end{aligned} \quad (5.29)$$

More explicitly, the local unitary transformation involves a controlled- X operator from every qubit in L_1 to its counterpart qubit in L_2 , followed by a unitary on the six qubits around each pair of corresponding vertices in the two layers. The unitary is diagonal in the computational basis of the six qubits $U = \sum_{a,b,c} \alpha(a,b,c) |a,b,c\rangle \langle a,b,c|$. Here $a, b, c = 0, 1, 2, 3$ label the

$(0, 0), (0, 1), (1, 0), (1, 1)$ state of each pair of corresponding qubits in the two layers. $\alpha(a, b, c)$ is given as follows:

$$\begin{aligned}\alpha(0, 0, 0) &= 1, & \alpha(1, 3, 2) &= -1, \\ \alpha(1, 1, 0) &= \alpha(2, 2, 0) = \alpha(3, 3, 0) = \alpha(1, 2, 3) &= i.\end{aligned}\tag{5.30}$$

α is invariant under cyclic permutations of a, b, c . All other terms of α are 1.

The equivalence between H_a and H_b [Eqns. (5.23) and (5.24)] can also be understood in the K -matrix formalism. These models have a Chern-Simons description [52] given by the following Lagrangian and respective K -matrices, where a_μ^I is a compact gauge field:

$$\mathcal{L} = \frac{1}{4\pi} K_{IJ} \epsilon^{\mu\nu\rho} a_\mu^I \partial_\nu a_\rho^J \tag{5.31}$$

$$K_a = \begin{pmatrix} 0 & 2 & 0 & 0 \\ 2 & 0 & 0 & 0 \\ 0 & 0 & 2 & 0 \\ 0 & 0 & 0 & -2 \end{pmatrix} \tag{5.32}$$

$$K_b = \begin{pmatrix} 2 & 0 & 0 & 0 \\ 0 & -2 & 0 & 0 \\ 0 & 0 & 2 & 0 \\ 0 & 0 & 0 & -2 \end{pmatrix}. \tag{5.33}$$

However, the K -matrix for a Chern-Simons Lagrangian is not unique. A change of variables can be performed by transforming the gauge fields according to $a_\mu^I \rightarrow a_\mu^{I'} = W_I^{I'} a_\mu^I$ where $W \in \text{GL}(n, \mathbb{Z})$ is an $n \times n$ matrix (with $n = 4$ for K_a and K_b) with integer coefficients and determinant equal to 1. This transformation can then be absorbed into the K -matrix via $K_{IJ} \rightarrow K'_{I'J'} = W_{I'}^I K_{IJ} W_{J'}^J = (W^T K W)_{I'J'}$. The following matrix W can then be used to relate the above two K -matrices:

$$W = \begin{pmatrix} 0 & -1 & +1 & 0 \\ +1 & +1 & 0 & 0 \\ -1 & -1 & +1 & 0 \\ 0 & 0 & 0 & +1 \end{pmatrix}. \tag{5.34}$$

In particular, $K_b = W^T K_a W$. This shows that H_a and H_b represent the same phase.

Using such a local unitary transformation it is possible to map between the X-cube model and the semionic X-cube model when both are augmented with double semion layers. This is because we can apply the local unitary transformation between a double semion layer and the Hamiltonian terms in the overlapping layer of the X-cube model and map from

$$\begin{aligned} A_v &\rightarrow A_v, & A_v A_s &\rightarrow A_s, & B_p^{(0)} B_d^{(1)} &\rightarrow B_p^{(1)}, \\ B_d^{(1)} &\rightarrow B_d^{(1)}, & C_c^{(0)} (B_o^{(1)})^{\otimes 6} &\rightarrow C_c^{(1)}, & B_o^{(1)} &\rightarrow B_o^{(1)}. \end{aligned} \quad (5.35)$$

Of course, the X-cube and semionic X-cube models are different from simple decoupled stacks of toric code and double semion models, so there are some subtleties involved in applying the mapping in Eq. 5.29. In particular, the X-cube and semionic X-cube models are ‘coupled’ toric codes and double semions such that loop configurations on the side surfaces of the same cube should exist at the same time. While performing the mapping, care must be taken that this constraint is not violated. Indeed this is the case because in mapping between H_a and H_b , f_1 maps to $f_1 f_2$ and $f_1 f_2$ to f_1 , therefore the loop configuration in the first layer is always preserved. Applying the same mapping to the X-cube or semionic X-cube models together with double semion stacks, the loop configurations in these models are also always preserved.

In this way, it is possible to map the ground state of the X-cube model to the ground state of the semionic X-cube model after inserting three stacks of double semion layers in the xy , yz , zx directions respectively. Ref. 57 discussed an ungauged version of the semionic X-cube model as a symmetry protected topological (SPT) phase with subsystem symmetry. Using a similar transformation, one can show that the ungauged model is equivalent (with the addition of 2D \mathbb{Z}_2 SPT layers) to a ‘weak’ subsystem SPT model which is a stack of 2D SPTs.

5.7 Loop excitations

In three dimensions, gapped topological phases harbor fractional loop-like excitations in addition to point-like particles. Moreover, these loop-shaped excitations may exhibit non-trivial braiding statistics with point particles, as well as from three-loop braiding processes in which two loops are wound around one another while simultaneously linked to a third loop 16, 49, 51. In conventional 3D topological phases (discrete gauge theories), the set of fractional particle and loop excitations, the braiding statistics between

particles and loops, along with the three-loop braiding statistics, fully characterize the topological order (see, for example, Refs. [7, 50]). In this section, we demonstrate that the framework developed in the prior sections can be extended to accommodate the universal data pertaining to loop excitations of conventional topological orders. This is of note because conventional 3D topological orders are themselves a subset of the foliated fracton orders (with trivial foliation structure). Since the notions of ordinary superselection sector and quotient superselection sector coincide for these phases, there is no need to distinguish between them here.

The conventional notion of *superselection sector* does not capture loop-like excitations of gapped phases, because loop excitations contained in a ball-shaped region \mathcal{R} can be shrunk to a point and annihilated via the action of a local operator with support in \mathcal{R} . However, it is possible to incorporate a description of these excitations by modifying the topology of the region. Instead of a ball-shaped region \mathcal{R} , consider a region \mathcal{S} with the topology of a solid torus. We assume that the diameter of \mathcal{S} (but not necessarily the thickness) is large compared to the correlation length of the gapped medium. The superselection sectors defined with reference to such a region \mathcal{S} include the original sectors corresponding to fractional point particles, as well as new sectors which correspond to fractional loop excitations. For example, for the 3+1D \mathbb{Z}_2 gauge theory, there are four such superselection sectors: the vacuum, an electric point charge e , a magnetic flux loop m , and a dyonic loop ϵ , which is a composite of e and m excitations and carries both charge and flux. The interferometric operators for these sectors correspond to processes in which a charge is wound around a flux loop, or in which a flux loop is nucleated from the vacuum, stretched and pulled around a charge, and annihilated into the vacuum on the other side. It is also possible to capture the notion of three-loop braiding by extending the notion of superselection sector to regions with the topology of Hopf-linked solid tori. We will not elaborate further here.

5.8 Discussion

In this paper, we have proposed a way to characterize fractional excitations in fracton models that reflects the universal properties of the underlying foliated fracton order. A foliated fracton phase is defined to be the equivalence class of 3D gapped fracton models up to the addition of 2D gapped topological layers and adiabatic deformation. Correspondingly, we propose to characterize

fractional excitations in fracton models by modding out the contributions from the 2D layers. We define a *quotient superselection sector* (QSS), coarsening the notion of superselection sectors, as an equivalence class of point excitations that can be related to one another by adding or removing both local excitations and 2D quasiparticles. Moreover, we define their ‘statistics’ in an interferometric way that is indifferent to statistics arising from the exchange or braiding of 2D quasi-particles in the system. Using this approach, we can characterize the universal features of fractional excitations in a foliated fracton phase using a finite data set and compare this structure between models. The examples we studied fall into three classes, as summarized in the following table. (From our preliminary studies, the Chamon model [2, 6] belongs to the class of X-cube model with 4 foliations. Details about this model will be presented in future work.)

Class	Independent Fracton QSS	Independent Lineon QSS	Models
X-cube 3-foliation	1	2	X-cube, semionic X-cube, \mathbb{Z}_N X-cube, Checkerboard (2 copies)
X-cube 4-foliation	1	3	Kagome X-cube Hyperkagome X-cube Chamon model
Anisotropic 2-foliation	0	2	Anisotropic model

Within each class, the quasiparticle statistics given by interferometric detection also take the same form. Of course, this is not meant to be a complete list. It will be interesting to study the fractional excitations in the Majorana checkerboard model [47], the non-abelian fracton models [46], the twisted fracton models [44], the cage-net models [26], and so forth. Compared to the systematic characterization of 2D fractional excitations in terms of unitary modular tensor categories, our understanding of fractional excitations in 3D fracton models is very limited. To achieve a more complete understanding, we must collect more data and determine what types of quotient superselection sectors can exist and what kinds of quasiparticle statistics are possible.

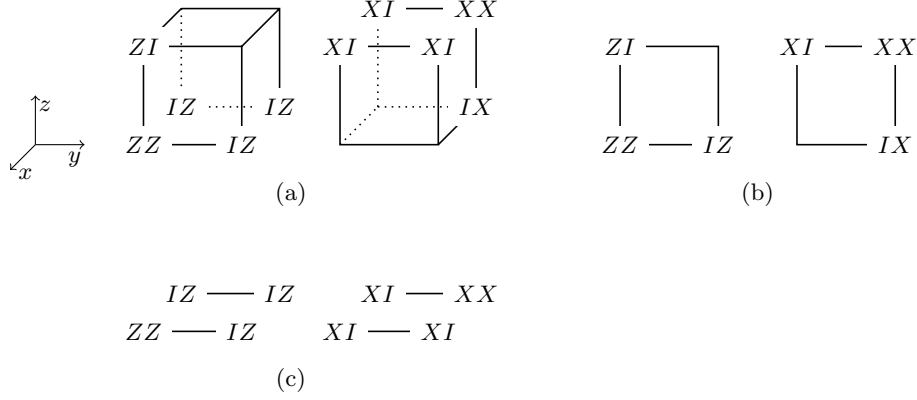


Figure 5.23: Terms of (a) the anisotropic model Hamiltonian H_{aniso} , (b) the 2D toric code Hamiltonian H_{TC} , which acts on qubits in the $x = 0$ layer, and (c) the Hamiltonian H_0 , which acts on the $z = 0$ layer.

5.9 Appendix: Renormalization group transformation for the anisotropic model

In this appendix, we discuss the renormalization group transformation for the anisotropic model introduced in Sec. 5.5.7. The procedure utilizes 2D toric code resource states to grow the system size in the x or y directions, and product state ancilla degrees of freedom to grow the system in the z direction. Hence the model has foliated fracton order with 2 underlying foliations. To describe these transformations, it is convenient to re-arrange the qubits so that two qubits lie at each vertex of a cubic lattice. They may then be referred to by labels $(x, y, z, \alpha = 1, 2)$. In this geometry the Hamiltonian terms take the form pictured in Fig. 5.23(a).

To disentangle the layer $x = 0$ from the rest of the system, we act with the local unitary operator

$$S = \prod_{y,z} \text{CNOT}_{(-1,y,z,2),(0,y,z,2)} \text{CNOT}_{(0,y,z,1),(1,y,z,1)}, \quad (5.36)$$

which satisfies $SH_{\text{aniso}}S^\dagger \cong H'_{\text{aniso}} + H_{\text{TC}}$. Here, H_{aniso} is the original Hamiltonian for the anisotropic model, H'_{aniso} is the Hamiltonian for the model with the $x = 0$ layer missing, and H_{TC} is the toric code Hamiltonian on the $x = 0$ layer, whose stabilizer terms are depicted in Fig. 5.23(b). An analogous transformation can be used to disentangle 2D toric code layers along xz planes. In order to grow the system size, this procedure is simply reversed: 2D toric code resource states are added to the 3D system then sewn into the bulk by

the circuit S (note that $S = S^{-1}$).

On the other hand, to disentangle the $z = 0$ layer from the other system, we perform the operation

$$S = \prod_{x,y} \text{CNOT}_{(x,y,1,1),(x,y,0,1)} \text{CNOT}_{(x,y,0,2),(x,y,-1,2)}, \quad (5.37)$$

which acts as $SH_{\text{aniso}}S^\dagger \cong H'_{\text{aniso}} + H_0$. The decoupled Hamiltonian H_0 , acting on the $z = 0$ layer, is a sum of terms depicted in Fig. 5.23(c). This Hamiltonian has trivial topological order with a product state ground state. Therefore, the anisotropic model has an underlying foliation structure composed of 2 foliations of 2D topologically ordered gapped states parallel to the xz and yz planes.

5.10 Appendix: Field theory of the anisotropic model

In this appendix we derive a quantum field theory (QFT) for the anisotropic model introduced in Sec. 5.5.7. The QFT and its derivation are analogous to that of the X-cube model in 42.

We will consider the \mathbb{Z}_N generalization of the anisotropic model. The stabilizer terms in the Hamiltonian [Eq. (5.20)] are shown in Fig. 5.24. The \mathbb{Z}_N rotor degrees of freedom (X and Z) are defined the same way as in Sec. 5.5.5.

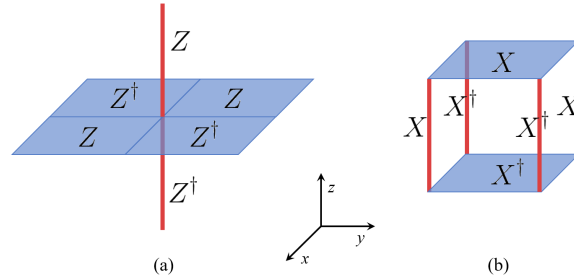


Figure 5.24: The Hamiltonian terms of the \mathbb{Z}_N anisotropic model. Rotor degrees of freedom lie on the red edges and blue plaquettes.

In order to connect the lattice model to a field theory, we rewrite the lattice operators as exponents of fields (A_b and B_b with $b = 1, 2$):

$$\begin{aligned} Z_{p(\mathbf{x})}(t) &\sim \exp \left(i \int_{x-a/2}^{x+a/2} dx' \int_{y-a/2}^{y+a/2} dy' A_1(t, x', y', z) \right) \\ Z_{e(\mathbf{x})}(t) &\sim \exp \left(i \int_{z-a/2}^{z+a/2} dz' A_2(t, x, y, z') \right). \end{aligned} \quad (5.38)$$

The X operators are related to the B fields by replacing $Z \rightarrow X$ and $A \rightarrow B$ above. $Z_{p(\mathbf{x})}(t)$ denotes a $Z(t)$ operator (in the Heisenberg representation) at the xy plane plaquette $p(\mathbf{x})$, which is centered at \mathbf{x} , while $Z_{e(\mathbf{x})}(t)$ denotes a $Z(t)$ operator at the z axis edge $e(\mathbf{x})$. If a is the cubic lattice spacing, then the Z (or X) operators are related to the exponent of small integrals of the gauge field A (or B) over plaquettes or lines of length a . The A and B fields should not be confused with the stabilizer operators A_v and B_c appearing in the Hamiltonian [Eq. (5.20)].

The field theory is then derived by first rewriting the stabilizer terms in the Hamiltonian in terms of the field variables. To do this, we express the stabilizers, Fig. 5.24(a) and (b) as exponents of current densities, e^{iI^0} and e^{iJ^0} , respectively. The current densities are

$$\begin{aligned} I^0 &= \frac{N}{2\pi} (\partial_x \partial_y A_1 + \partial_z A_2) \\ J^0 &= \frac{N}{2\pi} (\partial_x \partial_y B_1 + \partial_z B_2). \end{aligned} \quad (5.39)$$

It helps to think of the lattice operators in Fig. 5.24 as discretized versions of the above current densities, which can be made more precise by the correspondence in Eq. (5.38).

The Lagrangian is

$$\begin{aligned} L &= \frac{N}{2\pi} (A_1 \partial_t B_2 + A_2 \partial_t B_1) + B_0 \underbrace{\frac{N}{2\pi} (\partial_x \partial_y A_1 + \partial_z A_2)}_{I^0} \\ &\quad + A_0 \underbrace{\frac{N}{2\pi} (\partial_x \partial_y B_1 + \partial_z B_2)}_{J^0} - \sum_{a=0,1,2} (A_a J^a + B_a I^a). \end{aligned} \quad (5.40)$$

There are six fields in total: A_a and B_a for $a = 0, 1, 2$. The first term results because A and B are conjugate fields. In the next two terms, B_0 and A_0 act as Lagrange multipliers, which project into the ground state Hilbert space by projecting out excitations. The final term couples A and B to source fields J and I . Similar to the lattice model, the field theory also exhibits a self-duality given by

$$\begin{aligned} A_a &\leftrightarrow B_a \\ J_a &\leftrightarrow I_a. \end{aligned} \quad (5.41)$$

By construction, and the fact that the Hamiltonian terms commute, the Lagrangian exhibits a gauge invariance due to the vanishing Poisson bracket

$$\{I^0(t, \mathbf{x}), J^0(t, \mathbf{x}')\} = 0 \quad (5.42)$$

where

$$\begin{aligned} \{A_1(t, \mathbf{x}), B_2(t, \mathbf{x}')\} &= \{A_2(t, \mathbf{x}), B_1(t, \mathbf{x}')\} = \frac{2\pi}{N} \delta^3(\mathbf{x} - \mathbf{x}') \\ \{A_1(t, \mathbf{x}), B_1(t, \mathbf{x}')\} &= \{A_1(t, \mathbf{x}), B_2(t, \mathbf{x}')\} = 0. \end{aligned} \quad (5.43)$$

The vanishing Poisson bracket is the field theory analog of the fact that the terms in the lattice model commute. The gauge transformation for A_1 and A_2 can be derived from

$$\begin{aligned} \forall_{a=1,2} : A_a(t, \mathbf{x}) \rightarrow & A_a(t, \mathbf{x}) - \int_{\mathbf{x}'} \left\{ A_a(t, \mathbf{x}), \right. \\ & \left. \underbrace{\frac{N}{2\pi} [\partial'_x \partial'_y B_1(t, \mathbf{x}') + \partial'_z B_2(t, \mathbf{x}')] }_{J^0(t, \mathbf{x}')} \right\} \zeta(t, \mathbf{x}'). \end{aligned} \quad (5.44)$$

The transformation for A_0 is then found by requiring that the Lagrangian is invariant under the transformation (ignoring the source field J for now). We then find that the Lagrangian is invariant under the following gauge transformation:

$$\begin{aligned} A_0 &\rightarrow A_0 - \partial_t \zeta \\ A_1 &\rightarrow A_1 + \partial_z \zeta \\ A_2 &\rightarrow A_2 + \partial_x \partial_y \zeta. \end{aligned} \quad (5.45)$$

As required by the duality (Eq. [\(5.41\)](#)), the Lagrangian is also invariant by a similar transformation of the B field. In order for the Lagrangian to be gauge invariant in the presence of the source fields, the source fields must obey the following conserved current constraints:

$$\begin{aligned} \partial_t J^0 - \partial_z J^1 - \partial_x \partial_y J^2 &= 0 \\ \partial_t I^0 - \partial_z I^1 - \partial_x \partial_y I^2 &= 0. \end{aligned} \quad (5.46)$$

The field theory is invariant under the following form of spacetime transformations:

$$t \rightarrow \tilde{t}(t) \quad x \rightarrow \tilde{x}(x) \quad y \rightarrow \tilde{y}(y) \quad z \rightarrow \tilde{z}(z) \quad (5.47)$$

where $\tilde{t}(t)$, $\tilde{x}(x)$, $\tilde{y}(y)$, and $\tilde{z}(z)$ are smooth and monotonic functions. The gauge fields transform under the spacetime transformation as

$$\begin{aligned} A_0(x^\mu) &\rightarrow \frac{d\tilde{t}}{dt} A_0(\tilde{x}^\mu) \\ A_1(x^\mu) &\rightarrow \frac{d\tilde{z}}{dz} A_1(\tilde{x}^\mu) \\ A_2(x^\mu) &\rightarrow \frac{d\tilde{x}}{dx} \frac{d\tilde{y}}{dy} A_2(\tilde{x}^\mu). \end{aligned} \quad (5.48)$$

References

- [1] Daniel Arovas, J. R. Schrieffer, and Frank Wilczek. “Fractional Statistics and the Quantum Hall Effect”. In: *Phys. Rev. Lett.* 53 (7 Aug. 1984), pp. 722–723. DOI: [10.1103/PhysRevLett.53.722](https://doi.org/10.1103/PhysRevLett.53.722).
- [2] S. Bravyi, B. Leemhuis, and B.M. Terhal. “Topological order in an exactly solvable 3D spin model”. In: *Annals of Physics* 326 (Apr. 2011), pp. 839–866. DOI: [10.1016/j.aop.2010.11.002](https://doi.org/10.1016/j.aop.2010.11.002).
- [3] Sergey Bravyi and Jeongwan Haah. “Energy Landscape of 3D Spin Hamiltonians with Topological Order”. In: *Phys. Rev. Lett.* 107 (15 Oct. 2011), p. 150504. DOI: [10.1103/PhysRevLett.107.150504](https://doi.org/10.1103/PhysRevLett.107.150504).
- [4] D. Bulmash and M. Barkeshli. “Generalized $U(1)$ Gauge Field Theories and Fractal Dynamics”. In: *ArXiv e-prints* (June 2018). arXiv: [1806.01855](https://arxiv.org/abs/1806.01855) [[cond-mat.str-el](https://arxiv.org/archive/cond-mat)].
- [5] Daniel Bulmash and Maissam Barkeshli. “Higgs mechanism in higher-rank symmetric $U(1)$ gauge theories”. In: *Phys. Rev. B* 97 (23 June 2018), p. 235112. DOI: [10.1103/PhysRevB.97.235112](https://doi.org/10.1103/PhysRevB.97.235112).
- [6] Claudio Chamon. “Quantum Glassiness in Strongly Correlated Clean Systems: An Example of Topological Overprotection”. In: *Phys. Rev. Lett.* 94 (4 Jan. 2005), p. 040402. DOI: [10.1103/PhysRevLett.94.040402](https://doi.org/10.1103/PhysRevLett.94.040402).
- [7] Meng Cheng, Nathanan Tantivasadakarn, and Chenjie Wang. “Loop Braiding Statistics and Interacting Fermionic Symmetry-Protected Topological Phases in Three Dimensions”. In: *Phys. Rev. X* 8 (1 Mar. 2018), p. 011054. DOI: [10.1103/PhysRevX.8.011054](https://doi.org/10.1103/PhysRevX.8.011054).
- [8] T. Devakul and D. J. Williamson. “Universal quantum computation using fractal symmetry-protected cluster phases”. In: *ArXiv e-prints* (June 2018). arXiv: [1806.04663](https://arxiv.org/abs/1806.04663) [[quant-ph](https://arxiv.org/archive/quant)].
- [9] T. Devakul et al. “Fractal Symmetric Phases of Matter”. In: *ArXiv e-prints* (May 2018). arXiv: [1805.04097](https://arxiv.org/abs/1805.04097) [[cond-mat.str-el](https://arxiv.org/archive/cond-mat)].

- [10] Trithep Devakul, S. A. Parameswaran, and S. L. Sondhi. “Correlation function diagnostics for type-I fracton phases”. In: *Phys. Rev. B* 97 (4 Jan. 2018), p. 041110. DOI: [10.1103/PhysRevB.97.041110](https://doi.org/10.1103/PhysRevB.97.041110).
- [11] A. Gromov. “Fractional Topological Elasticity and Fracton Order”. In: *ArXiv e-prints* (Dec. 2017). arXiv: [1712.06600 \[cond-mat.str-el\]](https://arxiv.org/abs/1712.06600).
- [12] Jeongwan Haah. “Local stabilizer codes in three dimensions without string logical operators”. In: *Phys. Rev. A* 83 (4 Apr. 2011), p. 042330. DOI: [10.1103/PhysRevA.83.042330](https://doi.org/10.1103/PhysRevA.83.042330).
- [13] Gábor B. Halász, Timothy H. Hsieh, and Leon Balents. “Fracton Topological Phases from Strongly Coupled Spin Chains”. In: *Phys. Rev. Lett.* 119 (25 Dec. 2017), p. 257202. DOI: [10.1103/PhysRevLett.119.257202](https://doi.org/10.1103/PhysRevLett.119.257202).
- [14] Huan He et al. “Entanglement entropy from tensor network states for stabilizer codes”. In: *Phys. Rev. B* 97 (12 Mar. 2018), p. 125102. DOI: [10.1103/PhysRevB.97.125102](https://doi.org/10.1103/PhysRevB.97.125102).
- [15] Timothy H. Hsieh and Gábor B. Halász. “Fractons from partons”. In: *Phys. Rev. B* 96 (16 Oct. 2017), p. 165105. DOI: [10.1103/PhysRevB.96.165105](https://doi.org/10.1103/PhysRevB.96.165105).
- [16] Shenghan Jiang, Andrej Mesaros, and Ying Ran. “Generalized Modular Transformations in $(3 + 1)$ D Topologically Ordered Phases and Triple Linking Invariant of Loop Braiding”. In: *Phys. Rev. X* 4 (3 Sept. 2014), p. 031048. DOI: [10.1103/PhysRevX.4.031048](https://doi.org/10.1103/PhysRevX.4.031048).
- [17] Alexei Kitaev. “Anyons in an exactly solved model and beyond”. In: *Annals of Physics* 321.1 (2006). January Special Issue, pp. 2–111. ISSN: 0003-4916. DOI: [10.1016/j.aop.2005.10.005](https://doi.org/10.1016/j.aop.2005.10.005).
- [18] A. Kubica and B. Yoshida. “Ungauging quantum error-correcting codes”. In: *ArXiv e-prints* (May 2018). arXiv: [1805.01836 \[quant-ph\]](https://arxiv.org/abs/1805.01836).
- [19] H. Ma, M. Hermele, and X. Chen. “Fracton topological order from Higgs and partial confinement mechanisms of rank-two gauge theory”. In: *ArXiv e-prints* (Feb. 2018). arXiv: [1802.10108 \[cond-mat.str-el\]](https://arxiv.org/abs/1802.10108).
- [20] H. Ma and M. Pretko. “Higher Rank Deconfined Quantum Criticality and the Exciton Bose Condensate”. In: *ArXiv e-prints* (Mar. 2018). arXiv: [1803.04980 \[cond-mat.str-el\]](https://arxiv.org/abs/1803.04980).
- [21] Han Ma et al. “Fracton topological order via coupled layers”. In: *Phys. Rev. B* 95 (24 June 2017), p. 245126. DOI: [10.1103/PhysRevB.95.245126](https://doi.org/10.1103/PhysRevB.95.245126).
- [22] Han Ma et al. “Topological entanglement entropy of fracton stabilizer codes”. In: *Phys. Rev. B* 97 (12 Mar. 2018), p. 125101. DOI: [10.1103/PhysRevB.97.125101](https://doi.org/10.1103/PhysRevB.97.125101).

- [23] R. M. Nandkishore and M. Hermele. “Fractons”. In: *ArXiv e-prints* (Mar. 2018). arXiv: [1803.11196 \[cond-mat.str-el\]](https://arxiv.org/abs/1803.11196).
- [24] Shriya Pai and Michael Pretko. “Fractonic line excitations: An inroad from three-dimensional elasticity theory”. In: *Phys. Rev. B* 97 (23 June 2018), p. 235102. DOI: [10.1103/PhysRevB.97.235102](https://doi.org/10.1103/PhysRevB.97.235102).
- [25] O. Petrova and N. Regnault. “Simple anisotropic three-dimensional quantum spin liquid with fractonlike topological order”. In: *Phys. Rev. B* 96 (22 Dec. 2017), p. 224429. DOI: [10.1103/PhysRevB.96.224429](https://doi.org/10.1103/PhysRevB.96.224429).
- [26] A. Prem et al. “Cage-Net Fracton Models”. In: *ArXiv e-prints* (June 2018). arXiv: [1806.04687 \[cond-mat.str-el\]](https://arxiv.org/abs/1806.04687).
- [27] A. Prem et al. “Pinch Point Singularities of Tensor Spin Liquids”. In: *ArXiv e-prints* (June 2018). arXiv: [1806.04148 \[cond-mat.str-el\]](https://arxiv.org/abs/1806.04148).
- [28] Abhinav Prem, Jeongwan Haah, and Rahul Nandkishore. “Glassy quantum dynamics in translation invariant fracton models”. In: *Phys. Rev. B* 95 (15 Apr. 2017), p. 155133. DOI: [10.1103/PhysRevB.95.155133](https://doi.org/10.1103/PhysRevB.95.155133).
- [29] Abhinav Prem, Michael Pretko, and Rahul M. Nandkishore. “Emergent phases of fractonic matter”. In: *Phys. Rev. B* 97 (8 Feb. 2018), p. 085116. DOI: [10.1103/PhysRevB.97.085116](https://doi.org/10.1103/PhysRevB.97.085116).
- [30] Michael Pretko. “Emergent gravity of fractons: Mach’s principle revisited”. In: *Phys. Rev. D* 96 (2 July 2017), p. 024051. DOI: [10.1103/PhysRevD.96.024051](https://doi.org/10.1103/PhysRevD.96.024051).
- [31] Michael Pretko. “Generalized electromagnetism of subdimensional particles: A spin liquid story”. In: *Phys. Rev. B* 96 (3 July 2017), p. 035119. DOI: [10.1103/PhysRevB.96.035119](https://doi.org/10.1103/PhysRevB.96.035119).
- [32] Michael Pretko. “Higher-spin Witten effect and two-dimensional fracton phases”. In: *Phys. Rev. B* 96 (12 Sept. 2017), p. 125151. DOI: [10.1103/PhysRevB.96.125151](https://doi.org/10.1103/PhysRevB.96.125151).
- [33] Michael Pretko. “Subdimensional particle structure of higher rank $U(1)$ spin liquids”. In: *Phys. Rev. B* 95 (11 Mar. 2017), p. 115139. DOI: [10.1103/PhysRevB.95.115139](https://doi.org/10.1103/PhysRevB.95.115139).
- [34] Michael Pretko and Leo Radzihovsky. “Fracton-Elasticity Duality”. In: *Phys. Rev. Lett.* 120 (19 May 2018), p. 195301. DOI: [10.1103/PhysRevLett.120.195301](https://doi.org/10.1103/PhysRevLett.120.195301).
- [35] A. Rasmussen, Y.-Z. You, and C. Xu. “Stable Gapless Bose Liquid Phases without any Symmetry”. In: *ArXiv e-prints* (Jan. 2016). arXiv: [1601.08235 \[cond-mat.str-el\]](https://arxiv.org/abs/1601.08235).

- [36] A. T. Schmitz et al. “Recoverable information and emergent conservation laws in fracton stabilizer codes”. In: *Phys. Rev. B* 97 (13 Apr. 2018), p. 134426. DOI: [10.1103/PhysRevB.97.134426](https://doi.org/10.1103/PhysRevB.97.134426).
- [37] Bowen Shi and Yuan-Ming Lu. “Deciphering the nonlocal entanglement entropy of fracton topological orders”. In: *Phys. Rev. B* 97 (14 Apr. 2018), p. 144106. DOI: [10.1103/PhysRevB.97.144106](https://doi.org/10.1103/PhysRevB.97.144106).
- [38] W. Shirley, K. Slagle, and X. Chen. “Universal entanglement signatures of foliated fracton phases”. In: *ArXiv e-prints* (Mar. 2018). arXiv: [1803.10426](https://arxiv.org/abs/1803.10426) [[cond-mat.str-el](https://arxiv.org/abs/1803.10426)].
- [39] W. Shirley et al. “Fracton Models on General Three-Dimensional Manifolds”. In: *ArXiv e-prints* (Dec. 2017). arXiv: [1712.05892](https://arxiv.org/abs/1712.05892) [[cond-mat.str-el](https://arxiv.org/abs/1712.05892)].
- [40] Wilbur Shirley, Kevin Slagle, and Xie Chen. “Foliated fracton order in the checkerboard model”. In: *Phys. Rev. B* 99 (11 Mar. 2019), p. 115123. DOI: [10.1103/PhysRevB.99.115123](https://doi.org/10.1103/PhysRevB.99.115123).
- [41] Kevin Slagle and Yong Baek Kim. “Fracton topological order from nearest-neighbor two-spin interactions and dualities”. In: *Phys. Rev. B* 96 (16 Oct. 2017), p. 165106. DOI: [10.1103/PhysRevB.96.165106](https://doi.org/10.1103/PhysRevB.96.165106).
- [42] Kevin Slagle and Yong Baek Kim. “Quantum field theory of X-cube fracton topological order and robust degeneracy from geometry”. In: *Phys. Rev. B* 96 (19 Nov. 2017), p. 195139. DOI: [10.1103/PhysRevB.96.195139](https://doi.org/10.1103/PhysRevB.96.195139).
- [43] Kevin Slagle and Yong Baek Kim. “X-cube model on generic lattices: Fracton phases and geometric order”. In: *Phys. Rev. B* 97 (16 Apr. 2018), p. 165106. DOI: [10.1103/PhysRevB.97.165106](https://doi.org/10.1103/PhysRevB.97.165106).
- [44] H. Song et al. “Twisted Fracton Models in Three Dimensions”. In: *ArXiv e-prints* (May 2018). arXiv: [1805.06899](https://arxiv.org/abs/1805.06899) [[cond-mat.str-el](https://arxiv.org/abs/1805.06899)].
- [45] S. Vijay. “Isotropic Layer Construction and Phase Diagram for Fracton Topological Phases”. In: *ArXiv e-prints* (Jan. 2017). arXiv: [1701.00762](https://arxiv.org/abs/1701.00762) [[cond-mat.str-el](https://arxiv.org/abs/1701.00762)].
- [46] S. Vijay and L. Fu. “A Generalization of Non-Abelian Anyons in Three Dimensions”. In: *ArXiv e-prints* (June 2017). arXiv: [1706.07070](https://arxiv.org/abs/1706.07070) [[cond-mat.str-el](https://arxiv.org/abs/1706.07070)].
- [47] Sagar Vijay, Jeongwan Haah, and Liang Fu. “A new kind of topological quantum order: A dimensional hierarchy of quasiparticles built from stationary excitations”. In: *Phys. Rev. B* 92 (23 Dec. 2015), p. 235136. DOI: [10.1103/PhysRevB.92.235136](https://doi.org/10.1103/PhysRevB.92.235136).
- [48] Sagar Vijay, Jeongwan Haah, and Liang Fu. “Fracton topological order, generalized lattice gauge theory, and duality”. In: *Phys. Rev. B* 94 (23 Dec. 2016), p. 235157. DOI: [10.1103/PhysRevB.94.235157](https://doi.org/10.1103/PhysRevB.94.235157).

- [49] Chenjie Wang and Michael Levin. “Braiding Statistics of Loop Excitations in Three Dimensions”. In: *Phys. Rev. Lett.* 113 (8 Aug. 2014), p. 080403. DOI: [10.1103/PhysRevLett.113.080403](https://doi.org/10.1103/PhysRevLett.113.080403)
- [50] Chenjie Wang and Michael Levin. “Topological invariants for gauge theories and symmetry-protected topological phases”. In: *Phys. Rev. B* 91 (16 Apr. 2015), p. 165119. DOI: [10.1103/PhysRevB.91.165119](https://doi.org/10.1103/PhysRevB.91.165119)
- [51] Juven C. Wang and Xiao-Gang Wen. “Non-Abelian string and particle braiding in topological order: Modular $SL(3, \mathbb{Z})$ representation and $(3 + 1)$ -dimensional twisted gauge theory”. In: *Phys. Rev. B* 91 (3 Jan. 2015), p. 035134. DOI: [10.1103/PhysRevB.91.035134](https://doi.org/10.1103/PhysRevB.91.035134)
- [52] X. G. Wen and A. Zee. “Classification of Abelian quantum Hall states and matrix formulation of topological fluids”. In: *Phys. Rev. B* 46 (4 July 1992), pp. 2290–2301. DOI: [10.1103/PhysRevB.46.2290](https://doi.org/10.1103/PhysRevB.46.2290)
- [53] Frank Wilczek. “Quantum Mechanics of Fractional-Spin Particles”. In: *Phys. Rev. Lett.* 49 (14 Oct. 1982), pp. 957–959. DOI: [10.1103/PhysRevLett.49.957](https://doi.org/10.1103/PhysRevLett.49.957)
- [54] Dominic J. Williamson. “Fractal symmetries: Ungauging the cubic code”. In: *Phys. Rev. B* 94 (15 Oct. 2016), p. 155128. DOI: [10.1103/PhysRevB.94.155128](https://doi.org/10.1103/PhysRevB.94.155128)
- [55] Cenke Xu. “Gapless bosonic excitation without symmetry breaking: An algebraic spin liquid with soft gravitons”. In: *Phys. Rev. B* 74 (22 Dec. 2006), p. 224433. DOI: [10.1103/PhysRevB.74.224433](https://doi.org/10.1103/PhysRevB.74.224433)
- [56] Beni Yoshida. “Exotic topological order in fractal spin liquids”. In: *Phys. Rev. B* 88 (12 Sept. 2013), p. 125122. DOI: [10.1103/PhysRevB.88.125122](https://doi.org/10.1103/PhysRevB.88.125122)
- [57] Y. You et al. “Subsystem symmetry protected topological order”. In: *ArXiv e-prints* (Mar. 2018). arXiv: [1803.02369](https://arxiv.org/abs/1803.02369) [cond-mat.str-el].
- [58] Y. You et al. “Symmetric Fracton Matter: Twisted and Enriched”. In: *ArXiv e-prints* (May 2018). arXiv: [1805.09800](https://arxiv.org/abs/1805.09800) [cond-mat.str-el]

FOLIATED FRACTON ORDER IN THE CHECKERBOARD MODEL

6.1 Introduction

Fracton models [2, 6, 10, 13, 14, 16, 22, 24, 26, 29, 41, 42, 44, 45, 47–50, 53, 55] are a collection of gapped three-dimensional lattice models that share a range of exotic properties [3, 4, 8, 9, 18, 27, 30, 37, 39, 43, 51, 54]. Most saliently, they contain quasiparticle excitations with constrained mobility and exhibit a ground state degeneracy that scales exponentially with linear system size [2, 49]. Moreover, the entanglement entropy of a region contains a sub-leading correction to the area law that is proportional to the diameter of the region [15, 23, 38, 40]. At the same time, each model appears to differ drastically from other models. Most strikingly, some fracton models contain string-like operators as logical operators on the ground space while others do not [13, 53]. Furthermore, the quasiparticle content in varying models differ in number, allowed movement pattern, and statistics [39]. Broadly speaking, the models fall into two classes: type-I models, whose quasiparticles live at points, along lines, or within planes of the ambient space, and type-II models, i.e. fractal spin liquids [13, 53], in which the quasiparticles may only move in coordination as the corners of fractal-like objects. The scaling constants in the ground state degeneracy and entanglement entropy vary between models as well [50].

A natural question to ask is whether the ‘fracton order’ in various models is the same or different. In other words, we want to know whether the differences between a given pair of models are merely superficial or if they reflect a fundamental distinction between the two models in terms of their universal properties. This question has been difficult to answer in the absence of a clear definition of ‘fracton order’ and a clear distinction between universal and non-universal properties of fracton models.

In [41], we addressed this question by presenting an explicit definition of the so-called *foliated fracton phases* (FFP), which covers a large subset of type-I

fracton models.¹ Based on this definition, in Refs. [39] and [40] we discussed universal properties of FFPs pertaining to their entanglement entropy and fractional excitation types and statistics. Consideration of these properties subsequently enables us to compare the foliated fracton order in different models.

The basic idea behind the definition of FFP is that we are concerned only with the non-trivial behavior intrinsic to three dimensions, and hence we should ‘mod out’ the topological behavior arising from the 2D layers of the underlying foliation structure. That is, when determining the FFP equivalence relation between 3D fracton models, 2D models should be considered as free resources. Thus, two 3D models are considered as equivalent if they can be smoothly connected after the addition of gapped 2D layers. This drastically changes the usual notion of gapped topological phase as two models in the same FFP can have different ground state degeneracy and different numbers of fractional excitations since the 2D resources can carry non-trivial ground state degeneracy and fractional excitations themselves. By modding out features coming from 2D layers, the universal properties of the foliated fracton models can be characterized by a much simpler and robust set of data which can then be compared between models.

In particular, we demonstrated in [41] that the X-cube model [50] belongs to a FFP. Its universal properties can be analyzed as discussed in Refs. [39, 40]. In fact, we showed that the X-cube model is a renormalization group fixed point in the FFP as the system size can be increased (or decreased) by adding (or removing) layers of 2D toric codes and applying local unitary transformations. In this paper, we show that the checkerboard model [50] is also a fixed point of a FFP. By comparing the universal properties of the X-cube and checkerboard models and by establishing carefully an exact mapping, we actually show that the checkerboard model is equivalent to two copies of the X-cube model up to a generalized local unitary transformation [7].

The paper is organized as follows: In section 6.2, we briefly review the definition of the model and some simple properties. In section 6.3, the RG transformation for the model is presented which utilizes 2D toric code bilayers as resources. In section 6.4, we show that the model can be defined on general

¹Gapless $U(1)$ fracton models [5, 12, 20, 21, 25, 28, 31–36, 52] and type-II fracton models (in which excitations are created at corners of fractal operators) [13, 53] are not captured by the notion of foliated fracton phases.

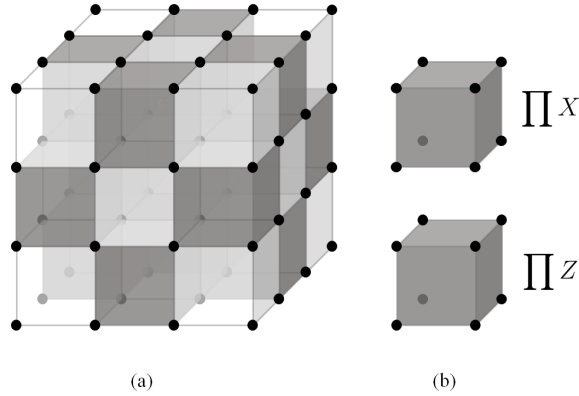


Figure 6.1: (a) A - B checkerboard bipartition of cubic lattice cells. The darkened cells belong to the A sublattice. Black dots represent qubits. (b) X_c and Z_c Hamiltonian terms. Here, $\prod X$ ($\prod Z$) denotes a product of X (Z) operators over the depicted qubits.

three-manifolds equipped with a total foliation structure and derive the general formula for ground state degeneracy. In section 6.5, entanglement entropy in the ground state wave function is studied using the scheme proposed in Ref. [40]. In section 6.6, the fractional excitations of the model are studied using the framework developed in Ref. [39]. This analysis collectively points to the fact that the checkerboard model is equivalent to two copies of the X-cube model as a foliated fracton phase. We present an explicit mapping between the two in section 6.7. Finally we conclude with a brief discussion in section 6.8.

6.2 The checkerboard model

The checkerboard model, as first discussed in [50], is defined on a cubic lattice with one qubit degree of freedom per vertex. The elementary cubes of the lattice are bipartitioned into A and B 3D checkerboard sublattices, and the Hamiltonian is defined as follows:

$$H = - \sum_{c \in A} X_c - \sum_{c \in A} Z_c, \quad (6.1)$$

where in both sums, c indexes all cubes in the A sublattice, and X_c (Z_c) is defined as the product of Pauli X (Z) operators over the vertices of the cube c (see Fig. 6.1). The model constitutes a stabilizer code Hamiltonian [11]; i.e. it is a sum of commuting frustration-free products of Pauli operators, and hence is exactly solvable.

Although there is exactly one Hamiltonian term per qubit, when periodic

boundary conditions are imposed, these terms collectively satisfy certain relations which result in a non-trivial ground state degeneracy (GSD). (Note that all three dimensions of the lattice must be even in order for the checkerboard sublattice structure to exist under periodic boundary conditions.) In particular, for each xy , yz , and xz layer of elementary cubes L , we have the following relation:

$$\prod_{c \in L \cap A} X_c = 1, \quad (6.2)$$

and likewise for Z_c . For a lattice of size $2L_x \times 2L_y \times 2L_z$, there are thus $4(L_x + L_y + L_z)$ such relations, of which 6 are generated by the remaining relations and hence are redundant [50]. The GSD therefore obeys the formula

$$\log_2 \text{GSD} = 4L_x + 4L_y + 4L_z - 6. \quad (6.3)$$

A simple observation is that the number of logical qubits (i.e. $\log_2 \text{GSD}$) is exactly double that of the X-cube model defined on an $L_x \times L_y \times L_z$ size lattice, which has a code space of $2L_x + 2L_y + 2L_z - 3$ qubits. The characteristic sub-extensive scaling of the GSD can be understood in terms of the renormalization group (RG) transformation discussed in the next section. Therein, two toric code layers are added in order to increase the system size by 2 lattice spacings in one direction, corresponding to an increase in GSD by a factor of 16.

The logical operators of the model, which map between ground states, correspond to processes in which particle-antiparticle pairs are created out of the vacuum, wound around the spatial manifold, and then annihilated. A salient feature of the model is that these fractional excitations exist within a hierarchy of subdimensional mobility: *planons* are free to move within a plane but cannot leave the plane; *lineons* can move freely along a straight line; whereas *fractons* are fully immobile and cannot be moved whatsoever without creating additional excitations. Moreover, the model has a simple self-duality realized by Hadamard rotation, which is reflected naturally in the particle content. The full structure of excitations is examined more closely in Sec. 6.6.

6.3 Entanglement renormalization

In this section, we discuss an entanglement renormalization group transformation [1, 7, 19, 46] for the checkerboard model which utilizes toric code bilayers as 2D resources of long-range entanglement, thus establishing the model as a

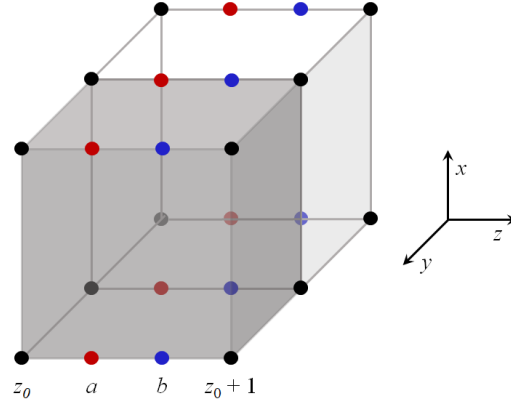


Figure 6.2: Qubits involved in the RG transformation for the checkerboard model. A single unit cell of the original $2L_x \times 2L_y \times 2L_z$ cubic lattice is depicted here. The black qubits belong to the original checkerboard model. The red and blue qubits comprise the toric code bilayer used as an entanglement resource in the RG procedure and are placed at the vertices of square lattices which are respectively embedded in the $z = a$ and $z = b$ planes. The shaded cube belongs to the A sublattice of the checkerboard bipartition.

fixed-point representative of a foliated fracton phase. The procedure presented here can be compared to the corresponding procedure for the X-cube model [41], which uses single toric code layers as 2D resource states. To realize the RG transformation, we construct a local unitary operator S which sews a single toric code bilayer ground state (i.e. two copies of the toric code) into a $2L_x \times 2L_y \times 2L_z$ checkerboard ground state to yield a $2L_x \times 2L_y \times 2(L_z + 1)$ checkerboard ground state. (Since all lattice dimensions must be even, this is the minimal re-sizing allowed.) Arbitrary re-scaling of the model may then be achieved by reversing or iterating this transformation.²

To describe the exact transformation, it is helpful to refer to Fig. 6.2. We label vertices of the original lattice by integral vectors (x, y, z) where $x = 1, 2, \dots, 2L_x$ and equivalently for y and z . We then consider the tensor product $|\psi_{\text{CB}}\rangle \otimes |\psi_{\text{TC}}^a\rangle \otimes |\psi_{\text{TC}}^b\rangle$ of the $2L_x \times 2L_y \times 2L_z$ checkerboard ground state $|\psi_{\text{CB}}\rangle$ with a toric code bilayer ground state $|\psi_{\text{TC}}^a\rangle \otimes |\psi_{\text{TC}}^b\rangle$ living on augmenting $z = a$ and $z = b$ planes lying between the original $z = z_0$ and $z = z_0 + 1$ lattice layers ($z_0 < a < b < z_0 + 1$). The states $|\psi_{\text{TC}}^a\rangle$ and $|\psi_{\text{TC}}^b\rangle$ are defined as ground states of Hamiltonians H_{TC}^a and H_{TC}^b on square lattices commensurate with the original cubic lattice. The toric code bilayer qubits, in

²This is possible because the model is a zero-correlation length fixed point of the RG flow.

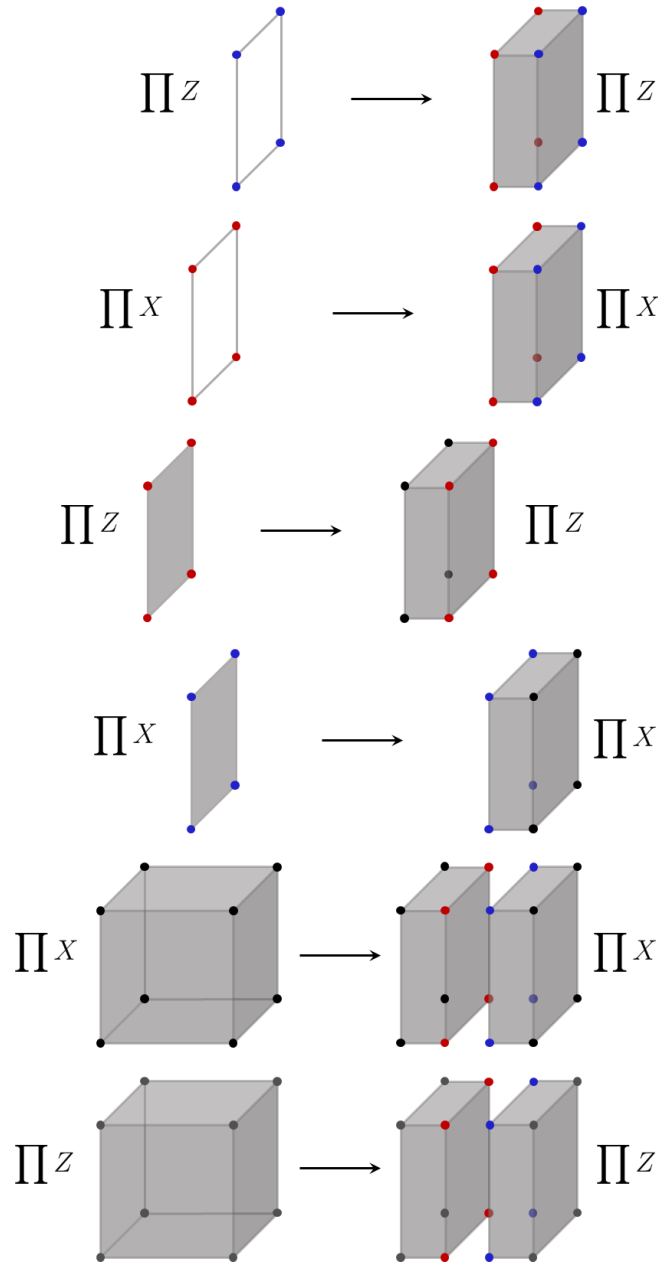


Figure 6.3: Action of the local unitary S on the stabilizer generators of the composite ground state $|\psi_{CB}\rangle \otimes |\psi_{TC}^a\rangle \otimes |\psi_{TC}^b\rangle$. Here Π^X (Π^Z) denotes the product of Pauli X (Z) operators over all depicted qubits. On the left side, the shaded cells correspond to the original A sublattice, whereas on the right side shaded cells correspond to the enlarged A sublattice.

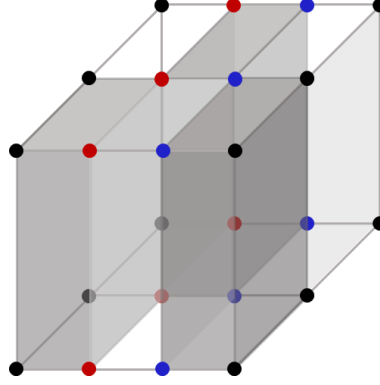


Figure 6.4: Modified checkerboard sublattice structure after the red and blue qubit layers have been incorporated into the model via the RG transformation. The new A sublattice corresponds to the shaded cells.

addition to the original checkerboard model qubits, therefore lie at the vertices of an enlarged $2L_x \times 2L_y \times 2(L_z + 1)$ cubic lattice. H_{TC}^a and H_{TC}^b are defined as

$$\begin{aligned} H_{\text{TC}}^a &= - \sum_{p \in A} Z_p - \sum_{p \in B} X_p \\ H_{\text{TC}}^b &= - \sum_{p \in A} X_p - \sum_{p \in B} Z_p \end{aligned} \quad (6.4)$$

where p runs over all plaquettes in the A or B sublattice and X_p (Z_p) is the product of Pauli X (Z) operators over the vertices of plaquette p . A plaquette p is in sublattice A (B) if it is contained within an A (B) sublattice cube in the original $2L_x \times 2L_y \times 2L_z$ checkerboard lattice. (These Hamiltonians are identical to Kitaev's toric code [17], except that the underlying square lattice is equivalent to the medial lattice of the square lattice in Kitaev's construction.) This information is summarized on the left hand side of Fig. 6.3, which depicts the stabilizer generators of the composite state $|\psi_{\text{CB}}\rangle \otimes |\psi_{\text{TC}}^a\rangle \otimes |\psi_{\text{TC}}^b\rangle$.

To complete the RG procedure, we apply a local unitary operator S in order to yield the enlarged checkerboard ground state $|\psi_{\text{CB}}\rangle' = S(|\psi_{\text{CB}}\rangle \otimes |\psi_{\text{TC}}^a\rangle \otimes |\psi_{\text{TC}}^b\rangle)$. Here,

$$S = \prod_{(x,y)} \text{CX}_{(x,y,b)}^{(x,y,a)} \prod_{(x,y)} \text{CX}_{(x,y,a)}^{(x,y,z_0)} \text{CX}_{(x,y,z_0+1)}^{(x,y,b)} \quad (6.5)$$

where $\prod_{(x,y)} = \prod_{x=1}^{2L_x} \prod_{y=1}^{2L_y}$ and $\text{CX}_{(x,y,b)}^{(x,y,a)}$ is defined as the controlled X (i.e. controlled NOT) quantum gate with control qubit (x, y, a) and target qubit

(x, y, b) . Note that $\text{CX}_{(x,y,a)}^{(x,y,z_0)}$ and $\text{CX}_{(x,y,z_0+1)}^{(x,y,b)}$ commute with one another but not with $\text{CX}_{(x,y,b)}^{(x,y,a)}$. To see that S correctly maps the composite tensor product state to the enlarged checkerboard ground state $|\psi_{\text{CB}}'\rangle$ one can examine the conjugate action of S on the original stabilizer generators. This is shown graphically in Fig. 6.3, recalling that CX acts by conjugation as

$$\begin{aligned} ZI &\rightarrow ZI & IZ &\leftrightarrow ZZ \\ XI &\leftrightarrow XX & IX &\rightarrow IX. \end{aligned} \tag{6.6}$$

In particular,

$$S(H + H_{\text{TC}}^a + H_{\text{TC}}^b) S^\dagger \cong H' \tag{6.7}$$

where H is the original Hamiltonian and H' is the enlarged $2L_x \times 2L_y \times 2(L_z + 1)$ Hamiltonian, and the \cong operator denotes that the two operators have identical ground spaces. The enlarged A sublattice is depicted in Fig. 6.4.

6.4 General three-manifolds

In this section, we employ the notion of singular compact total foliation (SCTF), discussed also in [41], to generalize the checkerboard model to compact 3-manifolds other than the 3-torus. An SCTF is a discrete sample of compact leaves of three transversely intersecting (possibly singular) two-dimensional foliations of a 3-manifold M , labelled x , y , and z respectively. For example, the xy , yz , and xz planes of a cubic lattice embedded in a three-torus may be viewed as the leaves of an SCTF.

For the checkerboard model, each foliating leaf can be thought of as a bilayer of the underlying lattice of qubits. Thus, to generalize the model we take an SCTF of a 3-manifold M and split each leaf into a bilayer of closely-spaced adjacent parallel leaves. These bilayers constitute a refined SCTF which forms the scaffolding of the embedded lattice. Qubits are placed at triple intersection points of foliating leaves. The elementary 3-cells of the resulting cellulation are then bipartitioned into A - B subsets according to the following rule: a 3-cell c belongs to A if it lies within 0 or 2 bilayers, whereas c belongs to B if it lies within 1 or 3 bilayers. See Fig. 6.5 for an example of such a structure for the 3-manifold $S^2 \times S^1$.

The Hamiltonian of Eq. (6.1) is then readily applied to this generalized checkerboard lattice structure, where in this setting, the X_c (Z_c) operator corresponds to products of Pauli X (Z) operators over the vertices of 3-cell c .

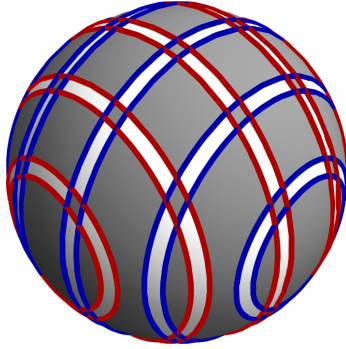


Figure 6.5: An example of a checkerboard lattice structure embedded in $S^2 \times S^1$. Depicted here is an S^2 cross-section. The closely-spaced adjacent circles represent bilayers, and the shaded cells belong to the A sublattice.

As for the checkerboard bipartition of cubic lattice cells, by construction the generalized A - B bipartition has the property that all 3-cells of a given partition have an even number of vertices and share an even number of vertices with one another. The Hamiltonian defined in this way is therefore guaranteed to contain mutually commuting terms.

The RG procedure for the checkerboard model introduced in Sec. 6.3 can be readily generalized to the model defined via an SCTF on a general 3-manifold. The formula for the GSD in Eq. (6.3) therefore generalizes to the form

$$\log_2 \text{GSD} = 4g_x L_x + 4g_y L_y + 4g_z L_z - c \quad (6.8)$$

where L_μ is the number of leaves in foliation μ , and g_μ is the genus.³ The constant c can be computed by using the RG procedure to increasingly coarsen the lattice until the minimal lattice embedding is achieved. We consistently find that $c = 2c_{\text{XC}}$, where c_{XC} is the corresponding constant correction to the GSD of the X-cube model defined on the same manifold with the same SCTF (see Table 1 of [41]). In all cases the total GSD of the checkerboard model is therefore exactly twice the GSD of the corresponding X-cube model.

6.5 Entanglement entropy schemes

Entanglement entropy is a useful way to characterize fracton models [15, 23, 38, 40]. In this section, we briefly discuss the structure of entanglement entropy in the checkerboard model.

³For non-orientable manifolds, a modified formula is satisfied instead [41]

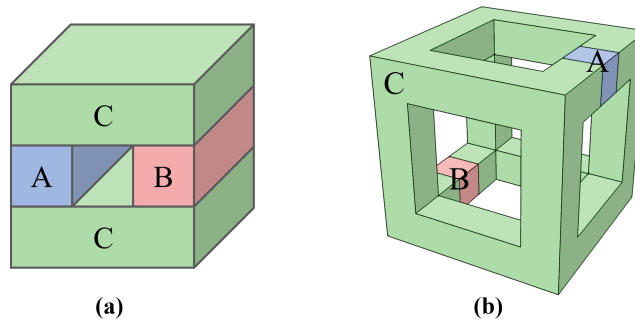


Figure 6.6: (a) 3D solid torus $I(A; B|C)$ scheme and (b) 3D wire-frame $I(A; B|C)$ scheme. In both cases the regions are contained within an overall cube of side length L .

Fig. 6.6 shows two schemes that can be used to characterize the entanglement structure in the checkerboard model. In both schemes, the quantity to be calculated is

$$I(A; B|C) = S_{AB} + S_{BC} - S_C - S_{ABC} \quad (6.9)$$

Applying scheme (a), as proposed in Ref. [23, 38], to the checkerboard model, we find that

$$I_a(A; B|C) = 4L + 2 \quad (6.10)$$

when the overall cubic shape is of linear size L and is aligned with the cubic lattice of the model. L is measured in units of twice the lattice constant of the underlying cubic lattice. As discussed in Ref. [40], the $4L$ term in I_a helps to identify the triple foliation structure revealed by the RG scheme in section 6.3, since it corresponds to a sum of the topological entanglement entropies of the underlying toric code bilayers.

As discussed in Ref. [40], to characterize foliated topological order beyond the existence of foliation structure, we can use the scheme in Fig. 6.6 (b). The foliating layers do not contribute to $I_b(A; B|C)$ in this case and a nonzero $I_b(A; B|C)$ hence represents nontrivial foliated fracton order. Direct calculation shows that

$$I_b(A; B|C) = 2 \quad (6.11)$$

for the checkerboard model. This is exactly twice the value calculated for the X-cube model. It is also interesting to note that I_a for the checkerboard model is also exactly twice the value of I_a for the X-cube model, which must be the case in light of the generalized local unitary equivalence demonstrated in Sec. 6.7.

6.6 Fractional excitations

In Ref. [39], we propose to characterize fractional excitations in foliated fracton phases using *quotient superselection sectors* and their statistics. In particular, a quotient superselection sector (QSS) is defined as a class of fractional excitations that can be mapped into each other through local operations or by attaching 2D point-like excitations (planons). The universal quasiparticle statistics of a QSS is then captured by applying a set of interferometric operators to the surrounding region of an isolated excitation such that the resulting statistics is the same for excitations in the same QSS.

Applying these general principles to the checkerboard model, we find that there are six elementary QSS generators, giving rise to a total of $2^6 = 64$ QSS sectors. It is instructive to take a $2 \times 2 \times 2$ cell of the underlying cubic lattice as shown in Fig. 6.8 and to divide the A checkerboard sublattice into four further sublattices R , G , B , and Y . The six QSS generators can be taken to be fracton excitations corresponding to a violation of the X_c or Z_c term in the R , G , and B sublattice cubes respectively, which we label as f_R^X , f_G^X , f_B^X , f_R^Z , f_G^Z , and f_B^Z . Two neighboring fracton excitations in the same sublattice combine into a planon while two neighboring fracton excitations in different sublattices combine into a lineon. Because of this, we could also choose the generating set of QSS to contain two fractons f_R^X , f_R^Z and four lineons $f_R^X f_G^X$, $f_R^X f_B^X$, $f_R^Z f_G^Z$, and $f_R^Z f_B^Z$. As explained in Ref. [39], when compared to the X-cube model, we see that this is exactly double the QSS content of the X-cube model.

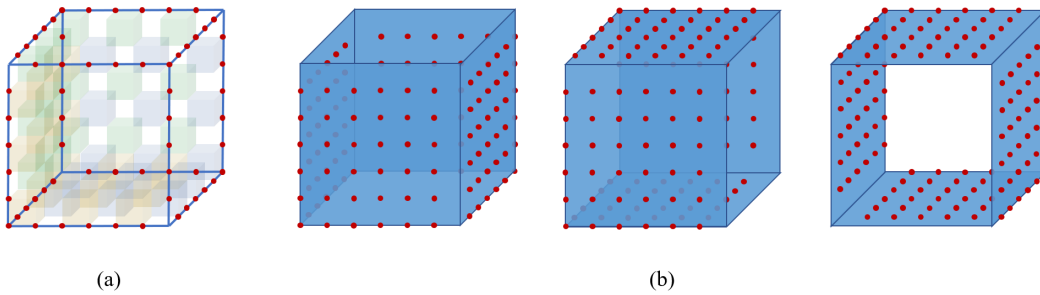


Figure 6.7: Examples of (a) a wireframe operator and (b) membrane operators in the checkerboard model. The operators are tensor products of Pauli X or Z over the red qubits. Shaded cubes belong to the A sublattice.

To detect the quotient charge of an isolated point excitation (i.e. which QSS it belongs to), we can apply interferometric operators as shown in Fig. 6.7.

The operators are tensor products of Pauli X or Z over the red qubits. The wireframe operator can be obtained as a product of all the X_c or Z_c cube operators inside the wireframe. The membrane operators can be obtained as a product of all the cube operators in every other layer inside the overall cube. The number of independent interferometric operators is twice that of the X-cube model and, as shown in Ref. [39], there is a mapping between quotient superselection sectors and interferometric operators of the two models which preserves the fusion rules and quasi-particle statistics.

6.7 Relation to two copies of the X-cube model

In this section, we exhibit an exact local unitary mapping between the checkerboard model ground space on a $2L_x \times 2L_y \times 2L_z$ lattice (denoted G_{CB}) and the ground space of two copies of the X-cube model tensored with product state ancilla qubits on an $L_x \times L_y \times L_z$ lattice (denoted $G_{2\text{XC}}$). The mapping is not a full equivalence of Hamiltonians as it rearranges the energy levels of excitations, but the Hamiltonians are shown to be equivalent as stabilizer codes, and thus have coinciding ground spaces. The X-cube model, as originally discussed in [50], is defined on a cubic lattice with one qubit per edge, and Hamiltonian

$$H_{\text{XC}} = - \sum_v (A_v^{xy} + A_v^{yz} + A_v^{xz}) - \sum_c B_c, \quad (6.12)$$

where v runs over all vertices of the lattice and c runs over all elementary cubes of the lattice. The operator A_v^{xy} is defined as the product of Pauli Z operators over the four edges adjacent to vertex v along the xy plane, while B_c is given by the product of Pauli X operators over the edges of the cube c .

To match the degrees of freedom of the two systems, we start with an $L_x \times L_y \times L_z$ cubic lattice whose points are labelled by vectors (x, y, z) and belong to the set Λ ($x = 1, 2, \dots, L_x$ and equivalently for y and z). We then place one set of qubits on the edges of the lattice, corresponding to one copy of the X-cube model with Hamiltonian H_{XC}^1 , and another set of qubits on the edges of the dual lattice (i.e. the plaquettes of the direct lattice), corresponding to the second copy of the X-cube model, whose Hamiltonian H_{XC}^2 is transformed relative to Eq. (6.12) via a global Hadamard rotation ($X \leftrightarrow Z$). Finally, ancilla qubits are placed at the vertices and body-centers of the lattice, and initialized in +1 eigenstates of the Pauli Z and X operators respectively. As shown in Fig. 6.8, all the qubits together constitute a cubic

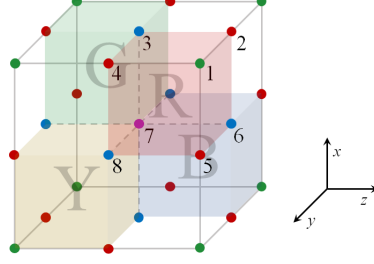


Figure 6.8: Matching of qubits between the checkerboard model and two copies of the X-cube model tensored with ancilla qubits. A $2 \times 2 \times 2$ cell of the checkerboard model cubic lattice is shown here, corresponding to a single unit cell of Λ , whose vertices lie at the green points. Shaded cubes belong to sublattice A of the checkerboard bipartition. The red and blue qubits located respectively on the direct lattice (solid lines) and dual lattice edges (dashed lines) belong to the two X-cube copies, whereas the green and purple qubits at the vertices and body-center are ancilla degrees of freedom. The numbers label the qubits of a single unit cell of Λ .

lattice of dimensions $2L_x \times 2L_y \times 2L_z$ and half the lattice spacing of the original model. There are thus 8 qubits in each unit cell of Λ , which are numbered according to the scheme in Fig. 6.8.

To demonstrate equivalence of the two ground spaces, consider the local unitary operator $U = U_2 U_1$ where

$$U_1 = \prod_{v \in \Lambda} \text{CX}_{v,1}^{v,2} \text{CX}_{v,1}^{v,4} \text{CX}_{v,1}^{v,5} \text{CX}_{v,3}^{v,7} \text{CX}_{v,6}^{v,7} \text{CX}_{v,8}^{v,7}$$

and

$$U_2 = \prod_{v \in \Lambda} \text{CX}_{v,1}^{v,7} \times \\ \text{CX}_{v,2}^{v,3} \text{CX}_{v-\hat{y},4}^{v,3} \text{CX}_{v,2}^{v,6} \text{CX}_{v-\hat{y},5}^{v,6} \text{CX}_{v,4}^{v,8} \text{CX}_{v,5}^{v,8} \times \\ \text{CX}_{v,1}^{v,8} \text{CX}_{v,1}^{v+\hat{y},3} \text{CX}_{v,1}^{v+\hat{y},6} \text{CX}_{v,2}^{v,7} \text{CX}_{v-\hat{y},4}^{v,7} \text{CX}_{v-\hat{y},5}^{v,7}.$$

Here $\text{CX}_{u,b}^{v,a}$ denotes a controlled X gate with control qubit a at point $v \in \Lambda$ and target qubit b at point $u \in \Lambda$. The conjugate action of U on the stabilizer generators of the code space $G_{2\text{XC}}$ is shown graphically in Fig. 6.9. Note that, because two of the three vertex stabilizers generate the third, it is sufficient to consider the action on just two vertex terms. The image stabilizers on the right-hand side are products of stabilizer terms for the checkerboard model, and generate a stabilizer code identical to that of the checkerboard Hamiltonian. In particular,

$$U H_{\text{CB}} U^\dagger \cong H^0 + H_{\text{XC}}^1 + H_{\text{XC}}^2 \quad (6.13)$$

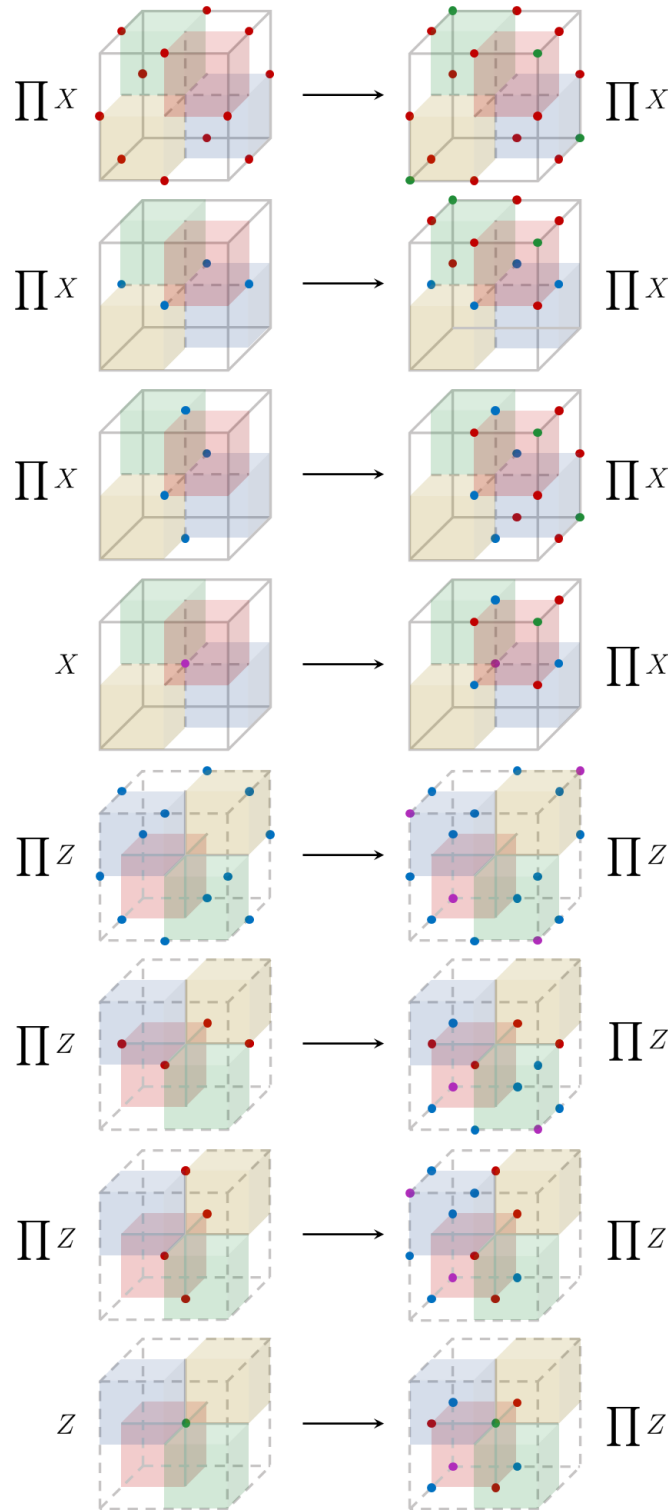


Figure 6.9: Action of U on the stabilizer generators of G_{2XC} . Here $\prod X$ ($\prod Z$) denotes the product of Pauli X (Z) operators over all depicted qubits. Solid lines correspond to direct lattice edges, whereas dashed lines correspond to dual lattice edges. From top to bottom, the image terms equate to $X_R X_G X_B X_Y$, $X_R X_G$, $X_R X_B$, X_R , $Z_R Z_G Z_B Z_Y$, $Z_R Z_G$, $Z_R Z_B$, and Z_R operators in the checkerboard model (Eq. (6.1)) respectively, where R , G , B , and Y refer to the red, green, blue, and yellow cubes.

where H_{CB} is the checkerboard Hamiltonian and H^0 acts on the ancilla degrees of freedom.

6.8 Discussion

In this paper we show that the checkerboard model (first discussed in [50]) belongs to a foliated fracton phase, as defined in [41]. Moreover, we identify the foliated fracton order in the checkerboard model to be equivalent to that of two copies of the X-cube model (also introduced in [50]). This is, in a sense, similar to the equivalence between the 2D color code and two copies of the 2D toric code as conventional topological order.

The existence of such an equivalence is far from obvious as the two models in their original form appear to have significant differences. The checkerboard model has elementary (with minimum energy) lineons whose string operators may anti-commute with each other, which is not the case for the elementary lineons of the X-cube model. Moreover, in the checkerboard model an elementary lineon is the composite of two elementary fractons, which is not the case in the X-cube model. Such differences may seem significant, but they are actually superficial as they depend sensitively on which excitations are considered the ‘elementary’ ones, which is not a universal property of a phase.

The explicit mapping (Fig. 6.3) between the two models allows us to see that an elementary fracton in the checkerboard model is related to a composite fracton in the pair of X-cube models, which is a bound state of elementary X-cube fractons and lineons (along with a possible ancillary bosonic excitation). The elementary lineon in the checkerboard model, which is a bound state of two elementary fractons, is then related to a composite lineon in the X-cube models, which is a bound state of two composite fractons: i.e. a bound state of fracton dipoles (2D particles) and elementary lineons in the X-cube models. Because these composite lineons are made of conjugate fracton dipoles and lineons, their string operators may anti-commute, similar to the string operators in the checkerboard model. This resolves the apparent differences between the checkerboard and pair of X-cube models discussed in the previous paragraph.

While the superficial differences can obscure the intrinsic relation between the fracton orders in different fracton models, by considering their universal properties such as the foliation-free entanglement entropy and fractional

statistics, we are able to see clearly the equivalence between the checkerboard model and two copies of the X-cube. Note that the mapping we found between the two models is special in that we only need to add product state ancillas before doing local unitary transformations. In general, if two models have the same foliated fracton universal properties, then to connect them we may need to add two dimensional gapped states as resource before applying local unitary operations. In [39], we present such an example (between the X-cube model and the semionic X-cube model).

With the definition given in [41] and the universal properties defined in Refs. [40] and [39], we have established a useful set of tools to study foliated fracton order. It would be interesting to explore various other models and identify different types of foliated fracton order, from which a more systematic understanding of the phenomenon may be established.

References

- [1] Miguel Aguado and Guifré Vidal. “Entanglement Renormalization and Topological Order”. In: *Phys. Rev. Lett.* 100 (7 Feb. 2008), p. 070404. DOI: 10.1103/PhysRevLett.100.070404. URL: <https://link.aps.org/doi/10.1103/PhysRevLett.100.070404>.
- [2] S. Bravyi, B. Leemhuis, and B.M. Terhal. “Topological order in an exactly solvable 3D spin model”. In: *Annals of Physics* 326 (Apr. 2011), pp. 839–866. DOI: 10.1016/j.aop.2010.11.002.
- [3] Sergey Bravyi and Jeongwan Haah. “Energy Landscape of 3D Spin Hamiltonians with Topological Order”. In: *Phys. Rev. Lett.* 107 (15 Oct. 2011), p. 150504. DOI: 10.1103/PhysRevLett.107.150504. URL: <https://link.aps.org/doi/10.1103/PhysRevLett.107.150504>.
- [4] Daniel Bulmash and Maissam Barkeshli. “Generalized $U(1)$ Gauge Field Theories and Fractal Dynamics”. In: *arXiv:1806.01855* (June 2018). URL: <http://arxiv.org/abs/1806.01855>.
- [5] Daniel Bulmash and Maissam Barkeshli. “The Higgs Mechanism in Higher-Rank Symmetric $U(1)$ Gauge Theories”. In: *arXiv:1802.10099* (Feb. 2018). URL: <https://arxiv.org/abs/1802.10099>.
- [6] Claudio Chamon. “Quantum Glassiness in Strongly Correlated Clean Systems: An Example of Topological Overprotection”. In: *Phys. Rev. Lett.* 94 (4 Jan. 2005), p. 040402. DOI: 10.1103/PhysRevLett.94.040402. URL: <https://link.aps.org/doi/10.1103/PhysRevLett.94.040402>.

- [7] Xie Chen, Zheng-Cheng Gu, and Xiao-Gang Wen. “Local unitary transformation, long-range quantum entanglement, wave function renormalization, and topological order”. In: *Phys. Rev. B* 82 (15 Oct. 2010), p. 155138. DOI: 10.1103/PhysRevB.82.155138. URL: <https://link.aps.org/doi/10.1103/PhysRevB.82.155138>.
- [8] Trithep Devakul, S. A. Parameswaran, and S. L. Sondhi. “Correlation function diagnostics for type-I fracton phases”. In: *Phys. Rev. B* 97 (4 Jan. 2018), p. 041110. DOI: 10.1103/PhysRevB.97.041110. URL: <https://link.aps.org/doi/10.1103/PhysRevB.97.041110>.
- [9] Trithep Devakul and Dominic J. Williamson. “Universal quantum computation using fractal symmetry-protected cluster phases”. In: *arXiv:1806.04663* (June 2018). URL: <http://arxiv.org/abs/1806.04663>.
- [10] Trithep Devakul et al. “Fractal Symmetric Phases of Matter”. In: *arXiv:1805.04097* (May 2018). URL: <http://arxiv.org/abs/1805.04097>.
- [11] Daniel Gottesman. “Stabilizer Codes and Quantum Error Correction”. In: *quant-ph/9705052* (May 1997). URL: <http://arxiv.org/abs/quant-ph/9705052>.
- [12] Andrey Gromov. “Fractional Topological Elasticity and Fracton Order”. In: *arXiv:1712.06600* (Dec. 2017). URL: <http://arxiv.org/abs/1712.06600>.
- [13] Jeongwan Haah. “Local stabilizer codes in three dimensions without string logical operators”. In: *Phys. Rev. A* 83 (4 Apr. 2011), p. 042330. DOI: 10.1103/PhysRevA.83.042330. URL: <https://link.aps.org/doi/10.1103/PhysRevA.83.042330>.
- [14] Gábor B. Halász, Timothy H. Hsieh, and Leon Balents. “Fracton Topological Phases from Strongly Coupled Spin Chains”. In: *Phys. Rev. Lett.* 119 (25 Dec. 2017), p. 257202. DOI: 10.1103/PhysRevLett.119.257202. URL: <https://link.aps.org/doi/10.1103/PhysRevLett.119.257202>.
- [15] Huan He et al. “Entanglement entropy from tensor network states for stabilizer codes”. In: *Phys. Rev. B* 97 (12 Mar. 2018), p. 125102. DOI: 10.1103/PhysRevB.97.125102. URL: <https://link.aps.org/doi/10.1103/PhysRevB.97.125102>.
- [16] Timothy H. Hsieh and Gábor B. Halász. “Fractons from partons”. In: *Phys. Rev. B* 96 (16 Oct. 2017), p. 165105. DOI: 10.1103/PhysRevB.96.165105. URL: <https://link.aps.org/doi/10.1103/PhysRevB.96.165105>.

- [17] A. Yu. Kitaev. “Fault tolerant quantum computation by anyons”. In: *Annals Phys.* 303 (2003), pp. 2–30. DOI: 10.1016/S0003-4916(02)00018-0.
- [18] Aleksander Kubica and Beni Yoshida. “Ungauging quantum error-correcting codes”. In: *arXiv:1805.01836* (May 2018). URL: <http://arxiv.org/abs/1805.01836>.
- [19] Michael A. Levin and Xiao-Gang Wen. “String-net condensation: A physical mechanism for topological phases”. In: *Phys. Rev. B* 71 (4 Jan. 2005), p. 045110. DOI: 10.1103/PhysRevB.71.045110. URL: <https://link.aps.org/doi/10.1103/PhysRevB.71.045110>.
- [20] Han Ma, Michael Hermele, and Xie Chen. “Fracton topological order from Higgs and partial confinement mechanisms of rank-two gauge theory”. In: *arXiv:1802.10108* (Feb. 2018). URL: <https://arxiv.org/abs/1802.10108>.
- [21] Han Ma and Michael Pretko. “Higher Rank Deconfined Quantum Criticality and the Exciton Bose Condensate”. In: *arXiv:1803.04980* (Mar. 2018). URL: <http://arxiv.org/abs/1803.04980>.
- [22] Han Ma et al. “Fracton topological order via coupled layers”. In: *Phys. Rev. B* 95 (24 June 2017), p. 245126. DOI: 10.1103/PhysRevB.95.245126. URL: <https://link.aps.org/doi/10.1103/PhysRevB.95.245126>.
- [23] Han Ma et al. “Topological entanglement entropy of fracton stabilizer codes”. In: *Phys. Rev. B* 97 (12 Mar. 2018), p. 125101. DOI: 10.1103/PhysRevB.97.125101. URL: <https://link.aps.org/doi/10.1103/PhysRevB.97.125101>.
- [24] R. M. Nandkishore and M. Hermele. “Fractons”. In: *ArXiv e-prints* (Mar. 2018). arXiv: 1803.11196 [cond-mat.str-el].
- [25] Shriya Pai and Michael Pretko. “Fractonic line excitations: an inroad from 3d elasticity theory”. In: *arXiv:1804.01536* (Apr. 2018). URL: <http://arxiv.org/abs/1804.01536>.
- [26] O. Petrova and N. Regnault. “Simple anisotropic three-dimensional quantum spin liquid with fractonlike topological order”. In: *Phys. Rev. B* 96 (22 Dec. 2017), p. 224429. DOI: 10.1103/PhysRevB.96.224429. URL: <https://link.aps.org/doi/10.1103/PhysRevB.96.224429>.
- [27] Abhinav Prem, Jeongwan Haah, and Rahul Nandkishore. “Glassy quantum dynamics in translation invariant fracton models”. In: *Phys. Rev. B* 95 (15 Apr. 2017), p. 155133. DOI: 10.1103/PhysRevB.95.155133. URL: <https://link.aps.org/doi/10.1103/PhysRevB.95.155133>.

- [28] Abhinav Prem, Michael Pretko, and Rahul M. Nandkishore. “Emergent phases of fractonic matter”. In: *Phys. Rev. B* 97 (8 Feb. 2018), p. 085116. DOI: 10.1103/PhysRevB.97.085116. URL: <https://link.aps.org/doi/10.1103/PhysRevB.97.085116>.
- [29] Abhinav Prem et al. “Cage-Net Fracton Models”. In: *arXiv:1806.04687* (June 2018). URL: <http://arxiv.org/abs/1806.04687>.
- [30] Abhinav Prem et al. “Pinch Point Singularities of Tensor Spin Liquids”. In: *arXiv:1806.04148* (June 2018). URL: <http://arxiv.org/abs/1806.04148>.
- [31] Michael Pretko. “Emergent gravity of fractons: Mach’s principle revisited”. In: *Phys. Rev. D* 96 (2 July 2017), p. 024051. DOI: 10.1103/PhysRevD.96.024051. URL: <https://link.aps.org/doi/10.1103/PhysRevD.96.024051>.
- [32] Michael Pretko. “Generalized electromagnetism of subdimensional particles: A spin liquid story”. In: *Phys. Rev. B* 96 (3 July 2017), p. 035119. DOI: 10.1103/PhysRevB.96.035119. URL: <https://link.aps.org/doi/10.1103/PhysRevB.96.035119>.
- [33] Michael Pretko. “Higher-spin Witten effect and two-dimensional fracton phases”. In: *Phys. Rev. B* 96 (12 Sept. 2017), p. 125151. DOI: 10.1103/PhysRevB.96.125151. URL: <https://link.aps.org/doi/10.1103/PhysRevB.96.125151>.
- [34] Michael Pretko. “Subdimensional particle structure of higher rank $U(1)$ spin liquids”. In: *Phys. Rev. B* 95 (11 Mar. 2017), p. 115139. DOI: 10.1103/PhysRevB.95.115139. URL: <https://link.aps.org/doi/10.1103/PhysRevB.95.115139>.
- [35] Michael Pretko and Leo Radzihovsky. “Fracton-Elasticity Duality”. In: *Phys. Rev. Lett.* 120 (19 May 2018), p. 195301. DOI: 10.1103/PhysRevLett.120.195301. URL: <https://link.aps.org/doi/10.1103/PhysRevLett.120.195301>.
- [36] Alex Rasmussen, Yi-Zhuang You, and Cenke Xu. “Stable Gapless Bose Liquid Phases without Any Symmetry”. In: *arXiv:1601.08235* (Jan. 2016). URL: <http://arxiv.org/abs/1601.08235> (visited on 02/02/2016).
- [37] A. T. Schmitz et al. “Recoverable Information and Emergent Conservation Laws in Fracton Stabilizer Codes”. In: *arXiv:1712.02375* (Dec. 2017). URL: <http://arxiv.org/abs/1712.02375>.
- [38] Bowen Shi and Yuan-Ming Lu. “Deciphering the nonlocal entanglement entropy of fracton topological orders”. In: *Phys. Rev. B* 97 (14 Apr. 2018), p. 144106. DOI: 10.1103/PhysRevB.97.144106. URL: <https://link.aps.org/doi/10.1103/PhysRevB.97.144106>.

- [39] Wilbur Shirley, Kevin Slagle, and Xie Chen. “Fractional excitations in foliated fracton phases”. In: (2018). Fractional excitations in foliated fracton phases.
- [40] Wilbur Shirley, Kevin Slagle, and Xie Chen. “Universal entanglement signatures of foliated fracton phases”. In: *arXiv:1803.10426* (Mar. 2018). URL: <http://arxiv.org/abs/1803.10426>.
- [41] Wilbur Shirley et al. “Fracton Models on General Three-Dimensional Manifolds”. In: *arXiv:1712.05892* (2017). URL: <http://arxiv.org/abs/1712.05892>.
- [42] Kevin Slagle and Yong Baek Kim. “Fracton topological order from nearest-neighbor two-spin interactions and dualities”. In: *Phys. Rev. B* 96 (16 Oct. 2017), p. 165106. DOI: 10.1103/PhysRevB.96.165106. URL: <https://link.aps.org/doi/10.1103/PhysRevB.96.165106>.
- [43] Kevin Slagle and Yong Baek Kim. “Quantum field theory of X-cube fracton topological order and robust degeneracy from geometry”. In: *Phys. Rev. B* 96 (19 Nov. 2017), p. 195139. DOI: 10.1103/PhysRevB.96.195139. URL: <https://link.aps.org/doi/10.1103/PhysRevB.96.195139>.
- [44] Kevin Slagle and Yong Baek Kim. “X-cube model on generic lattices: Fracton phases and geometric order”. In: *Phys. Rev. B* 97 (16 Apr. 2018), p. 165106. DOI: 10.1103/PhysRevB.97.165106. URL: <https://link.aps.org/doi/10.1103/PhysRevB.97.165106>.
- [45] Hao Song et al. “Twisted Fracton Models in Three Dimensions”. In: *arXiv:1805.06899* (May 2018). URL: <http://arxiv.org/abs/1805.06899>.
- [46] G. Vidal. “Entanglement Renormalization”. In: *Phys. Rev. Lett.* 99.22 (2007), p. 220405. DOI: 10.1103/PhysRevLett.99.220405.
- [47] Sagar Vijay. “Isotropic Layer Construction and Phase Diagram for Fracton Topological Phases”. In: *arXiv:1701.00762* (Jan. 2017). URL: <http://arxiv.org/abs/1701.00762>.
- [48] Sagar Vijay and Liang Fu. “A Generalization of Non-Abelian Anyons in Three Dimensions”. In: *arXiv:1706.07070* (June 2017). URL: <http://arxiv.org/abs/1706.07070>.
- [49] Sagar Vijay, Jeongwan Haah, and Liang Fu. “A new kind of topological quantum order: A dimensional hierarchy of quasiparticles built from stationary excitations”. In: *Phys. Rev. B* 92 (23 Dec. 2015), p. 235136. DOI: 10.1103/PhysRevB.92.235136. URL: <http://link.aps.org/doi/10.1103/PhysRevB.92.235136>.

- [50] Sagar Vijay, Jeongwan Haah, and Liang Fu. “Fracton topological order, generalized lattice gauge theory, and duality”. In: *Phys. Rev. B* 94 (23 Dec. 2016), p. 235157. DOI: 10.1103/PhysRevB.94.235157. URL: <https://link.aps.org/doi/10.1103/PhysRevB.94.235157>.
- [51] Dominic J. Williamson. “Fractal symmetries: Ungauging the cubic code”. In: *Phys. Rev. B* 94 (15 Oct. 2016), p. 155128. DOI: 10.1103/PhysRevB.94.155128. URL: <https://link.aps.org/doi/10.1103/PhysRevB.94.155128>.
- [52] Cenke Xu. “Gapless bosonic excitation without symmetry breaking: An algebraic spin liquid with soft gravitons”. In: *Phys. Rev. B* 74 (22 Dec. 2006), p. 224433. DOI: 10.1103/PhysRevB.74.224433. URL: <http://link.aps.org/doi/10.1103/PhysRevB.74.224433>.
- [53] Beni Yoshida. “Exotic topological order in fractal spin liquids”. In: *Phys. Rev. B* 88 (12 Sept. 2013), p. 125122. DOI: 10.1103/PhysRevB.88.125122. URL: <https://link.aps.org/doi/10.1103/PhysRevB.88.125122>.
- [54] Yizhi You et al. “Subsystem symmetry protected topological order”. In: *arXiv:1803.02369* (Mar. 2018). URL: <http://arxiv.org/abs/1803.02369>.
- [55] Yizhi You et al. “Symmetric Fracton Matter: Twisted and Enriched”. In: *arXiv:1805.09800* (May 2018). URL: <http://arxiv.org/abs/1805.09800>.

FOLIATED FRACTON ORDER IN THE MAJORANA CHECKERBOARD MODEL

7.1 Introduction

Gapped quantum systems, such as discrete gauge theories and fractional quantum Hall states, can reside in non-trivial phases in the absence of symmetry if they are ‘topological’ [41]. Such systems have low-energy effective descriptions given by topological quantum field theory (TQFT) [2, 23, 43]. However, a class of recently discovered three-dimensional gapped lattice models known as *fracton* models belong to non-trivial phases but defy such a characterization [3, 6, 9–11, 13, 18, 20, 22, 31–35, 37–39, 44, 45]. Their most salient, unifying properties are the presence of point-like fractional excitations with fundamentally constrained mobility and a degenerate ground space which grows exponentially with linear system size. These features preclude a TQFT description.

A particularly exotic class of fracton models are the fractal spin liquids, in which the operators that transport point-like fractional excitations are constrained to have certain fractal geometries [9, 10, 44]. This class includes so-called Type-II models such as the Haah code [10] whose fractional excitations are all fully immobile as individual particles. On the other hand, so-called Type-I models may contain mobile fractional excitations.¹ A large subclass of Type-I models exhibit three categories of point-like excitations: *fractons*, which are fully immobile, *lineons*, which can move along a line, and *planons*, which are mobile within a plane [3, 38]. The concept of *foliated fracton order* was introduced recently in an attempt to systematize the study of these models [25–27, 29, 30]. This notion builds on the observation that many of these models have a foliated structure of long-range entanglement, in the sense that layers of 2D topological orders can be disentangled from the bulk via local unitary operations, i.e. under entanglement renormalization group flow. The identification of this structure has shed light on the scaling of

¹It should be noted that the Type-I family includes certain fractal spin liquids with string operators [44] as well as models with fully mobile point excitations and loop excitations interacting non-trivially with fractonic excitations [5, 21]

ground space growth, the structure of fractional excitations in such models, and entanglement entropic signatures discussed previously in the literature [12, 19, 24, 29]. Furthermore, a more coarse notion of gapped phases of matter is motivated by this observation: in particular, a *foliated fracton phase* is defined as an equivalence class of Hamiltonians under adiabatic deformation augmented with the possible addition of layers of 2D topological orders.

It remains unclear to what extent this framework captures known Type-I fracton models. Partial progress has been made toward understanding the phase relations between these models [26, 27], but the picture is far from complete. Moreover, all examples of foliated fracton order that have been studied thus far are in models with bosonic degrees of freedom, and it is not yet clear whether the notion can be extended to fermionic models.

In this paper we address these questions by demonstrating that a prototypical example, the Majorana checkerboard model introduced in Ref. [38], exhibits foliated fracton order. In fact, we find that this model is actually a fermionic version of a previously known fractonic spin model called the semionic X-cube model, which was originally described via the coupled layers construction of Ref. [18]. As it has been shown that the semionic X-cube model has the same foliated fracton order as the X-cube model [27], the Majorana checkerboard model thus has the same order as well.

The paper's contents are as follows: in Sec. [7.2] we briefly review the Majorana checkerboard model. In Sec. [7.3] we describe a renormalization group (RG) transformation for the model which utilizes layers of toric code as resources of entanglement, hence establishing that it possesses foliated fracton order. In Sec. [7.4] we discuss entanglement entropic signatures of the foliated fracton order in the model, and in Sec. [7.5] we discuss the structure of quotient superselection sectors (QSS). In the following Sec. [7.6] we describe a mapping from the Majorana checkerboard model to a spin Hamiltonian (plus decoupled fermions), and in Sec. [7.7] a mapping from this stabilizer code spin Hamiltonian to the semionic X-cube model, hence establishing its equivalence to the X-cube model as a foliated fracton order. Finally we conclude with a discussion in Sec. [7.8].

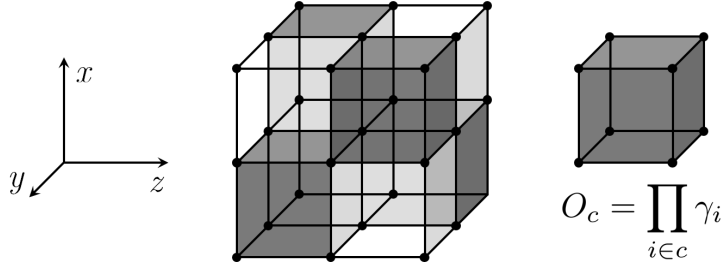


Figure 7.1: Bipartition of a cubic lattice into A (shaded) and B (unshaded) checkerboard sublattices. Majorana fermions are placed at the vertices of the lattice. The operator O_c acts on cubes c in the A sublattice and is defined as the product of the 8 Majoranas at the corners of cube c .

7.2 The Majorana Checkerboard Model

The Majorana checkerboard model was first introduced in Ref. [38] as a Majorana stabilizer code with one Majorana fermion on each vertex of a cubic lattice. The elementary cubes are bipartitioned into A - B checkerboard sublattices (as shown in Fig. [7.1]), and the Hamiltonian is given by

$$H = - \sum_{c \in A} O_c \quad (7.1)$$

where $O_c = \prod_{i \in c} \gamma_i$ is the product of the eight Majorana operators at the corners of cube c . The Hamiltonian terms mutually commute as they share either zero or two Majorana operators, and their energies can be simultaneously minimized. The model exhibits a ground state degeneracy (GSD) on a $2L_x \times 2L_y \times 2L_z$ cubic lattice under periodic boundary conditions which satisfies [38]

$$\log_2 \text{GSD} = 2L_x + 2L_y + 2L_z - 3. \quad (7.2)$$

Note that the number of logical qubits in the ground space is half that of the spin checkerboard model on the same lattice [39], as per the doubling lemma of Ref. [4].

As discussed in detail in Ref. [38], the model exhibits point-like excitations with a dimensional hierarchy of constrained mobility as depicted in Fig. [7.2]. Fractons, which are fundamentally immobile, are created at the corners of rectangular membrane operators. Lineons, which can move along a line only, are created at the endpoints of rigid string operators and can be thought of as composites of two fractons. Finally, planons, which are free to move within a

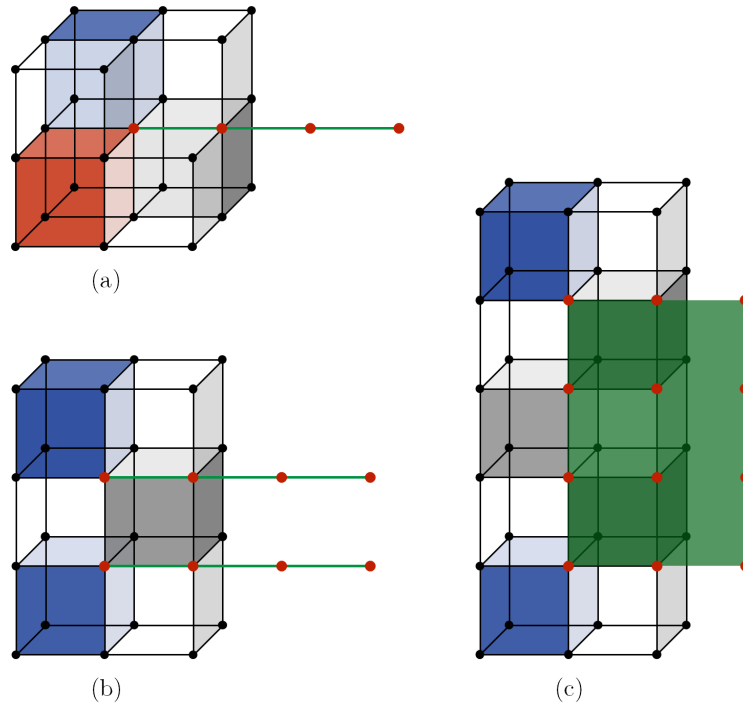


Figure 7.2: Point-like excitations in the Majorana checkerboard model. The colored cubes correspond to stabilizer terms which are violated by a given excitation. The operator which creates a given excitation is denoted by the product of the red Majoranas depicted. (a) A *lineon* created at the end of a rigid string operator (green). (b) A *planon* created at the end of a flexible string operator. (c) A *fracton* created at the corner of a rectangular membrane operator (green).

plane, can be thought of as composites of two lineons, or as composites of two fractons in their own right. In Sec. [7.5](#), we discuss how the notion of *quotient superselection sectors* can be used to analyze the fractional excitations of the model.

7.3 Entanglement renormalization

Entanglement renormalization group (RG) flow is a powerful tool to study the long-range entanglement structure of gapped systems [\[1, 7, 16, 36\]](#). The essential idea is to coarse-grain the underlying lattice via local unitary transformations on the ground space of a given model.^{[2](#)} In this section, we discuss an entanglement RG transformation for the Majorana checkerboard model, which utilizes copies of the toric code as 2D resource layers. The

²It should be noted that entanglement, or wavefunction, RG is related to but distinct from the Wilsonian RG (see references).

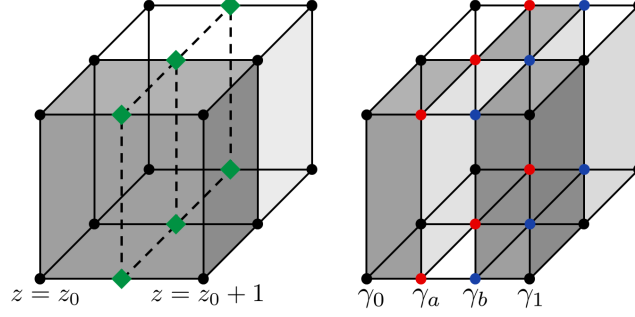


Figure 7.3: Degrees of freedom in (left) the original Majorana checkerboard model (black dots represent Majorana fermions) augmented with one copy of the toric code (green diamonds represent qubits), and (right) the enlarged Majorana checkerboard model, in which the red and blue dots represent added Majoranas along $z = a$ and $z = b$ and the black dots correspond to the original Majoranas.

existence of this transformation establishes the presence of foliated fracton order in the model. It can be compared to the analogous RG procedure for the X-cube model [30]. The transformation consists of a fermion parity-preserving local unitary map S between the Majorana checkerboard model on a $2L_x \times 2L_y \times 2L_z$ cubic lattice (described by Hamiltonian H_0), augmented with one copy of the toric code (H_{2D}), and the Majorana checkerboard model on a $2L_x \times 2L_y \times 2(L_z + 1)$ size lattice (H_1):

$$S(H_0 + H_{2D})S^\dagger \cong H_1. \quad (7.3)$$

Here the relation \cong denotes that the two Hamiltonians are equivalent as stabilizer codes and thus have identical ground spaces. We call the 2D topological layers the “resource layers” for the RG transformation. An equivalent transformation applies in the x and y directions as well.

In particular, suppose the toric code layer is inserted between layers z_0 and $z_0 + 1$ of the original lattice. Its degrees of freedom consist of qubits placed between the lattice sites of these two layers, as shown in Fig. 7.3. Its Hamiltonian is given as

$$H_{2D} = - \sum_{p \in A} \prod_{i \in p} Z_i - \sum_{p \in B} \prod_{i \in p} X_i. \quad (7.4)$$

Here, the 2D A - B checkerboard sublattices coincide with the 3D A - B checkerboard sublattices. The unitary S maps the combined Majorana and spin degrees of freedom to a pure Majorana system with two additional

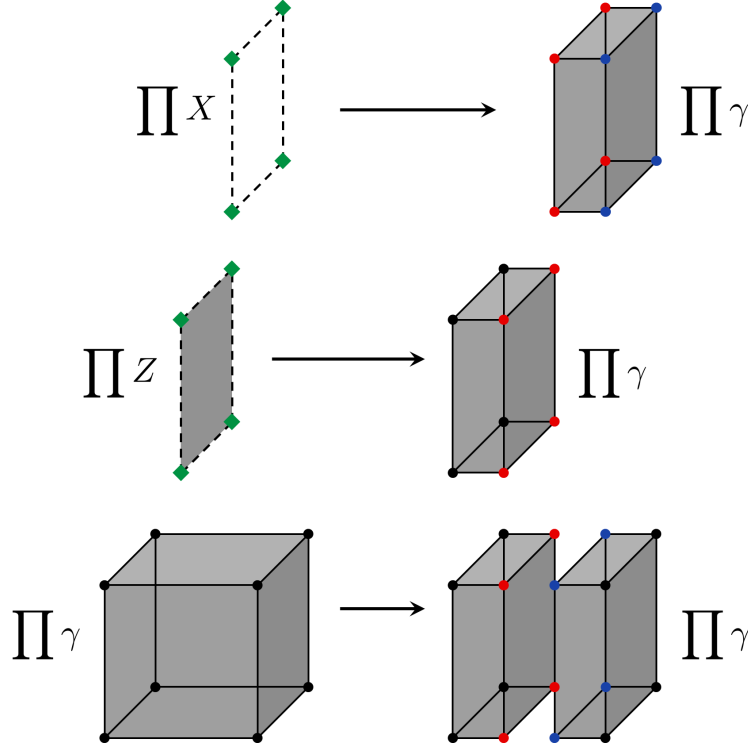


Figure 7.4: Mapping of Hamiltonian stabilizers under the local unitary transformation S .

Majoranas on the links between z_0 and $z_0 + 1$. The latter system constitutes an enlarged $2L_x \times 2L_y \times 2(L_z + 1)$ size cubic lattice of Majorana fermions. The two systems have identical Hilbert spaces. To see this, for each (x, y) coordinate, denote the Majorana at $z = z_0$ by γ_0 , the Majorana at $z = z_1$ by γ_1 , and the added Majoranas by γ_a and γ_b (as in Fig. 7.3). On the left hand side of Fig. 7.3, the combination of γ_0 , γ_1 , and the spin forms a four-dimensional Hilbert space whose operator algebra is generated by γ_0 , γ_1 , X , and Z . On the right hand side of Fig. 7.3, the combination of γ_0 , γ_a , γ_b , and γ_1 also forms a four-dimensional Hilbert space. The two sides can be mapped into each other under the following correspondence of operators:

$$X \rightarrow \gamma_a \gamma_b, \quad Z \rightarrow \gamma_0 \gamma_a, \quad \gamma_0 \rightarrow \gamma_0 \gamma_a \gamma_b, \quad \gamma_1 \rightarrow \gamma_1. \quad (7.5)$$

This mapping preserves the commutation relations of the local operator algebra at each (x, y) coordinate as well as the global fermionic parity, hence it describes a parity-preserving local unitary transformation. In fact, it is exactly the local unitary map S that is needed to implement the RG transformation. Fig. 7.4 illustrates the mapping of Hamiltonian stabilizers under this unitary.

Evidently, the resultant Hamiltonian generates the same stabilizer group as the enlarged Majorana checkerboard Hamiltonian. In other words, we find that the ground space of the original model tensored with the added toric code ground space is local unitarily equivalent to the ground space of the enlarged Majorana checkerboard model.

7.4 Entanglement Signatures

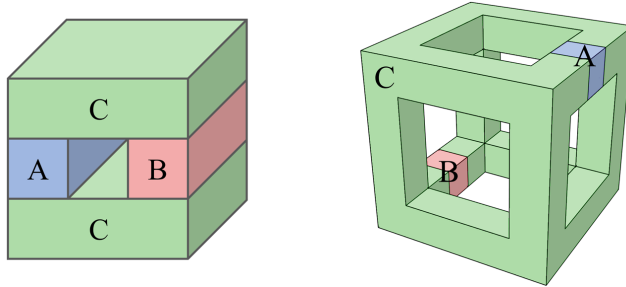


Figure 7.5: (Left) Solid torus and (right) wireframe entanglement entropy schemes.

In this section we briefly discuss entanglement entropic signatures of the foliated fracton order in the Majorana checkerboard model. The results suggest that the model may lie in the X-cube foliated fracton phase. Two entanglement schemes, solid torus and wireframe, among others, have proven useful in characterizing such orders [19, 24, 29]. In each scheme the quantity to be computed is the conditional mutual information

$$I(A; B|C) = S_{AC} + S_{BC} - S_C - S_{ABC} \quad (7.6)$$

where S_R refers to the entanglement entropy of region R . The geometries of the A , B , and C regions for the two schemes are depicted in Fig. 7.5. These schemes generalize the notion of topological entanglement entropy in two dimensions [14, 15].

A simple technique for computing the ground state entanglement entropy of generic Majorana stabilizer codes is discussed in Appendix 7.9. Applied to the Majorana checkerboard model, one finds that $I(A; B|C) = 2L + 1$ for the solid torus scheme where L is the length of the overall cubic region measured in twice the lattice constant, and $I(A; B|C) = 1$ for the wireframe scheme. For both schemes these results hold provided the overall cubic region is aligned with the axes of the cubic lattice. (In fact, the entanglement entropy of the

Majorana checkerboard model for a given region is exactly half of that for the equivalent region of the spin checkerboard model (29).

As discussed in Ref. (29), the solid torus scheme serves as a diagnostic of the underlying foliation structure, and indeed the result is consistent with the triple foliation structure composed of 2D toric code layers identified in the RG transformation of the section prior. On the other hand, the wireframe scheme is engineered such that the contributions from the foliating layers completely cancel, resulting in a constant value which characterizes the foliated fracton phase. In the case of the Majorana checkerboard model, the result $I(A; B|C) = 1$ is consistent with our finding that the model belongs to the X-cube foliated fracton phase, as discussed in Sections (7.6) and (7.7).

7.5 Quotient Superselection Sectors

In Ref. (27), the notion of *quotient superselection sectors* was introduced as a way to universally characterize fractional excitations in a given foliated fracton phase. A quotient superselection sector (QSS) is defined as an equivalence class of ordinary superselection sectors modulo the planon superselection sectors that come from the resource layers used in the RG procedure. In other words, two point-like fractional excitations belong to the same QSS if they are related to each other through local operations and the addition or removal of planon excitations that are unitarily equivalent to anyons in the resource layers. In the Majorana checkerboard model, all planons are transformed into toric code anyons under the inverse RG transformation of Sec. (7.3). To see this, note that the planon string operators are mapped into toric code string operators under the inverse RG transformation S^\dagger .

To describe the QSS of the Majorana checkerboard model, it is helpful to further partition the A checkerboard sublattice into 4 sublattices labelled R , G , B , and Y , as in Fig. (7.7). Excited states may be labelled according to which Hamiltonian stabilizers they violate (e.g. the error syndrome). Planon excitations violate two stabilizers corresponding to adjacent sites of either the R , G , B , or Y sublattice. For instance, the planon depicted in Fig. (7.2) violates two adjacent B sublattice Hamiltonian terms. Thus, the addition of planons on a given sublattice acts as a pair creation/annihilation, or hopping, operator for excitations of the stabilizers on that sublattice. As a result, we find that the QSS are characterized by the parity of the error syndrome on each

sublattice, and can be labelled accordingly. For instance, the lineon depicted in Fig. 7.2 belongs to the RB QSS because the state violates one R stabilizer and one B stabilizer. However, since a local fermionic excitation corresponds to a violation of one stabilizer of each of the R , G , B , and Y sublattices, the $RGBY$ QSS is in fact identified with the vacuum sector (and RB is identified with GY , and so forth). Therefore, a complete list of the 8 QSS is given in the first column of Table I.

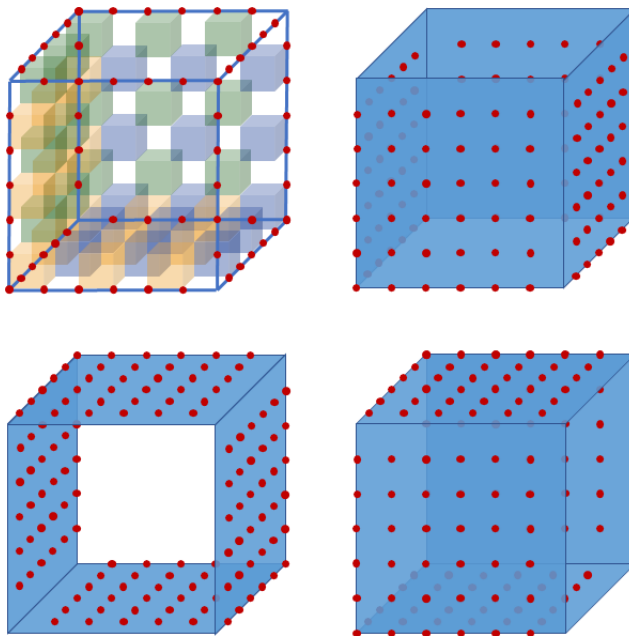


Figure 7.6: Interferometric operators in the Majorana checkerboard, which correspond to products of Majoranas over the red sites. $RGBY$ wireframe operator (top left), and BY , GB , and GY cylindrical membrane operators (top right, bottom left, bottom right).

In fact, in terms of the mobility of the excitations and their fusion rules, there is an exact correspondence between the QSS of the Majorana checkerboard model and those of the X-cube foliated fracton phase, given in the table. In particular, the three lineon sectors of the X-cube model correspond to the BY , GB , and GY lineon sectors of the Majorana checkerboard model, which likewise obey a triple fusion rule. On the other hand, the R , G (RB), B (RG), and Y (RY) fracton sectors correspond to the fractonic sectors f , $f \times \ell_x$, $f \times \ell_y$, and $f \times \ell_z$ of the X-cube model. Of course, there is an ambiguity as to which of the Majorana checkerboard fracton sectors is chosen to correspond to the f sector. In our case we have chosen the R sector. As we will see in the following sections, this correspondence must exist due to the

Majorana QSS	X-cube QSS	Majorana IOs	X-cube IOs
1	1	1	1
R	f	$RGBY$	F
BY	ℓ_x	BY	X
GB	ℓ_y	GB	Y
GY	ℓ_z	GY	Z
RBY	$\ell_x \times f$	RG	XF
RGB	$\ell_y \times f$	RY	YF
RGY	$\ell_z \times f$	RB	ZF

Table 7.1: Correspondences between the quotient superselection sectors (QSS) and interferometric operators (IOs) of the Majorana checkerboard and X-cube models.

local unitary equivalence of the model with a fermionic version of the semionic X-cube model, which is known to lie in the X-cube foliated fracton phase.

Ref. [27] also introduced the notion of *interferometric operators*, which are classes of unitary operators that detect the QSS content of a given region but are insensitive to the planon content of the region. The equivalence of the foliated fracton order in the Majorana checkerboard model with that of the X-cube model manifests not only as a correspondence between QSS, but furthermore as a correspondence between the interferometric operators of the two models. As discussed in Ref. [27], there are 8 classes of interferometric operators for the X-cube model, which include a wireframe operator F and three cylinder membrane operators X , Y , and Z (whose axes lie along the x , y , and z directions), and the composites XF , YF , and ZF . Each of these classes corresponds to a class of operators in the Majorana checkerboard model whose regions of support have the identical geometry (wireframe or cylinder with axis along the x , y , or z direction) and whose interferometric statistics agree exactly with the corresponding statistics of the X-cube model.

These interferometric operators can be written as products of Hamiltonian terms within a large cubic region. In particular, we will denote by $RGBY$ the product of all R , G , B , and Y cube terms within the large cubic region, by BY the product of all B and Y cube terms, and so on and so forth. In this notation, the wireframe operator corresponds to $RGBY$ whereas the 3 cylindrical membrane operators correspond to BY , GB , and GY respectively. These operators are illustrated in Fig. 7.6 and the full correspondence is given in the table above. As an example, the X membrane operator yields

a π phase when it acts on a state with quotient charge l_y , l_z , fl_y , or fl_z . Correspondingly, the BY membrane operator has a π statistic with the GB , GY , RGB , and RGY quotient sectors.

7.6 Mapping the Majorana Checkerboard Model to a Spin Model

7.6.1 Mapping to a spin model

In this section, we describe a local unitary transformation from the Majorana checkerboard model to a bosonic stabilizer code augmented with decoupled fermionic degrees of freedom. A mapping of the same spirit between the Majorana color code on the square-octagon lattice [4, 40] and the Wen plaquette model plus decoupled fermions on a square lattice [42] is briefly discussed in Appendix 7.10

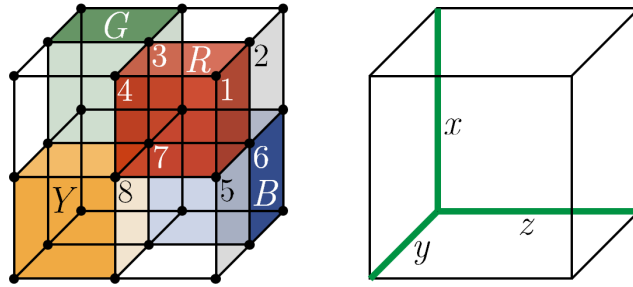


Figure 7.7: (Left) Unit cell of the Majorana checkerboard model with the Majorana degrees of freedom labelled from 1 to 8. The unit cell contains one cube of each of the R , G , B , and Y sublattices. (Right) Unit cell of the spin model containing a qubit degree of freedom on the green edges labelled x , y and z .

For our purposes we consider a unit cell of the Majorana checkerboard model as a $2 \times 2 \times 2$ cell of the underlying cubic lattice, which contains one cube of each of the R , G , B , and Y sublattices and 8 Majorana fermion degrees of freedom, labelled as shown in Fig. 7.7(a). The spin model we consider has one qubit degree of freedom on each edge of a cubic lattice, and thus has 3 qubits per unit cell, which are labelled according to the direction of the edge as in Fig. 7.7(b). This bosonic Hilbert space augmented with 2 Majorana fermions per unit cell, labelled γ_A and γ_B , is identical to the Hilbert space of the Majorana checkerboard model (each being 16-dimensional in a unit cell). We describe a parity-preserving local unitary transformation U^\dagger from the composite spin and Majorana Hilbert space to the pure Majorana Hilbert space via its action on the generators of the operator algebra. In particular, within each unit cell,

U^\dagger maps

$$X^x \rightarrow \gamma_1 \gamma_5, \quad Z^x \rightarrow \gamma_5 \gamma_6 \gamma_7 \gamma_8 \quad (7.7)$$

$$X^y \rightarrow \gamma_3 \gamma_4, \quad Z^y \rightarrow \gamma_2 \gamma_3 \gamma_6 \gamma_7 \quad (7.8)$$

$$X^z \rightarrow \gamma_6 \gamma_7, \quad Z^z \rightarrow \gamma_3 \gamma_4 \gamma_7 \gamma_8 \quad (7.9)$$

$$\gamma_A \rightarrow \gamma_2 \gamma_3 \gamma_4, \quad \gamma_B \rightarrow \gamma_1 \gamma_5 \gamma_6 \gamma_7 \gamma_8. \quad (7.10)$$

Note that the commutation relations of the algebra are preserved as well as the global fermionic parity.

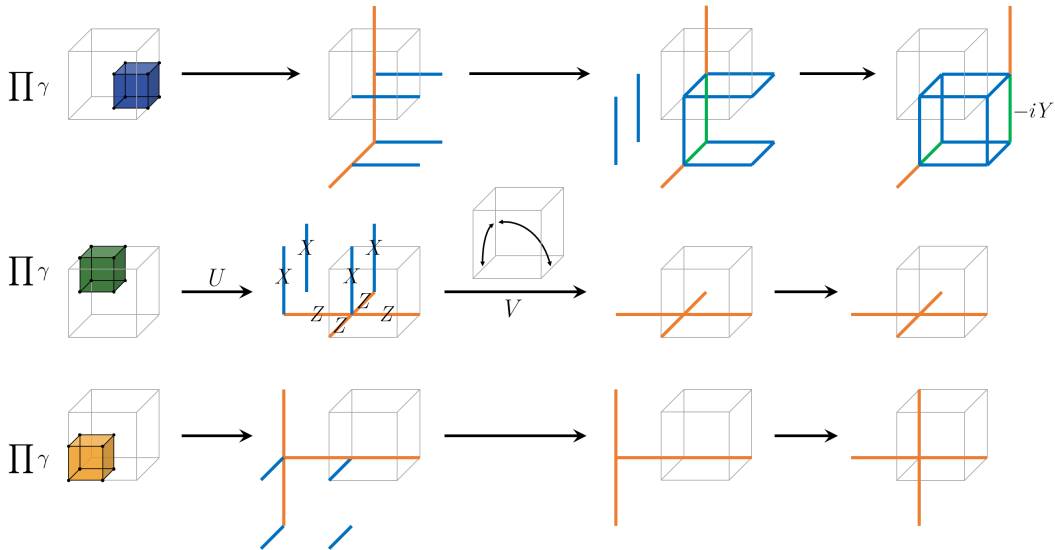


Figure 7.8: Mapping from the green, blue, and yellow sublattice cube terms of the Majorana checkerboard Hamiltonian to the stabilizer terms of the new spin Hamiltonian H_{spin}^0 . The spin stabilizers are tensor products of Pauli operators acting on the qubits on the colored edges: blue for Pauli X , green for $-iY = XZ$, and orange for Z . The first step is the unitary U , whereas the second step is the unitary V . A unit cell of V is depicted in the inset, where an arrow between two qubits represents the gate $H(CZ)H$. The final step of the transformation is simply a redefinition of the unit cell.

The G , B , and Y sublattice stabilizer terms of the Majorana checkerboard model are transformed under U to the bosonic stabilizers shown in Fig. 7.8, whereas the R sublattice terms map to the local parity check $\gamma_A \gamma_B$. Therefore U decouples the system into a bosonic stabilizer code and a trivial Majorana stabilizer code.

The bosonic code can be further massaged into a more amenable form. In

particular, consider the local unitary operator

$$V = H \left(\prod_i CZ_{i,y}^{i,z} CZ_{i+\hat{x},y}^{i,z} \right) H, \quad (7.11)$$

where the index i runs over all unit cells of the underlying cubic lattice, the operator $CZ_{j,\nu}^{i,\mu}$ is the controlled- Z operator acting on the μ -oriented edge of unit cell i and the ν -oriented edge of unit cell j , and H is a global Hadamard rotation. The unitary V is depicted graphically in Fig. 7.8. Under conjugation by $H(CZ)H$, the two-qubit Pauli operators transform as follows:

$$\begin{aligned} XI &\rightarrow XI, & IX &\rightarrow IX, \\ ZI &\rightarrow ZX, & IZ &\rightarrow XZ. \end{aligned} \quad (7.12)$$

Hence, the stabilizers of the qubit stabilizer code are transformed under V as shown in Fig. 7.8. Finally, it is convenient to redefine the unit cell by shifting the vertical edges by one unit to the right, thus yielding the stabilizer terms on the far right side of Fig. 7.8. Let us denote the Hamiltonian corresponding to these stabilizers as H_{spin}^0 . In summary, we find that

$$(UV)H(UV)^\dagger \cong H_{\text{spin}}^0 + H_f, \quad (7.13)$$

where H is the Majorana checkerboard Hamiltonian and $H_f = -i \sum \gamma_A \gamma_B$ stabilizes the ancillary Majorana degrees of freedom. Here the relation \cong denotes that the two Hamiltonians have identical ground spaces.

7.6.2 Analysis of the spin model

It is instructive to consider a Hamiltonian H_{spin} which is equivalent as a stabilizer code to H_{spin}^0 , but whose form is analogous to that of the X-cube model [39]. This representation will highlight the differences between this spin model and the X-cube model; as we will see in the next section, the model is in fact a stabilizer code realization of the *semionic* X-cube model [18]. In particular, we define

$$H_{\text{spin}} = - \sum_v (A_v^x + A_v^y + A_v^z) - \sum_c B_c^{\text{spin}} \quad (7.14)$$

where v runs over all vertices and c over all elementary cubes. Here A_v^μ are vertex terms and B_c^{spin} is a cube term, as depicted in Fig. 7.9. Note that B_c^{spin} can be decomposed as a product of Pauli Z operators followed by the product of Pauli X operators over the 12 edges of the cube c . The vertex

terms are identical to those of the X-cube model, whereas the cube term differs inasmuch as it contains factors of Z operators in addition to the product of X operators. Note that H_{spin} indeed generates the same stabilizer group as H_{spin}^0 : the additional vertex term is generated by the other two vertex terms and hence redundant, whereas B_c^{spin} is generated by the stabilizer in the top right corner of Fig. 7.8 along with two nearby vertex terms. The fractional excitations of the model can be organized into fracton and lineon sectors, which respectively correspond to violations of the cube and vertex terms.

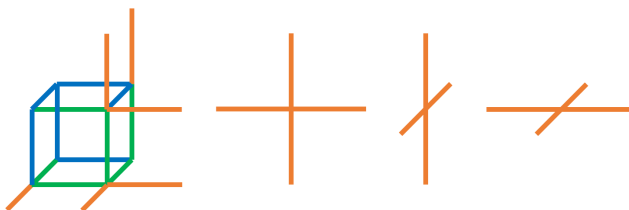


Figure 7.9: Cube (B_c^{spin} , left) and vertex (A_v^u , right) terms of the stabilizer code Hamiltonian H_{spin} . The stabilizers are tensor products of Pauli operators acting on the qubits on the colored edges: blue for Pauli X , green for $-iY = XZ$, and orange for Z .

The fracton sector of H_{spin} is identical to the fracton sector of the X-cube model. In particular, fractons are created at the corners of rectangular membrane operators, which are products of Pauli Z operators and hence commute with all vertex terms but anti-commute with the cube stabilizers at the corners of the membrane. Moreover, fracton dipoles, which are composites of adjacent fracton excitations, are planons, as in the X-cube model.

Conversely, the lineon sector of the model is subtly different from that of the X-cube model. As in the X-cube model, the product of all cube terms B_c^{spin} within a large cubic region yields a large operator with support near the wireframe of the large cubic region, as depicted in Fig. 7.10. (It is for this reason that we have chosen the particular form of B_c^{spin}). In fact, this wireframe operator corresponds to a physical process in which lineons travel along all of the edges of the cube, fusing and splitting at the corners according to triple fusion rules in which a lineon in each of the x , y , and z directions come together and annihilate into the vacuum. Thus, the rigid string operators which transport lineons in this model have the same form as the edges of the wireframe operator.

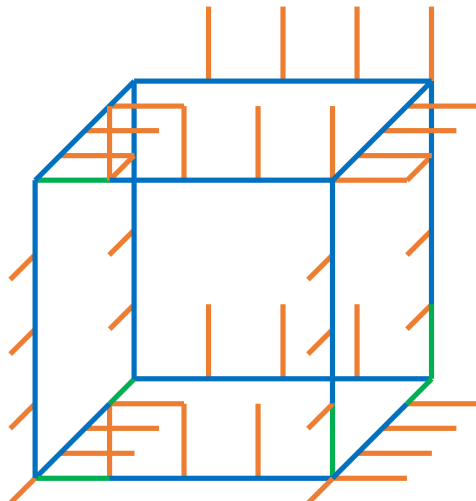


Figure 7.10: Wireframe operator of the spin model H_{spin} , which is equal to the product of cube terms B_c^{spin} within the large cubic region.

From this observation, it becomes clear by inspecting the wireframe operator in Fig. 7.10 that pairs of perpendicularly-moving lineons which are involved in a triple fusion rule have a mutual ‘semionic braiding’ statistic, in the sense that the rigid string operators which create these lineons *anti-commute* with each other. This property lies in stark contrast to the X-cube model where lineons satisfying a triple fusion rule always have trivial mutual ‘braiding’. In fact, this characteristic is the only essential difference between the X-cube model and the spin model here.

The structure of non-local excitations in H_{spin} is highly reminiscent of the discussion of quasiparticles in the *semionic X-cube model* of Ref. [18]. Indeed, it was shown that that model differs fundamentally from the X-cube model only insofar as lineons satisfying a triple fusion rule have mutually anti-commuting, as opposed to commuting, string operators. Therefore, we see that in fact the semionic X-cube model and our spin Hamiltonian have isomorphic structures of non-local excitations in terms of fusion and braiding. It is thus natural to expect that they are in fact equivalent models under local unitary transformation. We will see in the next section an explicit description of such a transformation.

7.7 Mapping the Spin Model to the Semionic X-Cube Model

In this section, we describe a local unitary transformation between the ground spaces of the semionic X-cube model and the stabilizer code spin model H_{spin}

obtained in the previous section.

7.7.1 Semionic X-cube model

The semionic X-cube model, as first discussed in Ref. [18] is obtained by coupling together three mutually perpendicular interpenetrating stacks of 2D double semion models [16] on the square-octagon lattice. For our purposes, it is more convenient to work with a microscopic realization of the double semion model whose degrees of freedom are qubits on a square lattice (see Appendix 7.11). The Hamiltonian takes the form

$$H_{\text{DS}} = - \sum_v A_v - \sum_p \tilde{B}_p \quad (7.15)$$

where v runs over all vertices of the square lattice and p runs over all plaquettes. The vertex term A_v is defined as the product of Pauli Z operators over the edges adjacent to v , whereas the plaquette term B_p is defined as follows:

$$\tilde{B}_p = B_p \prod_{v \in p} \frac{1 + A_v}{2}, \quad (7.16)$$

where v runs over the vertices surrounding plaquette p and B_p is a unitary operator which is depicted graphically in Fig. 7.11(a). Explicitly,

$$B_p = X_1 X_2 X_3 X_4 S_1 S_2 S_3 S_4 S_5 S_6 S_7 S_8 C Z_{14} C Z_{23} \quad (7.17)$$

where the qubits are numbered as in Fig. 7.11(a). Here CZ_{ij} denotes the controlled- Z gate between qubits i and j and $S = i^{\frac{1-Z}{2}} = \text{diag}(1, i)$.

To obtain the semionic X-cube model, we consider three stacks of double semion layers in the x , y , and z directions, whose edges coincide with the edges of a cubic lattice. The layers in the stack are oriented as illustrated in Fig. 7.11(b). Each edge thus lies at the intersection of two double semion layers, and contains two qubit degrees of freedom. The two qubits on each edge are subsequently subjected to a ZZ coupling. To be precise, we consider the following Hamiltonian:

$$H = \sum_L H_{\text{DS}}^L - J \sum_e Z_e^{\mu_1} Z_e^{\mu_2}, \quad (7.18)$$

where L indexes the layers of all three stacks, e runs over all edges of the cubic lattice, H_{DS}^L is the double semion Hamiltonian in layer L , and $Z_{\mu_1}^1$ and $Z_{\mu_2}^1$ are Pauli operators acting on the two qubits on edge e . In the strong coupling

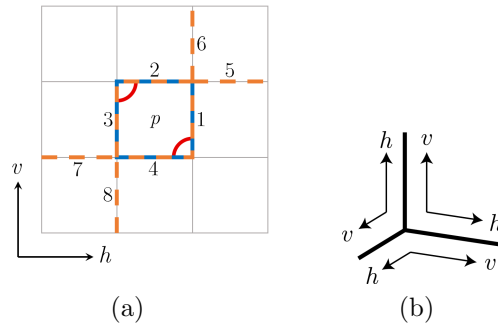


Figure 7.11: (a) The component B_p of the double semion model plaquette term \tilde{B}_p . Here, dashed orange edges represent the phase gate $S = i^{\frac{1-Z}{2}}$, blue-orange dashed edges represent the operator XS and the red arcs represents the controlled- Z gate between the two linked edges. The action of the CZ gates precede the action of the XS operators. (b) The orientations of the double semion layers in the three stacks prior to coupling.

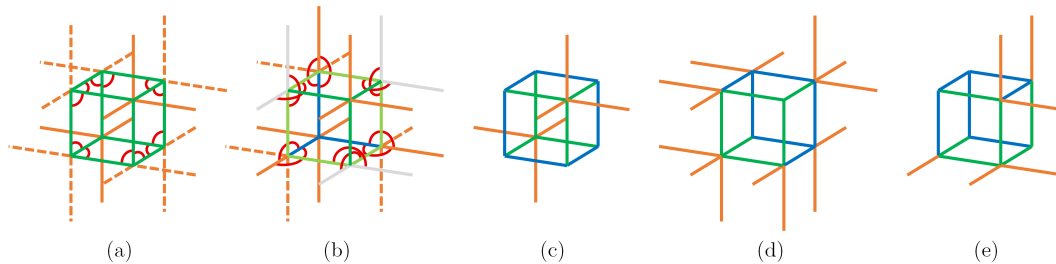


Figure 7.12: Graphical depictions of the operators (a) B_c^a , (b) B_c^b , (c) B_c^c , (d) B_c^d , and (e) B_c^e . Operators B_c^c , B_c^d , and B_c^e are simply tensor products of Pauli operators acting on the qubits on the colored edges: blue for Pauli X , green for $-iY = XZ$, and orange for Z . Conversely, B_c^a and B_c^b are each composed of two pieces: first, the tensor product of the controlled- Z two-qubit gates depicted as red arcs linking the two qubits. Second, the tensor product of single-qubit gates illustrated: blue, orange, and green for the Pauli operators, dashed orange for the phase gate S , and light green edges for the operator XSZ . The gray edges are simply placeholders.

limit $J \rightarrow \infty$, the two qubits on each edge effectively combine into one degree of freedom. The effective Hamiltonian to leading order in $1/J$ is given by

$$H_{\text{sem}} = - \sum_v (A_v^x + A_v^y + A_v^z) - \sum_c \tilde{B}_c^{\text{sem}}, \quad (7.19)$$

where the vertex terms A_v^μ are the same as those of the X-cube model and H_{spin} . In fact, note that this Hamiltonian is identical to H_{spin} apart from the cube term \tilde{B}_c^{sem} . The cube term \tilde{B}_c^{sem} can be written as

$$\tilde{B}_c^{\text{sem}} = B_c^a \prod_{v \in c} \prod_{\mu=x,y,z} \frac{1 + A_v^\mu}{2}. \quad (7.20)$$

Here the factors on the right-hand side project into the subspace satisfying the vertex constraints at the corners of the cube c . The unitary operator B_c^a is depicted graphically in Fig. 7.12(a). It can be decomposed as a unitary operator diagonal in the Pauli Z basis followed by a product of the Pauli X operators around the 12 edges of the cube c .

7.7.2 Mapping to H_{spin}

First, let us define a modified spin Hamiltonian \tilde{H}_{spin} which is identical to H_{spin} except for the replacement $B_c^{\text{spin}} \rightarrow \tilde{B}_c^{\text{spin}}$ where

$$\tilde{B}_c^{\text{spin}} = B_c^{\text{spin}} \prod_{v \in c} \prod_{\mu=x,y,z} \frac{1 + A_v^\mu}{2}. \quad (7.21)$$

Here v runs over the corners of the cube c . Since the additional factors on the right-hand side simply project into the subspace satisfying all of the vertex constraints around c , it is clear that \tilde{H}_{spin} has the same ground space as the stabilizer code H_{spin} . We will now describe a local unitary operator W such that $W^\dagger H_{\text{sem}} W = \tilde{H}_{\text{spin}}$, demonstrating that H_{spin} is in fact a stabilizer code realization of the semionic X-cube model.

The operator W can be decomposed as $W = W_2 W_1$ where W_1 and W_2 are both unitary. Consider as a unit cell the three edges depicted on the right-hand side of Fig. 7.7(b). The first factor W_1 is defined as

$$W_1 = \prod_i (CS_{i,y}^{i,x} \times CS_{i,z}^{i,y} \times CS_{i,x}^{i,z}) \quad (7.22)$$

where $CS_{j,\nu}^{i,\mu}$ is a controlled-phase gate between the μ -oriented edge in unit cell i and the ν -oriented edge in unit cell j , and the index i runs over all unit cells

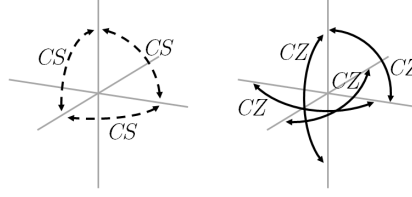


Figure 7.13: Illustration of a unit cell of the unitary operators W_1 (left) and W_2 (right). Here the dashed arrows represent controlled-phase gates between the two endpoints, whereas the solid arrows represent controlled- Z gates.

(see Fig. 7.13). In matrix form, $CS = \text{diag}(1, 1, 1, i)$. The action of CS by conjugation is given by

$$X_1 \rightarrow X_1 S_2 CZ_{12} \quad (7.23)$$

$$X_2 \rightarrow X_2 S_1 CZ_{12} \quad (7.24)$$

where CZ_{12} is the controlled- Z gate acting on qubits 1 and 2, and S_1 (X_1) and S_2 (X_2) are the S (X) operators acting on qubits 1 and 2 respectively. It hence follows that $W_1^\dagger B_c^a W_1 = B_c^b$, where B_c^b is the operator depicted in Fig. 7.12(b). Furthermore, since B_c^b is equivalent to B_c^c within the subspace satisfying the vertex constraints around c (see Fig. 7.14), it follows that

$$W_1^\dagger \tilde{B}_c^{\text{sem}} W_1 = B_c^c \prod_{v \in c} \prod_{\mu=x,y,z} \frac{1 + A_v^\mu}{2}. \quad (7.25)$$

Here B_c^c is the operator depicted in Fig. 7.12(c).



Figure 7.14: Operator relations that hold within the subspace satisfying the vertex constraints. These relations can be used to equate B_c^b and B_c^c within this subspace. Here, the red arcs represent controlled- Z gates, solid orange represents Z , dashed orange represents S , and dotted orange represents $S^\dagger = SZ$.

The second factor W_2 is defined as (see Fig. 7.13)

$$W_2 = \prod_i (CZ_{i+\hat{x},x}^{i,x} \times CZ_{i+\hat{y},y}^{i,y} \times CZ_{i+\hat{z},z}^{i,z} \times CZ_{i,z}^{i,x}) \quad (7.26)$$

where $CZ_{j,\nu}^{i,\mu}$ is a controlled- Z gate between the μ -oriented edge in unit cell i and the ν -oriented edge in unit cell j , and the index i runs over all unit cells.

Since CZ acts by conjugation as

$$\begin{aligned} XI &\rightarrow XZ, & IX &\rightarrow ZX, \\ ZI &\rightarrow ZI, & IZ &\rightarrow IZ. \end{aligned} \tag{7.27}$$

it follows that $W_2^\dagger B_c^d W_2 = B_c^d$, where B_c^d is depicted graphically in Fig. 7.12(d). Finally, this yields the result

$$W^\dagger \tilde{B}_c^{\text{sem}} W = B_c^e \prod_{v \in c} \prod_{\mu=x,y,z} \frac{1 + A_v^\mu}{2} \tag{7.28}$$

due to the equivalence of B_c^d and B_c^e within the projected subspace. The unitary B_c^e is depicted in Fig. 7.12(e). Since $B_c^e = B_c^{\text{spin}}$, it thus follows that $W^\dagger \tilde{B}_c^{\text{sem}} W = \tilde{B}_c^{\text{spin}}$. Since W is diagonal in the Z basis, it leaves the vertex terms unaffected, and hence altogether $W^\dagger H_{\text{sem}} W = \tilde{H}_{\text{spin}}$.

We have therefore verified the intuitive correspondence between the Majorana checkerboard model and the semionic X-cube model (plus decoupled fermionic modes) by explicitly describing a local unitary transformation between the two models. As an intermediate step we have demonstrated how to decouple the fermionic degrees of freedom of the Majorana checkerboard model from a hidden bosonic stabilizer code representation of the semionic X-cube model. Indeed, in light of the exact correspondence between the structure of non-local excitations of H_{spin} and H_{sem} , the existence of such a local unitary equivalence is to be expected.

In a previous work, it was demonstrated that the semionic X-cube model lies in the same foliated fracton phase as the X-cube model [27]. Indeed, the anti-commutation of string operators which satisfy a triple fusion rule in the semionic X-cube model can be completely cancelled by the addition of three mutually perpendicular stacks of 2D double semion layers. Consequently, the result of the current work implies that the Majorana checkerboard model too lies in the X-cube foliated fracton phase.

7.8 Discussion

To summarize, we have shown in this paper that the Majorana checkerboard model, first introduced in Ref. [38], has foliated fracton order as defined in Ref. [29, 30]. That is, 2D topological states are extracted from the bulk when renormalization group transformations are applied to the ground state wavefunction to reduce the total system size. Moreover, we show

through explicit mapping that the Majorana checkerboard model has the same foliated fracton order as the X-cube model. This equivalence may not be straightforward to see given the many differences between the two models: The Majorana checkerboard model is fermionic while the X-cube model is bosonic; moreover, the Majorana checkerboard model has a ‘dimensional hierarchy’ of quasiparticle fusion while this does not seem to be the case in the X-cube model. By calculating the universal properties of foliated fracton phases as discussed in Ref. [25–27, 29], we see that the two models could actually be in the same foliated fracton phase, and the explicit mapping discussed in section 7.6 and section 7.7 further confirms this result.

So far we have found, using the same procedure as in this paper, phase relations between several type I fracton models including the X-cube model, the checkerboard model (as two copies of X-cube) [26], the semionic X-cube model [27] and the Majorana checkerboard model. These models all belong to the same foliated fracton phase. On the other hand, other types of foliated fracton phase can also exist. We have found that some Type-I fracton models have foliated fracton order distinct from that of the X-cube model. These results will be presented in a separate work [28].

7.9 Appendix: Entanglement entropy in Majorana codes

In this appendix, we show that the entanglement entropy of a subregion of a Majorana code is equal to half that of the corresponding ‘doubled’ CSS code. This self-dual CSS code is constructed by replacing each Majorana fermion with a qubit, and each Majorana stabilizer by one X type qubit stabilizer and one Z type qubit stabilizer [4]. For instance, the spin checkerboard model arises as the ‘double’ of the Majorana checkerboard model. The method of calculation straightforwardly generalizes that of qubit stabilizer codes [8].

Consider a Majorana code with stabilizer group S generated by n independent commuting Majorana stabilizer operators g_1, \dots, g_n on a Hilbert space of $2n$ Majorana modes. The stabilizers are of the form $g_i = \prod_{j \in S_i} i^{1/2} \gamma_j$, where S_i labels the support of g_i . To calculate the ground state entanglement entropy of a subregion A , the ground state density matrix $\rho = |\psi\rangle\langle\psi|$ may be written as

$$\rho = \frac{1}{2^{2n}} \sum_{g \in S} g. \quad (7.29)$$

The reduced density matrix $\rho_A = \text{Tr}_{\bar{A}} \rho$ can be evaluated by taking the partial

trace over individual stabilizer group elements.

If the support of g intersects with \bar{A} , then g may be expressed as $g = \gamma_1 \dots \gamma_m \otimes h$ where h has support exclusively in A . Since the first factor has vanishing trace, it follows that $\text{Tr}_{\bar{A}} g = 0$. Thus

$$\rho_A = \frac{1}{2^{2n}} \sum_{g \in S} \text{Tr}_{\bar{A}} g = \frac{1}{2^{2n_A}} \sum_{g \in S_A} g \quad (7.30)$$

where n_A is the number of Majorana modes in A and S_A is the stabilizer subgroup generated by elements g with support exclusively in A . This operator is proportional to the projector on to the subspace stabilized by S_A , which has dimension $2^{(n_A - |S_A|)}$ where $|S_A|$ is the number of independent generators of S_A . The entanglement entropy is therefore

$$E_A = -\text{Tr} \rho_A \log \rho_A = n_A - |S_A|. \quad (7.31)$$

The corresponding ‘doubled’ CSS code has $2n$ qubits, n independent X type stabilizer generators, and n independent Z type generators. The entanglement entropy of region A is [8]

$$E_A^{\text{CSS}} = 2n_A - |S_A^{\text{CSS}}| = 2n_A - 2|S_A| = 2E_A. \quad (7.32)$$

7.10 Appendix: Mapping the Majorana color code to the toric code

In this appendix, we briefly discuss a unitary mapping which decouples the fermionic modes of the Majorana color code on the square-octagon lattice [4, 17, 40] from its underlying toric code topological order.

In this model, one Majorana fermion lies at each vertex of the square-octagon lattice (Fig. 7.15). The Hamiltonian has the form

$$H = - \sum_p O_p \quad (7.33)$$

where p runs over all plaquettes, square or octagonal, and O_p takes the form

$$O_p \equiv \prod_{v \in p} i^{1/2} \gamma_v. \quad (7.34)$$

Since the square-octagon lattice is three-colorable, the plaquette terms are mutually commuting and unfrustrated.

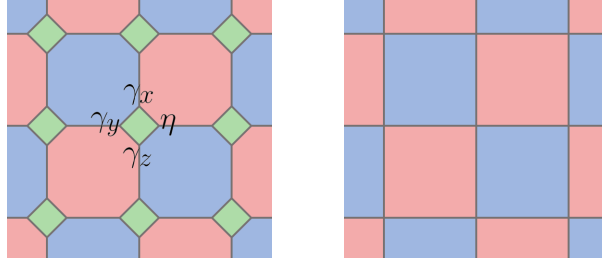


Figure 7.15: (Left) Square-octagon lattice of the Majorana color code, containing one Majorana fermion at each vertex. The 4 Majoranas around each green plaquette are labelled η , γ_x , γ_y and γ_z . (Right) Square lattice of the Wen plaquette model, containing a qubit and two ancillary Majoranas γ_A and γ_B at each vertex.

To decouple the fermionic modes, we identify the 4 Majorana Hilbert space around each green square plaquette with the Hilbert space of one qubit and 2 Majoranas. Denote the 4 Majoranas by η , γ_x , γ_y , and γ_z (as shown in Fig. 7.16), and the Pauli operators and 2 Majoranas of the latter space by X , Z , γ_A , and γ_B . We can unitarily map between these two Hilbert spaces according to the following transformation of operators:

$$\eta \rightarrow \gamma_A, \quad \gamma_x \rightarrow \gamma_B X, \quad \gamma_y \rightarrow \gamma_B Y, \quad \gamma_z \rightarrow \gamma_B Z \quad (7.35)$$

where $Y = iXZ$ is the Pauli operator. This local mapping preserves the commutation relations and the fermionic parity, hence it represents a parity-preserving local unitary operator.

The plaquette terms of the Majorana color code Hamiltonian transform according to Fig. 7.16. In particular, the green square terms $-\eta\gamma_x\gamma_y\gamma_z$ are mapped into stabilizer generators for the ancillary fermionic modes, $-i\gamma_A\gamma_B$, whereas the red and blue octagon terms are mapped into stabilizer generators $X_i Z_{i+\hat{x}} X_{i+\hat{x}+\hat{y}} Z_{i+\hat{y}}$ of the Wen plaquette model [42] (modulo two nearby fermionic stabilizers), which is local unitarily equivalent to the toric code.

7.11 Appendix: Double semion model on a square lattice

In this appendix, we briefly discuss a local unitary transformation that allows one to write the double semion model, originally defined on the honeycomb lattice [16], as a model of qubits on the edges of a square lattice.

The double semion model contains one qubit on each edge of the honeycomb

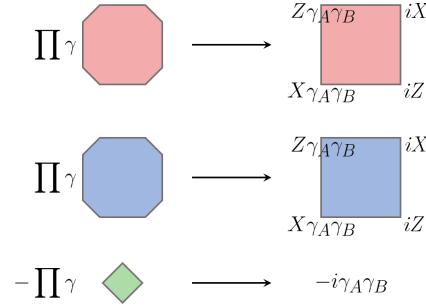


Figure 7.16: Transformation of plaquette stabilizers under the unitary mapping defined by (7.35).

lattice, and has Hamiltonian

$$H = - \sum_v A_v - \sum_p \tilde{B}_h \quad (7.36)$$

where v indexes vertices and h indexes hexagonal plaquettes. The vertex constraint is $A_v = Z_1 Z_2 Z_3$ acting on the 3 adjacent edges, and the hexagon term is

$$\begin{aligned} \tilde{B}_h &= B_h \prod_{v \in p} \frac{1 + A_v}{2}, \\ B_h &= \prod_{e \in h} X_e \prod_{l \in h} S_l. \end{aligned} \quad (7.37)$$

Here e runs over the 6 edges of hexagon h , whereas l runs over the 6 legs external to h , as shown in Fig. 7.17(a). $S = i^{\frac{1-Z}{2}}$ is the phase gate.

It is possible to disentangle the qubits lying on the short edges of the honeycomb lattice from the rest of the system, leaving behind a square lattice. In particular, the unitary operator U accomplishes this task, which is a translation-invariant array of CX gates as shown in Fig. 7.17(b). To be precise,

$$U^\dagger H U \cong H' + H_0 \quad (7.38)$$

where H_0 stabilizes the ancillary qubits and H' is the double semion Hamiltonian on the square lattice:

$$H' = - \sum_v A_v - \sum_p \tilde{B}_p. \quad (7.39)$$

Here $A_v = Z_1 Z_2 Z_3 Z_4$, acting on the 4 adjacent edges, and

$$\tilde{B}_p = B_p \prod_{v \in p} \frac{1 + A_v}{2}, \quad (7.40)$$

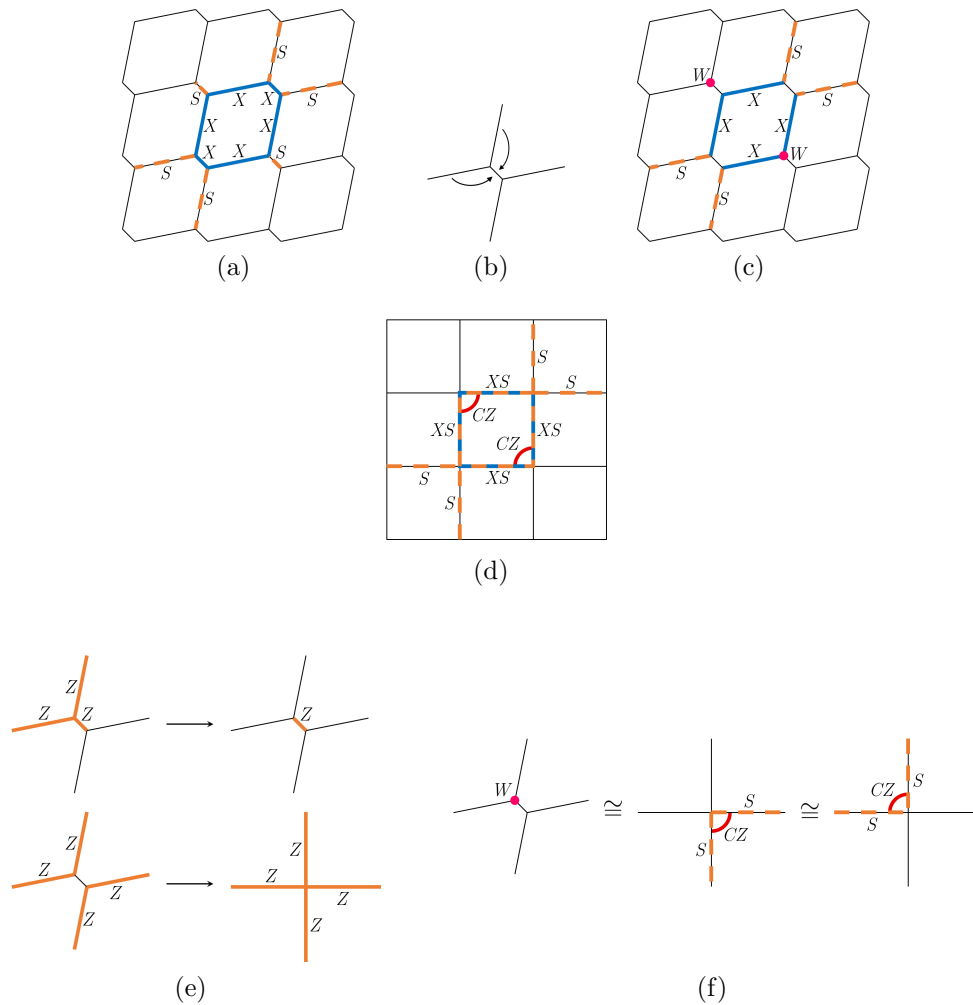


Figure 7.17: (a) The component B_h of the double semion plaquette term on the honeycomb lattice. (b) A unit cell of the local unitary U which disentangles the short edge qubits from the rest of the system. The arrow represents the CX gate with control at the tail and target at the head. (c) The image operator $B'_h = U^\dagger B_h U$ (here, the W gates precede the X gates, and act on the 3 edges adjacent to the magenta vertices). (d) The component B_p of the plaquette term on the square lattice (here, the CZ gates precede the XS gates). (e) Mapping of vertex constraints under conjugation by U . The top constraints become terms in the ancillary Hamiltonian H_0 , whereas the bottom constraints (product of two vertex constraints) become the vertex terms of the square lattice Hamiltonian. (f) Operator relations which hold within the subspace satisfying the vertex (and ancillary) constraints.

where B_p is depicted graphically in Fig. 7.17(d). The relation \cong indicates that the two sides have identical ground spaces.

To see this, note that $S_3 \rightarrow W_{123}$ under conjugation by $CX_{13}CX_{23}$, where we have defined $W_{123} = i^{\frac{1-Z_1Z_2Z_3}{2}}$, and thus B_h is mapped to the operator B'_h shown in Fig. 7.17(c). Moreover, U maps the original vertex constraints according to Fig. 7.17(e), yielding the vertex terms on the square lattice as well as the ancillary terms comprising H_0 . Finally, B'_h is equivalent to B_p in the subspace satisfying the vertex constraints, due to the relations shown in Fig. 7.17(f).

References

- [1] Miguel Aguado and Guifré Vidal. “Entanglement Renormalization and Topological Order”. In: *Phys. Rev. Lett.* 100 (7 Feb. 2008), p. 070404. DOI: [10.1103/PhysRevLett.100.070404](https://doi.org/10.1103/PhysRevLett.100.070404). URL: <https://link.aps.org/doi/10.1103/PhysRevLett.100.070404>.
- [2] Michael F. Atiyah. “Topological quantum field theory”. en. In: *Publications Mathématiques de l’IHÉS* 68 (1988), pp. 175–186. URL: http://www.numdam.org/item/PMIHES_1988__68__175_0.
- [3] S. Bravyi, B. Leemhuis, and B.M. Terhal. “Topological order in an exactly solvable 3D spin model”. In: *Annals of Physics* 326 (Apr. 2011), pp. 839–866. DOI: [10.1016/j.aop.2010.11.002](https://doi.org/10.1016/j.aop.2010.11.002).
- [4] Sergey Bravyi, Barbara M Terhal, and Bernhard Leemhuis. “Majorana fermion codes”. In: *New Journal of Physics* 12.8 (2010), p. 083039. URL: <http://stacks.iop.org/1367-2630/12/i=8/a=083039>.
- [5] Daniel Bulmash and Maissam Barkeshli. “Gauging fractons: immobile non-Abelian quasiparticles, fractals, and position-dependent degeneracies”. In: *arXiv e-prints*, arXiv:1905.05771 (May 2019).
- [6] Claudio Chamon. “Quantum Glassiness in Strongly Correlated Clean Systems: An Example of Topological Overprotection”. In: *Phys. Rev. Lett.* 94 (4 Jan. 2005), p. 040402. DOI: [10.1103/PhysRevLett.94.040402](https://doi.org/10.1103/PhysRevLett.94.040402). URL: <https://link.aps.org/doi/10.1103/PhysRevLett.94.040402>.
- [7] Xie Chen, Zheng-Cheng Gu, and Xiao-Gang Wen. “Local unitary transformation, long-range quantum entanglement, wave function renormalization, and topological order”. In: *Phys. Rev. B* 82 (15 Oct. 2010), p. 155138. DOI: [10.1103/PhysRevB.82.155138](https://doi.org/10.1103/PhysRevB.82.155138). URL: <https://link.aps.org/doi/10.1103/PhysRevB.82.155138>.

- [8] David Fattal et al. “Entanglement in the stabilizer formalism”. In: *arXiv:quant-ph/0406168* (June 2004). URL: <http://arxiv.org/abs/quant-ph/0406168>.
- [9] Jeongwan Haah. “Bifurcation in entanglement renormalization group flow of a gapped spin model”. In: *Phys. Rev. B* 89 (7 Feb. 2014), p. 075119. DOI: [10.1103/PhysRevB.89.075119](https://doi.org/10.1103/PhysRevB.89.075119). URL: <https://link.aps.org/doi/10.1103/PhysRevB.89.075119>.
- [10] Jeongwan Haah. “Local stabilizer codes in three dimensions without string logical operators”. In: *Phys. Rev. A* 83 (4 Apr. 2011), p. 042330. DOI: [10.1103/PhysRevA.83.042330](https://doi.org/10.1103/PhysRevA.83.042330). URL: <https://link.aps.org/doi/10.1103/PhysRevA.83.042330>.
- [11] Gábor B. Halász, Timothy H. Hsieh, and Leon Balents. “Fracton Topological Phases from Strongly Coupled Spin Chains”. In: *Phys. Rev. Lett.* 119 (25 Dec. 2017), p. 257202. DOI: [10.1103/PhysRevLett.119.257202](https://doi.org/10.1103/PhysRevLett.119.257202). URL: <https://link.aps.org/doi/10.1103/PhysRevLett.119.257202>.
- [12] Huan He et al. “Entanglement entropy from tensor network states for stabilizer codes”. In: *Phys. Rev. B* 97 (12 Mar. 2018), p. 125102. DOI: [10.1103/PhysRevB.97.125102](https://doi.org/10.1103/PhysRevB.97.125102). URL: <https://link.aps.org/doi/10.1103/PhysRevB.97.125102>.
- [13] Timothy H. Hsieh and Gábor B. Halász. “Fractons from partons”. In: *Phys. Rev. B* 96 (16 Oct. 2017), p. 165105. DOI: [10.1103/PhysRevB.96.165105](https://doi.org/10.1103/PhysRevB.96.165105). URL: <https://link.aps.org/doi/10.1103/PhysRevB.96.165105>.
- [14] Alexei Kitaev and John Preskill. “Topological entanglement entropy”. In: *Phys. Rev. Lett.* 96 (2006), p. 110404. DOI: [10.1103/PhysRevLett.96.110404](https://doi.org/10.1103/PhysRevLett.96.110404).
- [15] M. Levin and X.-G. Wen. “Detecting Topological Order in a Ground State Wave Function”. In: *Phys. Rev. Lett.* 96.11, 110405 (Mar. 2006), p. 110405. DOI: [10.1103/PhysRevLett.96.110405](https://doi.org/10.1103/PhysRevLett.96.110405).
- [16] Michael A. Levin and Xiao-Gang Wen. “String-net condensation: A physical mechanism for topological phases”. In: *Phys. Rev. B* 71 (4 Jan. 2005), p. 045110. DOI: [10.1103/PhysRevB.71.045110](https://doi.org/10.1103/PhysRevB.71.045110). URL: <https://link.aps.org/doi/10.1103/PhysRevB.71.045110>.
- [17] Daniel Litinski and Felix von Oppen. “Quantum computing with Majorana fermion codes”. In: *Phys. Rev. B* 97 (20 May 2018), p. 205404. DOI: [10.1103/PhysRevB.97.205404](https://doi.org/10.1103/PhysRevB.97.205404). URL: <https://link.aps.org/doi/10.1103/PhysRevB.97.205404>.

- [18] Han Ma et al. “Fracton topological order via coupled layers”. In: *Phys. Rev. B* 95 (24 June 2017), p. 245126. DOI: [10.1103/PhysRevB.95.245126](https://doi.org/10.1103/PhysRevB.95.245126). URL: <https://link.aps.org/doi/10.1103/PhysRevB.95.245126>.
- [19] Han Ma et al. “Topological entanglement entropy of fracton stabilizer codes”. In: *Phys. Rev. B* 97 (12 Mar. 2018), p. 125101. DOI: [10.1103/PhysRevB.97.125101](https://doi.org/10.1103/PhysRevB.97.125101). URL: <https://link.aps.org/doi/10.1103/PhysRevB.97.125101>.
- [20] Rahul M. Nandkishore and Michael Hermele. “Fractons”. In: *Annual Review of Condensed Matter Physics* 10.1 (2019), pp. 295–313. DOI: [10.1146/annurev-conmatphys-031218-013604](https://doi.org/10.1146/annurev-conmatphys-031218-013604), eprint: <https://doi.org/10.1146/annurev-conmatphys-031218-013604>. URL: <https://doi.org/10.1146/annurev-conmatphys-031218-013604>.
- [21] Abhinav Prem and Dominic J. Williamson. “Gauging permutation symmetries as a route to non-Abelian fractons”. In: *arXiv e-prints*, arXiv:1905.06309 (May 2019).
- [22] Abhinav Prem et al. “Cage-Net Fracton Models”. In: *Phys. Rev. X* 9 (2 Apr. 2019), p. 021010. DOI: [10.1103/PhysRevX.9.021010](https://doi.org/10.1103/PhysRevX.9.021010). URL: <https://link.aps.org/doi/10.1103/PhysRevX.9.021010>.
- [23] Albert S. Schwarz. “Topological quantum field theories”. In: (2000). arXiv: [hep-th/0011260 \[hep-th\]](https://arxiv.org/abs/hep-th/0011260).
- [24] Bowen Shi and Yuan-Ming Lu. “Deciphering the nonlocal entanglement entropy of fracton topological orders”. In: *Phys. Rev. B* 97 (14 Apr. 2018), p. 144106. DOI: [10.1103/PhysRevB.97.144106](https://doi.org/10.1103/PhysRevB.97.144106). URL: <https://link.aps.org/doi/10.1103/PhysRevB.97.144106>.
- [25] Wilbur Shirley, Kevin Slagle, and Xie Chen. “Foliated fracton order from gauging subsystem symmetries”. In: *SciPost Phys.* 6.4 (2019), p. 041. DOI: [10.21468/SciPostPhys.6.4.041](https://doi.org/10.21468/SciPostPhys.6.4.041).
- [26] Wilbur Shirley, Kevin Slagle, and Xie Chen. “Foliated fracton order in the checkerboard model”. In: *Phys. Rev. B* 99 (11 Mar. 2019), p. 115123. DOI: [10.1103/PhysRevB.99.115123](https://doi.org/10.1103/PhysRevB.99.115123). URL: <https://link.aps.org/doi/10.1103/PhysRevB.99.115123>.
- [27] Wilbur Shirley, Kevin Slagle, and Xie Chen. “Fractional excitations in foliated fracton phases”. In: *arXiv e-prints*, arXiv:1806.08625 (June 2018).
- [28] Wilbur Shirley, Kevin Slagle, and Xie Chen. “Twisted foliated fracton phases”. In: *arXiv e-prints*, arXiv:1907.09048 (July 2019).

- [29] Wilbur Shirley, Kevin Slagle, and Xie Chen. “Universal entanglement signatures of foliated fracton phases”. In: *SciPost Phys.* 6 (1 2019), p. 15. DOI: [10.21468/SciPostPhys.6.1.015](https://doi.org/10.21468/SciPostPhys.6.1.015). URL: <https://scipost.org/10.21468/SciPostPhys.6.1.015>.
- [30] Wilbur Shirley et al. “Fracton Models on General Three-Dimensional Manifolds”. In: *Phys. Rev.* X8.3 (2018), p. 031051. DOI: [10.1103/PhysRevX.8.031051](https://doi.org/10.1103/PhysRevX.8.031051). arXiv: [1712.05892](https://arxiv.org/abs/1712.05892) [cond-mat.str-el].
- [31] Kevin Slagle, David Aasen, and Dominic Williamson. “Foliated Field Theory and String-Membrane-Net Condensation Picture of Fracton Order”. In: *SciPost Phys.* 6 (4 2019), p. 43. DOI: [10.21468/SciPostPhys.6.4.043](https://doi.org/10.21468/SciPostPhys.6.4.043). URL: <https://scipost.org/10.21468/SciPostPhys.6.4.043>.
- [32] Kevin Slagle and Yong Baek Kim. “Fracton topological order from nearest-neighbor two-spin interactions and dualities”. In: *Phys. Rev. B* 96 (16 Oct. 2017), p. 165106. DOI: [10.1103/PhysRevB.96.165106](https://doi.org/10.1103/PhysRevB.96.165106). URL: <https://link.aps.org/doi/10.1103/PhysRevB.96.165106>.
- [33] Kevin Slagle and Yong Baek Kim. “X-cube model on generic lattices: Fracton phases and geometric order”. In: *Phys. Rev. B* 97 (16 Apr. 2018), p. 165106. DOI: [10.1103/PhysRevB.97.165106](https://doi.org/10.1103/PhysRevB.97.165106). URL: <https://link.aps.org/doi/10.1103/PhysRevB.97.165106>.
- [34] Hao Song et al. “Twisted fracton models in three dimensions”. In: *Phys. Rev. B* 99 (15 Apr. 2019), p. 155118. DOI: [10.1103/PhysRevB.99.155118](https://doi.org/10.1103/PhysRevB.99.155118). URL: <https://link.aps.org/doi/10.1103/PhysRevB.99.155118>.
- [35] Kevin T. Tian and Zhenghan Wang. “Generalized Haah Codes and Fracton Models”. In: *arXiv e-prints*, arXiv:1902.04543 (Feb. 2019), arXiv:1902.04543. arXiv: [1902.04543](https://arxiv.org/abs/1902.04543) [quant-ph].
- [36] G. Vidal. “Entanglement Renormalization”. In: *Phys. Rev. Lett.* 99.22 (2007), p. 220405. DOI: [10.1103/PhysRevLett.99.220405](https://doi.org/10.1103/PhysRevLett.99.220405).
- [37] Sagar Vijay and Liang Fu. “A Generalization of Non-Abelian Anyons in Three Dimensions”. In: *arXiv:1706.07070* (June 2017). URL: <http://arxiv.org/abs/1706.07070>.
- [38] Sagar Vijay, Jeongwan Haah, and Liang Fu. “A new kind of topological quantum order: A dimensional hierarchy of quasiparticles built from stationary excitations”. In: *Phys. Rev. B* 92 (23 Dec. 2015), p. 235136. DOI: [10.1103/PhysRevB.92.235136](https://doi.org/10.1103/PhysRevB.92.235136). URL: <http://link.aps.org/doi/10.1103/PhysRevB.92.235136>.
- [39] Sagar Vijay, Jeongwan Haah, and Liang Fu. “Fracton topological order, generalized lattice gauge theory, and duality”. In: *Phys. Rev. B* 94 (23 Dec. 2016), p. 235157. DOI: [10.1103/PhysRevB.94.235157](https://doi.org/10.1103/PhysRevB.94.235157). URL: <https://link.aps.org/doi/10.1103/PhysRevB.94.235157>.

- [40] Sagar Vijay, Timothy H. Hsieh, and Liang Fu. “Majorana Fermion Surface Code for Universal Quantum Computation”. In: *Phys. Rev. X* 5 (4 Dec. 2015), p. 041038. DOI: [10.1103/PhysRevX.5.041038](https://doi.org/10.1103/PhysRevX.5.041038) URL: <https://link.aps.org/doi/10.1103/PhysRevX.5.041038>.
- [41] X. G. Wen. “TOPOLOGICAL ORDERS IN RIGID STATES”. In: *International Journal of Modern Physics B* 04.02 (1990), pp. 239–271. DOI: [10.1142/S0217979290000139](https://doi.org/10.1142/S0217979290000139).
- [42] Xiao-Gang Wen. “Quantum Orders in an Exact Soluble Model”. In: *Phys. Rev. Lett.* 90 (1 Jan. 2003), p. 016803. DOI: [10.1103/PhysRevLett.90.016803](https://doi.org/10.1103/PhysRevLett.90.016803) URL: <https://link.aps.org/doi/10.1103/PhysRevLett.90.016803>.
- [43] Edward Witten. “Topological quantum field theory”. In: *Comm. Math. Phys.* 117.3 (1988), pp. 353–386. URL: [https://projecteuclid.org:443/euclid.cmp/1104161738](https://projecteuclid.org/443/euclid.cmp/1104161738).
- [44] Beni Yoshida. “Exotic topological order in fractal spin liquids”. In: *Phys. Rev. B* 88 (12 Sept. 2013), p. 125122. DOI: [10.1103/PhysRevB.88.125122](https://doi.org/10.1103/PhysRevB.88.125122). URL: <https://link.aps.org/doi/10.1103/PhysRevB.88.125122>.
- [45] Yizhi You and Felix von Oppen. “Majorana Quantum Lego, a Route Towards Fracton Matter”. In: (2018). arXiv: [1812.06091](https://arxiv.org/abs/1812.06091) [[cond-mat.str-el](https://arxiv.org/abs/1812.06091)].

EMERGENT FERMIONIC GAUGE THEORY AND FOLIATED FRACTON ORDER IN THE CHAMON MODEL

8.1 Introduction

Gapped quantum systems can form nontrivial phases of matter in the absence of symmetry if they exhibit long-range entanglement in the many-body ground state [10]. The traditional examples of long-range entangled phases are those with intrinsic topological order such as fractional quantum Hall states [33, 67] and discrete gauge theories [30, 41], which are characterized at low energy by topological quantum field theories [69]. In 2005, Chamon discovered a three-dimensional exactly solvable lattice model [9] that represents the first example of a new kind of long-range entangled order known as *fractonic order* [61, 62].

Quantum phases with fractonic order cannot be described by topological quantum field theory due to an intertwining of universal properties with lattice geometry [18, 52, 61, 62]. In particular, fractonic orders are characterized by a ground state degeneracy that scales exponentially with linear system size, and the existence of fractional excitations with constrained mobility [3, 20–22, 62]. The Chamon model, for instance, harbors three kinds of quasiparticles: *planons*, which are mobile within a plane, *lineons*, which can move along a line, and *fractons*, which are fundamentally immobile as individual particles [3]. In recent years, a wide range of fracton orders have been discovered theoretically, each exhibiting a different manifestation of constrained quasiparticle mobility and subextensive ground state degeneracy [1, 2, 4–8, 11, 12, 19–21, 23, 24, 26–29, 36, 37, 39, 40, 42, 43, 50–52, 54, 57, 59–62, 64, 65, 71–73, 75]. Notable examples include the Haah cubic code [23] and the X-cube model [62]. It is natural to ask how the variety of fractonic orders can be systematically characterized within a common theoretical framework.

Many fractonic orders have a unified characterization as emergent gauge theories of discrete *subsystem* symmetries, which have either planar or fractal geometry [32, 45, 62, 68]. For example, the X-cube model is obtained by gauging three orthogonal sets of planar Ising symmetries of a cubic lattice spin-1/2 paramagnet (referred to as a *3-foliated* gauge theory) [62]. The

gauging procedure has been extended to fermion parity subsystem symmetries in fermionic systems, whose gauging yields gapped fractonic gauge theories with emergent fermionic charges [44, 56]. On one hand, a large class of fractonic orders, including those belonging to the class of Calderbank-Shor-Steane (CSS) stabilizer codes, can be obtained via this procedure [32]. On the other hand, it remains unclear how, or if, certain fracton models including the Chamon model, can be obtained by gauging and hence characterized by emergent gauge theory.

In a parallel development, the concept of *foliated fracton order* (FFO) was recently introduced in an effort to systematically characterize fractonic orders with planon excitations [45, 49]. A lattice model is said to have FFO if the lattice size can be systematically reduced by removing, or *exfoliating*, layers of 2D topological orders from the bulk 3D system via a finite-depth quantum circuit. Such a transformation maps a subset of the bulk planon excitations into anyons of the exfoliated 2D orders. For instance, for the X-cube model, it is possible to exfoliate layers of 2D toric code normal to the three cubic lattice directions, hence the X-cube model is said to have a *3-foliation* structure. The notion of FFO has been shown to apply to a large class of models beyond the X-cube model [46, 48, 63]. However, thus far it has remained unknown whether the fractonic order of the Chamon model is foliated.

The purpose of this paper is to fill the gaps in the fracton literature by presenting two new results on the Chamon model. First, we show that the model is characterized by a 4-foliated gauge theory coupled to a fermionic subsystem symmetry-protected topological (SSPT) state. In other words, it can be obtained by gauging four sets of planar \mathbb{Z}_2 symmetries that protect a non-trivial SSPT state [74, 75] in a fermionic lattice system, then performing a local unitary transformation. This is a surprising result because there is no *a priori* clear division of fractional excitations into gauge charge and gauge flux sectors (as is the case for CSS codes). Instead, it is necessary to expand the unit cell and divide the excitations into charge and flux sectors according to the sublattice on which they reside. This is reminiscent of the gauge theory description of the much simpler 2D Wen plaquette model [66].

Second, we show that the Chamon model exhibits FFO with a 4-foliation structure composed of 2D toric code resource layers. In particular, we describe an entanglement renormalization group transformation [15, 19, 58] that maps

a copy of the Chamon model on a $3L \times 3L \times 3L$ cubic lattice to a coarse-grained Chamon model on an $L \times L \times L$ lattice tensored with four decoupled stacks of 2D toric codes. This 4-foliation structure is consistent with the four orientations of planons in the Chamon model, and is most easily described in terms of its action on the planon excitations. We have also obtained an explicit translation-invariant Clifford circuit realizing this transformation.

The paper is organized as follows. In Sec. 8.2, we review the Chamon model and its essential properties. In Sec. 8.3, we explain the characterization of the Chamon model in terms of emergent fermionic gauge theory. In Sec. 8.4, we describe the FFO exhibited by the Chamon model. We conclude with a discussion in Sec. 8.5.

8.2 The Chamon model

The Chamon model was originally defined on an FCC lattice with one qubit per site [3, 9], exhibiting the tetrahedral point group symmetry of the lattice. For our purposes it will be more convenient to place the model on a cubic lattice with one qubit per site, by performing an isometry of \mathbb{R}_3 defined by

$$\begin{aligned} \left(0, \frac{1}{2}, \frac{1}{2}\right) &\rightarrow (1, 0, 0) \\ \left(\frac{1}{2}, 0, \frac{1}{2}\right) &\rightarrow (0, 1, 0) \\ \left(\frac{1}{2}, \frac{1}{2}, 0\right) &\rightarrow (0, 0, 1). \end{aligned} \tag{8.1}$$

In this formulation the Hamiltonian has the form

$$H_C = - \sum_c O_c \tag{8.2}$$

where c indexes the elementary cubes of the lattices and O_c is the six-body Pauli operator depicted in Fig. 8.1(a). For any pair of cubes c, c' , it holds that $[O_c, O_{c'}] = 0$, thus H_C is an exactly solvable stabilizer code Hamiltonian [70]. The ground state degeneracy (GSD) of the model on an $L_x \times L_y \times L_z$ periodic cubic lattice has the form

$$\log_2 \text{GSD} = L_x + L_y + L_z + \text{gcd}(L_x, L_y, L_z) - 3, \tag{8.3}$$

The linear component of this formula arises from the following relations between stabilizer generators:

$$\prod_{c \in P} O_c = 1 \tag{8.4}$$

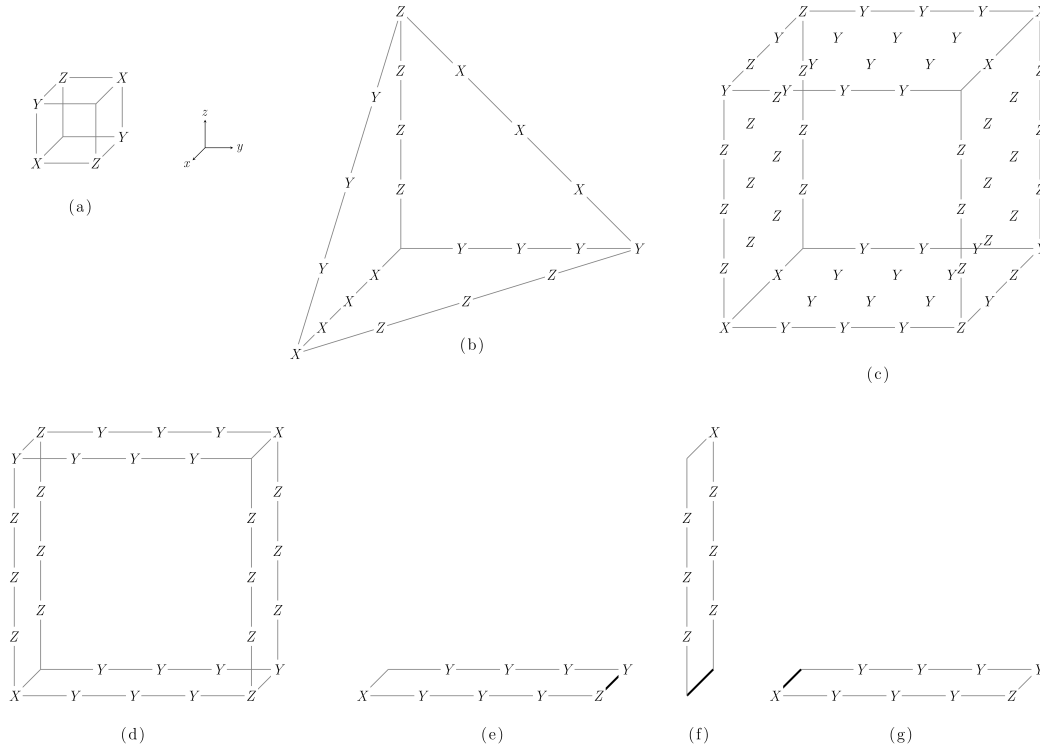


Figure 8.1: (a) The operator O_c , which is a tensor product of the six Pauli operators. (b) A tetrahedral wireframe operator, which is equal to a product of O_c operators inside the tetrahedron. (c) A stabilizer operator bounding a cubic region. (d) A loop operator for an elementary planon of the Chamon model, which is a product of O_c operators within the loop. (e-g) Three planon string operators W_3 , W_2 , and W_1 forming a T-junction (the bold edge represents the same edge in each subfigure). The fermionic exchange statistic of the elementary planon is given by $W_3 W_2^\dagger W_1 W_3^\dagger W_2 W_1^\dagger = -1$.

where P is any dual lattice plane normal to the x , y , z , or $w = (1, 1, 1)$ directions. This gives a total of $L_x + L_y + L_z + L_w$ relations, where $L_w = \text{gcd}(L_x, L_y, L_z)$ is the number of planes normal to w under periodic boundary conditions. It is straightforward to confirm the constant correction numerically.

The model hosts fractional excitations of all mobility types: fractons, lineons, and planons. The excitation structure can be understood by examining the form of stabilizer operators corresponding to processes of quasiparticle creation, movement, and re-annihilation. These operators are given by certain products of O_c terms, of which there are two types. The first type of operator is a wireframe operator, which is a product of all O_c terms within a polyhedral region bounded by x , y , z , and w planes. Due to the relations in

(8.4), such operators are supported on the edges of the polyhedron, for instance the tetrahedral wireframe operator pictured in Fig. 8.1(b). Lineon excitations are created at the endpoints of truncated wireframe operators. There are six kinds of lineons, with mobility in the x , y , z , $(0, 1, -1)$, $(-1, 0, 1)$, and $(1, -1, 0)$ directions, respectively. The lineons obey triple fusion rules in which three distinctly oriented lineons fuse together into the vacuum, which is possible when their respective string operators form the corner of a wireframe operator. For example, x , y , z , and $(1, -1, 0)$, $(0, 1, -1)$, z lineon triples fuse into the vacuum, whereas x , y , $(1, -1, 0)$ and x , y , $(-1, 0, 1)$ triples do not.

The second kind of operator is slightly more complicated: it is given by the product of all O_c terms lying in *even* dual lattice planes normal to a particular direction $\mu = x, y, z, w$ within a polyhedral region bounded by x , y , z , and w planes. Such operators are supported on all surfaces of the polyhedron except those normal to μ . An example of such an operator bounding a cubic region is shown in Fig. 8.1(c). Truncating to a single face gives a membrane operator which creates fracton excitations at its corners.

There are four types of planons mobile within planes normal to the x , y , z , and w directions respectively. For each direction, there is one independent species of planon per lattice spacing, referred to as an elementary planon. The loop operator for an elementary planon can be obtained by taking the product of all O_c operators in a large region within a single x , y , z , or w plane, for instance as depicted in Fig. 8.1(d). These elementary planons can be viewed as either lineon dipoles or as fracton dipoles, *i.e.* composite excitations of a pair of adjacent lineons or fractons, since the loop operator can be viewed as either the first or second kind of operator described in the previous paragraph. Hence, any lineon or fracton can be regarded as a semi-infinite stack of planons, so the exchange and braiding statistics of fractional excitations in the model are entirely characterized by the planon statistics. There are two important features: first, each of the elementary planons have fermionic exchange statistics. Second, adjacent parallel planons have a mutual π braiding statistic. These facts can be verified by examining the structure of the planon string operators as shown in Fig. 8.1(e-g). Since the elementary planons can be regarded as lineon dipoles, this also implies that intersecting lineons have a mutual π braiding statistic.

8.3 Emergent fermionic gauge theory

In this section we demonstrate that the Chamon model is equivalent under a generalized local unitary transformation [10] to a fractonic gauge theory coupled to a fermionic subsystem symmetry-protected topological (SSPT) state [74, 75]. We begin with the SSPT matter Hamiltonian H_M , which is symmetric under four stacks of \mathbb{Z}_2 planar symmetries. We then gauge the symmetry to obtain a spin model H_G . Finally, we transform H_G into the Chamon model H_C via a generalized local unitary.

We also sketch an argument that H_M is a weak SSPT in the sense of Refs. [13, 14].

8.3.1 Matter Hamiltonian

First we describe the matter Hamiltonian H_M . We consider a cellulation of \mathbb{R}_3 obtained by slicing along lattice planes of integer spacing normal to the x , y , z , and $w = (1, 1, 1)$ directions. The x , y , and z planes divide \mathbb{R}_3 into unit volume elementary cubes, and each cube is further sliced into three 3-cells by the w planes: two types of tetrahedra and one octahedron, as pictured in Fig. 8.2. The Hilbert space of H_M is composed of one fermionic orbital per tetrahedron and one qubit per octahedron. The Hamiltonian has the form

$$H_M = - \sum_t i\gamma_t \gamma'_t - \sum_o \mathcal{X}_o \quad (8.5)$$

where t indexes tetrahedra and o octahedra, and

$$\mathcal{X}_o \equiv X_o \prod_{a=0}^1 \prod_{b=0}^1 \prod_{c=0}^1 \prod_{d=0}^1 Z_{o+a\hat{y}-b\hat{z}+c(1,-1,0)+d(-1,0,1)} \quad (8.6)$$

where $o + \vec{r}$ represents the octahedron displaced from o by \vec{r} (see Fig. 8.3(a)). The terms of H_M mutually commute, hence the model is exactly solvable.

H_M is symmetric under four stacks of unitary \mathbb{Z}_2 planar subsystem symmetries, normal to the x , y , z , and w directions. Each symmetry generator is associated with a *dual* lattice plane of the tetrahedral-octahedral honeycomb. Let P denote the set of all 3-cells lying in a dual lattice plane. Then the corresponding symmetry of H_M is

$$S_P = \prod_{t \in P} i\gamma_t \gamma'_t \prod_{o \in P} X_o. \quad (8.7)$$

There is one symmetry generator for every such P . To see that the \mathcal{X}_o terms commute with all of these symmetries, note that each of the x , y , z , and w planes contains at least one of the \hat{y} , \hat{z} , $(1, -1, 0)$, or $(-1, 0, 1)$ vectors.

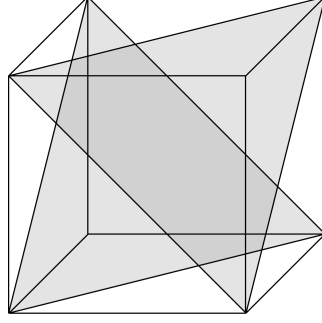


Figure 8.2: The tetrahedral-octahedral honeycomb. Each cube of a cubic lattice is split into two tetrahedra and one octahedron by $(1, 1, 1)$ planes (shaded).

We note that the subsystem symmetries obey the global relations

$$\prod_{P_x} S_{P_x} = \prod_{P_y} S_{P_y} = \prod_{P_z} S_{P_z} = \prod_{P_w} S_{P_w} \quad (8.8)$$

where the products are over all dual lattice planes P_μ normal to μ . Importantly, we also note that the product of symmetries over all *even* dual lattice planes in all four directions is equal to the *global* fermion parity \mathbb{Z}_2^F , which is thus generated by the subsystem symmetry group. Therefore, a bosonic system will be obtained upon gauging the symmetries.

8.3.2 Gauging

We now discuss the gauging of symmetries according to the general prescription [34, 44, 45, 56]. The first step is to identify a set of ‘minimal couplings’ that generate the algebra of symmetric operators together with the on-site symmetry representations (Pauli X on qubits and $i\gamma\gamma'$ on fermion orbitals). There is one minimal coupling for each edge e of the tetrahedral-octahedral honeycomb, acting on the degrees of freedom associated with the four 3-cells adjacent to e (two octahedra o and o' and two oppositely oriented tetrahedra t and t'), which we choose to be

$$M_e \equiv Z_o Z_{o'} \gamma_t \gamma_{t'}. \quad (8.9)$$

The second step is to introduce a gauge qubit degree of freedom for each minimal coupling, hence one per edge. We simultaneously restrict the Hilbert space by introducing generalized Gauss’s law constraints for each matter degree of freedom. The constraints have the form

$$X_o \prod_{e \in o} X_e = 1, \quad i\gamma_t \gamma_{t'} \prod_{e \in t} X_e = 1 \quad (8.10)$$

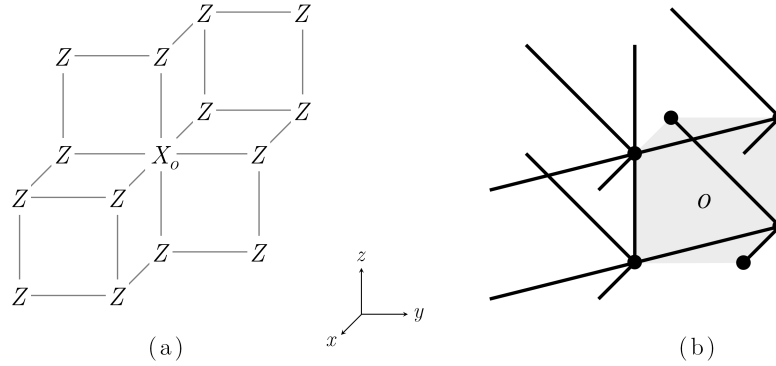


Figure 8.3: (a) Depiction of the operator \mathcal{X}_o . Each Pauli operator acts on an octahedral qubit, whose center-points form a cubic lattice. The octahedron o is indicated by subscript. (b) The set of edges E_o with respect to the octahedron o , whose vertices are the six dots.

for each octahedron o and tetrahedron t .

The third step is to couple the gauge and matter degrees of freedom by introducing a gauged Hamiltonian that preserves the constraints. In particular, in the gauged Hamiltonian the minimal coupling for each edge e is composed with the gauge qubit operator Z_e :

$$M_e \rightarrow M_e Z_e. \quad (8.11)$$

This modification is non-unique, since there are multiple ways to express the operator \mathcal{X}_o in terms of the minimal couplings. We choose the expression

$$\mathcal{X}_o = X_o \prod_{e \in E_o} M_e \quad (8.12)$$

where E_o is the set of edges depicted in Fig. 8.3(b). Hence

$$\mathcal{X}_o \rightarrow X_o \prod_{e \in E_o} M_e Z_e. \quad (8.13)$$

The final step is to add a set of terms $B_{v,\mu}$ for each vertex v to the gauged Hamiltonian in order to gap out the gauge flux excitations. Here $\mu = x, y, z, w$ and $B_{v,\mu}$ is defined as the tensor product of Pauli Z operators over the six links adjacent to v in the plane normal to μ . Thus, the gauged Hamiltonian takes the form

$$\tilde{H}_M = - \sum_t i\gamma_t \gamma'_t - \sum_o X_o \prod_{e \in E_o} M_e Z_e - \sum_{v,\mu} B_{v,\mu}, \quad (8.14)$$

subject to the constraints (8.10).

The matter degrees of freedom can be eliminated via the unitary

$$\begin{aligned} X_o &\rightarrow X_o \prod_{e \in o} X_e & Z_o &\rightarrow Z_o \\ \gamma_t &\rightarrow \gamma_t \prod_{e \in t} X_e & \gamma'_t &\rightarrow \gamma'_t \\ X_e &\rightarrow X_e & Z_e &\rightarrow M_e \bar{Z}_e, \end{aligned} \quad (8.15)$$

which maps the constraints of (8.10) to $X_o = 1$ and $i\gamma_t\gamma'_t = 1$ respectively. The \bar{Z}_e operators are defined in Fig. 8.4 such that \bar{Z}_e and $\bar{Z}_{e'}$ anticommute if e and e' belong to the same tetrahedron, and commute otherwise. In the constrained space, \tilde{H}_M is mapped to a bosonic Hamiltonian H_G acting on the pure gauge qubit Hilbert space:

$$H_G = - \sum_c \bar{A}_c - \sum_{v,\mu} \bar{B}_{v,\mu}, \quad (8.16)$$

where

$$\bar{A}_t \equiv \prod_{e \in c} X_e, \quad \bar{A}_o \equiv \prod_{e \in o} X_e \prod_{e \in E_o} \bar{Z}_e, \quad (8.17)$$

and $\bar{B}_{v,\mu}$ is the image of $B_{v,\mu}$ under the unitary (8.15). The terms of H_G mutually commute, hence they define a Pauli stabilizer code.

8.3.3 Excitation content and ground state degeneracy of the gauged Hamiltonian

To analyze the properties of H_G , it is helpful to express the Hamiltonian in terms of operators \bar{X}_e and \bar{Z}_e associated with edge e of the tetrahedral-octahedral honeycomb. These operators are defined in Fig.8.4. We have already used the \bar{Z}_e operators in the unitary (8.15). In particular,

$$\bar{A}_c = \prod_{e \in c} \bar{X}_e, \quad \bar{B}_{v,\mu} = \prod_{v \ni e \perp \mu} \bar{Z}_e \quad (8.18)$$

where the second product is over the six edges e adjacent to v in the plane normal to μ . These operators are defined in Fig. 8.4 and satisfy the relations

$$\bar{X}_e^2 = \bar{Z}_e^2 = 1, \quad \left\{ \bar{X}_e, \bar{Z}_e \right\} = \left[\bar{X}_e, \bar{Z}_{e'} \right] = 0 \quad (8.19)$$

where e and e' are distinct edges. On the other hand, if e and e' are nearby, then it is generically the case that

$$\left[\bar{X}_e, \bar{X}_{e'} \right] \neq 0, \quad \left[\bar{Z}_e, \bar{Z}_{e'} \right] \neq 0. \quad (8.20)$$

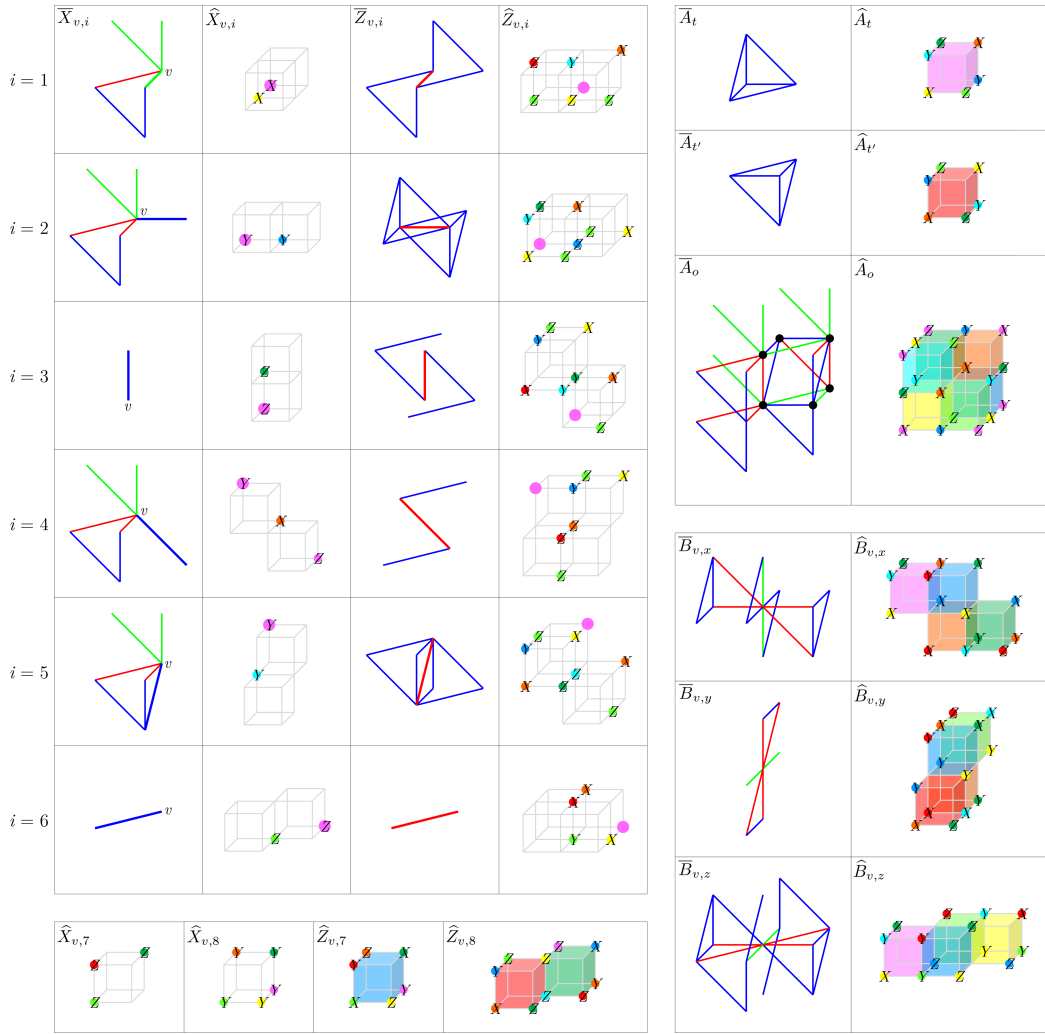


Figure 8.4: Definitions of the Pauli operators introduced in this section. The operators $\overline{X}_{v,i}$ and $\overline{Z}_{v,i}$ acting on \mathcal{H}_G for $i = 1, \dots, 6$ are defined in the table on the left, which are equivalent to the \overline{X}_e and \overline{Z}_e operators for the bold edge e . Red, green, and blue edges respectively represent the action of Pauli Z , Y , and X . The operators $\widehat{X}_{v,i}$ and $\widehat{Z}_{v,i}$ acting on \mathcal{H}_C for $i = 1, \dots, 8$ are defined in the tables on the left, with v given by the enlarged magenta dot in each figure (an unlabelled enlarged dot has no Pauli action). The 3-cell operators \overline{A}_t , $\overline{A}_{t'}$, and \overline{A}_o , and vertex operators $\overline{B}_{v,\mu}$ of H_G are defined in the tables on the right. The vertices of octahedron o are indicated by black dots, whereas the vertex v for each $\overline{B}_{v,\mu}$ operator is the central vertex. The operators \widehat{A}_t , $\widehat{A}_{t'}$, \widehat{A}_o , $\widehat{B}_{v,x}$, $\widehat{B}_{v,y}$, and $\widehat{B}_{v,z}$ acting on \mathcal{H}_C are likewise defined in the tables on the right. These operators, together with $\widehat{Z}_{v,7}$ and $\widehat{Z}_{v,8}$, generate the stabilizer group of H_C . The shaded cubes indicate that a given operators is equal to a product of the corresponding cube terms of H_C (the color of each cube corresponds to the vertex of minimum x , y , and z coordinates).

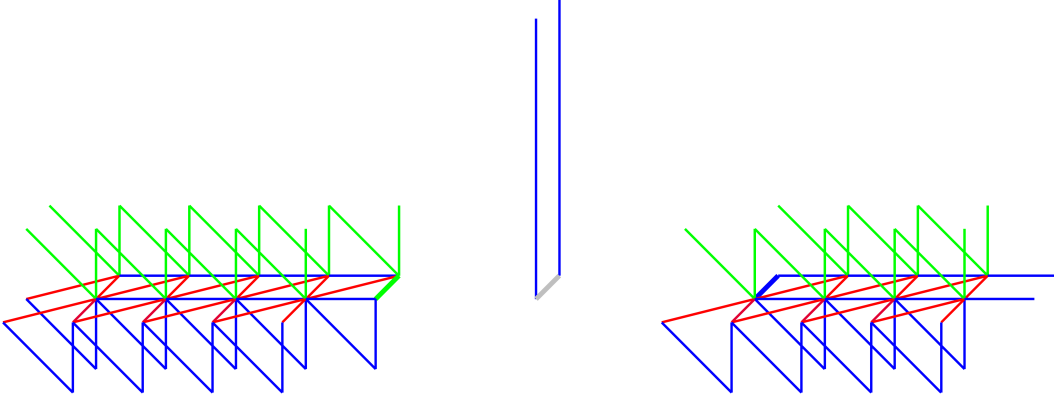


Figure 8.5: Three fracton dipole string operators W_3 , W_2 , and W_1 forming a T-junction (the bold edge represents the same edge in each subfigure). The fermionic exchange statistic of the fracton dipole is given by $W_3W_2^\dagger W_1W_3^\dagger W_2W_1^\dagger = -1$. The red, green and blue edges represent Pauli operators Z , Y and X . The bold gray edge has no Pauli action.

It is instructive to note that due to (8.18), there is a formal relation between H_G and a certain 4-foliated version of the X-cube model, H_{4XC} , described in Appendix 8.6. Roughly speaking, H_G is obtained from H_{4XC} by replacing $X_e \rightarrow \bar{X}_e$ and $Z_e \rightarrow \bar{Z}_e$.

H_G has six qubits and six stabilizer generators per unit cell (since one of the four $\bar{B}_{v,\mu}$ terms is redundant). The stabilizer generators obey the following relations:

$$\prod_{c \in P} \bar{A}_c = 1, \quad \prod_{v \in P'} \bar{B}_{v,\mu} = 1, \quad (8.21)$$

where $c \in P$ indexes all 3-cells in a dual lattice plane P , and $v \in P'$ indexes all vertices belonging to a direct lattice plane P . However, three of these relations are redundant, hence the ground state degeneracy (GSD) of H_G on an $L_x \times L_y \times L_z$ lattice with periodic boundary conditions satisfies

$$\log_2 \text{GSD} = 2L_x + 2L_y + 2L_z + 2 \text{gcd}(L_x, L_y, L_z) - 3. \quad (8.22)$$

The fractional excitations of H_G can be split into two sectors, which we refer to as electric charges and magnetic fluxes. The magnetic sector consists of lineons created at the endpoints of rigid string operators, which are finite segments of *wireframe* operators equal to the product of all \bar{A}_c terms within a polyhedral region bounded by x , y , z , and w planes. Rigid string operators are equal to the product of \bar{X}_e operators over all edges of the string, which follows from the first expression of (8.18). There are six species of lineons, corresponding

to the six orientations of edges in the tetrahedral-octahedral honeycomb: x , y , z , $(1, -1, 0)$, $(0, 1, -1)$, and $(-1, 0, 1)$. Triples of lineons meeting at a single vertex fuse into the vacuum if their string operators belong to the corner of a wireframe operator. For example, x , y , z , and $(1, -1, 0)$, $(0, 1, -1)$, z lineon triples fuse into the vacuum, whereas x , y , $(1, -1, 0)$ and x , y , $(-1, 0, 1)$ triples do not. Due to these triple fusion rules, composite excitations of two adjacent parallel lineons, i.e. lineon dipoles, are planons. There are four species of lineon dipoles in the model: those mobile in planes normal to the x , y , z , or w directions. The loop operators for lineon dipoles are wireframe operators with a slab geometry.

The electric sector consists of fractons created at the corners of dual lattice membrane operators composed of a product of \bar{Z}_e operators over all dual lattice faces comprising the membrane (each dual lattice face corresponds to a direct lattice edge e). Each fracton excitation is associated with a 3-cell of the tetrahedral-octahedral honeycomb. Fracton dipoles composed of a tetrahedral fracton and an adjacent octahedral fracton, are planons. There are four species of fracton dipoles in the model: those mobile in planes normal to the x , y , z , or w directions.

The charge and flux sectors of H_G interact via generalized long-range Aharonov-Bohm statistical interactions. In particular, a phase of -1 is obtained when a lineon dipole flux encircles a fractonic charge, and likewise when a fracton dipole charge encircles a lineonic flux. These interactions arise from the commutation relations of (8.19).

There are also nontrivial statistical interactions within both the electric and magnetic sectors, due to the nontrivial commutation relations of (8.20). In the electric sector, the tetrahedral fractons are fermionic, whereas the octahedral fractons are bosonic. Therefore, each of the fracton dipoles is a fermion. This self-exchange statistic can be explicitly computed using the formula $\theta = W_3 W_2^\dagger W_1 W_3^\dagger W_2 W_1^\dagger$ where W_i are three fracton dipole string operators with a common endpoint [31, 35], as in Fig. 8.5.

In the magnetic sector, the lineons exhibit nontrivial exchange statistics and nontrivial braiding statistics with other lineons. In particular, any pair of lineons intersecting in an x , y , z , or w plane has a mutual π braiding statistic, arising from the anticommutation of intersecting lineon string operators. This can be observed from the form of the wireframe operators, an example of which

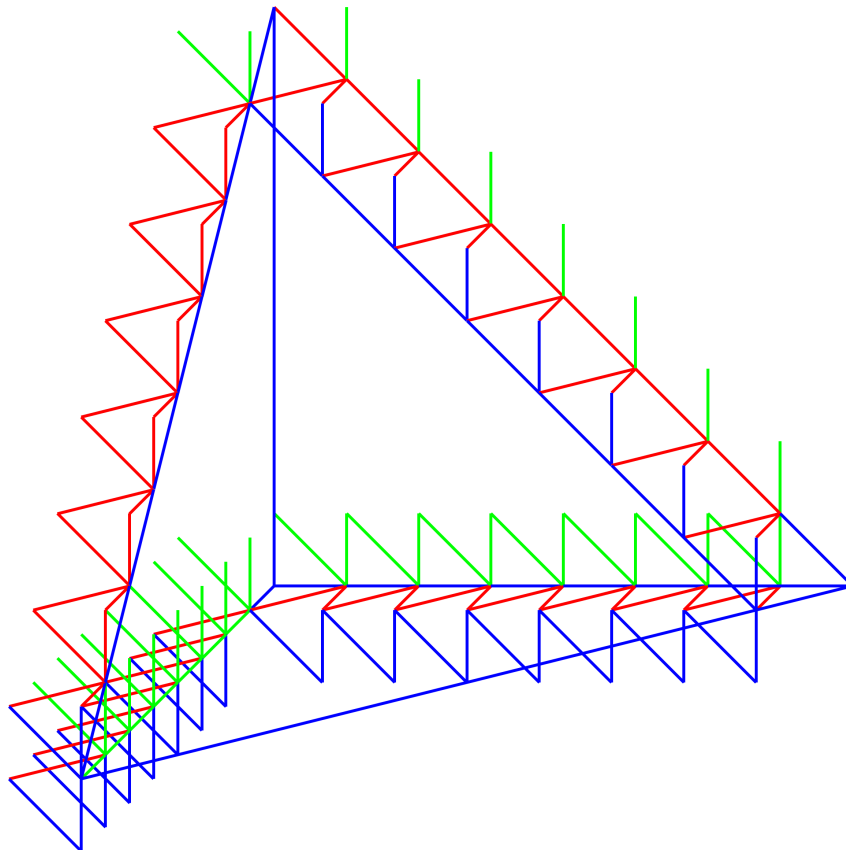


Figure 8.6: A tetrahedral wireframe operator for H_G , given by a product of \overline{A}_c terms over 3-cells inside the tetrahedron. The red, green and blue edges represent Pauli operators Z , Y and X .

is shown in Fig. 8.6. As a result, lineon dipoles in adjacent planes likewise have a π braiding statistic. Moreover, each lineon dipole is a fermion.

8.3.4 Mapping to the Chamon model

We now describe a generalized local unitary (gLU) transformation that maps the ground space of H_G to that of the Chamon model H_C . Based on the expressions (8.3) and (8.22) for the ground state degeneracy of these models, it is clear that for this transformation to work, a unit cell of H_G must correspond to a $2 \times 2 \times 2$ cell of H_C . Therefore, in this section we will place the Chamon model qubits on the sites of a cubic lattice with *half-integer* coordinates. With respect to the integer cubic lattice, the Chamon model has eight qubits and eight stabilizer generators per unit cell, forming a Hilbert space \mathcal{H}_C as shown in Fig. 8.7. We label the qubits with a double subscript v, i with $i = 1, \dots, 8$ and v the vertex of the integer lattice coinciding with qubit 1.

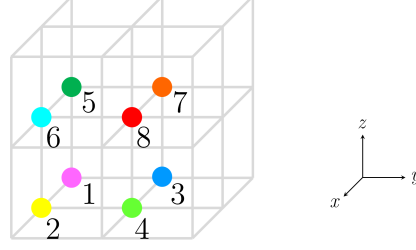


Figure 8.7: A $2 \times 2 \times 2$ cell of the Chamon model, regarded as a unit cell in the transformation between H_C and H_G . There are eight qubits in the unit cell, each represented by a dot of a distinct color.

On the other hand, the gauged model H_G has only six qubits per unit cell (one per edge of the tetrahedral-octahedral honeycomb). To match the degrees of freedom, we add two ancillary qubits per unit cell to the Hilbert space of H_G , forming a Hilbert space \mathcal{H}_G which has eight qubits per unit cell and can thus be identified with \mathcal{H}_C . Each of the eight qubits is likewise labelled with a double subscript v, i with $i = 1, \dots, 8$. Qubits 1 through 6 are those associated with the edges emanating from v in the $x, y, z, (0, 1, -1), (-1, 0, 1),$ and $(1, -1, 0)$ directions, respectively, and 7 and 8 are the two ancillary qubits. We also add two additional terms $\bar{Z}_{v,7} \equiv Z_{v,7}$ and $\bar{Z}_{v,8} \equiv Z_{v,8}$ for each vertex v to H_G , defining an augmented Hamiltonian H'_G .

To facilitate the transformation, in Fig. 8.4 we define operators $\widehat{X}_{v,i}$ and $\widehat{Z}_{v,i}$ on \mathcal{H}_C that obey relations identical to $\bar{X}_{v,i}$ and $\bar{Z}_{v,i}$ for $i = 1, \dots, 8$:

$$\begin{aligned} \widehat{X}_{v,i}^2 = \widehat{Z}_{v,i}^2 = 1, \quad & [[\widehat{X}_{v,i}, \widehat{X}_{v',j}]] = [[\bar{X}_{v,i}, \bar{X}_{v',j}]], \\ & [[\widehat{X}_{v,i}, \widehat{Z}_{v',j}]] = [[\bar{X}_{v,i}, \bar{Z}_{v',j}]], \\ & [[\widehat{Z}_{v,i}, \widehat{Z}_{v',j}]] = [[\bar{Z}_{v,i}, \bar{Z}_{v',j}]]. \end{aligned} \quad (8.23)$$

where $[[A, B]] \equiv A^{-1}B^{-1}AB$. (Each of these group commutators is a ± 1 phase). Due to these relations, and the fact that $\bar{Z}_{v,i}$ and $\bar{X}_{v,i}$ generate the operator algebra of \mathcal{H}_G , it follows that there exists an operator algebra automorphism V mapping

$$\bar{X}_{v,i} \rightarrow \widehat{X}_{v,i}, \quad \bar{Z}_{v,i} \rightarrow \widehat{Z}_{v,i}. \quad (8.24)$$

Moreover, as shown in Fig. 8.4, V maps the terms of H'_G to a set of stabilizers

$$\{\widehat{A}_t, \widehat{A}_{t'}, \widehat{A}_o, \widehat{B}_{v,x}, \widehat{B}_{v,y}, \widehat{B}_{v,z}, \widehat{Z}_{v,7}, \widehat{Z}_{v,8}\} \quad (8.25)$$

that generates the stabilizer group of H_C . Therefore,

$$VH'_G V^\dagger \sim H_C \quad (8.26)$$

where \sim denotes equality of ground spaces. In the supplementary Mathematica file we demonstrate that V is in fact a finite-depth Clifford circuit. Thus, we have arrived at the first main result of the paper: the Chamon model H_C is generalized local unitary equivalent to the gauged Hamiltonian H_G . Appendix 8.7 provides an alternative description of this transformation in terms of the polynomial description of translation invariant Pauli stabilizer codes.

To better understand this equivalence, we consider how the transformation acts on the fractional excitation superselection sectors. First, we note that the wireframe operators of H_G are mapped by V into wireframe operators (with even-length edges) of the Chamon model H_C . Therefore, the lineons of H_G become the lineons of H_C under the transformation. This is consistent with the fact that both models exhibit a mutual π braiding statistic between intersecting lineons sharing an x , y , z , or w plane. Second, we note that the loop operators for fracton dipoles of H_G are transformed into loop operators for the elementary planons of the Chamon model lying in even dual lattice planes. In other words, adjacent fracton dipoles are mapped into pairs of elementary planons of H_C separated by two lattice spacings. This is consistent with the fact that the fracton dipoles of H_G have fermionic exchange statistics but trivial mutual braiding statistics, as the elementary planons in the Chamon model are fermions that braid non-trivially with their nearest neighbors only.

8.3.5 Weak SSPT

In this section we argue based on the excitation content of H_G that the matter Hamiltonian H_M represents a weak subsystem symmetry-protected topological (SSPT) state. A weak SSPT is defined as one that can be obtained by stacking 2D SPTs onto a trivial state in such a way that all planar symmetries are preserved [13, 14]. In the presence of fermionic degrees of freedom, this definition can be extended to allow for stacking of non-invertible 2D topological states. In particular, we consider starting with a completely trivial state (Ising paramagnet plus atomic insulator) on the matter Hilbert space of H_M . We then stack alternating layers of invertible topological orders corresponding to the $\nu = 4$ and $\nu = -4$ states of the Kitaev 16-fold way [31] onto each plane of the tetrahedral-octahedral honeycomb. Finally, each of the S_P symmetry generators is modified such that it is the product of the original S_P with the total fermion parities of the two Kitaev states adjacent to P . It is easy to see

that this modification preserves all the relations of the symmetry group. We conjecture that this state belongs to the same universality class as the model H_M .

To see why this is reasonable, it is helpful to consider the same construction on the gauged level, which should yield a model gLU-equivalent to the Chamon model. In the gauged system, the stacking of Kitaev states is equivalent to stacking alternating layers of fermion parity-gauged $\nu = 4$ and $\nu = -4$ states, *i.e.* semion-fermion and anti-semion-fermion topological orders, onto an untwisted fermionic gauge theory (equivalent to the model described by polynomial matrix $T\Sigma$ of Appendix 8.6). After stacking, bound states of the emergent fermion and the fracton dipole living in the same plane are condensed, confining all of the original lineons in the model but leaving deconfined bound states formed out of a lineon fused with the a semion (or anti-semion) in each of the two parallel planes. This step is equivalent to modifying the symmetry generators S_P on the ungauged level. It is clear that this procedure results in the correct braiding statistics of gauge flux planons, *i.e.* a mutual semionic statistic between adjacent lineon dipoles. Each of these bound-state lineons can be mapped to a (possibly dyonic) lineon of the Chamon model, therefore the condensed model has the same fractional excitation content as the Chamon model.

8.4 Foliated fracton order

A model is said to have *foliated fracton order* (FFO) if its system size can be systematically reduced by disentangling, or *exfoliating*, layers of 2D topological orders from the bulk system via generalized local unitary (gLU) transformation [49]. If there are n different orientations of such 2D states, the model is said to have an n -foliation structure. The first known example of FFO was the X-cube model, which has a 3-foliation structure, followed by a handful of other examples including 1-, 2-, and 3-foliated models [46–48, 63].

In this section we demonstrate that the Chamon model hosts 4-foliated fracton order, with foliation layers normal to the x , y , z , and $w = (1, 1, 1)$ directions. In particular, we show that the system size can be decreased by a constant factor m by exfoliating stacks of 2D toric codes [30] in four directions from the bulk system, where m is any odd integer. This result consistent with previous studies on entanglement signatures [17] and compactification [16] of the model.

H_C is defined on a cubic lattice, which we will take to have integer coordinates in this section and refer to as Λ . The combination of Hamiltonian and its underlying lattice is denoted $H_C(\Lambda)$. We also define coarse-grained cubic lattices $m\Lambda$ whose lattice constants are the integer m . For a given odd m , we posit the existence of a Clifford circuit U satisfying

$$UH_C(\Lambda)U^\dagger \sim H_C(m\Lambda) + H_{2D}(m\Lambda) \quad (8.27)$$

where \sim denotes equality of ground spaces, and the Hamiltonian H_{2D} describes four stacks of decoupled 2D toric codes normal to the x , y , z , and w directions respectively, each with $\frac{m-1}{2}$ toric codes per lattice spacing. We construct such a circuit explicitly in the supplementary Mathematica file in the $m = 3, 5$ cases. In the case of general m , we show in Appendix 8.8 the unitary U exists, although we do not explicitly equate the model $H_{2D}(m\Lambda)$ to stacks of toric codes. In the following discussion, we explain the Chamon model's foliation structure (8.27) on the level of its fractional excitations.

In general, gapped long-range entangled phases are characterized by the structure of fractional excitations above the ground state. In FFOs, exfoliation of a set of 2D topological states corresponds to a factorization of the fusion group A of quasiparticle superselection sectors into two subgroups $A' \boxtimes A_{2D}$. Here, we use \boxtimes to denote a product of fusion groups such that there are no nontrivial mutual statistics between the two factors. A' is the fusion group of the coarse-grained fracton order, and A_{2D} is the fusion group of planons in the exfoliated topological layers.

In the case of the Chamon model, we find that the fusion group $A_C(\Lambda)$ on lattice Λ obeys the following property:

$$A_C(\Lambda) \cong A_C(m\Lambda) \boxtimes A_{2D}(m\Lambda) \quad (8.28)$$

where

$$A_{2D} = A_{2D}^x \boxtimes A_{2D}^y \boxtimes A_{2D}^z \boxtimes A_{2D}^w \quad (8.29)$$

and A_{2D}^x , A_{2D}^y , A_{2D}^z , and A_{2D}^w are the fusion groups of stacks of 2D toric codes in the x , y , z , and w directions respectively, each with $\frac{m-1}{2}$ toric codes per lattice spacing. Here \cong denotes a locality-preserving isomorphism.

To see this, note that by the transformation of the previous section, the fusion rules of $H_C(\Lambda)$ are identical to those of the 4-foliated X-cube model

Figure 8.8: Planon diagrams depicting coarse-grained bases of μ -normal planons in a given direction $\mu = x, y, z, w$ for the (a) $m = 3$ and (b) $m = 5$ cases. Each basis is translation-invariant with respect to the enlarged unit cell of $2m\Lambda$. Each vertical line is commensurate with a μ -normal lattice plane, hence the numbers 0 to $2m$ represent dual lattice coordinates. A box lying in column k represents a planon living in that dual lattice plane. On the other hand, each horizontal row represents a single generator of our chosen basis, equal to the fusion product of all elementary planons in the row. Since each unit cell contains $2m$ basis planons, A and G (K) belong to different unit cells for the $m = 3$ ($m = 5$) case. The planon bases are partitioned into m subsets of two generators per unit cell, such that they have pairwise trivial mutual braiding statistics. (Recall that adjacent planons of the Chamon model have a mutual π braiding statistic). For $m = 3$, the subsets are colored black (ADG), red (BC), and blue (EF), whereas for $m = 5$ they are colored black (AFK), green (BE), red (CD), purple (GJ), and blue (HI). The black planons are excitations of the coarse-grained Chamon model $H_C(m\Lambda)$, as they are fermions (being composed of an odd number of fermions with trivial mutual statistics) with a mutual π braiding statistic between adjacent pairs. On the other hand, each of the remaining $m - 1$ pairs of planons generates a decoupled layer of 2D toric code. These diagrams verify the relation (8.33).

$H_{4XC}(2\Lambda)$ discussed in Appendix 8.6 (since H_C is gLU equivalent to H_G whose fusion rules are the same as H_{4XC}). The fusion group of H_{4XC} is known to have the form $A_{4XC} = Q_{4XC} \times P_{4XC}$ where P_{4XC} is the subgroup consisting of all planon excitations [47], and Q_{4XC} is a (non-unique) finite subgroup generated by one fracton and three lineons. As an aside, this observation forms the basis of the notion of *quotient superselection sectors* (QSS), which are defined as equivalence classes of superselection sectors modulo planons [47]. According to this definition the group of QSS of H_{4XC} (and hence of H_C) is $A_{4XC}/P_{4XC} \cong Q_{4XC}$.

Hence, we have that $A_C = Q_C \times P_C$ where Q_C is an order 16 subgroup and $P_C = P_C^x \boxtimes P_C^y \boxtimes P_C^z \boxtimes P_C^w$ is the subgroup of all planons. The decomposition of (8.28) is implied by the following decomposition of P :

$$P_C(\Lambda) \cong P_C(m\Lambda) \boxtimes A_{2D}(m\Lambda), \quad (8.30)$$

since Q_C can always be chosen such that Q_C and $A_{2D}(m\Lambda)$ have no nontrivial mutual statistics, i.e.

$$A_C(\Lambda) \cong [Q_C \times P_C(m\Lambda)] \boxtimes A_{2D}(m\Lambda). \quad (8.31)$$

The equivalence (8.30) can in turn be factored by direction:

$$P_C^\mu(\Lambda) \cong P_C^\mu(m\Lambda) \boxtimes A_{2D}^\mu(m\Lambda). \quad (8.32)$$

Thus, we can focus on the group of planons in a single direction, $P_C^\mu(\Lambda)$. Recall from Sec. 8.2 that for a given direction, there is one independent planon per lattice spacing whose loop operator is given by the product of O_c terms in a particular dual lattice plane. The total group is generated by the set of all such elementary planons. Each elementary planon has fermionic exchange statistics. Moreover, neighboring planons have mutual semionic braiding statistics.

To demonstrate (8.30), we need to find an alternative set of generating planons that splits into two parts: one that generates $P_C^\mu(m\Lambda)$ and one that generates $A_{2D}^\mu(m\Lambda)$. Actually, we will show the following equivalent relation:¹

$$P_C^\mu(\Lambda) \cong P_C^\mu(m\Lambda) \boxtimes A_{2D}^\mu(2m\Lambda) \boxtimes A_{2D}^\mu(2m\Lambda). \quad (8.33)$$

Factorization of this form for $m = 3$ and $m = 5$ are depicted in the planon diagrams of Fig. ??, demonstrating that the fractional excitation structure of H_C indeed exhibits the decomposition of (8.28). It is straightforward to generalize these diagrams for larger m . Thus, we conclude that the Chamon model exhibits a 4-foliation structure of 2D toric code layers in the x , y , z , and w directions.

8.5 Discussion

In this work, we have carried out a comprehensive investigation of the Chamon model, which is historically significant as the first fracton model to appear in the literature. Specifically, we have demonstrated two results: first, its characterization as a twisted 4-foliated gauge theory with emergent fermionic charge. Second, we have found that it has a 4-foliation structure composed of 2D toric code layers. The foliation structure is consistent with a conjecture of Ref. [15], which outlines conditions under which a copy of 2D toric code can be extracted from a 3D stabilizer code model under a local unitary. The emergent gauge theory structure found in this paper, has been used by two of the authors to write a topological defect network for the Chamon model [55].

The transformation between the Chamon model and the 4-foliated X-cube variant H_G is reminiscent of previous findings about the checkerboard

¹The additional coarse-graining by a factor of two is necessary to pair up 3-fermion states so they can be transformed into pairs of toric codes.

model [46] and the Majorana checkerboard model [61], which were respectively shown to be equivalent to two copies of the (3-foliated) X-cube model, and to the semionic X-cube model [63] (plus transparent fermions), each of which has a clear gauge theory description. It is similarly reminiscent of the equivalence between the Wen plaquette model [66] and the 2D toric code [31]. These transformations all have in common that the original model, *e.g.* Chamon, has an enhanced translation symmetry compared with the transformed model, *e.g.* H_G . Therefore, the respective gauge theory descriptions are enriched by translation symmetry via a nontrivial permutation on the fractonic superselection sectors. We leave a detailed exploration of this topic to future studies.

While it is known that CSS stabilizer codes can generically be characterized via emergent gauge theory, our results raise the question of how generally non-CSS codes in three dimensions admit such a description. It seems plausible that all stabilizer codes possess a gauge theory description and hence it could be enlightening to study more examples. For instance, one could check whether a gauge theory description, analogous to the Chamon model, is possible for the fracton models in Ref. [25]. Another question raised by this work is that of strong subsystem symmetry-protected topological (SPT) states in fermionic systems, whose classification is an open problem. We have argued that the Chamon model is dual to a weak subsystem SPT.

More generally, it is an open question to what extent the framework of emergent gauge theory has utility in the classification of fractonic phases of matter. To our knowledge, among the class of exactly solvable lattice models, there are no examples that are explicitly known to not admit a gauge theory description. It would be interesting to either find such an example, or demonstrate that none exist. On the other hand, there are examples of fractonic orders with excitations of infinite order which are unlikely to have any characterization in terms of finite gauge groups (although they arise naturally as infinite-component $U(1)$ Chern-Simons gauge theories [38]).

Finally, it is worthwhile to note that some of the fractonic excitations in the Chamon model exhibit non-bosonic self-exchange statistics [53]. For the present analysis it has been sufficient to consider in detail the statistics of planon excitations. A systematic investigation of fracton self-statistics in n -foliated models is left to future work.

8.6 Appendix: Relation between H_G and the 4-foliated X-cube model

In this section we introduce the 4-foliated X-cube model H_{4XC} and describe its relation to H_G . The fusion structure of excitations of H_{4XC} is identical to that of H_G . However, the models differ in terms of the self and mutual statistics of the excitations. In this section we will use the $\mathbb{Z}_2[x, y, z, 1/x, 1/y, 1/z]$ Laurent polynomial ring formalism for describing translation-invariant Pauli stabilizer codes [20]. In this formalism, Pauli operators in a cubic lattice system with n qubits per site are represented by length $2n$ column vectors whose entries are elements of $\mathbb{Z}_2[x, y, z, 1/x, 1/y, 1/z]$. The first n entries represent the Pauli X components, and the last n entries the Pauli Z components.

The Hilbert space of H_{4XC} is the same as that of H_G . It is composed of one qubit on each edge of the tetrahedral-octahedral honeycomb. The Hamiltonian has the form

$$H_{4XC} = - \sum_c A_c - \sum_{v,\mu} B_{v,\mu} \quad (8.34)$$

where c runs over all 3-cells of the honeycomb, v all vertices, $\mu = x, y, z, w$, and

$$A_c = \prod_{e \in c} X_e, \quad B_{v,\mu} = \prod_{v \ni e \perp \mu} Z_e. \quad (8.35)$$

This model is described by the polynomial matrix

$$\Sigma = \begin{pmatrix} A & 0 \\ 0 & B \end{pmatrix} \quad (8.36)$$

where

$$A = \begin{pmatrix} 1 & yz & y+z \\ 1 & zx & z+x \\ 1 & xy & x+y \\ 1 & x & x+1 \\ 1 & y & y+1 \\ 1 & z & z+1 \end{pmatrix}, \quad B = \begin{pmatrix} 0 & 1 + \frac{1}{x} & 1 + \frac{1}{x} \\ 1 + \frac{1}{y} & 0 & 1 + \frac{1}{y} \\ 1 + \frac{1}{z} & 1 + \frac{1}{z} & 0 \\ \frac{1}{y} + \frac{1}{z} & 0 & 0 \\ 0 & \frac{1}{x} + \frac{1}{z} & 0 \\ 0 & 0 & \frac{1}{x} + \frac{1}{y} \end{pmatrix}. \quad (8.37)$$

The columns of A represents the 3-cell terms A_t , $A_{t'}$ and A_o , whereas the columns of A represent the vertex terms $B_{v,x}$, $B_{v,y}$, and $B_{v,z}$, which together generate $B_{v,w}$. Note that $\Sigma^\dagger \Omega_6 \Sigma = 0$ where † represents transposition combined with spatial inversion, $\Omega_k = \begin{pmatrix} 0 & I_k \\ I_k & 0 \end{pmatrix}$ is the $2k \times 2k$ symplectic

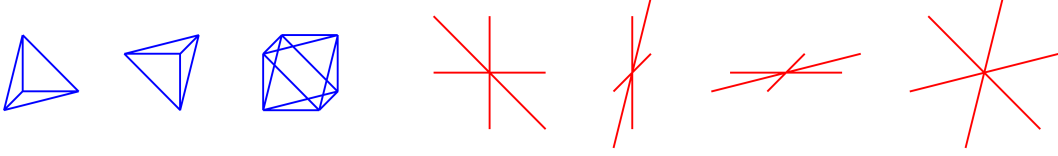


Figure 8.9: The terms $A_t, A_{t'}, A_o, B_{v,x}, B_{v,y}, B_{v,z}$ and $B_{v,w}$ of H_{4XC} , where t and t' are oppositely oriented tetrahedral cells and o an octahedral cell. Here blue represents Pauli X and red Pauli Z . Each term is a tensor product of the depicted Pauli operators.

form, and I_k the $k \times k$ identity matrix. Thus, the terms of H_{4XC} are mutually commuting.

H_G can be obtained from H_{4XC} via a pair of locality-preserving, invertible but non-isomorphic transformations of the Pauli group \mathcal{P} :

$$W: \mathcal{P} \rightarrow \mathcal{P}, \quad T: \mathcal{P} \rightarrow \mathcal{P}. \quad (8.38)$$

In the polynomial formalism, these transformations correspond to multiplication by invertible but non-symplectic matrices:

$$W = \begin{pmatrix} I_6 & 0 \\ \tilde{W} & I_6 \end{pmatrix}, \quad T = \begin{pmatrix} I_6 & \tilde{T} \\ 0 & I_6 \end{pmatrix} \quad (8.39)$$

where

$$\tilde{W} = \begin{pmatrix} 1 & 1 & 0 & z & z & 0 \\ 0 & 0 & 0 & 0 & 0 & 0 \\ 1 & 1 & 0 & z & z & 0 \\ \frac{1}{y} & \frac{1}{y} & 0 & \frac{z}{y} & \frac{z}{y} & 0 \\ 0 & 0 & 0 & 0 & 0 & 0 \\ \frac{1}{y} & \frac{1}{y} & 0 & \frac{z}{y} & \frac{z}{y} & 0 \end{pmatrix}, \quad \tilde{T} = \begin{pmatrix} 0 & 1 + \frac{y}{x} & 0 & 0 & z + 1 & 0 \\ 0 & 0 & 0 & 0 & 0 & 0 \\ 1 + \frac{x}{z} & 1 + \frac{y}{z} & 0 & 0 & x + 1 & 0 \\ 1 + \frac{x}{yz} & 1 + \frac{1}{z} & 1 + \frac{1}{y} & 0 & 1 + \frac{x}{y} & 0 \\ 0 & 1 + \frac{y}{xz} & 0 & 0 & 0 & 0 \\ 1 + \frac{1}{y} & 1 + \frac{1}{x} & 1 + \frac{z}{xy} & 1 + \frac{z}{x} & 1 + \frac{z}{y} & 0 \end{pmatrix}. \quad (8.40)$$

Note that $T^2 = W^2 = 1$. It holds that

$$\bar{A}_c = T(W(A_c)), \quad \bar{B}_{v,\mu} = T(W(B_{v,\mu})). \quad (8.41)$$

Therefore, the Hamiltonian H_G is represented by the polynomial matrix $\bar{\Sigma} = TW\Sigma$. Since $\bar{\Sigma}^\dagger \Omega_6 \bar{\Sigma} = 0$, the terms of H_G mutually commute hence defining a stabilizer code. Note that

$$TW = \begin{pmatrix} I_6 + \tilde{T}\tilde{W} & \tilde{T} \\ \tilde{W} & I_6 \end{pmatrix}. \quad (8.42)$$

The T and W transformations can also be used to define two other non-CSS stabilizer code Hamiltonians, represented by the polynomial matrices $W\Sigma$ and $T\Sigma$ satisfying $\Sigma^\dagger W^\dagger \Omega_6 W \Sigma = 0$ and $\Sigma^\dagger T^\dagger \Omega_6 T \Sigma = 0$. The Hamiltonians represented by Σ , $\bar{\Sigma}$, $W\Sigma$, and $T\Sigma$ can each be obtained via a gauging procedure of four stacks of planar \mathbb{Z}_2 symmetries. The procedure was described explicitly for H_G , represented by $\bar{\Sigma}$, in Sec. 8.3.2. On the other hand, Σ , $W\Sigma$, and $T\Sigma$ can be obtained by gauging the following matter Hamiltonians, respectively:

$$H_M^{(1)} = - \sum_t X_t - \sum_o X_o, \quad (8.43)$$

$$H_M^{(2)} = - \sum_t X_t - \sum_o \mathcal{X}_o, \quad (8.44)$$

$$H_M^{(3)} = - \sum_t i\gamma_t \gamma'_t - \sum_o X_o. \quad (8.45)$$

The Hilbert space of $H_M^{(3)}$ is the same as that of H_M , whereas those of $H_M^{(1)}$ and $H_M^{(2)}$ differ in that the fermionic orbital on each tetrahedral 3-cell is replaced by a qubit. The symmetries of $H_M^{(3)}$ are the same as those of H_M , whereas for $H_M^{(1)}$ and $H_M^{(2)}$ they are simply a product of Pauli X operators over all 3-cells in a given dual lattice plane.

Therefore, each of the models Σ , $\bar{\Sigma}$, $W\Sigma$, and $T\Sigma$ represents a distinct kind of fractonic gauge theory. Σ is coupled to a trivial bosonic paramagnet, $T\Sigma$ to a trivial atomic insulator/paramagnet state, $W\Sigma$ to a bosonic SSPT state, and $\bar{\Sigma}$ to a fermionic SSPT. The fusion rules of all four models are identical; moreover the generalized Aharonov-Bohm statistics between gauge charge and flux sectors have identical form. However, the models differ in terms of the statistics *within* the charge and flux sectors. Acting on Σ , the W matrix represents a *twist* of the gauge flux statistics, whereas the T matrix represents a *transmutation* of the gauge charge statistics. This can be seen from the equations

$$\begin{aligned} W^\dagger \Omega_6 W &= \begin{pmatrix} \widetilde{W} + \widetilde{W}^\dagger & I_6 \\ I_6 & 0 \end{pmatrix}, & T^\dagger \Omega_6 T &= \begin{pmatrix} 0 & I_6 \\ I_6 & \widetilde{T} + \widetilde{T}^\dagger \end{pmatrix}, \\ W^\dagger T^\dagger \Omega_6 T W &= \begin{pmatrix} \widetilde{W} + \widetilde{W}^\dagger & I_6 \\ I_6 & \widetilde{T} + \widetilde{T}^\dagger \end{pmatrix}. \end{aligned} \quad (8.46)$$

The off-diagonal components represent the Aharonov-Bohm interactions whereas the diagonal components represent the statistics within the charge

and flux sectors. Therefore, Σ and $W\Sigma$ have purely bosonic gauge charge statistics, whereas the tetrahedral fractonic charges of $\bar{\Sigma}$ and $T\Sigma$ are fermionic. On the other hand, Σ and $W\Sigma$ have purely bosonic gauge flux lineons, whereas intersecting lineons of $\bar{\Sigma}$ and $W\Sigma$ have a mutual semionic braiding statistic.

8.7 Appendix: Polynomial representation of the transformation from H_G to H_C

In this appendix we express the transformation from the gauge theory Hamiltonian H_G to the Chamon model H_C in terms of the Laurent polynomial formalism. Regarding a $2 \times 2 \times 2$ cell as the unit cell with qubits labelled as in Fig. 8.7, H_C is represented by the 16×8 stabilizer map

$$\hat{\Sigma} = \begin{pmatrix} 0 & x & y & 0 & 0 & xz & yz & 0 \\ 1 & 0 & 0 & y & z & 0 & 0 & yz \\ 1 & 0 & 0 & x & z & 0 & 0 & xz \\ 0 & 1 & 1 & 0 & 0 & z & z & 0 \\ 0 & x & y & 0 & 0 & x & y & 0 \\ 1 & 0 & 0 & y & 1 & 0 & 0 & y \\ 1 & 0 & 0 & x & 1 & 0 & 0 & x \\ 0 & 1 & 1 & 0 & 0 & 1 & 1 & 0 \\ 0 & 0 & y & xy & z & xz & 0 & 0 \\ 0 & 0 & y & y & z & z & 0 & 0 \\ 1 & x & 0 & 0 & 0 & 0 & z & xz \\ 1 & 1 & 0 & 0 & 0 & 0 & z & z \\ 1 & x & 0 & 0 & 0 & 0 & y & xy \\ 1 & 1 & 0 & 0 & 0 & 0 & y & y \\ 0 & 0 & 1 & x & 1 & x & 0 & 0 \\ 0 & 0 & 1 & 1 & 1 & 1 & 0 & 0 \end{pmatrix}. \quad (8.47)$$

We define a matrix C whose first (last) 8 columns represent the operators $\widehat{X}_{v,i}$ ($\widehat{Z}_{v,i}$) for $i = 1, \dots, 8$:

$$C = \begin{pmatrix} 1 & 1 & 0 & z & z & 0 & 0 & 1 & 0 & 0 & 0 & 0 & 0 & 1 & 0 \\ 1 & 0 & 0 & 0 & 0 & 0 & 0 & 1 & 0 & 1 + \frac{y}{x} & \frac{z}{x} & \frac{yz}{x} & z & y & 0 & 0 \\ 0 & 1 & 0 & 0 & 0 & 0 & 0 & 0 & 0 & 0 & \frac{z}{y} & z & \frac{xz}{y} & 0 & 0 & 1 + \frac{x}{y} \\ 0 & 0 & 0 & 0 & 0 & 0 & 0 & \frac{1}{y} & 0 & 0 & 0 & 0 & 0 & 1 & \frac{1}{y} & 0 \\ 0 & 0 & 0 & 0 & 0 & 0 & 0 & 1 & 0 & 0 & 1 & 0 & 0 & 0 & 1 & 0 \\ 0 & 0 & 0 & 0 & 1 & 0 & 0 & 0 & 1 & 1 & 1 & 0 & 0 & 0 & 0 & 0 \\ 0 & 0 & 0 & 1 & 0 & 0 & 0 & \frac{1}{y} & 1 & 1 & 1 & 0 & 1 + \frac{x}{y} & 1 & 0 & \frac{1}{z} + \frac{x}{yz} \\ 0 & 0 & 0 & 0 & 0 & 0 & 0 & 0 & 0 & 0 & \frac{1}{y} & 0 & 0 & 1 & \frac{1}{y} & 0 \\ 0 & 1 & 1 & y+z & z & y & 0 & 1 & 0 & 0 & 0 & 0 & 0 & 0 & 1 & 1 \\ 0 & 0 & 0 & 0 & 0 & 0 & 0 & 1 & 1 & 0 & 0 & 0 & 0 & 0 & 1 & 1 \\ 0 & 1 & 0 & 0 & 0 & 0 & 0 & 0 & 0 & 1 & \frac{z}{y} & z & \frac{xz}{y} & 0 & 0 & \frac{x}{y} \\ 0 & 0 & 0 & 0 & 0 & 1 & \frac{1}{y} & \frac{1}{y} & 1 + \frac{1}{y} & 1 + \frac{1}{x} & 1 + \frac{z}{xy} & 1 + \frac{z}{x} & 1 + \frac{z}{y} & 1 & 0 & \frac{1}{y} \\ 0 & 0 & 1 & 0 & 0 & 0 & 1 & 1 & 0 & 1 & 1 & 0 & x & 0 & 0 & \frac{x}{z} \\ 0 & 0 & 0 & 0 & 1 & 0 & 0 & 0 & 1 & 1 & 1 & 0 & 1 & 0 & 0 & \frac{1}{z} \\ 0 & 0 & 0 & 0 & 0 & 0 & 0 & \frac{1}{y} & 0 & 0 & 0 & 1 & 0 & 0 & 0 & \frac{1}{z} \\ 0 & 0 & 0 & 0 & 0 & 0 & \frac{1}{y} & 0 & \frac{1}{y} & 0 & 0 & 1 & 0 & 0 & \frac{1}{y} & \frac{1}{z} \\ 0 & 0 & 0 & 0 & 0 & 0 & \frac{1}{y} & 0 & \frac{1}{y} & 0 & 0 & 1 & 0 & 0 & \frac{1}{y} & \frac{1}{z} \end{pmatrix}. \quad (8.48)$$

In this section, we will redefine the matrices W and T from the previous appendix such that they accommodate the two ancillary qubits. In particular,

$$W = \begin{pmatrix} I_8 & 0 \\ \widetilde{W} \oplus I_2 & I_8 \end{pmatrix}, \quad T = \begin{pmatrix} I_8 & \widetilde{T} \oplus I_2 \\ 0 & I_8 \end{pmatrix} \quad (8.49)$$

Then, we define a matrix $U = CWT$ satisfying $U^\dagger \Omega_8 U = \Omega_8$ and $UTW = C$. Therefore U is a Clifford QCA that maps $\overline{X}_{v,i} \rightarrow \widehat{X}_{v,i}$ and $\overline{Z}_{v,i} \rightarrow \widehat{Z}_{v,i}$. Moreover,

$$U\overline{\Sigma} = \widehat{\Sigma}V \quad (8.50)$$

where V is the invertible matrix

$$V = \begin{pmatrix} 1 & 0 & 0 & \frac{1}{y} & 0 & \frac{1}{y} & 0 & 0 \\ 0 & 0 & 1 & 0 & 0 & \frac{1}{x} & 0 & 0 \\ 0 & 0 & 1 & \frac{1}{y} & \frac{1}{y} & \frac{1}{y} & \frac{1}{y} & 0 \\ 0 & 0 & 1 & 0 & \frac{1}{xy} & \frac{1}{xy} & 0 & 0 \\ 0 & 0 & 1 & \frac{1}{z} & 0 & 0 & 0 & \frac{1}{z} \\ 0 & 0 & 1 & 0 & 0 & 0 & 0 & 0 \\ 0 & 0 & 1 & \frac{1}{yz} & \frac{1}{yz} & 0 & 0 & 0 \\ 0 & 1 & 0 & 0 & \frac{1}{yz} & 0 & 0 & \frac{1}{yz} \end{pmatrix}. \quad (8.51)$$

Therefore, U maps the ground space of H_G to that of H_C . In the supplementary Mathematica file, we demonstrate that U is actually a finite-depth Clifford circuit (*i.e.*, it can be decomposed into a product of elementary symplectic transformations). This demonstrates that H_G and H_C are gLU equivalent.

8.8 Appendix: Entanglement renormalization of the Chamon model

In this section, we study the entanglement renormalization (ER) on the Chamon model using the polynomial formalism [19, 20]. The stabilizer map σ and the excitation map ϵ for the Chamon model can be written as

$$\sigma = \begin{pmatrix} (1+x^{-1})(y^{-1}+z^{-1}) \\ (1+y^{-1})(x^{-1}+z^{-1}) \end{pmatrix} \quad (8.52)$$

and

$$\epsilon = \sigma^\dagger \Omega_1 = \begin{pmatrix} (1+y)(x+z) & (1+x)(y+z) \end{pmatrix}. \quad (8.53)$$

respectively [20]. Our approach to doing ER involves going to a basis of stabilizer terms such that the associated basis excitations include the bosonic planon charges. Then we write the creation operators or movers of these bosonic charges and apply translation invariant gates (up to coarse-graining) to reduce them into a canonical form of unit vectors. The excitations that form the bosonic planons and the relative positions between them are shown in Fig. ???. Before stating an explicit ER result for the Chamon model, we first prove that a coarse-grained copy of itself can be extracted under ER of the Chamon model. In particular, we have the following theorem.

Theorem 8.8.1. *For any odd m , there exists a Clifford circuit U such that*

$$UH_C(\Lambda)U^\dagger \sim H_C(m\Lambda) + H_B(m\Lambda), \quad (8.54)$$

for some Pauli Hamiltonian H_B . Here \sim denotes equality of ground spaces.

Proof. We first write down two fracton creation operators,

$$s_1 = x^{m-1}(1+y+\dots+y^{m-1})(1+z/x+\dots+(z/x)^{m-1})(1,0)^T$$

and

$$s_2 = y^{m-1}(1+x+\dots+x^{m-1})(1+z/y+\dots+(z/y)^{m-1})(0,1)^T,$$

which create fracton excitations at the sites corresponding to the polynomials $(1+y^m)(x^m+z^m)$ and $(1+x^m)(y^m+z^m)$ respectively. Note that s_1 and s_2 are

related via permutation of x and y . In other words, the action of the excitation map as defined in Eq. 8.53 on operators s_1 and s_2 is given by

$$\begin{aligned}\epsilon s_1 &= (1 + y^m)(x^m + z^m) \\ \epsilon s_2 &= (1 + x^m)(y^m + z^m).\end{aligned}$$

Under coarse-graining of the lattice, the translation group is reduced such that the translation variables modify to $x' = x^m, y' = y^m, z' = z^m$. On the coarse-grained lattice, the representation of the creation operators s_1 and s_2 is given by $s_1^{(m)}$ and $s_2^{(m)}$ respectively. Namely, $\phi_{\#}^m(s_1) = s_1^{(m)}$ and $\phi_{\#}^m(s_2) = s_2^{(m)}$ where $\phi_{\#}^m$ is the map that implements coarse-graining by a factor of m . We now state two lemmas about $s_1^{(m)}$ and $s_2^{(m)}$, one about the commutation relation and the other about reducing them to a canonical form via elementary symplectic transformations. The proofs of these lemmas are given after this proof.

Lemma 8.8.1. *For odd m , $s_1^{(m)\dagger} \Omega_m s_2^{(m)} = 1$ where $\Omega_m = \begin{pmatrix} 0 & \mathbb{1} \\ \mathbb{1} & 0 \end{pmatrix}$ is a $2m \times 2m$ symplectic form and $\mathbb{1}$ is an $m \times m$ Identity matrix.*

Lemma 8.8.2. *For odd m , the creation operators $s_1^{(m)}$ and $s_2^{(m)}$ can be mapped to*

$$\begin{aligned}s_1^{(m)} &= \left(1 \ 0 \cdots 0 \mid 0 \ \cdots \ 0 \right)^T, \\ s_2^{(m)} &= \left(0 \ 0 \cdots 0 \mid 1 \ \cdots \ 0 \right)^T\end{aligned}\tag{8.55}$$

via translation invariant elementary symplectic transformations. Here, as shown, $s_1^{(m)}$ and $s_2^{(m)}$, respectively, have only one nonzero entry at the 1st and (m^3+1) -th vector components.

The excitation represented as a singleton element, (1) before coarse-graining, is represented by the unit vector $e_1 = (1, 0, 0, \dots, 0)^T$ with m entries after coarse graining. Considering the action of ϵ on the creation operators $s_1^{(m)}, s_2^{(m)}$ yields $\epsilon s_1^{(m)} = (1 + y')(x' + z')e_1$ and $\epsilon s_2^{(m)} = (1 + x')(y' + z')e_1$, the excitation map becomes

$$\epsilon = \left(\begin{array}{cccc|cccc} (1+y)(x+z) & \star & \star & \cdots & \star & (1+x)(y+z) & \star & \star & \cdots & \star \\ 0 & \star & \star & \cdots & \star & 0 & \star & \star & \cdots & \star \\ \vdots & \vdots & \vdots & \vdots & \vdots & \vdots & & & & \\ 0 & \star & \star & \cdots & \star & 0 & \star & \star & \cdots & \star \end{array} \right)\tag{8.56}$$

where we suppressed the \prime in the coarse-grained translation variables and where \star indicates unknown entries. Since

$$\left((1+x^{-1})(y^{-1}+z^{-1}) \ 0 \ 0 \ \cdots \ 0 \ (1+y^{-1})(x^{-1}+z^{-1}) \ 0 \ 0 \ \cdots \ 0 \right)^T \in \ker \epsilon,$$

the topological order condition $\ker \epsilon = \text{im} \sigma = \text{im} \Omega_q \epsilon^\dagger$ implies that the rows of ϵ must generate

$$\left((1+y)(x+z) \ 0 \ 0 \ \cdots \ 0 \ (1+x)(y+z) \ 0 \ 0 \ \cdots \ 0 \right)^T.$$

This implies that we can insert this as a row in the excitation map as follows,

$$\epsilon = \left(\begin{array}{cccc|cccc} (1+y)(x+z) & 0 & 0 & \cdots & 0 & (1+x)(y+z) & 0 & 0 & \cdots & 0 \\ (1+y)(x+z) & \star & \star & \cdots & \star & (1+x)(y+z) & \star & \star & \cdots & \star \\ 0 & \star & \star & \cdots & \star & 0 & \star & \star & \cdots & \star \\ \vdots & \vdots & \vdots & \vdots & \vdots & \vdots & & & & \\ 0 & \star & \star & \cdots & \star & 0 & \star & \star & \cdots & \star \end{array} \right). \quad (8.57)$$

On applying appropriate row operations, we get

$$\epsilon = \left(\begin{array}{cccc|cccc} (1+y)(x+z) & 0 & 0 & \cdots & 0 & (1+x)(y+z) & 0 & 0 & \cdots & 0 \\ 0 & \star & \star & \cdots & \star & 0 & \star & \star & \cdots & \star \\ 0 & \star & \star & \cdots & \star & 0 & \star & \star & \cdots & \star \\ \vdots & \vdots & \vdots & \vdots & \vdots & \vdots & & & & \\ 0 & \star & \star & \cdots & \star & 0 & \star & \star & \cdots & \star \end{array} \right). \quad (8.58)$$

Thus, we have extracted a copy of the Chamon model. \square

We now give proofs of the two lemmas that were used in proving Theorem 8.8.1.

Proof of Lemma 8.8.1. The polynomial given by $s_1^\dagger \Omega_1 s_2$ encodes the commutation of translates of s_1 and s_2 . Here, $\Omega_m = \begin{pmatrix} 0 & \mathbb{1} \\ \mathbb{1} & 0 \end{pmatrix}$ is an $2m \times 2m$ symplectic form and $\mathbb{1}$ is an $m \times m$ Identity matrix. Let us denote the coefficient of g in the polynomial $s_1^\dagger \Omega_1 s_2$ as $(s_1^\dagger \Omega_1 s_2)_g$. We note that two Pauli operators a and b commute if $(a^\dagger \Omega_q b)_1 = 0$.

Note that s_1 and s_2 can be expressed as follows,

$$s_1 = (1 + y + \dots + y^{m-1})(x^{m-1} + zx^{m-2} + \dots + z^{m-1})(1, 0)^T$$

and

$$s_2 = (1 + x + \dots + x^{m-1})(y^{m-1} + zy^{m-2} + \dots + z^{m-1})(0, 1)^T.$$

Since all powers of translation variables are less than m , under coarse-graining by a factor of m in each direction, we are left with $2m$ -dimensional vectors for s_1 and s_2 with only 1s and 0s. For s_1 , the 1s appear in the first half and for s_2 , in the second half. Due to this form, $s_1^{(m)\dagger}\Omega_m s_2^{(m)} = (s_1^{(m)\dagger}\Omega_m s_2^{(m)})_1$ i.e. only the coefficient of 1 contributes and there are no monomials. Since the commutation relation between the operators s_1 and s_2 i.e. $(s_1^\dagger\Omega_1 s_2)_1$ is not affected by coarse-graining, we get

$$\begin{aligned} & s_1^{(m)\dagger}\Omega_m s_2^{(m)} \\ &= (s_1^{(m)\dagger}\Omega_m s_2^{(m)})_1 \\ &= (s_1^\dagger\Omega_1 s_2)_1 \\ &= m \pmod{2} \end{aligned} \tag{8.59}$$

Thus, $s_1^{(m)\dagger}\Omega_m s_2^{(m)} = 1$ when m is odd.

□

Proof of Lemma 8.8.2. For both s_1 and s_2 , the degrees of translation variables x , y and z range from 0 to $m - 1$. Thus, after coarse-graining, $s_1^{(m)}$ and $s_2^{(m)}$ are both supported on at only one unit cell (at location 1). In particular, $s_1^{(m)}$ is a Laurent polynomial vector over $\mathbb{F}_2[1]$, satisfying $s_1^{(m)\dagger}\Omega_m s_1^{(m)} = 0$. Since $\mathbb{F}_2[1]$ is a principal ideal domain, we can find an elementary symplectic transformation E_1 composed of CNOT gates that turns s_1 into a vector with a single nonzero component, say, g at the first entry. Since the only nonzero component in $\mathbb{F}_2[1]$ is 1, $g = 1$.

Since the transformation E_1 acts only at the origin, $E_1 s_2^{(m)}$ still acts only at location 1 and thus is a Laurent polynomial vector over $\mathbb{F}_2[1]$. Since $s_1^{(m)\dagger}\Omega_m s_2^{(m)} = 1$, the $(m^3 + 1)$ -th component of $E_1 s_2^{(m)}$ must be 1. Since $E_1 s_2^{(m)}$ can have non-zero entries i.e. 1s only in the second half of the vector, they can all be cancelled out via CNOT gates without affecting the form of $s_1^{(m)}$. Thus, the we get the form of $s_1^{(m)}$ and $s_2^{(m)}$ as desired. □

8.8.1 Explicit ER circuit

In the supplementary Mathematica file, we have constructed a circuit U which carries out an explicit ER of the Chamon model given as follows:

$$\begin{aligned} UH_C(\Lambda)U^\dagger &\sim H_C(3\Lambda) + H_{2D}(6\Lambda) + H_{2D}(6\Lambda), \\ H_{2D} &= H_x^{\text{toric}} + H_y^{\text{toric}} + H_z^{\text{toric}} + H_w^{\text{toric}}. \end{aligned} \quad (8.60)$$

Here, H_μ^{toric} is a stack of 2D toric codes along the μ direction with one layer per lattice spacing.

References

- [1] Sergey Bravyi and Jeongwan Haah. “Energy landscape of 3D spin hamiltonians with topological order”. In: *Physical Review Letters* 107.15 (Oct. 2011), p. 150504. ISSN: 00319007. DOI: 10.1103/PhysRevLett.107.150504. arXiv: 1105.4159. URL: <https://link.aps.org/doi/10.1103/PhysRevLett.107.150504>.
- [2] Sergey Bravyi and Jeongwan Haah. “Quantum self-correction in the 3D cubic code model”. In: *Physical Review Letters* 111.20 (Nov. 2013), p. 200501. ISSN: 00319007. DOI: 10.1103/PhysRevLett.111.200501. arXiv: 1112.3252. URL: <https://link.aps.org/doi/10.1103/PhysRevLett.111.200501>.
- [3] Sergey Bravyi, Bernhard Leemhuis, and Barbara M. Terhal. “Topological order in an exactly solvable 3D spin model”. In: *Ann. Phys.* 326.4 (2010), p. 839. ISSN: 00034916. DOI: 10.1016/j.aop.2010.11.002. arXiv: 1006.4871. URL: <http://arxiv.org/abs/1006.4871> <http://dx.doi.org/10.1016/j.aop.2010.11.002>.
- [4] Benjamin J. Brown and Dominic J. Williamson. “Parallelized quantum error correction with fracton topological codes”. In: (Jan. 2019), pp. 1–13. arXiv: 1901.08061. URL: <http://arxiv.org/abs/1901.08061>.
- [5] Daniel Bulmash and Maissam Barkeshli. “Gauging fractons: immobile non-Abelian quasiparticles, fractals, and position-dependent degeneracies”. In: (May 2019). arXiv: 1905.05771. URL: <http://arxiv.org/abs/1905.05771>.
- [6] Daniel Bulmash and Thomas Iadecola. “Braiding and gapped boundaries in fracton topological phases”. In: *Phys. Rev. B* 99 (12 Mar. 2019), p. 125132. DOI: 10.1103/PhysRevB.99.125132. arXiv: 1810.00012. URL: <https://link.aps.org/doi/10.1103/PhysRevB.99.125132>.
- [7] Claudio Castelnovo and Claudio Chamon. “Topological quantum glassiness”. In: *Philosophical Magazine* 92.1-3 (2012), pp. 304–323. ISSN: 14786435. DOI: 10.1080/14786435.2011.609152. arXiv: 1108.2051. URL: <https://doi.org/10.1080/14786435.2011.609152>.

- [8] Claudio Castelnovo, Claudio Chamon, and David Sherrington. “Quantum mechanical and information theoretic view on classical glass transitions”. In: *Physical Review B* 81.18 (May 2010), p. 184303. ISSN: 10980121. DOI: 10.1103/PhysRevB.81.184303. arXiv: 1003.3832. URL: <https://link.aps.org/doi/10.1103/PhysRevB.81.184303>.
- [9] Claudio Chamon. “Quantum glassiness in strongly correlated clean systems: An example of topological overprotection”. In: *Physical Review Letters* 94.4 (Jan. 2005), p. 40402. ISSN: 00319007. DOI: 10.1103/PhysRevLett.94.040402. arXiv: 0404182 [cond-mat]. URL: <https://link.aps.org/doi/10.1103/PhysRevLett.94.040402>.
- [10] Xie Chen, Zheng-Cheng Gu, and Xiao-Gang Wen. “Local unitary transformation, long-range quantum entanglement, wave function renormalization, and topological order”. In: *Physical Review B* 82.15 (Oct. 2010). ISSN: 1550-235X. DOI: 10.1103/physrevb.82.155138. URL: <http://dx.doi.org/10.1103/PhysRevB.82.155138>.
- [11] Trithep Devakul. “Z₃ topological order in the face-centered-cubic quantum plaquette model”. In: *Physical Review B* 97.15 (Apr. 2018), p. 155111. ISSN: 24699969. DOI: 10.1103/PhysRevB.97.155111. arXiv: 1712.05377. URL: <https://link.aps.org/doi/10.1103/PhysRevB.97.155111>.
- [12] Trithep Devakul, S. A. Parameswaran, and S. L. Sondhi. “Correlation function diagnostics for type-I fracton phases”. In: *Physical Review B* 97.4 (Jan. 2018), p. 41110. ISSN: 24699969. DOI: 10.1103/PhysRevB.97.041110. arXiv: 1709.10071. URL: <https://link.aps.org/doi/10.1103/PhysRevB.97.041110>.
- [13] Trithep Devakul, Wilbur Shirley, and Juven Wang. “Strong planar subsystem symmetry-protected topological phases and their dual fracton orders”. In: *Physical Review Research* 2.1 (Mar. 2020). DOI: 10.1103/physrevresearch.2.012059. URL: <https://doi.org/10.1103/2Fphysrevresearch.2.012059>.
- [14] Trithep Devakul, Dominic J. Williamson, and Yizhi You. “Classification of subsystem symmetry-protected topological phases”. In: *Physical Review B* 98.23 (Dec. 2018), p. 235121. ISSN: 24699969. DOI: 10.1103/PhysRevB.98.235121. arXiv: 1808.05300. URL: <http://arxiv.org/abs/1808.05300>.
- [15] Arpit Dua et al. “Bifurcating entanglement-renormalization group flows of fracton stabilizer models”. In: *Physical Review Research* 2.3 (July 2020). ISSN: 2643-1564. DOI: 10.1103/physrevresearch.2.033021. URL: <http://dx.doi.org/10.1103/PhysRevResearch.2.033021>.

- [16] Arpit Dua et al. “Compactifying fracton stabilizer models”. In: *Phys. Rev. B* 99.24 (Mar. 2019). ISSN: 2469-9950. DOI: 10.1103/physrevb.99.245135. arXiv: 1903.12246. URL: <http://arxiv.org/abs/1903.12246>.
- [17] Arpit Dua et al. “Sorting topological stabilizer models in three dimensions”. In: *Physical Review B* 100.15 (Oct. 2019). DOI: 10.1103/physrevb.100.155137. URL: <https://doi.org/10.1103/PhysRevB.100.155137>.
- [18] Pranay Gorantla et al. “Low-energy limit of some exotic lattice theories and UV/IR mixing”. In: *Physical Review B* 104.23 (Dec. 2021). ISSN: 2469-9969. DOI: 10.1103/physrevb.104.235116. URL: <http://dx.doi.org/10.1103/PhysRevB.104.235116>.
- [19] Jeongwan Haah. “Bifurcation in entanglement renormalization group flow of a gapped spin model”. In: *Physical Review B* 89.7 (Feb. 2014), p. 75119. ISSN: 10980121. DOI: 10.1103/PhysRevB.89.075119. arXiv: 1310.4507. URL: <https://link.aps.org/doi/10.1103/PhysRevB.89.075119>.
- [20] Jeongwan Haah. “Commuting Pauli Hamiltonians as Maps between Free Modules”. In: *Communications in Mathematical Physics* 324.2 (2013), pp. 351–399. ISSN: 00103616. DOI: 10.1007/s00220-013-1810-2. arXiv: 1204.1063. URL: <http://dx.doi.org/10.1007/s00220-013-1810-2>.
- [21] Jeongwan Haah. “Lattice quantum codes and exotic topological phases of matter”. In: (May 2013). ISSN: 00029629. DOI: 10.1097/MAJ.0b013e3181d65685. arXiv: 1305.6973. URL: <http://arxiv.org/abs/1305.6973>.
- [22] Jeongwan Haah. “Local stabilizer codes in three dimensions without string logical operators”. In: *Physical Review A* 83.4 (Apr. 2011). ISSN: 1094-1622. DOI: 10.1103/physreva.83.042330. URL: <http://dx.doi.org/10.1103/PhysRevA.83.042330>.
- [23] Jeongwan Haah. “Local stabilizer codes in three dimensions without string logical operators”. In: *Physical Review A - Atomic, Molecular, and Optical Physics* 83.4 (Apr. 2011), p. 42330. ISSN: 10502947. DOI: 10.1103/PhysRevA.83.042330. arXiv: 1101.1962. URL: <https://link.aps.org/doi/10.1103/PhysRevA.83.042330>.
- [24] Gábor B. Halász, Timothy H. Hsieh, and Leon Balents. “Fracton Topological Phases from Strongly Coupled Spin Chains”. In: *Physical Review Letters* 119.25 (Dec. 2017), p. 257202. ISSN: 10797114. DOI: 10.1103/PhysRevLett.119.257202. arXiv: 1707.02308. URL: <https://link.aps.org/doi/10.1103/PhysRevLett.119.257202>.
- [25] Gábor B. Halász, Timothy H. Hsieh, and Leon Balents. “Fracton Topological Phases from Strongly Coupled Spin Chains”. In: *Physical Review Letters* 119.25 (Dec. 2017). ISSN: 1079-7114. DOI: 10.1103/

- physrevlett.119.257202. URL: <http://dx.doi.org/10.1103/PhysRevLett.119.257202>.
- [26] Huan He et al. “Entanglement entropy from tensor network states for stabilizer codes”. In: *Physical Review B* 97.12 (Mar. 2018), p. 125102. ISSN: 24699969. DOI: 10.1103/PhysRevB.97.125102. arXiv: 1710.04220. URL: <https://link.aps.org/doi/10.1103/PhysRevB.97.125102>.
- [27] Timothy H. Hsieh and Gábor B. Halász. “Fractons from partons”. In: *Phys. Rev. B* 96 (16 Oct. 2017), p. 165105. DOI: 10.1103/PhysRevB.96.165105. arXiv: 1703.02973. URL: <https://link.aps.org/doi/10.1103/PhysRevB.96.165105>.
- [28] Isaac H. Kim. “3D local qubit quantum code without string logical operator”. In: (2012). arXiv: 1202.0052. URL: <http://arxiv.org/abs/1202.0052>.
- [29] Isaac H. Kim and Jeongwan Haah. “Localization from superselection rules in translation invariant systems”. In: *Physical Review Letters* 116.2 (Jan. 2016), p. 027202. ISSN: 10797114. DOI: 10.1103/PhysRevLett.116.027202. arXiv: 1505.01480. URL: <http://arxiv.org/pdf/1505.01480.pdf>.
- [30] A. Yu Kitaev. “Fault-tolerant quantum computation by anyons”. In: *Annals of Physics* 303.1 (Jan. 2003), pp. 2–30. ISSN: 00034916. DOI: 10.1016/S0003-4916(02)00018-0. arXiv: 9707021 [quant-ph]. URL: <https://www.sciencedirect.com/science/article/pii/S0003491602000180?via=ihub> <http://www.sciencedirect.com/science/article/pii/S0003491602000180>.
- [31] Kitaev Alexei. “Anyons in an exactly solved model and beyond”. In: *Annals of Physics* 321.1 (2006), pp. 2–111. ISSN: 0003-4916. DOI: 10.1016/j.aop.2005.10.005. URL: <http://www.sciencedirect.com/science/article/pii/S0003491605002381>.
- [32] Aleksander Kubica and Beni Yoshida. *Ungauging quantum error-correcting codes*. 2018. arXiv: 1805.01836. URL: <http://arxiv.org/abs/1805.01836>.
- [33] R. B. Laughlin. “Anomalous Quantum Hall Effect: An Incompressible Quantum Fluid with Fractionally Charged Excitations”. In: *Phys. Rev. Lett.* 50 (18 May 1983), pp. 1395–1398. DOI: 10.1103/PhysRevLett.50.1395. URL: <https://link.aps.org/doi/10.1103/PhysRevLett.50.1395>.
- [34] Michael Levin and Zheng-Cheng Gu. “Braiding statistics approach to symmetry-protected topological phases”. In: *Physical Review B* 86.11 (Sept. 2012). DOI: 10.1103/physrevb.86.115109. URL: <https://doi.org/10.1103/physrevb.86.115109>.

- [35] Michael Levin and Xiao-Gang Wen. “Fermions, strings, and gauge fields in lattice spin models”. In: *Phys. Rev. B* 67 (24 June 2003), p. 245316. DOI: 10.1103/PhysRevB.67.245316. URL: <https://link.aps.org/doi/10.1103/PhysRevB.67.245316>.
- [36] Han Ma et al. “Fracton topological order via coupled layers”. In: *Physical Review B* 95.24 (June 2017), p. 245126. ISSN: 24699969. DOI: 10.1103/PhysRevB.95.245126. arXiv: 1701.00747. URL: <https://link.aps.org/doi/10.1103/PhysRevB.95.245126>.
- [37] Han Ma et al. “Topological entanglement entropy of fracton stabilizer codes”. In: *Physical Review B* 97.12 (Mar. 2018), p. 125101. ISSN: 24699969. DOI: 10.1103/PhysRevB.97.125101. arXiv: 1710.01744. URL: <https://link.aps.org/doi/10.1103/PhysRevB.97.125101>.
- [38] Xiuqi Ma et al. “Fractonic order in infinite-component Chern-Simons gauge theories”. In: (2020). DOI: 10.48550/ARXIV.2010.08917. URL: <https://arxiv.org/abs/2010.08917>.
- [39] Abhinav Prem and Dominic J. Williamson. “Gauging permutation symmetries as a route to non-Abelian fractons”. In: (May 2019). arXiv: 1905.06309. URL: <http://arxiv.org/abs/1905.06309>.
- [40] Abhinav Prem et al. “Cage-Net Fracton Models”. In: *Phys. Rev. X* 9 (2 Apr. 2019), p. 021010. DOI: 10.1103/PhysRevX.9.021010. arXiv: 1806.04687. URL: <https://link.aps.org/doi/10.1103/PhysRevX.9.021010>.
- [41] Mark Wild de Propitius and F. Alexander Bais. “Discrete Gauge Theories”. In: *Particles and Fields*. Ed. by Gordon Semenoff and Luc Vinet. New York, NY: Springer New York, 1999, pp. 353–439. ISBN: 978-1-4612-1410-6. DOI: 10.1007/978-1-4612-1410-6_8. URL: https://doi.org/10.1007/978-1-4612-1410-6_8.
- [42] Albert T. Schmitz, Sheng-Jie Huang, and Abhinav Prem. “Entanglement spectra of stabilizer codes: A window into gapped quantum phases of matter”. In: *Phys. Rev. B* 99 (20 May 2019), p. 205109. DOI: 10.1103/PhysRevB.99.205109. arXiv: 1901.10486. URL: <https://link.aps.org/doi/10.1103/PhysRevB.99.205109>.
- [43] Bowen Shi and Yuan Ming Lu. “Deciphering the nonlocal entanglement entropy of fracton topological orders”. In: *Physical Review B* 97.14 (Apr. 2018), p. 144106. ISSN: 24699969. DOI: 10.1103/PhysRevB.97.144106. arXiv: 1705.09300. URL: <https://link.aps.org/doi/10.1103/PhysRevB.97.144106>.
- [44] Wilbur Shirley. *Fractonic order and emergent fermionic gauge theory*. 2020. arXiv: 2002.12026 [cond-mat.str-el].

- [45] Wilbur Shirley, Kevin Slagle, and Xie Chen. “Foliated fracton order from gauging subsystem symmetries”. In: *SciPost Phys.* 6 (4 2019), p. 41. DOI: 10.21468/SciPostPhys.6.4.041. arXiv: 1806.08679. URL: <https://scipost.org/10.21468/SciPostPhys.6.4.041>.
- [46] Wilbur Shirley, Kevin Slagle, and Xie Chen. “Foliated fracton order in the checkerboard model”. In: (2018). arXiv: 1806.08633. URL: <http://arxiv.org/abs/1806.08633>.
- [47] Wilbur Shirley, Kevin Slagle, and Xie Chen. “Fractional excitations in foliated fracton phases”. In: (2018). arXiv: 1806.08625. URL: <http://arxiv.org/abs/1806.08625>.
- [48] Wilbur Shirley, Kevin Slagle, and Xie Chen. “Twisted foliated fracton phases”. In: (July 2019). arXiv: 1907.09048. URL: <http://arxiv.org/abs/1907.09048>.
- [49] Wilbur Shirley et al. “Fracton Models on General Three-Dimensional Manifolds”. In: *Physical Review X* 8.3 (2018). ISSN: 21603308. arXiv: 1712.05892. URL: <http://arxiv.org/abs/1712.05892>.
- [50] Kevin Slagle and Yong Baek Kim. “Fracton topological order from nearest-neighbor two-spin interactions and dualities”. In: *Physical Review B* 96.16 (Oct. 2017), p. 165106. ISSN: 24699969. DOI: 10.1103/PhysRevB.96.165106. arXiv: 1704.03870. URL: <https://link.aps.org/doi/10.1103/PhysRevB.96.165106>.
- [51] Kevin Slagle and Yong Baek Kim. “Quantum field theory of X-cube fracton topological order and robust degeneracy from geometry”. In: *Physical Review B* 96.19 (Nov. 2017), p. 195139. ISSN: 24699969. DOI: 10.1103/PhysRevB.96.195139. arXiv: 1708.04619. URL: <https://link.aps.org/doi/10.1103/PhysRevB.96.195139>.
- [52] Kevin Slagle and Yong Baek Kim. “X-cube model on generic lattices: Fracton phases and geometric order”. In: *Physical Review B* 97.16 (Apr. 2018), p. 165106. ISSN: 24699969. DOI: 10.1103/PhysRevB.97.165106. arXiv: 1712.04511. URL: <https://link.aps.org/doi/10.1103/PhysRevB.97.165106>.
- [53] Hao Song et al. “Fracton self-statistics”. In: (In preparation).
- [54] Hao Song et al. “Twisted fracton models in three dimensions”. In: *Phys. Rev. B* 99 (15 Apr. 2019), p. 155118. DOI: 10.1103/PhysRevB.99.155118. arXiv: 1805.06899. URL: <https://link.aps.org/doi/10.1103/PhysRevB.99.155118>.
- [55] Zijian Song et al. *Topological defect network representations of fracton stabilizer codes*. 2021. arXiv: 2112.14717 [cond-mat.str-el].

- [56] Nathanan Tantivasadakarn. “Jordan-Wigner dualities for translation-invariant Hamiltonians in any dimension: Emergent fermions in fracton topological order”. In: *Physical Review Research* 2.2 (June 2020). DOI: 10.1103/physrevresearch.2.023353. URL: <https://doi.org/10.1103/physrevresearch.2.023353>.
- [57] Nathanan Tantivasadakarn, Wenjie Ji, and Sagar Vijay. “Hybrid fracton phases: Parent orders for liquid and nonliquid quantum phases”. In: *Physical Review B* 103.24 (June 2021). DOI: 10.1103/physrevb.103.245136. URL: <https://doi.org/10.1103/physrevb.103.245136>.
- [58] G. Vidal. “Entanglement renormalization”. In: *Physical Review Letters* 99.22 (Nov. 2007), p. 220405. ISSN: 00319007. DOI: 10.1103/PhysRevLett.99.220405. arXiv: 0512165 [cond-mat]. URL: <http://link.aps.org/doi/10.1103/PhysRevLett.99.220405>.
- [59] Sagar Vijay. “Isotropic Layer Construction and Phase Diagram for Fracton Topological Phases”. In: (2017). arXiv: 1701.00762. URL: <http://arxiv.org/abs/1701.00762>.
- [60] Sagar Vijay and Liang Fu. “A Generalization of Non-Abelian Anyons in Three Dimensions”. In: (2017). arXiv: 1706.07070. URL: <http://arxiv.org/abs/1706.07070>.
- [61] Sagar Vijay, Jeongwan Haah, and Liang Fu. “A new kind of topological quantum order: A dimensional hierarchy of quasiparticles built from stationary excitations”. In: *Physical Review B* 92.23 (Dec. 2015), p. 235136. ISSN: 1550235X. DOI: 10.1103/PhysRevB.92.235136. arXiv: 1505.02576. URL: <https://link.aps.org/doi/10.1103/PhysRevB.92.235136>.
- [62] Sagar Vijay, Jeongwan Haah, and Liang Fu. “Fracton Topological Order, Generalized Lattice Gauge Theory and Duality”. In: *Physical Review B* 94.23 (Dec. 2016), p. 235157. ISSN: 24699969. DOI: 10.1103/PhysRevB.94.235157. arXiv: 1603.04442. URL: <http://arxiv.org/abs/1603.04442> <http://dx.doi.org/10.1103/PhysRevB.94.235157>.
- [63] Taige Wang, Wilbur Shirley, and Xie Chen. “Foliated fracton order in the Majorana checkerboard model”. In: (Apr. 2019). arXiv: 1904.01111. URL: <http://arxiv.org/abs/1904.01111>.
- [64] Zack Weinstein, Gerardo Ortiz, and Zohar Nussinov. “Universality Classes of Stabilizer Code Hamiltonians”. In: (July 2019). arXiv: 1907.04180. URL: <https://arxiv.org/abs/1907.04180>.
- [65] Zack Weinstein et al. “Absence of Finite Temperature Phase Transitions in the X-Cube Model and its Z_p Generalization”. In: (2018). arXiv: 1812.04561.

- [66] Xiao Gang Wen. “Quantum Orders in an Exact Soluble Model”. In: *Physical Review Letters* 90.1 (Jan. 2003), p. 4. ISSN: 10797114. DOI: 10.1103/PhysRevLett.90.016803. arXiv: 0205004 [quant-ph]. URL: <https://link.aps.org/doi/10.1103/PhysRevLett.90.016803>.
- [67] Xiao-Gang Wen. “Topological orders and edge excitations in fractional quantum Hall states”. In: *Advances in Physics* 44.5 (Oct. 1995), pp. 405–473. DOI: 10.1080/00018739500101566. URL: <https://doi.org/10.1080%2F00018739500101566>.
- [68] Dominic J. Williamson. “Fractal symmetries: Ungauging the cubic code”. In: *Physical Review B* 94.15 (Oct. 2016), p. 155128. ISSN: 24699969. DOI: 10.1103/PhysRevB.94.155128. arXiv: 1603.05182. URL: <https://link.aps.org/doi/10.1103/PhysRevB.94.155128>.
- [69] Edward Witten. “Topological quantum field theory”. In: *Communications in Mathematical Physics* 117.3 (1988), pp. 353–386. DOI: [cnp/1104161738](https://doi.org/10.1007/BF01206733). URL: <https://doi.org/>.
- [70] Xuefeng Yin, Jianjun Zhang, and Xiaofang Wang. “Sequential injection analysis system for the determination of arsenic by hydride generation atomic absorption spectrometry”. In: *Fenxi Huaxue* 32.10 (2004), pp. 1365–1367. ISSN: 02533820. DOI: 10.1017/CB09781107415324.004. arXiv: arXiv:1011.1669v3. URL: <http://arxiv.org/abs/quant-ph/9705052>.
- [71] Beni Yoshida. “Exotic topological order in fractal spin liquids”. In: *Physical Review B* 88.12 (Sept. 2013), p. 125122. ISSN: 10980121. DOI: 10.1103/PhysRevB.88.125122. arXiv: 1302.6248. URL: <https://link.aps.org/doi/10.1103/PhysRevB.88.125122>.
- [72] Yizhi You. “Non-Abelian defects in Fracton phase of matter”. In: (Jan. 2019). arXiv: 1901.07163v1. URL: <https://arxiv.org/pdf/1901.07163.pdf>.
- [73] Yizhi You et al. “Fractonic Chern-Simons and BF theories”. In: (Apr. 2019). arXiv: 1904.11530. URL: <https://arxiv.org/abs/1904.11530>.
- [74] Yizhi You et al. “Subsystem symmetry protected topological order”. In: *Physical Review B* 98.3 (2018). ISSN: 24699969. DOI: 10.1103/PhysRevB.98.035112. arXiv: 1803.02369.
- [75] Yizhi You et al. “Symmetric Fracton Matter: Twisted and Enriched”. In: (2018). arXiv: 1805.09800. URL: <http://arxiv.org/abs/1805.09800>.

TWISTED FOLIATED FRACTON PHASES

9.1 Introduction

The discovery of various “fracton” models [3, 6, 7, 11, 22, 23, 25, 33, 35, 40, 41, 56, 58, 62–67, 77, 79] has greatly expanded our understanding of gapped phases in three-dimensional systems. A salient feature characterizing this set of models is the existence of gapped fractional point excitations with restricted mobility. Gapped fracton models¹ are divided into two major classes according to how the motion of point excitations is constrained: type I and type II. In type II models, fractional point excitations can only move in coordination as a set and individually they cannot move at all. These excitations are said to be immobile and are called ‘fractons’. In type I models, on the other hand, apart from fracton excitations, there can also exist lineons and planons – fractional excitations which can move by themselves within a plane or along a line. The restricted mobility of the point excitations leads to various new features in the fracton models: a slow thermalization process [4, 37–39, 48], stable extensive ground state degeneracy, unusual entanglement scaling [24, 34, 49, 53], etc. [5, 9, 27, 36, 74, 75, 78].

Among the type I fracton models, we have found that many of them have a hidden ‘foliation’ structure and are said to have ‘foliated fracton order’ (FFO) [53, 54]. That is, starting from a model with a larger system size, we can apply a finite depth local unitary transformation and map the model to a smaller system size together with decoupled layers of 2D gapped states, as illustrated in Fig. 9.1(a). As there should be no fundamental change in the order of the system simply due to the change in system size, we should think of the 2D gapped states as free resources in the study of these 3D fracton models even though the 2D gapped states can have highly nontrivial topological order of their own. Correspondingly, we define two foliated fracton models to have the same ‘foliated fracton order’ if they can be related through a finite depth local unitary transformation upon the addition of decoupled stacks of 2D layers of gapped states, as shown in Fig. 9.1(b).

¹There are also gapless $U(1)$ fracton models which will not be addressed in this work (see Refs. [8, 21, 28, 32, 42, 47, 59, 73, 76]).

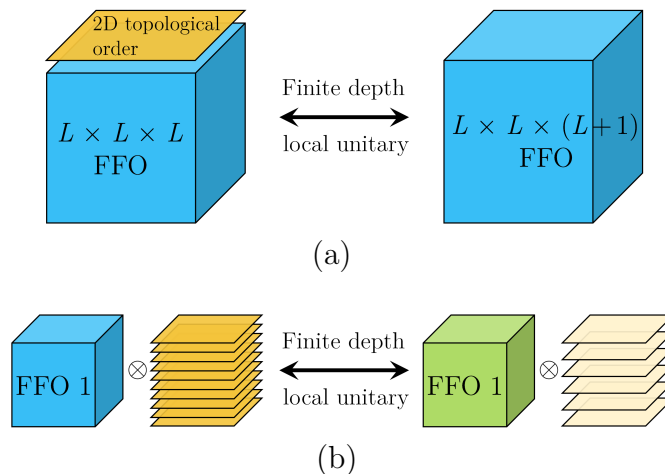


Figure 9.1: Foliated fracton order: (a) In a model with FFO, different system sizes are related through the addition or removal of 2D layers and finite depth local unitary transformations. (b) Two models have the same FFO if they are related through the addition of decoupled stacks of 2D layers and finite depth local unitary transformation.

Using this definition, we have found that many of the type I fracton models with a foliation structure actually have the same foliated fracton order. In particular, we have shown explicitly that the spin checkerboard model, the Majorana checkerboard model, and the semionic X-cube model all have the same FFO as the X-cube model (or multiple copies of it) [51, 52, 69]. The untwisted string-membrane-net model discussed in Ref. [55] was also shown to be equivalent to the X-cube model. As the X-cube model [67] can be obtained by gauging the intersecting planar subsystem symmetries of a trivial 3D paramagnet [50, 67], the X-cube FFO is considered to be untwisted. It is similar to the toric code model as an untwisted Z_2 gauge theory which can be obtained by gauging the global Z_2 symmetry of a trivial 2D paramagnet. It is known that 2D Z_2 gauge theory can also be ‘twisted’ where the gauge flux becomes a semionic excitation. It can be obtained from gauging the 2D symmetry protected topological order with Z_2 symmetry as shown in Ref. [30]. It is then natural to ask whether there exists twisted FFO.

In this paper, we identify three-dimensional fracton models with a ‘twisted’ FFO. That is, these models have an FFO that is different from that of the X-cube model. Moreover, they can be obtained by gauging a 3D model with subsystem planar symmetries that is not a trivial paramagnet. In other words, the ungauged model has (strong) symmetry protected topological order with

subsystem planar symmetries. Note that although twisted fracton models have already appeared in the literature [15, 60, 81], they have not been studied in terms of their foliated fracton order. We discuss two (sets of) examples in detail. One is 3-foliated, meaning that we can decouple 2D topological layers in three different directions using finite depth local unitary transformations. The X-cube model is also 3-foliated in this sense and we can consider this new model as the twisted version of two copies of the X-cube model. The other example is 1-foliated, meaning that we can only decouple 2D topological layers in one direction from the model. The untwisted version of a 1-foliated model with Z_2 symmetries would simply be a decoupled stack of 2D toric codes.

The paper is organized as follows: In section 9.2, we discuss the 3-foliated model by presenting the construction of the model, demonstrating its foliation structure and then showing that its FFO is different from that of the X-cube model. In section 9.3, we do the same for the 1-foliated model. We discuss in section 9.4 how to ‘ungauge’ the models into models with subsystem symmetry protected topological order before summarizing in section 9.5.

9.2 Twisted 3-Foliated Model

In this section, we describe a model that is foliated in the x , y , and z directions by layers of a twisted 2D $Z_2 \times Z_2$ gauge theory. We will see that its foliated fracton order (FFO) is twisted in the sense that its FFO is distinct from that of the X-cube model or copies of it. (A brief review of the X-cube model is given in Appendix 9.6.) Ungauging this fracton model results in a paramagnetic model with (strong) subsystem symmetry protected topological (SSPT) order under 3 sets of intersecting planar subsystem symmetries.

The model is constructed by strongly coupling intersecting layers of a set of 3 perpendicular stacks of twisted 2D $Z_2 \times Z_2$ gauge theories, in a manner akin to the construction of the X-cube and semionic X-cube models from stacks of 2D toric code layers and 2D double semion layers respectively. These constructions are discussed in Refs. [33] and [64]. Like the semionic X-cube model, the 3-foliated model constructed in this section belongs to the class of exactly solvable *twisted fracton models* considered in Ref. [60]. Here, we are able to extend our understanding by studying the model through the lens of the coupled layer construction and as an FFO. Unlike the semionic X-cube model, this $Z_2 \times Z_2$ model has twisted FFO; thus, there is a distinction between

a fracton model being *twisted* in the sense of Ref. [60], and a model having *twisted* FFO.

9.2.1 Model Construction

9.2.1.1 2D $Z_2 \times Z_2$ twisted gauge theory

First, we briefly review the properties of $Z_2 \times Z_2$ twisted gauge theories in 2D, and describe an exactly solvable model for one such theory. Twisted gauge theories may be thought of as Hamiltonian realizations of 2+1d Dijkgraaf-Witten models [16], or as the result of gauging global symmetries in paramagnets with non-trivial symmetry-protected topological (SPT) order [30]. For $Z_2 \times Z_2$ symmetry, there are $2^3 = 8$ distinct SPT phases in 2D, corresponding to the 8 elements of $H^3(Z_2 \times Z_2, U(1))$ [12]. They are characterized by the topological invariants N_1 , N_2 , and N_{12} , each of which takes values 0 or 1. Upon gauging, the exchange statistics of the gauge fluxes are given by i^{N_1} and i^{N_2} , whereas the braiding statistics between the two fluxes is $i^{N_{12}}$. In all cases the statistics between gauge charge and corresponding gauge flux is -1 [68].

Here, we will focus on the twisted gauge theory obtained from the SPT phase with $N_{12} = 1$ and $N_1 = N_2 = 0$. In this case, the elementary gauge charges e_A and e_B and bosonic gauge fluxes m_A and m_B obey the following fusion rules:

$$e_A^2 = e_B^2 = 1 \quad m_A^2 = e_B \quad m_B^2 = e_A. \quad (9.1)$$

Thus, as an intrinsic topological order, this theory is equivalent to the Z_4 toric code, with m_A and m_B mapping onto the \tilde{e} and \tilde{m} Z_4 anyons of the Z_4 toric code, respectively.

There is a convenient isomorphism between the Z_4 clock and shift algebra and the two qubit operator algebra, $\tilde{Z} \rightarrow X^A S^B$, $\tilde{X} \rightarrow X^B C Z^{AB}$, where \tilde{Z} and \tilde{X} are the clock and shift generators of the Z_4 operator algebra with $\tilde{Z}\tilde{X} = i\tilde{X}\tilde{Z}$, Z and X are the clock and shift (Pauli) operators of the Z_2 algebra, S is the one-qubit phase gate $\text{diag}(1, i)$, CZ is the two-qubit controlled-Z operator $\text{diag}(1, 1, 1, -1)$, and A and B label the two qubits. Applied to the Z_4 toric code degrees of freedom, this mapping naturally allows one to write the $Z_2 \times Z_2$ twisted gauge theory as a $Z_2 \times Z_2$ string-net model, such that the gauge charges correspond to violations of the plaquette terms.

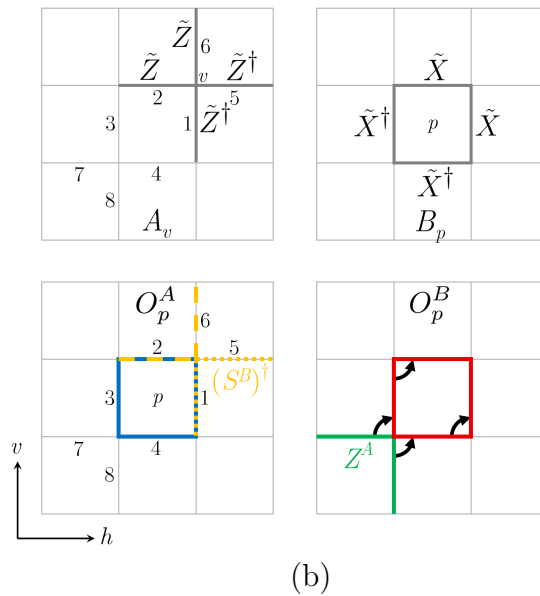
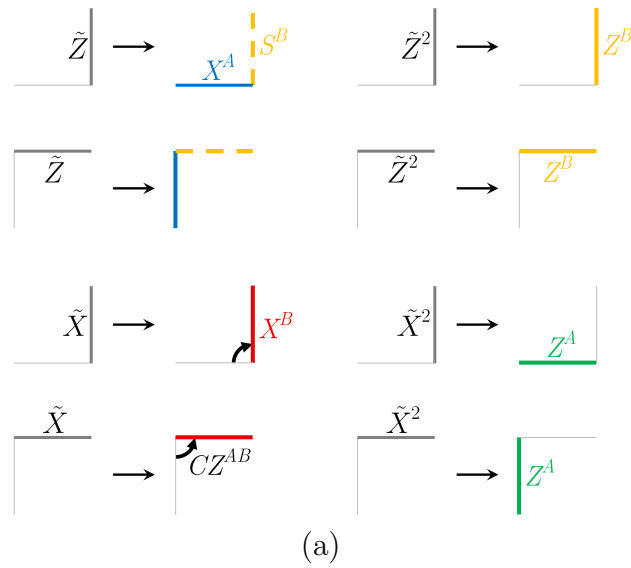


Figure 9.2: (a) Transformation from Z_4 qudit degrees of freedom to two Z_2 qubit degrees of freedom. (b) Operators A_v , B_p , O_p^A , and O_p^B . In the bottom figures, blue represents X^A , red represents X^B , dashed yellow represents S^B , dotted yellow represents $(S^B)^\dagger$, green represents Z^A , and the black arrows represent CZ^{AB} from A to B . The action of Z , S , and CZ gates *precede* the action of the X gates.

In particular, consider the Z_4 toric code Hamiltonian on a square lattice:

$$H_{TC} = - \sum_v (A_v + A_v^2 + A_v^3) - \sum_p (B_p + B_p^2 + B_p^3) \quad (9.2)$$

where $A_v = \tilde{Z}_1^\dagger \tilde{Z}_5^\dagger \tilde{Z}_6 \tilde{Z}_2$ and $B_p = \tilde{X}_1 \tilde{X}_2 \tilde{X}_3^\dagger \tilde{X}_4^\dagger$ per Fig. 9.2. The A_v^2 and B_p^2 terms are redundant, but we keep them in the Hamiltonian so that the transformed Hamiltonian has a convenient correspondence with the string-net formulation 31.

After mapping to qubit degrees of freedom and shifting qubit A downward and to the left by half a lattice spacing [as shown in Fig. 9.2(a)], H_{TC} is transformed into the $Z_2 \times Z_2$ twisted gauge theory Hamiltonian

$$H_{2D} = - \sum_v (Q_v^A + Q_v^B) - \sum_p (O_p^A + O_p^B + \text{h.c.}), \quad (9.3)$$

where $Q_v^\mu = \prod_{l \in v} Z_l^\mu$, and (see Fig. 9.2)

$$\begin{aligned} O_p^A &= X_1^A X_2^A X_3^A X_4^A (S_1^B)^\dagger (S_5^B)^\dagger S_6^B S_2^B, \\ O_p^B &= X_1^B X_2^B X_3^B X_4^B C Z_{32}^{AB} C Z_{41}^{AB} C Z_{73}^{AB} C Z_{84}^{AB} Z_7^A Z_8^A. \end{aligned} \quad (9.4)$$

In particular, $A_v \rightarrow O_p^A$, $A_v^3 \rightarrow (O_p^A)^\dagger$, $B_p \rightarrow O_p^B$, $B_p^3 \rightarrow (O_p^B)^\dagger$, $A_v^2 \rightarrow Q_v^A$, and $B_p^2 \rightarrow Q_v^B$. Note that $(X^B C Z^{AB})^\dagger = X^B C Z^{AB} Z^A$.

As this transformation is an exact mapping, it is obviously possible to carry through the following construction in terms of the original Z_4 degrees of freedom. As we will see however, the $Z_2 \times Z_2$ degrees of freedom provide a more natural language to analyze the emergent fracton order.

9.2.1.2 Coupled layers construction

The construction of the 3-foliated fracton model is a straightforward generalization of the construction of the X-cube and semionic X-cube models in Refs. 33. We first start with 3 mutually perpendicular intersecting stacks of the $Z_2 \times Z_2$ twisted gauge theory model H_{2D} , oriented as in Fig. 9.3. Recall that H_{2D} contains 2 qubit degrees of freedom (A and B) on each edge of a square lattice. Each edge of the 2D layers coincides with another edge from an orthogonal layer to form a cubic lattice, with each edge containing 4 qubits. Then, couplings of the form $Z^A Z^A$ and $Z^B Z^B$ between qubits on the same edge are added to the Hamiltonian.

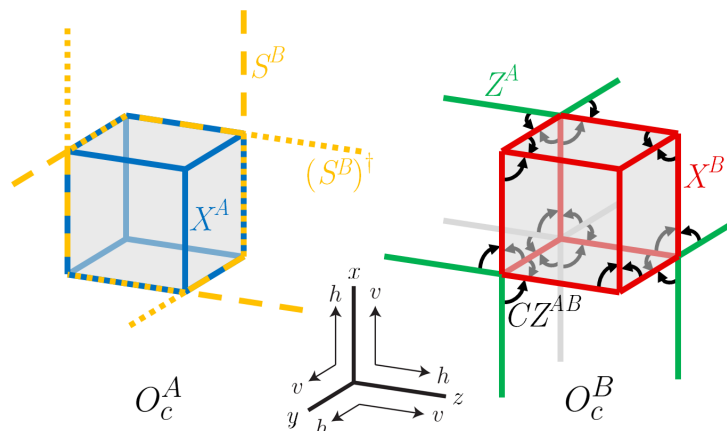


Figure 9.3: Cube operators of H_{3D} . Here, blue represents X^A , red represents X^B , dashed yellow represents S^B , dotted yellow represents $(S^B)^\dagger$, green represents Z^A , and the black arrows represent CZ^{AB} from A to B . The action of Z , S , and CZ gates precede the action of the X gates.

In the strong coupling limit, the four qubits at each edge merge into two. The following effective Hamiltonian emerges at lowest order in perturbation theory:

$$\begin{aligned}
 H_{3D} = & - \sum_v \sum_{\sigma=x,y,z} (Q_{v,\sigma}^A + Q_{v,\sigma}^B) \\
 & - \sum_c (O_c^A + O_c^B + \text{h.c.}),
 \end{aligned} \tag{9.5}$$

where v runs over vertices of the cubic lattice and c runs over the elementary cubes. $Q_{v,\sigma}^\mu$ are vertex terms equal to products of Pauli Z^μ operators over the links adjacent to v in the plane normal to σ . The cube operators O_c^A and O_c^B are depicted graphically in Fig. 9.3. The terms of H_{3D} are mutually commuting and unfrustrated and thus the model is exactly solvable. It bears striking similarity to (two copies of) the X-cube model: the vertex terms are identical, and the cube terms are similar in that they involve products of Pauli X operators over the edges of the cube. However, they contain additional phase factors not present in the X-cube terms.

As in the X-cube model, excitations of the vertex constraints are lineons whereas excitations of the cube terms are fractons. Lineons are created at the endpoints of open rigid string operators, whereas fractons are created at the corners of membrane operators. Examples of these operators are given in the discussion of interferometric operators in Sec. 9.2.3.2. Like the X-cube model, planons also exist as fracton dipoles and lineon dipoles, as will be

discussed in detail below.

9.2.2 Fractional excitations

In the intermediate coupling regime, the transition to the strong-coupling phase can be thought of as a condensation of A and B type charge loops; correspondingly the ground state of H_{3D} may be viewed as a condensate of charge loops. This mechanism has been studied in detail and dubbed p -string condensation in Ref. [33]. The structure of excitations in the condensed phase can be understood in terms of the degrees of freedom of the pre-condensed stacks of twisted $Z_2 \times Z_2$ gauge theories. Similar to the case of the X-cube model discussed in Refs. [33], the 2D gauge charges of the original decoupled stacks fractionalize into fracton dipoles (a pair of adjacent fractons whose axis is normal to the 2D layer), and remain as Z_2 planons. These planons will be labelled $e_{\mu\nu,i}^A$ and $e_{\mu\nu,i}^B$ where $\mu\nu, i$ refers to the plane of mobility (μ and ν the planar axes and i the coordinate in the normal direction). In the charge loop picture, individual fractons correspond to endpoints of open charge strings above the condensate. They will be denoted as f_{ijk}^A and f_{ijk}^B , where ijk denotes spatial location, and likewise inherit Z_2 fusion rules:

$$(f_{ijk}^A)^2 = (f_{ijk}^B)^2 = (e_{\mu\nu,i}^A)^2 = (e_{\mu\nu,i}^B)^2 = 1. \quad (9.6)$$

As in the X-cube coupled layers construction, individual gauge fluxes of the original stacks are confined upon condensation due to their statistical interaction with the charge loops. However, composites of an A (B) flux and an A (B) anti-flux in orthogonal planes have trivial statistics with the charge loops, and thus survive the condensation. These composites become A and B type lineons of the condensed phase, labelled as $l_{\mu,ij}^A$ and $l_{\mu,ij}^B$ with μ the axis of mobility and i and j the normal coordinates. By convention $l_{\mu,ij}^A$ ($l_{\mu,ij}^B$) consists of a flux in the $\mu\nu$ plane and an anti-flux in the $\rho\mu$ plane. They inherit the fusion rules from the 2D gauge fluxes, and therefore obey:

$$\begin{aligned} (l_{\mu,ij}^A)^2 &= e_{\mu\nu,i}^B \times e_{\rho\mu,j}^B \\ (l_{\mu,ij}^B)^2 &= e_{\mu\nu,i}^A \times e_{\rho\mu,j}^A \\ (l_{\mu,ij}^A)^4 &= (l_{\mu,ij}^B)^4 = 1. \end{aligned} \quad (9.7)$$

In these equations, the fracton dipoles' planes of mobility intersect along the lineon axis. There are also triple fusion rules between intersecting lineons

along orthogonal axes (coordinate labels have been suppressed):

$$l_x^A \times l_y^A \times l_z^A = l_x^B \times l_y^B \times l_z^B = 1. \quad (9.8)$$

Whereas individual lineons are restricted to move along a line, adjacent lineon anti-lineon pairs, called lineon *dipoles*, are free to move in a plane normal to the axis of separation, and are hence planons. This is because lineons arise as bound states of flux anti-flux pairs in orthogonal planes. A lineon dipole therefore contains four original flux (or anti-flux) excitations. However, the flux anti-flux pair in the plane shared by the two lineons annihilate one another, leaving behind a flux anti-flux pair in adjacent parallel planes. Lineon dipoles will be denoted $m_{\mu\nu,i,i+1}^A$ and $m_{\mu\nu,i,i+1}^B$ where $\mu\nu$ refers to the plane of mobility and i and $i+1$ are the coordinates in the normal direction of the parallel planes containing the flux and anti-flux respectively. The following fusion rules hold by definition:

$$\begin{aligned} m_{\mu\nu,i,i+1}^A &= l_{\mu,ij}^A \times \bar{l}_{\mu,i+1,j}^A = l_{\nu,ki}^A \times \bar{l}_{\nu,k,i+1}^A \\ m_{\mu\nu,i,i+1}^B &= l_{\mu,ij}^B \times \bar{l}_{\mu,i+1,j}^B = l_{\nu,ki}^B \times \bar{l}_{\nu,k,i+1}^B, \end{aligned} \quad (9.9)$$

where \bar{l} refers to the anti-lineon of l . Combining Eq. (9.7) and Eq. (9.9) yields the rules

$$\begin{aligned} (m_{\mu\nu,i,i+1}^A)^2 &= e_{\mu\nu,i}^B \times e_{\mu\nu,i+1}^B \\ (m_{\mu\nu,i,i+1}^B)^2 &= e_{\mu\nu,i}^A \times e_{\mu\nu,i+1}^A. \end{aligned} \quad (9.10)$$

The statistics of excitations in the condensed phase can also be inferred from the anyon statistics of the decoupled stacks. In particular, the fracton dipole $e_{\mu\nu,i}^A$ ($e_{\mu\nu,i}^B$) exhibits a -1 braiding statistic when wound around type A (B) lineons mobile within the dipole's plane of movement. In particular, these lineons are $l_{\nu,ij}^A$ ($l_{\nu,ij}^B$) and $l_{\mu,ji}^A$ ($l_{\mu,ji}^B$). Moreover, coplanar lineons of opposite species $l_{\mu,ij}^A$ and $l_{\nu,ki}^B$ inherit the i braiding statistic between gauge fluxes m_A and m_B ; thus they exhibit an i statistical phase upon crossing. This property, along with the lineon fusion rules, are the essential features that distinguish the twisted 3-foliated model from the untwisted version, i.e. two copies of the X-cube model.

9.2.3 Foliation structure

In this section, we first show that the model described in the last section indeed has a foliated fracton order. That is, one can decouple 2D topological layers out

of the model while shrinking the system size as shown in Fig. 9.1 (a). Then we are going to look at some of the universal quantities of foliated fracton orders, including the quotient super-selection sectors and the entanglement signatures that we discussed in Refs. 52 and 53. It turns out that this model is trivial (the same as two copies of the X-cube model) in both aspects. However, it is not equivalent to two copies of the X-cube model as an FFO, which we will show in Sec. 9.2.4.

9.2.3.1 Resource layers

In this section, we demonstrate the 3-foliated structure of the model. We show that resource layers consisting of bilayer 2D $Z_2 \times Z_2$ twisted gauge theories can be decoupled from the model in all three directions. Rather than finding an exact local unitary transformation, we arrive at this conclusion by examining the structure of fractional excitations in an $L_x \times L_y \times L_z$ size 3D model, and find that it can be decomposed into two parts: one corresponding to a reduced $L_x \times L_y \times (L_z - 2)$ size 3D model, and the other corresponding to two layers of the twisted gauge theory described by H_{2D} . That is, the superselection sectors of the larger 3D model are identical to those of the smaller 3D model together with the decoupled 2D layers. We may then conclude the presence of such a foliation structure.

In gapped abelian phases, the superselection sectors form an abelian group under fusion. Decomposing this structure therefore amounts to finding a generating set of the fusion group which can be bipartitioned into sets A and B such that there are no statistical interactions between sectors of A and sectors of B .

For the model in question, S contains fractons, lineons, and planons. However, the elementary planons are either fracton dipoles or lineon dipoles (lineon anti-lineon pairs). Therefore, fusion with the appropriate planon effectively *transports* lineons or fractons in their directions of immobility. Hence, a generating set of S need only one lineon of each type in each direction, one fracton of each type, and a generating set of the planon subgroup $P \leq S$ (i.e. the subgroup of S generated by the set of all planons), which decomposes as $P = P_{xy} \times P_{yz} \times P_{zx}$ for the three different planes of mobility. This phenomenon also occurs in all of the stabilizer code models with FFO that have been previously studied. In fact, this observation is the basis of the notion

of *quotient superselection sectors* (QSS), which are elements of the quotient group $Q = S/P$ to be discussed below.

Suppose we wish to disentangle a resource layer in the z direction from the twisted 3-foliated model. Due to the above observation, a decomposition $S = S_{2D} \times S'$, where S_{2D} represents a single 2D resource layer and S' is the reduced 3D model, amounts to a decomposition $P = P_{2D} \times P' = (P_{2D} \times P'_{xy}) \times P_{yz} \times P_{zx}$, such that P_{2D} has no statistical interaction with P' . Moreover, P_{2D} must have trivial interactions with the generating lineons and fractons. However, these generators can always be chosen to lie away from the support of the P_{2D} string operators; thus, this latter condition is essentially vacuous.

Let us now consider P_{xy} , the subgroup of S consisting of planons mobile in the x and y directions. A generating set of P_{xy} is given by the set of elementary (minimally separated) fracton and lineon dipoles with z -oriented dipolar axis. It is possible to find an equivalent generating set that decouples into two subsets: one generates P'_{xy} , a reduced version of P_{xy} ; the other generates P_{2D} , which corresponds to two copies of the 2D $Z_2 \times Z_2$ twisted gauge theory modeled by H_{2D} . To illustrate this decomposition, it is convenient to use a graphical notation, as shown in Fig. 9.4. In Fig. 9.4(a), (part of) the generating set of elementary dipoles is depicted. Fig. 9.4(b) contains an equivalent but different generating set. In this set, the quasiparticles represented by rows 5-12 are completely decoupled from the remaining planons, in the sense that they form a closed group under fusion and have trivial braiding statistics with the other planons. These quasiparticles represent a generating set of the anyon sectors of two copies of the $Z_2 \times Z_2$ twisted gauge theory, i.e. a bilayer (rows 5-8 and rows 9-12). The remaining planons constitute a reduced version of the original planon group with two fewer lattice spacings in the z direction.

Importantly, this mapping of generating planons preserves the locality of the excitations in the z direction. In other words, each element of the generating set moves within a finite region in z before and after the mapping. Therefore, we expect that this mapping of excitations can be realized by a finite depth local unitary transformation with support in the vicinity of the decoupled resource bilayer.

Having established the foliation structure in the 3-foliated model, we now ask if it has the same FFO as the X-cube model (or copies of it). As defined

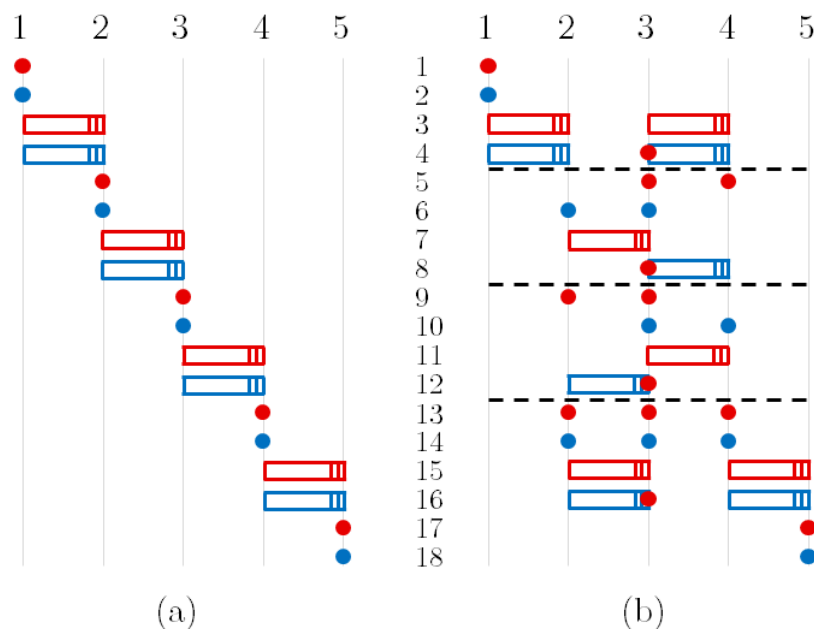


Figure 9.4: Disentangling an xy -plane $Z_2 \times Z_2$ twisted gauge theory resource bilayer from the twisted 3-foliated model, in terms of a generating set of the planon excitations. In this notation, the z axis lies along the horizontal direction, with the grid representing the lattice spacing. Each row represents one planon in the generating set. Lineon dipoles $m_{xy,i,i+1}^A$ and $m_{xy,i,i+1}^B$ are represented as respectively blue and red boxes spanning between z -coordinates i and $i + 1$, with a solid edge to represent the lineon and a triple edge to represent the anti-lineon. Conversely, fracton dipoles $e_{xy,i}^A$ and $e_{xy,i}^B$ are represented as blue and red dots at coordinate i . Figure (a) depicts a generating set consisting of all elementary fracton dipoles and lineon dipoles. The generating set of (b) is decomposed into two copies of the $Z_2 \times Z_2$ twisted gauge theory between the dashed lines and a reduced generating set for the remaining planons outside the lines, which constitutes a smaller version of the original planon group. Note that there are no non-trivial braiding statistics between the three components.

in Refs. [54] and [53], two gapped models have the same foliated fracton order (FFO) if they can be related by a local unitary transformation upon the possible addition of 2D topological order resource states. While this is a rather coarse equivalence relation, previous works have identified the structure of QSS and interferometric statistics, as well as the entanglement signatures discussed prior, as universal characteristics of FFO [52, 53]. As we are going to see in section 9.2.3.2 and 9.2.3.3, based on these properties alone it is plausible that the 3-foliated model has the same FFO as two copies of the X-cube model. However, as we are going to show in section 9.2.4, the 3-foliated model actually has a different FFO from two copies of the X-cube model. The QSS and entanglement signature hence provide an insufficient characterization of the universal properties of a foliated fracton phase.

9.2.3.2 Quotient superselection sectors and interferometric statistics

Consider the QSS fusion group $Q = S/P$. To reiterate, the essential idea behind QSS is that by modding out the planon subgroup P , we obtain a *finite* group which is characteristic of the foliated fracton order of a given model. Since lineon and fracton dipole sectors belong to P for the twisted 3-foliated model, it follows that all lineon superselection sectors $l_{\mu,ij}^A$ ($l_{\mu,ij}^B$) belong to one quotient sector, denoted l_μ^A (l_μ^B). Moreover all fracton sectors f_{ijk}^A (f_{ijk}^B) belong to a single quotient sector, denoted f^A (f^B). These quotient sectors generate the entire group Q .

However, lineon and fracton quotient sectors also obey some relations. First, since $e_{\mu\nu,i}^A \times e_{\rho\mu,j}^A$ and $e_{\mu\nu,i}^B \times e_{\rho\mu,j}^B$ belong to P , the lineon fusion rules (9.7) imply that $(l_\mu^A)^2 = (l_\mu^B)^2 = 1$ as quotient sectors. In other words, the lineon quotient sectors obey Z_2 fusion rules while the lineon superselection sectors obey Z_4 fusion rules. Second, the lineon triple fusion rules are inherited by the quotient group as

$$l_x^A \times l_y^A \times l_z^A = l_x^B \times l_y^B \times l_z^B = 1.$$

Finally, the fractons sectors obey $(f^A)^2 = (f^B)^2 = 1$. Therefore, altogether $Q \cong (Z_2)^{\times 6}$, with the generators f^A , f^B , l_x^A , l_x^B , l_y^A , and l_y^B . This QSS structure is isomorphic (in terms of fusion and particle mobility) to that of two copies of the X-cube model, one corresponding to each of the A and B sectors of Q .

Recall that the X-cube model has QSS group $(Z_2)^{\times 3}$ with generators f , l_x , and l_y , and triple fusion rule $l_x \times l_y \times l_z = 1$.

Interferometric operators for foliated orders, as introduced in Ref. [52], are unitary operators with support outside the region R , where a point excitation is located, that yield nontrivial statistical phases when acting on excitations belonging to nontrivial elements of Q , but act as the identity on excitations in P . As discussed in Ref. [52], for the X-cube model, there are 8 classes of such operators, which have a $Z_2 \times Z_2 \times Z_2$ group structure. They include a wireframe operator W which yields a -1 phase on the quotient sector f , and cylindrical membrane operators M_x , M_y , and M_z . The operator M_x yields a -1 phase on the l_y and l_z sectors, and similarly for M_y and M_z .

In the twisted 3-foliated model, the structure of interferometric operators is identical to that of two copies of the X-cube model, in terms of the geometry of the operators and their statistical interactions with the QSS. In particular, there are operators W^A , W^B , M_x^A , M_x^B , M_y^A , M_y^B , M_z^A , and M_z^B . The microscopic form of these operators may be computed by taking products of all the Hamiltonian terms of one kind within a large cubic region: the wireframe operators W^A and W^B correspond to products of cube operators O_c^A and O_c^B , whereas the membrane operators correspond to products of the vertex terms. Thus, the membrane operators are simply products of Pauli Z^A or Z^B operators over the support of the membrane, as in (two copies of) the X-cube model, whereas the wireframe operators are more complicated.

The rigid string and membrane operators, which create and transport lineons and fractons, have the identical form as these interferometric operators away from the excitations. The statistical interactions between interferometric operators and QSS can be verified by considering the commutation relations of these microscopic operators. One may also view the interferometric operators as planon loop operators for lineon or fracton dipoles with a macroscopic dipolar length.

9.2.3.3 Ground state degeneracy and entanglement signatures

To efficiently calculate the entanglement properties of the 3-foliated model, we consider a Z_4 Calderbank-Shor-Steane (CSS) stabilizer code formulation of the model. That is, the Hamiltonian can be expressed as a sum of products of either \tilde{Z} (the clock operator) or \tilde{X} (the shift operator) where all terms in the

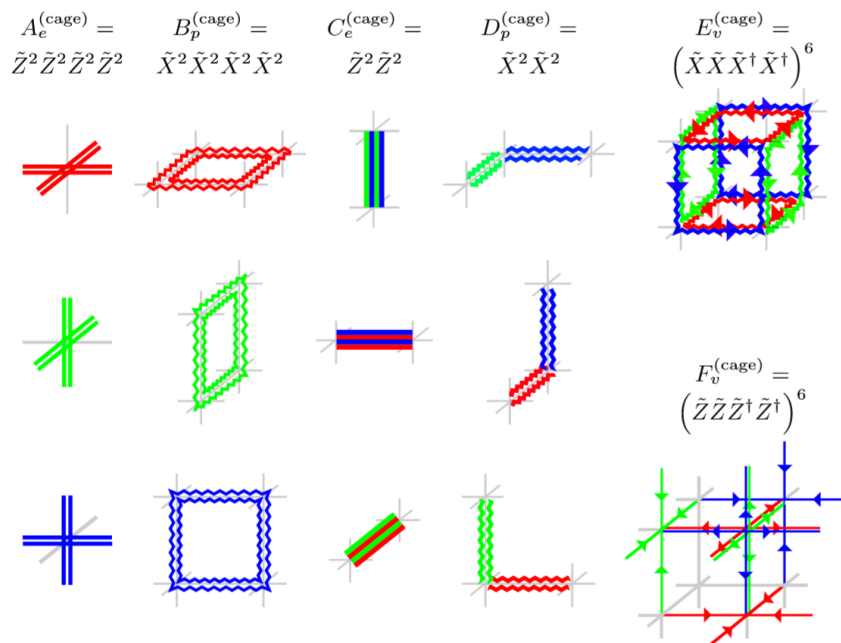


Figure 9.5: A graphical depiction of the terms in the CSS stabilizer version of the 3-foliated model in Eq. (9.5). Each picture above denotes a term in the stabilizer Hamiltonian. There are two Z_4 qudits on each edge, which will be denoted by two (out of three) different colors. Straight colored lines denote \tilde{Z} clock operators, while zig-zag colored lines denote \tilde{X} shift operators. A conjugate-transpose is taken for operators on edges with arrows that point in the negative x, y, or z direction. Double lines denote a \tilde{Z}^2 or \tilde{X}^2 operator. Above each column of pictures, we write the product of operators involved.

Hamiltonian commute with each other and each term has eigenvalue -1 in the ground state. This form of Hamiltonian is useful for doing computations, and will allow us to efficiently calculate ground state degeneracy and entanglement entropy. In Appendix 9.8 we will also express this model in the string-membrane-net and foliated field theory formulations.

To obtain a CSS version of the model, we can repeat the coupled layer construction from Sec. 9.2.1.2 but continue using the Z_4 clock and shift operators instead of mapping to pairs of qubits. The coupled layer construction was performed by adding Pauli $Z^A Z^A$ and $Z^B Z^B$ terms to couple the $Z_2 \times Z_2$ twisted gauge theory layers together. The Z^A and Z^B operators are written in terms of \tilde{Z}^2 and \tilde{X}^2 , as in Fig. 9.2(a). Thus, the $Z^A Z^A$ term that couples $Z_2 \times Z_2$ twisted gauge theory layers is mapped back to a $\tilde{Z}^2 \tilde{Z}^2$ term to couple Z_4 toric code layers together. Unmapping the $Z^B Z^B$ term is similar, although note that the \tilde{X}^2 operator is not on the same edge as the Z^B operator.

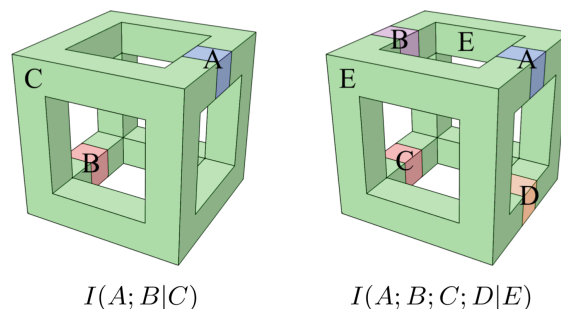


Figure 9.6: The wireframe geometries used to calculate the entanglement quantities in Eq. (9.12).

Therefore, the $Z^B Z^B$ term is mapped back to a $\tilde{X}^2 \tilde{X}^2$ operator, but where each \tilde{X}^2 is on a different link. The strong coupling limit is described by the CSS code Hamiltonian in Fig. 9.5.

Since the model is a stabilizer code, we can efficiently calculate its ground state degeneracy and entanglement entropy (see Appendix 9.7 for details). The ground state degeneracy of an $L_x \times L_y \times L_z$ system with periodic boundary conditions is

$$\text{GSD} = 2^{4L_x + 4L_y + 4L_z - 6}. \quad (9.11)$$

Two-dimensional topological orders can be characterized by their topological entanglement entropy [26, 29]. Ref. [53] discussed a generalization for foliated fracton orders given by the entanglement quantities $I(A; B|C)$ and $I(A; B; C; D|E)$ computed from subsystems with the wireframe geometries shown in Fig. 9.6. For the 3-foliated Hamiltonian (Eq. (9.5)), we find that

$$I(A; B|C) = I(A; B; C; D|E) = \log(4). \quad (9.12)$$

These entanglement signatures, as well as the ground state degeneracy, are equivalent to that of two copies of the X-cube model.²

9.2.4 Twisted foliated fracton order

While the 3-foliated model appears the same as two copies of the X-cube model in terms of QSS and entanglement signatures, they actually have different FFO. In this section we will demonstrate this difference in two separate ways.

²In [53], logarithms were evaluated in base 2. With this convention, the entanglement quantities in Eq. (9.12) are $I(A; B|C) = I(A; B; C; D|E) = \log_2(4) = 2$. The X-cube model has $I(A; B|C) = I(A; B; C; D|E) = \log_2(2) = 1$.

9.2.4.1 Lineon fusion rules

First, we will show that the Z_4 fusion rules of the lineon superselection sectors preclude a transformation to two copies of the X-cube model through local unitary and addition of 2D layers. It will be helpful to establish some terminology. A superselection sector that is a fusion product of planons in orthogonal planes, such that the mobility is restricted to the line of intersection of the two planes, will be referred to as a *superficial lineon*. Conversely, a lineon sector that cannot be decomposed as the fusion product of two planons, is referred to as an *intrinsic lineon* [41]. While intersecting stacks of decoupled 2D topological orders exhibit superficial lineon superselection sectors, only truly fractonic models host intrinsic lineon excitations.

The key to the argument is that all of the intrinsic lineons in the twisted 3-foliated model are order 4 under fusion (although they square to superficial lineons hence the QSS has order 2), whereas the X-cube model contains intrinsic lineons of order 2. By adding stacks of 2D topological orders, it is possible to modify the superselection sector group to include new intrinsic lineons of a *higher* order than the already existing intrinsic lineons. However, the fusion rules of the original intrinsic lineons are immutable, and moreover it is not possible to create a new intrinsic lineon of a *lower* order than the already existing sectors. Therefore, even after the free addition of 2D topological order resource states, the twisted 3-foliated model can never contain intrinsic lineons of order 2. Conversely, the X-cube model, and any number of copies of it, will always retain such an intrinsic lineon. Thus, the two models must have different FFO.

9.2.4.2 Redundancies among planons

Another way to see that the FFO of the 3-foliated model is different from that of two copies of the X-cube model is by looking at the planons. In fact, this can be a useful and generic way to study foliated fracton models. In the following, we are going to show that by examining the planons, we can deduce, first, that the X-cube model is different from a stack of 2D layers and secondly, that the 3-foliated model is different from the X-cube model (or 2 copies of it).

Consider a dimensional reduction procedure from a 3D model to a 2D model where the x and y directions remain infinite while the z direction is made finite. Such a ‘compactification’ process has been used in Ref. [17] to study fracton

models. We consider the situation where the system has periodic boundary condition in all three directions. As the model is now finite in the z direction, any string operator that extends around the z direction becomes finite and can be added to the Hamiltonian. The ground state degeneracy is reduced and the model becomes a 2D model with anyons moving in the 2D plane. Here, we consider what happens upon this compactification process in three different fracton models: a decoupled stack of 2D layers, the X-cube model and the 3-foliated model.

We start with a decoupled stack of 2D layers in the xy plane. In the 3D model, there is no string operator in the z direction, therefore after dimensional reduction no extra term can be added. All the planons in the xy planes survive the dimensional reduction. The number of planons grows exponentially with the height of the system in the z direction. We can choose a generating set of all the planons by choosing a generating set for each plane. Such a generating set satisfies the following properties:

- Each element in the generating set is constrained to move within a finite segment in z as they come from the 2D layers. We say that the generator planons are ‘local’.
- All other planons that are local can be generated by a subset of the generators that are within a finite distance in z . We say that the generating set is ‘locally complete’.
- Moreover, we can make sure the full generating set is not redundant. That is, no element in the generating set (or copies of it) can be generated by other elements in the generating set.

For the X-cube model and the 3-foliated model, these properties can no longer be satisfied at the same time.

Now we consider the X-cube model. A brief review of the X-cube model is given in Appendix [9.6](#). Upon dimensional reduction in the z direction, the string operators in the z direction can be added to the Hamiltonian. Among all the fractional excitations, only the planons in the xy planes survive the dimensional reduction procedure and we can choose a generating set for them consisting of the fracton dipoles e_i centered around plane i and the lineon dipoles $m_{i,i+1}$ living across planes i and $i + 1$. Such a generating set is local

and locally complete as we defined above. However, it is redundant as the product of all fracton dipoles and the product of all lineon dipoles are both trivial anyons.

$$\prod_i e_i = 1, \quad \prod_i m_{i,i+1} = 1 \quad (9.13)$$

That is, there exists global constraints among the planons. These global constraints cannot be removed without violating the ‘locally complete’ condition. If we remove e_1 and m_1 from the generating set, the set is no longer redundant, but e_1 and m_1 can not be locally generated. Therefore, the X-cube model is different from a stack of 2D layers.

Finally we turn to the 3-foliated model and see how it is different from both the stack of 2D layers and the X-cube model. Upon dimensional reduction, all other superselection sectors are removed except planons in the xy plane, which are the fracton dipoles $e_i^{A,B}$ and lineon dipoles $m_{i,i+1}^{A,B}$. The $e_i^{A,B}$ ’s and $m_{i,i+1}^{A,B}$ sectors form a locally complete generating set, but it is highly redundant. First, there are local redundancies of the form

$$\left(m_{i,i+1}^{A,B}\right)^2 = e_i^{B,A} \times e_{i+1}^{B,A} \quad (9.14)$$

Moreover, there are global redundancies of the form

$$\prod_i m_{i,i+1}^{B,A} = \prod_i e_i^{A,B} = 1 \quad (9.15)$$

The global redundancies are similar to that of the X-cube, but the local ones show that the 3-foliated model is different from the X-cube. Note that it is possible to have local redundancy in a locally complete generating set of the X-cube model. For example, if besides all the e_i s and $m_{i,i+1}$ s we add $\psi_i = e_i \times m_{i,i+1}$ to the generating set, it will have a local redundancy. However, such local redundancies can be locally removed. That is, if we use the relation $\psi_i = e_i \times m_{i,i+1}$ and eliminate ψ_i from the generating set, we can remove the redundancy. On the other hand, this is not true for the local redundancies in the 3-foliated model. In the 3-foliated model, we can start from the redundancy relation $\left(m_{1,2}^{A,B}\right)^2 = e_1^{B,A} \times e_2^{B,A}$ and remove it by eliminating $e_2^{B,A}$ from the generating set. Next, we move on to eliminate $e_3^{B,A}$ from the generating set using the redundancy relation $\left(m_{1,2}^{A,B} \times m_{2,3}^{A,B}\right)^2 = e_1^{B,A} \times e_3^{B,A}$. We can keep doing this, but the redundancy relation that we need to use involves more and more m sectors, and eventually it becomes a non-local relation. We say that

the local redundancy relations cannot be locally removed. In fact, a locally complete generating set always has to contain a finite density of e particles and all the m particles, therefore it is always redundant and the redundancy cannot be removed locally. Because of the existence of redundancy relations, especially local redundancy relations that cannot be locally removed, the 3-foliated model is different from both the stack of 2D layers and the X-cube model.

9.3 Twisted 1-foliated model

In this section, we discuss a model which is non-trivially 1-foliated. That is, growing the model in the z direction requires the addition of 2D topological order resource layers ($Z_2 \times Z_2$ twisted gauge theories for the model we study), whereas growing the model in the x or y directions simply requires product state resources. At the same time, the model is not local unitarily equivalent to a decoupled stack of 2D topological orders. Nonetheless, all of the fractional excitations of the model are planons, which are mobile in the xy directions; upon compactification in the z direction,³ the model reduces to a ‘giant’ 2D topological order where the number of superselection sectors grows exponentially with the original height in the z direction.

9.3.1 Model construction

9.3.1.1 Boson condensation

The model is constructed by condensing bosons in a decoupled stack of 2D $Z_2 \times Z_2$ twisted gauge theories (equivalently a stack of Z_4 toric codes, as discussed in Sec. 9.2.1.1), stacked in the z direction. The quasiparticle sectors of the stack consist of $Z_2 \times Z_2$ gauge charges e_i^A and e_i^B and gauge fluxes m_i^A and m_i^B . Composites of gauge charges in neighboring layers, $e_i^A e_{i-1}^B$, are then condensed to yield a new phase, whose fractional excitations can be understood in the conventional framework of 2D boson condensation in topological phases [2, 10].

In particular, charges e_i^A and e_{i-1}^B are identified as a new sector e_i . Moreover, individual fluxes are confined due to their non-trivial statistics with the condensed bosons, but flux pairs $m_i^A m_{i-1}^B$ survive the condensation as sectors labelled m_i . Sectors e_i and m_i have a mutual -1 braiding statistic, and

³I.e., a dimensional reduction from a 3D system to a 2D system with a large unit cell.

adjacent fluxes m_i and m_{i+1} inherit the i braiding statistic. Therefore, the fluxes obey the fusion rules

$$m_i^2 = e_{i-1} \times e_{i+1}. \quad (9.16)$$

Upon compactification, the model may be thought of as a 2D $\prod_{i=1}^L Z_2$ twisted gauge theory with type-II twists between adjacent fluxes.

9.3.1.2 Giant K -matrix

In 2D, abelian topological orders can be generically understood in terms of the K matrix Chern-Simons formalism [70]. In this description, N species of $U(1)$ gauge fields, a_I with $I = 1, \dots, N$, are governed by the Lagrangian

$$\mathcal{L} = \frac{1}{4\pi} K_{IJ} \epsilon^{\mu\nu\rho} a_\mu^I \partial_\nu a_\rho^J, \quad (9.17)$$

where K is an $N \times N$ symmetric integer matrix, with even integers along the diagonal for bosonic systems. The quasiparticles are represented by integer vectors $l = (l_1, \dots, l_N) \in \mathbb{Z}^N$, and have exchange statistics

$$\theta_l = \pi l^T K^{-1} l, \quad (9.18)$$

whereas their mutual braiding statistics are given by

$$\theta_{ll'} = 2\pi l^T K^{-1} l'. \quad (9.19)$$

Quasiparticles of the form Kl for $l \in \mathbb{Z}^N$ have trivial statistics with all other quasiparticles and thus correspond to local excitations. It is important to note that two K matrices, K and K' , are physically equivalent if there is a unimodular matrix W (i.e. with $\det W = 1$) such that $K' = W^T K W$. Such a transformation corresponds to a change of quasiparticle basis.

Here, we will employ the K matrix formalism to describe the excitation content of the 3D condensed phase of the prior section. In particular, the structure of planons is captured by a ‘giant’ $N \times N$ K -matrix, whose dimension is extensive in the height of the system, and in which spatial locality of excitations in the z direction is encoded in the indices of the vector l . In other words, the quasiparticle represented by $l = (\dots, 0, 1, 0, \dots)$, with nonzero value at index I , is a planon constrained to move near the xy plane with z coordinate equal to I units of the lattice spacing.

W matrix, which maps the e_i and m_i anyon basis to a new \tilde{e}_i and \tilde{m}_i basis:

$$W = \begin{matrix} & \tilde{e}_1 & \tilde{m}_1 & \tilde{e}^A & \tilde{m}^A & \tilde{e}^B & \tilde{m}^B & \tilde{e}_2 & \tilde{m}_2 & \tilde{e}_3 \\ \begin{matrix} e_1 \\ m_1 \\ e_2 \\ m_2 \\ e_3 \\ m_3 \\ e_4 \\ m_4 \\ e_5 \end{matrix} & \begin{pmatrix} \ddots & & & & & & & & & \\ & 1 & & & & & & & & \\ & & 1 & & & & & & & \\ & & & 1 & & & & & & \\ & & & & 1 & & & & & \\ & -1 & & & & 1 & & & & \\ & & & & & & 1 & & & \\ & & & & & & & 1 & & \\ & -1 & & 1 & & & & & 1 & \\ & & & & & & & & & 1 \\ & & & & & & & & & \ddots \end{pmatrix} \end{matrix}. \quad (9.22)$$

This W matrix transforms the K -matrix as follows:

$$W^T K W = \begin{matrix} & \tilde{e}_1 & \tilde{m}_1 & \tilde{e}^A & \tilde{m}^A & \tilde{e}^B & \tilde{m}^B & \tilde{e}_2 & \tilde{m}_2 & \tilde{e}_3 \\ \begin{pmatrix} \ddots & & & & & & & & & \\ & 0 & 2 & & & & & & & -1 \\ & 2 & 0 & & & & & & & \\ & & & 0 & 2 & -1 & 0 & & & \\ & & & 2 & 0 & 0 & 0 & & & \\ & & & -1 & 0 & 0 & 2 & & & \\ & & & 0 & 0 & 2 & 0 & & & \\ -1 & & & & & & & 0 & 2 & -1 \\ & & & & & & & 2 & 0 & \\ & & & & & & & -1 & 0 & \\ & & & & & & & & & \ddots \end{pmatrix} \end{matrix}.$$

Evidently, the transformed K -matrix is block diagonal. The 4×4 block (for anyons \tilde{e}^A through \tilde{m}^B), which we will call K_{2D} , represents a disentangled copy of 2D $Z_2 \times Z_2$ twisted gauge theory. To see that this is the case, note that K_{2D} has inverse

$$K_{2D}^{-1} = \frac{1}{4} \begin{matrix} & \tilde{e}^A & \tilde{m}^A & \tilde{e}^B & \tilde{m}^B \\ \begin{pmatrix} 0 & 2 & 0 & 0 \\ 2 & 0 & 0 & 1 \\ 0 & 0 & 0 & 2 \\ 0 & 1 & 2 & 0 \end{pmatrix} \end{matrix}. \quad (9.23)$$

On the other hand, it can easily be seen that the remaining rows and columns represent a smaller version of the original 3D model.

Because the ground state degeneracy of the system only grows with linear system size in the z direction but not in the x and y direction, the model is 1-foliated. That is, growing the model in the z direction requires the addition of 2D topological order resource layers, whereas growing the model in the x or y directions simply requires product state resources.

9.3.3 Nontrivial foliated fracton order

By examining the structure of the planon fusion group, we will demonstrate in this section that the 1-foliated model is not local unitarily equivalent to any decoupled stack of 2D topological orders, nor can it be made equivalent by adding any number of 2D topological order resource layers. In other words, the model represents a non-trivial foliated fracton phase. It is twisted in the sense that ungauging the model yields a nontrivial SSPT phase with 1 set of planar subsystem symmetries.

The situation is very similar to that of the 3-foliated model after dimension reduction. We can choose a locally complete generating set for the planons as $\{e_i, m_i, i = 1, \dots, L\}$. This generating set is redundant with local redundancy relations

$$m_i^2 = e_{i-1} \times e_{i+1} \quad (9.24)$$

We can start to remove the redundancy relations by eliminating the e 's from the generating set. However, the redundancy relations necessarily gets longer into the form $(m_2 \times m_4 \times \dots \times m_{2n})^2 = e_1 \times e_{2n+1}$. Therefore, the redundancy relations cannot be locally removed and we conclude that the 1-foliated model is not equivalent to a stack of 2D layers and is hence 'twisted'.

9.4 Mapping to subsystem SPT phases

The 3-foliated and 1-foliated model introduced in the previous two sections can be 'ungauged' into subsystem symmetry protected topological (SSPT) models [14, 61, 80]. As the fracton models have twisted foliated fracton order, correspondingly the ungauged model has nontrivial SSPT order. In this section, we first demonstrate how the mapping works, then explain in detail our definition of SSPT order, especially a subtle difference from that given in Ref. [14, 80].

9.4.1 The mapping

As the 3-foliated model has a ‘cage-net’ type construction [41] as discussed in section 9.2.1, it can be ‘ungauged’ through a duality transformation similar to that described in Ref. [81] (see also Refs. [67] [72]). In particular, the ‘matter’ degrees of freedom σ^A and σ^B live at the center of the cubes in the cubic lattice. The σ s can be chosen as spin 1/2 degrees of freedom with on-site symmetry generated by σ_x^A and σ_x^B . Upon ‘ungauging’, the fracton Hamiltonian in Eq. 9.5 gets mapped to a model of the σ s with planar subsystem symmetry. The Hamiltonian is

$$H_{\text{SSPT}} = - \sum_c \left(\tilde{O}_c^A + \tilde{O}_c^B + \text{h.c.} \right) \quad (9.25)$$

where \tilde{O}_c^A and \tilde{O}_c^B are obtained from O_c^A and O_c^B of Eq. 9.5 in the following way: (1) Replace the tensor product of 12 X^A (X^B) on the edges around the cube c in O_c^A (O_c^B) with the matter DOF $\sigma_{x,c}^A$ ($\sigma_{x,c}^B$) at the center of the cube. (2) Replace Z_c^A (Z_c^B) on each edge with the tensor product of 4 $\sigma_{z,c}^A$ ’s ($\sigma_{z,c}^B$ ’s) in the cubes containing the edge. Note that the phase factors in the O^A and O^B terms can always be expanded in the basis of Z^A and Z^B operators.⁴ Therefore, these replacement steps completely determine the \tilde{O} terms from the O terms. Moreover, as the σ_z^A and σ_z^B terms always appear as the tensor product of four around each edge, the new Hamiltonian terms are invariant under subsystem planar symmetries

$$U_{P_{\mu\nu}}^\alpha = \prod_{c \in P_{\mu\nu}} \sigma_{x,c}^\alpha \quad \text{with} \quad \begin{array}{l} \alpha = A, B \\ \mu\nu = xy, yz, zx \end{array} \quad (9.26)$$

where P_{xy} , P_{yz} , P_{zx} denote planes in the xy , yz , zx direction respectively.

For the 1-foliated model, which is obtained by condensing $e_{i-1}^B e_i^A$ charge pairs in a stack of $Z_2 \times Z_2$ twisted gauge theory models, the corresponding SSPT can be obtained from a stack of $Z_2 \times Z_2$ twisted SPT [12] [68] by condensing $e_{i-1}^B e_i^A$ charge pairs. In the SSPT model, condensing charge pairs simply means that the Z_2^B symmetry of the $(i-1)$ th layer is combined with Z_2^A symmetry of the i th layer into a single symmetry generator. That is, the Hamiltonian of the system is the same as that of a decoupled stack of $Z_2 \times Z_2$ twisted SPT, while the planar symmetry generators are tensor products of planar symmetry generators of the B part in layer $i-1$ and the A part in layer i .

⁴For example, $S = \frac{1+i}{2} + \frac{1-i}{2}Z$ and $CZ = \frac{1}{2}(1 \otimes 1 + Z \otimes 1 + 1 \otimes Z - Z \otimes Z)$.

9.4.2 Definition of SSPT order

As the SSPT models are obtained by ‘ungauging’ twisted fracton models, we expect the SSPT to be ‘twisted’ as well. To be more precise, a 3D system is said to have planar *subsystem symmetry protected topological* (SSPT) order if

Definition 1 *The model has a unique symmetric gapped ground state on any closed 3D manifold, which in the absence of symmetry can be mapped to a product state using a finite depth quantum circuit.*

Two SSPT models with the same subsystem symmetry are said to have the same SSPT order if

Definition 2 *The two models can be mapped to each other by adding 2D SPT layers with independent planar symmetries to each model and applying a symmetric finite depth quantum circuit.*

Note that there is some subtlety in comparing the subsystem symmetry group of two models as the total symmetry group depends on system size. We consider two subsystem symmetry groups to be the same if they can be made the same by adding independent planar symmetry generators to either side.

Accordingly,

Definition 3 *An SSPT model has nontrivial or ‘twisted’ SSPT order if it does not have the same SSPT order as a trivial paramagnet (a product state) with the same subsystem symmetry.*

It is easy to see that once the planar symmetries are gauged, this definition of SSPT order matches the definition of foliated fracton order illustrated in Fig. 9.1. This definition can be generalized to models and subsystem symmetries in other dimensions in a straight forward way.

Our definition is similar but also different from that in Ref. [14, 80]. The definition of Ref. [14, 80] makes use of a ‘linearly symmetric local unitary circuit’ while we use only symmetric finite depth circuits but allow the addition of SPT layers. That is, we require each unitary gate in the circuit to be symmetric while the definition in Ref. [14, 80] allows the individual gates to break symmetry and requires only a subsystem (linear or planar) composite of

them to be symmetric. A common consequence of these two definitions is that a pure stack of lower dimensional SPTs, where the subsystem symmetry acts as a global symmetry on each of them, is considered to be a trivial SSPT. On the other hand, the ‘linearly symmetric local unitary’ equivalence is stronger. In particular, in our definition we require the added SPT to come with their own independent symmetry generators. After they are added to the total system, the total subsystem symmetry group is always enlarged. The effect of the ‘linearly symmetric local unitary’ can also be interpreted as allowing the addition of subsystem SPTs. But once added, the symmetry generator of the SPT can be identified with one of the original symmetry generators of the system, hence directly changing the SPT signature associated with that generator. Our definition of equivalence is weaker (e.g. our definition classifies more models as nontrivial) and we have chosen it so that it matches with our definition of foliated fracton order once the subsystem symmetries are gauged.

Upon gauging, the equivalence condition in Ref. [14, 80] is different from the foliated fracton equivalence we used in this paper. Compared to the foliated fracton equivalence, it amounts to allowing charge condensation in fracton models, because prior to gauging the symmetry group does not necessarily become larger when SPT layers are added. Both the 1-foliated and 3-foliated model discussed above are trivial SSPTs phase under their definition [13], while they are nontrivial under our definition.

9.5 Summary

To summarize, in this paper we demonstrate the existence of twisted foliated fracton order, i.e. 3D gapped fracton models with a foliation structure but which are inequivalent to (copies of) the X-cube model. In particular, we discussed a 3-foliated model in section 9.2 and a 1-foliated model in section 9.3. We demonstrated the nontriviality of the models by studying the fractional excitations – the lineons and the planons – of the models. In particular, we used a dimensional reduction procedure to reduce the 3D model to a 2D model while keeping track of the locality of the planons along the reduced dimension. By studying the group structure of the local planons, we can discern the differences between stacks of 2D layers, the X-cube model and the twisted models. By using an ungauging procedure, we further mapped the twisted fracton models to nontrivial subsystem symmetry protected topological models.

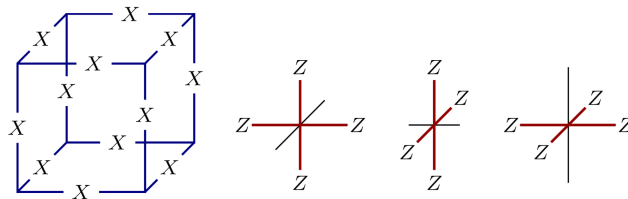


Figure 9.7: Cube and cross operators of the X-cube model Hamiltonian on a cubic lattice.

An interesting future direction is to understand the anyon condensation procedure in layers of 2D topological orders in more generality. For example, given such a condensation transition, how can one determine what the emergent phase is? More coarsely, one can ask if the phase is equivalent to a decoupled stack of 2D models, a liquid 3D topological order, or a nontrivial planon model. This question can be asked more generally in the context of topological defect network constructions [1, 71].

9.6 Appendix: The X-cube model

The X-cube model, as first discussed in Ref. [67], is defined on a cubic lattice with qubit degrees of freedom on the edges. The Hamiltonian

$$H = - \sum_v (A_v^x + A_v^y + A_v^z) - \sum_c B_c \quad (9.27)$$

contains two types of terms: cube terms B_c which are products of the twelve Pauli X operators around a cube c , and cross terms A_v^μ which are products of the four Pauli Z operators at a vertex v in the plane normal to the μ -direction where $\mu = x, y$, or z (Fig. 9.7).

Consider an $L_x \times L_y \times L_z$ cubic lattice with periodic boundary conditions. The ground state degeneracy (GSD) scales linearly with the size of the system in all three directions:

$$\log_2 \text{GSD} = 2L_x + 2L_y + 2L_z - 3. \quad (9.28)$$

There are hence a large number of ‘logical operators’ that commute with all of the terms in the Hamiltonian and map one ground state to another [24, 57]. An over-complete set of X -type logical operators is given by the set of closed string-like operators W_{ij}^μ , which is a product of X operators over all μ -oriented edges with coordinates (i, j) in the plane normal to μ (see Fig. 9.8).

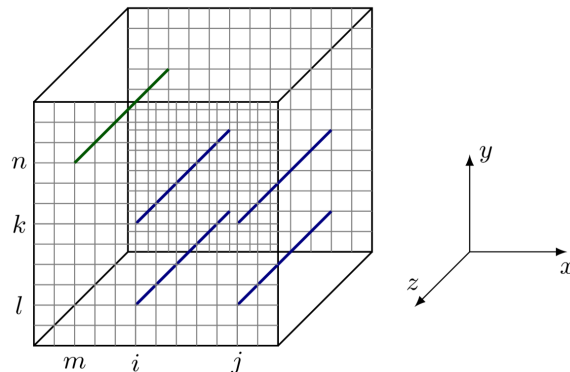


Figure 9.8: Visualization of logical operators in the X-cube model. The green string corresponds to W_{mn}^z . The product of the four operators corresponding to the blue strings is equal to the identity, as described in the main text.

This set is over-complete in the sense that products of the form $W_{ij}^\mu W_{il}^\mu W_{kl}^\mu W_{kj}^\mu$ are equal to a product of some B_c cube operators, and thus act trivially on the ground state manifold (here the four sets of coordinates lie about the corners of a rectangle in the plane normal to μ , as shown in Fig. 9.8). There are $L_x L_y + L_y L_z + L_z L_x - 2L_x - 2L_y - 2L_z + 3$ such relations corresponding to unique products of cube operators, thus implying Eq. (9.28).

Logical operators correspond to processes where particle anti-particle pairs are created out of the vacuum, wound around the torus, and then annihilated. Straight open string operators $W_{ij}^\mu(\mu_1, \mu_2)$ anti-commute with the vertex Hamiltonian terms at the endpoints μ_1 and μ_2 , corresponding to excitations which live on the vertices of the lattice. Here $W_{ij}^\mu(\mu_1, \mu_2)$ is defined to be the product of X operators over μ -oriented edges between $\mu = \mu_1$ and $\mu = \mu_2$ with coordinate (i, j) in the plane normal to μ (see Fig. 9.9). Conversely, acting with bent string operators introduces additional energetic costs at the corners. Therefore the particles living at the endpoints of straight open strings are energetically confined to live on a line; in this sense, they are dimension-1 particles [67]. These particles obey an unconventional fusion rule: triples of particles living along x -, y -, and z -oriented lines may annihilate into the vacuum. On the other hand, acting with a closed string operator around a rectangle creates an excitation at each corner of the rectangle. A pair of particles at adjacent corners may be viewed as a single dipole-like object which is itself a dimension-2 particle and is mobile in the plane normal to the edges connecting the two corners.

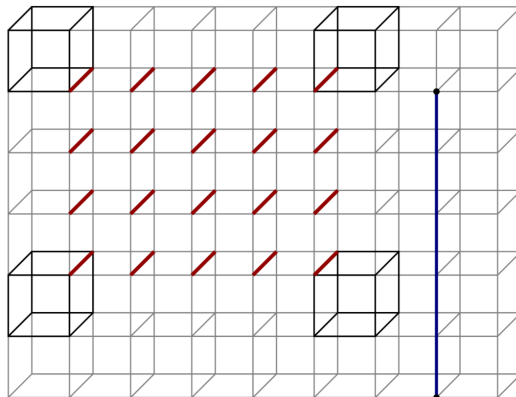


Figure 9.9: Visualization of particle creation operators in the X-cube model. The red links correspond to a membrane geometry on the dual lattice. The product of Z operators over these edges excites the (darkened) cube operators at the corners. The product of X operators over the links comprising the straight open blue string creates excitations at its endpoints (black dots).

In addition to these string-like operators, there are membrane-like operators which are products of Z operators over qubits corresponding to a membrane geometry on the dual lattice (see Fig. 9.9). A rectangular membrane operator anti-commutes with the cube Hamiltonian terms at its corners. A pair of adjacent corner excitations created by a rectangular membrane operator is likewise a dimension-2 dipolar particle, free to move in a plane perpendicular to its moment. A process whereby a pair of such membrane dipoles is created, separated, wound around the torus and annihilated, corresponds to a string-like Z -type logical operator.

9.7 Appendix: Ground state degeneracy

In this appendix, we review algorithms to compute the ground state degeneracy and entanglement entropy of a Z_D qudit stabilizer code [18–20].

Consider a stabilizer code of the form

$$H = - \sum_{\alpha=1}^k (s_{\alpha} + s_{\alpha}^{\dagger}), \quad (9.29)$$

$$s_{\alpha} = \omega^{p_{\alpha}} \prod_{i=1}^n X_i^{S_{\alpha,i}} Z_i^{S_{\alpha,i+n}}. \quad (9.30)$$

Each s_{α} is a product of Z_D clock and shift operators Z and X where $ZX = \omega XZ$ and $\omega = e^{2\pi i/D}$. Note that H is completely determined by the k -component integer vector p_{α} and $k \times 2n$ integer matrix S . Since we

require that H is a stabilizer code, any product of s_α that results in a multiple of the identity operator must be the identity operator exactly; i.e. H must be frustration-free.

Multiplying one stabilizer by another or applying unitary Clifford operators to H roughly corresponds to multiplying S on the left or right by an invertible integer matrix, along with some additional modifications to p_α . Analogous to the singular value decomposition, the Smith decomposition diagonalizes an integer matrix using invertible integer matrices. Therefore, we can compute the Smith normal form of S to obtain a new integer matrix S' which is diagonal, and the Hamiltonian H' defined by S' will have the same ground state degeneracy as H . Since S' is diagonal, H' consists of decoupled qudits, and the ground state degeneracy of H' is trivial to calculate (and the new phases $\omega^{p'_\alpha}$ do not affect the degeneracy). For the special case of Z_D qudits with D prime, the degeneracy can instead be calculated from the rank of S over the field Z_D .

An algorithm to compute the entanglement of a qubit stabilizer code is discussed in [18]. Similar to the ground state degeneracy calculation, the entanglement entropy is computed in terms of the rank of a matrix S_{AB} over the field Z_D when the qudit dimension D is prime. For non-prime D , the algorithm generalizes similarly to the degeneracy calculation and the entanglement entropy is calculated from the Smith diagonals of the same matrix.

9.8 Appendix: String-membrane-net realization

The 3-foliated model in Sec. 9.2.3.3 can also be written as a string-membrane-net (SMN) [55] or topological defect network [1, 71]. The string-membrane-net consists of *two* 3D Z_2 toric codes coupled to 2D Z_4 toric code (TC) layers. The coupling modifies the set of local excitations along the 2D layers, which in turn modifies the mobility of the excitations:

1. When a pair of charges $e_{3D}^{(1)}$ ($e_{3D}^{(2)}$) of the first (or second) 3D TC is created across a layer, a pair of charge $2e_{2D}$ (flux $2m_{2D}$) excitations is also created on the 2D TC layer.
2. When a pair of oppositely-charged Z_4 charge $\pm e_{2D}$ (or flux $\pm m_{2D}$) excitations is created on a 2D TC layer, an open π flux string excitation

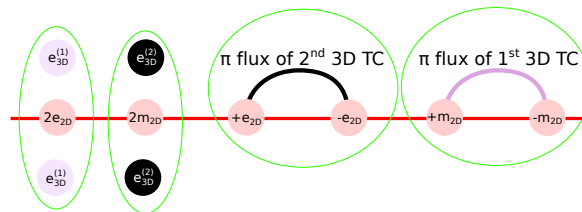


Figure 9.10: The four kinds of excitations (circled in green) that can be created locally in the 3-foliated string-membrane-net.

of the second (first) 3D TC is also created with endpoints on the two oppositely-charged 2D excitations.

See Fig. 9.10 for pictures of these local excitations.

Note that the mobility of particles is determined by the set of local excitations since charges can move by creating and annihilating local excitations, such as a pair of slightly displaced excitations of opposite charge. However, exotic sets of local excitations lead to more interesting mobility rules. For example, due to the first effect above, the 3D toric code (TC) charges ($e_{3D}^{(1)}$ and $e_{3D}^{(2)}$) are fractons since they must leave behind 2D TC excitations when they pass through layers. The second effect implies that an odd number of 2D TC charges ($e_{(2D)}$) or fluxes ($m_{(2D)}$) must be attached to the endpoints of 3D TC flux strings, which implies that an odd number of 2D TC charges or fluxes are linearly confined. However, a pair of 2D TC charges (or fluxes) from two intersecting layers is a lineon because this pair is confined to the intersection of the two layers by the 3D TC flux strings.

The Hamiltonian of the string-membrane-net can be written down on very general lattices. In particular, it is possible to consider lattices where there are many qubits between the toric code layers so that one can indeed think of the Hamiltonian as 2D toric codes coupled to two 3D toric codes. In Fig. 9.11, we depict the simplest example where the Hamiltonian is defined on a cubic lattice in which the toric code layers are placed a single lattice spacing apart from one another.

9.8.1 Unitary Mapping

To show that the string-membrane-net Hamiltonian (Fig. 9.11) is equivalent to the cage-net Hamiltonian in Fig. 9.5, we will show that there is a unitary

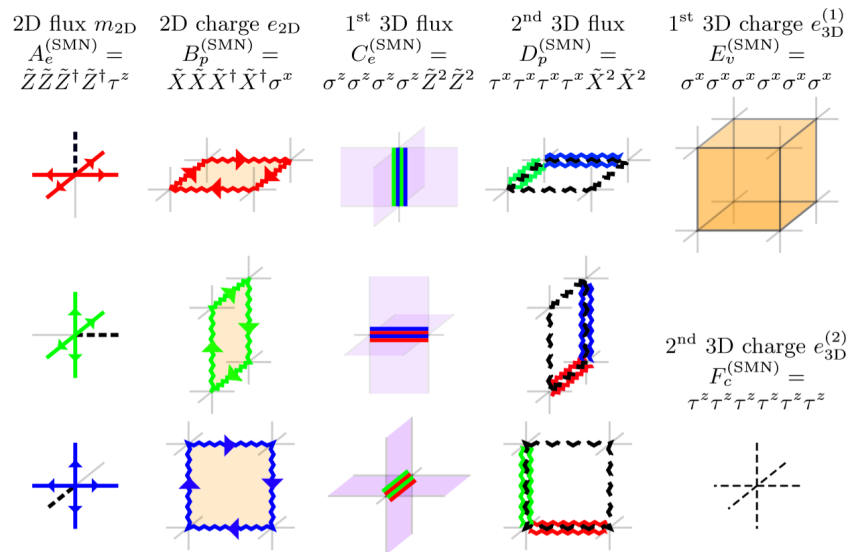


Figure 9.11: A depiction of the terms in the string-membrane-net Hamiltonian $H = -\sum_e A_e^{(SMN)} - \sum_p B_p^{(SMN)} - \sum_e C_e^{(SMN)} - \sum_p D_p^{(SMN)} - \sum_v E_v^{(SMN)} - \sum_c F_c^{(SMN)}$. The Hamiltonian consists of three stacks of Z_4 2D toric codes coupled to two Z_2 3D toric codes. The 2D toric codes consist of Z_4 qudits on the edges of stacks of 2D square lattices. The operators of the 2D toric codes on the xy , yz , and zx planes will be colored red, green, and blue. A straight red, green, or blue line denotes a Z_4 clock operator \tilde{Z} , while a zig-zag line denotes a Z_4 shift operator \tilde{X} with the algebra $\tilde{Z}\tilde{X} = i\tilde{X}\tilde{Z}$. When e.g. two red lines appear on the same edge, this denotes a \tilde{Z}^2 operator. A conjugate-transpose is taken for operators on edges with arrows that point in the negative x , y , or z direction. The first 3D toric code consists of Z_2 qubits on the plaquettes of the cubic lattice, for which purple and orange plaquettes denote Z_2 Pauli σ^z and σ^x operators, respectively. The second 3D toric code consists of Z_2 qubits on the links of the cubic lattice, which are denoted by dashed back lines; again, straight and zig-zag lines denote Pauli τ^z and τ^x operators. Thus, there are two Z_4 qudits and one Z_2 qubit on each edge, and a single Z_2 qubit on each plaquette. The Hamiltonian consists of these 14 different operators, along with their Hermitian conjugates. Above each column of operators, are written the name of the corresponding excitation and the individual Pauli, clock, and shift operators that the operators are composed of.

mapping between the ground spaces of the two Hamiltonians (augmented with some extra decoupled degrees of freedom).

To begin, it is convenient to replace the Z_2 qubits of the two 3D toric codes with Z_4 qudits. This will be achieved by making the following operator replacement in the string-membrane-net Hamiltonian (Fig. 9.11):

$$\begin{aligned}\sigma_p^z &\rightarrow (\tilde{\sigma}_p^z)^2 & \sigma_p^x &\rightarrow \tilde{\sigma}_p^x \\ \tau_e^x &\rightarrow (\tilde{\tau}_e^x)^2 & \tau_e^z &\rightarrow \tilde{\tau}_e^z\end{aligned}\quad (9.31)$$

and adding the following terms to the Hamiltonian:

$$-\sum_p (\tilde{\sigma}_p^x)^2 - \sum_e (\tilde{\tau}_e^z)^2 \quad (9.32)$$

We have replaced the Pauli operators σ^μ and τ^μ with clock and shift operators $\tilde{\sigma}^\mu$ and $\tilde{\tau}^\mu$, which have the algebra $\tilde{\sigma}^z \tilde{\sigma}^x = i \tilde{\sigma}^x \tilde{\sigma}^z$ and $\tilde{\tau}^z \tilde{\tau}^x = i \tilde{\tau}^x \tilde{\tau}^z$. The above replacement does not change the ground state since the new terms in the Hamiltonian will enforce $\tilde{\sigma} = \pm 1$ and $\tilde{\tau} = \pm 1$, and the modified Hamiltonian does not have any σ^z or τ^x operators, only $(\tilde{\sigma}^z)^2$ and $(\tilde{\tau}^x)^2$ operators. Thus, its ground state is still effectively described by qubits.

The next step is to act with the unitary shown in Fig. 9.12 which is composed of the Z_4 controlled-X operators:

$$CX = \frac{1}{4} \sum_{a=0}^3 \sum_{b=0}^3 i^{ab} Z^a \otimes X^b, \quad (9.33)$$

$$CX(Z \otimes 1)CX^\dagger = Z \otimes 1, \quad CX(X \otimes 1)CX^\dagger = X \otimes X^{-1}$$

$$CX(1 \otimes Z)CX^\dagger = Z \otimes Z, \quad CX(1 \otimes X)CX^\dagger = 1 \otimes X.$$

The replacement in Eq. (9.31) and unitary in Fig. 9.12 map the operators of the string-membrane-net Hamiltonian (Fig. 9.11) to those of the cage-net Hamiltonian (Fig. 9.5) as follows

$$\begin{aligned}A_e^{(\text{SMN})} &\rightarrow \tau_e^z, & C_e^{(\text{SMN})} &\rightarrow C_e^{(\text{cage})}, & E_v^{(\text{SMN})} &\rightarrow E_p^{(\text{cage})} \\ B_p^{(\text{SMN})} &\rightarrow \sigma_p^x, & D_p^{(\text{SMN})} &\rightarrow D_p^{(\text{cage})}, & F_v^{(\text{SMN})} &\rightarrow F_v^{(\text{cage})}.\end{aligned}\quad (9.34)$$

The $A_e^{(\text{SMN})}$ and $B_p^{(\text{SMN})}$ operators are mapped to τ_e^z and σ_p^x . This sets $\tau_e^z = \sigma_p^x = 1$ in the ground state of the new Hamiltonian. We also had to

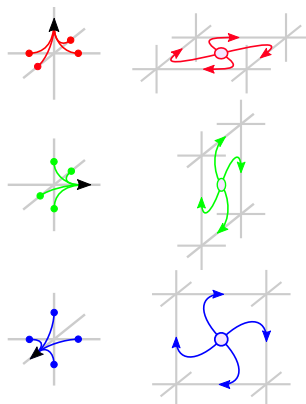


Figure 9.12: After applying the mapping in Eq. (9.31), the unitary depicted above maps the string-membrane-net model in Fig. 9.11 to the cage-net Hamiltonian in Fig. 9.5. The unitary is given by the composition of a unitary operator at each edge (left) and plaquette (right). These smaller unitary operators commute with each other. The operators on the left are products of four controlled-X operators (one for each line, defined in Eq. (9.33)) that are controlled by the 2D toric code qudit of the appropriate color at the colored dot, and act on the 3D toric code qudit at the end of the black arrow. The operators on the right are controlled-X operators that are controlled by the 3D toric code qudit at the center of the plaquette, and act on the 2D toric code qudit of the appropriate color at the end of the arrow.

add two new terms to the Hamiltonian in Eq. (9.32). These new terms are mapped to

$$(\tilde{\tau}_e^z)^2 \rightarrow (\tilde{\tau}_e^z)^2 A_e^{(\text{cage})} \quad (\tilde{\sigma}_p^x)^2 \rightarrow (\tilde{\sigma}_p^x)^2 B_p^{(\text{cage})} \quad (9.35)$$

But since $\tau_e^z = \sigma_p^x = 1$ in the ground state, the new terms are effectively mapped to $A_e^{(\text{cage})}$ and $B_p^{(\text{cage})}$. Therefore, the string-membrane-net Hamiltonian (Fig. 9.11) and cage-net Hamiltonian (Fig. 9.5) both have the same ground state (up to trivial decoupled degrees of freedom).

9.8.2 Field theory

It is also possible to describe this model using a foliated field theory. Foliated field theories, which were introduced in [55], are field theories that explicitly couple to a foliation structure via foliation fields e_μ^k [5].

⁵The X-cube field theory in [57] was written as a foliated field theory in [55].

The Lagrangian is

$$\begin{aligned}
 L = & \underbrace{\frac{4}{2\pi} \sum_k e^k \wedge B^k \wedge dA^k}_{\text{2D } Z_4 \text{ TC layers}} + \underbrace{\frac{2}{2\pi} b \wedge da + \frac{2}{2\pi} b' \wedge da'}_{\text{2} \times \text{3D } Z_2 \text{ TC}} \\
 & - \underbrace{\frac{4}{2\pi} \sum_k e^k \wedge (b \wedge A^k + a' \wedge B^k)}_{\text{coupling}} \tag{9.36}
 \end{aligned}$$

where A^k , B^k , a , and b' are 1-form gauge fields, b and a' are 2-form gauge fields, e^k are static foliation fields that describe the geometry of the foliations, and $k = 1, 2, \dots, n_f$ indexes the different foliation layers. The $n_f = 3$ foliation structure of a cubic lattice is described by $e^k_\mu = \lambda \delta^k_\mu$ where $\mu = 0, 1, 2, 3$ indexes the spacetime indices and λ is the density of foliation layers.

The Lagrangian has the following gauge invariance

$$\begin{aligned}
 A^k & \rightarrow A^k + d\zeta^k + \alpha' & B^k & \rightarrow B^k + d\chi^k + \beta \\
 & + \mu^k e^k & & + \nu^k e^k \\
 a & \rightarrow a + da - \sum_k 2\zeta^k e^k & b & \rightarrow b + d\beta \\
 a' & \rightarrow a' + da' & b' & \rightarrow b' + d\beta' - \sum_k 2\chi^k e^k
 \end{aligned} \tag{9.37}$$

where ζ^k , χ^k , μ^k , ν^k , α , and β' are arbitrary scalars and β and α' are arbitrary 1-forms. The Lagrangian is also self-dual under

$$A^k \leftrightarrow B^k \qquad a \leftrightarrow b' \qquad a' \leftrightarrow b. \tag{9.38}$$

This self-duality interchanges the two 3D toric codes and interchanges the 2D toric code charge and flux sectors.

9.8.3 1-foliated model

In this appendix, we write down a CSS code lattice model that can describe the twisted 1-foliated K-matrix model in Eq. (9.20). One option would be to consider the 1-foliated version of the string-membrane-net model in Fig. 9.11. This appears to work, but the second toric code does not have any affect in this 1-foliated case. Thus, we will consider the simpler case of a stack of 2D Z_4 toric codes coupled to a 3D Z_2 toric code. This model is a special case of the generalized string-membrane-net model in Appendix A of [55]. The model is summarized in Fig. 9.13.

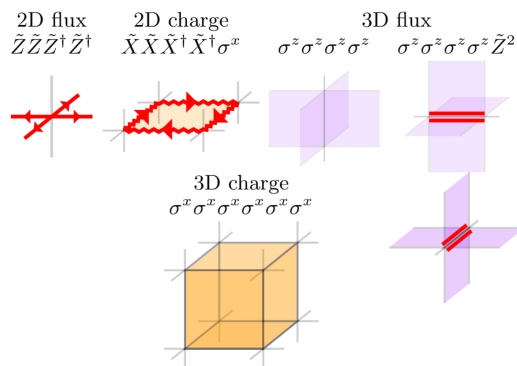


Figure 9.13: A depiction of the terms in the string-membrane-net Hamiltonian realization of the 1-foliated K-matrix in Eq. (9.20). The Hamiltonian consists of a single stack of Z_4 toric codes coupled to a Z_2 3D toric code. The 2D toric codes consist of Z_4 qudits on the edges of a stack of 2D square lattices. The pictorial notation is similar to that of Fig. 9.11. A straight red line denotes a Z_4 clock operator \tilde{Z} , while a zig-zag line denotes a Z_4 shift operator \tilde{X} with the algebra $\tilde{Z}\tilde{X} = i\tilde{X}\tilde{Z}$. The 3D toric code consists of Z_2 qubits on the plaquettes of the cubic lattice, for which purple and orange operators denote Z_2 Pauli σ^z and σ^x operators, respectively. Thus, there are two Z_4 qudits on each x -axis or y -axis edge, no qudits on the z -axis edges, and a single Z_2 qubit on each plaquette.

The anyon labels in Eq. (9.20) have the following correspondence with the excitations of the 1-foliated string-membrane-net:

K-matrix anyon	string-membrane-net
e_{2z+1}	pair of 2D fluxes
m_{2z+1}	2D charge
e_{2z+2}	3D charge
m_{2z+2}	2D fluxes - 3D flux - 2D flux

The anyon m_{2z+2} is equivalent to a pair of 2D fluxes on neighboring layers where the fluxes are attached to two ends of a 3D flux string. It is straightforward to check that the above anyons have the same braiding statistics as those defined in the K^{-1} matrix in Eq. (9.21). Therefore, the lattice model in Fig. 9.13 is a lattice realization of the K-matrix in Eq. (9.20).

References

- [1] David Aasen et al. “Topological Defect Networks for Fractons of all Types”. In: (Feb. 2020). arXiv: [2002.05166](https://arxiv.org/abs/2002.05166).

- [2] F. A. Bais and J. K. Slingerland. “Condensate-induced transitions between topologically ordered phases”. In: 79.4, 045316 (Jan. 2009), p. 045316. DOI: [10.1103/PhysRevB.79.045316](https://doi.org/10.1103/PhysRevB.79.045316). arXiv: [0808.0627](https://arxiv.org/abs/0808.0627) [[cond-mat.mes-hall](https://arxiv.org/abs/0808.0627)].
- [3] S. Bravyi, B. Leemhuis, and B.M. Terhal. “Topological order in an exactly solvable 3D spin model”. In: *Annals of Physics* 326 (Apr. 2011), pp. 839–866. DOI: [10.1016/j.aop.2010.11.002](https://doi.org/10.1016/j.aop.2010.11.002).
- [4] Sergey Bravyi and Jeongwan Haah. “Energy Landscape of 3D Spin Hamiltonians with Topological Order”. In: *Phys. Rev. Lett.* 107 (15 Oct. 2011), p. 150504. DOI: [10.1103/PhysRevLett.107.150504](https://doi.org/10.1103/PhysRevLett.107.150504).
- [5] Benjamin J. Brown and Dominic J. Williamson. “Parallelized quantum error correction with fracton topological codes”. In: *Physical Review Research* 2.1 (Mar. 2020). ISSN: 2643-1564. URL: <http://dx.doi.org/10.1103/PhysRevResearch.2.013303>.
- [6] D. Bulmash and M. Barkeshli. “Generalized $U(1)$ Gauge Field Theories and Fractal Dynamics”. In: (June 2018). arXiv: [1806.01855](https://arxiv.org/abs/1806.01855).
- [7] Daniel Bulmash and Maissam Barkeshli. “Gauging fractons: Immobile non-Abelian quasiparticles, fractals, and position-dependent degeneracies”. In: *Physical Review B* 100.15 (Oct. 2019). ISSN: 2469-9969.
- [8] Daniel Bulmash and Maissam Barkeshli. “Higgs mechanism in higher-rank symmetric $U(1)$ gauge theories”. In: *Phys. Rev. B* 97 (23 June 2018), p. 235112. DOI: [10.1103/PhysRevB.97.235112](https://doi.org/10.1103/PhysRevB.97.235112).
- [9] Daniel Bulmash and Thomas Iadecola. “Braiding and Gapped Boundaries in Fracton Topological Phases”. In: (Sept. 2018). DOI: [10.1103/PhysRevB.99.125132](https://doi.org/10.1103/PhysRevB.99.125132). URL: <https://arxiv.org/abs/1810.00012v3>.
- [10] F. J. Burnell. “Anyon Condensation and Its Applications”. In: *Annual Review of Condensed Matter Physics* 9 (Mar. 2018), pp. 307–327. DOI: [10.1146/annurev-conmatphys-033117-054154](https://doi.org/10.1146/annurev-conmatphys-033117-054154). arXiv: [1706.04940](https://arxiv.org/abs/1706.04940) [[cond-mat.str-el](https://arxiv.org/abs/1706.04940)].
- [11] Claudio Chamon. “Quantum Glassiness in Strongly Correlated Clean Systems: An Example of Topological Overprotection”. In: *Phys. Rev. Lett.* 94 (4 Jan. 2005), p. 040402. DOI: [10.1103/PhysRevLett.94.040402](https://doi.org/10.1103/PhysRevLett.94.040402).
- [12] Xie Chen et al. “Symmetry protected topological orders and the group cohomology of their symmetry group”. In: *Phys. Rev. B* 87 (15 Apr. 2013), p. 155114. DOI: [10.1103/PhysRevB.87.155114](https://doi.org/10.1103/PhysRevB.87.155114).

- [13] Trithep Devakul, Wilbur Shirley, and Juven Wang. “Strong planar subsystem symmetry-protected topological phases and their dual fracton orders”. In: *Physical Review Research* 2.1 (Mar. 2020). ISSN: 2643-1564. URL: <http://dx.doi.org/10.1103/PhysRevResearch.2.012059>
- [14] Trithep Devakul, Dominic J. Williamson, and Yizhi You. “Classification of subsystem symmetry-protected topological phases”. In: *Phys. Rev. B* 98 (23 Dec. 2018), p. 235121. DOI: [10.1103/PhysRevB.98.235121](https://link.aps.org/doi/10.1103/PhysRevB.98.235121). URL: <https://link.aps.org/doi/10.1103/PhysRevB.98.235121>.
- [15] Trithep Devakul et al. “Fractal Symmetric Phases of Matter”. In: *SciPost Physics* 6.1 (Jan. 2019). URL: <http://dx.doi.org/10.21468/SciPostPhys.6.1.007>.
- [16] Robbert Dijkgraaf and Edward Witten. “Topological Gauge Theories and Group Cohomology”. In: *Commun. Math. Phys.* 129 (1990), p. 393. DOI: [10.1007/BF02096988](https://doi.org/10.1007/BF02096988).
- [17] Arpit Dua et al. “Compactifying fracton stabilizer models”. In: *Physical Review B* 99.24 (June 2019). ISSN: 2469-9969. URL: <http://dx.doi.org/10.1103/PhysRevB.99.245135>.
- [18] David Fattal et al. “Entanglement in the stabilizer formalism”. In: *arXiv e-prints*, quant-ph/0406168 (June 2004), quant-ph/0406168. arXiv: [quant-ph/0406168](https://arxiv.org/abs/quant-ph/0406168).
- [19] Vlad Gheorghiu. “Standard form of qudit stabilizer groups”. In: *Physics Letters A* 378.5-6 (Jan. 2014), pp. 505–509. DOI: [10.1016/j.physleta.2013.12.009](https://doi.org/10.1016/j.physleta.2013.12.009). arXiv: [1101.1519](https://arxiv.org/abs/1101.1519).
- [20] Daniel Gottesman. “Stabilizer codes and quantum error correction”. PhD thesis. California Institute of Technology, Jan. 1997. eprint: [quant-ph/9705052](https://arxiv.org/abs/quant-ph/9705052).
- [21] Andrey Gromov. “Towards Classification of Fracton Phases: The Multipole Algebra”. In: *Physical Review X* 9.3 (Aug. 2019). ISSN: 2160-3308. URL: <http://dx.doi.org/10.1103/PhysRevX.9.031035>.
- [22] Jeongwan Haah. “Local stabilizer codes in three dimensions without string logical operators”. In: *Phys. Rev. A* 83 (4 Apr. 2011), p. 042330. DOI: [10.1103/PhysRevA.83.042330](https://doi.org/10.1103/PhysRevA.83.042330).
- [23] Gábor B. Halász, Timothy H. Hsieh, and Leon Balents. “Fracton Topological Phases from Strongly Coupled Spin Chains”. In: *Phys. Rev. Lett.* 119 (25 Dec. 2017), p. 257202. DOI: [10.1103/PhysRevLett.119.257202](https://doi.org/10.1103/PhysRevLett.119.257202).
- [24] Huan He et al. “Entanglement entropy from tensor network states for stabilizer codes”. In: *Phys. Rev. B* 97 (12 Mar. 2018), p. 125102. DOI: [10.1103/PhysRevB.97.125102](https://doi.org/10.1103/PhysRevB.97.125102).

- [25] Timothy H. Hsieh and Gábor B. Halász. “Fractons from partons”. In: *Phys. Rev. B* 96 (16 Oct. 2017), p. 165105. DOI: [10.1103/PhysRevB.96.165105](https://doi.org/10.1103/PhysRevB.96.165105).
- [26] Alexei Kitaev and John Preskill. “Topological entanglement entropy”. In: *Phys. Rev. Lett.* 96 (2006), p. 110404. DOI: [10.1103/PhysRevLett.96.110404](https://doi.org/10.1103/PhysRevLett.96.110404).
- [27] A. Kubica and B. Yoshida. “Ungauging quantum error-correcting codes”. In: (May 2018). arXiv: [1805.01836](https://arxiv.org/abs/1805.01836).
- [28] Ajesh Kumar and Andrew C. Potter. “Symmetry-enforced fractonicity and two-dimensional quantum crystal melting”. In: *Physical Review B* 100.4 (July 2019). ISSN: 2469-9969. URL: <http://dx.doi.org/10.1103/PhysRevB.100.045119>.
- [29] M. Levin and X.-G. Wen. “Detecting Topological Order in a Ground State Wave Function”. In: *Phys. Rev. Lett.* 96.11, 110405 (Mar. 2006), p. 110405. DOI: [10.1103/PhysRevLett.96.110405](https://doi.org/10.1103/PhysRevLett.96.110405).
- [30] Michael Levin and Zheng-Cheng Gu. “Braiding statistics approach to symmetry-protected topological phases”. In: *Phys. Rev. B* 86 (11 Sept. 2012), p. 115109. DOI: [10.1103/PhysRevB.86.115109](https://doi.org/10.1103/PhysRevB.86.115109). URL: <https://link.aps.org/doi/10.1103/PhysRevB.86.115109>.
- [31] Michael A. Levin and Xiao-Gang Wen. “String-net condensation: A physical mechanism for topological phases”. In: *Phys. Rev. B* 71 (4 Jan. 2005), p. 045110. DOI: [10.1103/PhysRevB.71.045110](https://doi.org/10.1103/PhysRevB.71.045110).
- [32] Han Ma, Michael Hermele, and Xie Chen. “Fracton topological order from the Higgs and partial-confinement mechanisms of rank-two gauge theory”. In: *Physical Review B* 98.3 (July 2018). ISSN: 2469-9969. URL: <http://dx.doi.org/10.1103/PhysRevB.98.035111>.
- [33] Han Ma et al. “Fracton topological order via coupled layers”. In: *Phys. Rev. B* 95 (24 June 2017), p. 245126. DOI: [10.1103/PhysRevB.95.245126](https://doi.org/10.1103/PhysRevB.95.245126).
- [34] Han Ma et al. “Topological entanglement entropy of fracton stabilizer codes”. In: *Phys. Rev. B* 97 (12 Mar. 2018), p. 125101. DOI: [10.1103/PhysRevB.97.125101](https://doi.org/10.1103/PhysRevB.97.125101).
- [35] Rahul M. Nandkishore and Michael Hermele. “Fractons”. In: *Annual Review of Condensed Matter Physics* 10.1 (Mar. 2019), pp. 295–313. ISSN: 1947-5462. DOI: [10.1146/annurev-conmatphys-031218-013604](https://doi.org/10.1146/annurev-conmatphys-031218-013604). URL: <http://dx.doi.org/10.1146/annurev-conmatphys-031218-013604>.
- [36] Shriya Pai and Michael Hermele. “Fracton fusion and statistics”. In: *Physical Review B* 100.19 (Nov. 2019). ISSN: 2469-9969. URL: <http://dx.doi.org/10.1103/PhysRevB.100.195136>.

- [37] Shriya Pai and Michael Pretko. “Dynamical Scar States in Driven Fracton Systems”. In: *Physical Review Letters* 123.13 (Sept. 2019). ISSN: 1079-7114. URL: <http://dx.doi.org/10.1103/PhysRevLett.123.136401>.
- [38] Shriya Pai, Michael Pretko, and Rahul M. Nandkishore. “Localization in Fractonic Random Circuits”. In: *Physical Review X* 9.2 (Apr. 2019). ISSN: 2160-3308. URL: <http://dx.doi.org/10.1103/PhysRevX.9.021003>.
- [39] Abhinav Prem, Jeongwan Haah, and Rahul Nandkishore. “Glassy quantum dynamics in translation invariant fracton models”. In: *Phys. Rev. B* 95 (15 Apr. 2017), p. 155133. DOI: [10.1103/PhysRevB.95.155133](https://doi.org/10.1103/PhysRevB.95.155133).
- [40] Abhinav Prem and Dominic Williamson. “Gauging permutation symmetries as a route to non-Abelian fractons”. In: *SciPost Physics* 7.5 (Nov. 2019). ISSN: 2542-4653. DOI: [10.21468/scipostphys.7.5.068](https://doi.org/10.21468/scipostphys.7.5.068). URL: <http://dx.doi.org/10.21468/SciPostPhys.7.5.068>.
- [41] Abhinav Prem et al. “Cage-Net Fracton Models”. In: *Physical Review X* 9.2 (Apr. 2019). ISSN: 2160-3308. URL: <http://dx.doi.org/10.1103/PhysRevX.9.021010>.
- [42] Michael Pretko. “Emergent gravity of fractons: Mach’s principle revisited”. In: *Phys. Rev. D* 96 (2 July 2017), p. 024051. DOI: [10.1103/PhysRevD.96.024051](https://doi.org/10.1103/PhysRevD.96.024051).
- [43] Michael Pretko. “Generalized electromagnetism of subdimensional particles: A spin liquid story”. In: *Phys. Rev. B* 96 (3 July 2017), p. 035119. DOI: [10.1103/PhysRevB.96.035119](https://doi.org/10.1103/PhysRevB.96.035119).
- [44] Michael Pretko. “Subdimensional particle structure of higher rank $U(1)$ spin liquids”. In: *Phys. Rev. B* 95 (11 Mar. 2017), p. 115139. DOI: [10.1103/PhysRevB.95.115139](https://doi.org/10.1103/PhysRevB.95.115139).
- [45] Michael Pretko. “The fracton gauge principle”. In: *Physical Review B* 98.11 (Sept. 2018). ISSN: 2469-9969. URL: <http://dx.doi.org/10.1103/PhysRevB.98.115134>.
- [46] Michael Pretko and Leo Radzihovsky. “Fracton-Elasticity Duality”. In: *Phys. Rev. Lett.* 120 (19 May 2018), p. 195301. DOI: [10.1103/PhysRevLett.120.195301](https://doi.org/10.1103/PhysRevLett.120.195301).
- [47] A. Rasmussen, Y.-Z. You, and C. Xu. “Stable Gapless Bose Liquid Phases without any Symmetry”. In: (Jan. 2016). arXiv: [1601.08235](https://arxiv.org/abs/1601.08235).
- [48] Pablo Sala et al. “Ergodicity Breaking Arising from Hilbert Space Fragmentation in Dipole-Conserving Hamiltonians”. In: *Physical Review X* 10.1 (Feb. 2020). ISSN: 2160-3308. URL: <http://dx.doi.org/10.1103/PhysRevX.10.011047>.

- [49] Bowen Shi and Yuan-Ming Lu. “Deciphering the nonlocal entanglement entropy of fracton topological orders”. In: *Phys. Rev. B* 97 (14 Apr. 2018), p. 144106. DOI: [10.1103/PhysRevB.97.144106](https://doi.org/10.1103/PhysRevB.97.144106).
- [50] Wilbur Shirley, Kevin Slagle, and Xie Chen. “Foliated fracton order from gauging subsystem symmetries”. In: *SciPost Physics* 6.4, 041 (Apr. 2019), p. 041. DOI: [10.21468/SciPostPhys.6.4.041](https://doi.org/10.21468/SciPostPhys.6.4.041). arXiv: [1806.08679](https://arxiv.org/abs/1806.08679).
- [51] Wilbur Shirley, Kevin Slagle, and Xie Chen. “Foliated fracton order in the checkerboard model”. In: 99.11, 115123 (Mar. 2019), p. 115123. DOI: [10.1103/PhysRevB.99.115123](https://doi.org/10.1103/PhysRevB.99.115123). arXiv: [1806.08633](https://arxiv.org/abs/1806.08633).
- [52] Wilbur Shirley, Kevin Slagle, and Xie Chen. “Fractional excitations in foliated fracton phases”. In: *Annals of Physics* 410, 167922 (Nov. 2019), p. 167922. DOI: [10.1016/j.aop.2019.167922](https://doi.org/10.1016/j.aop.2019.167922). arXiv: [1806.08625](https://arxiv.org/abs/1806.08625).
- [53] Wilbur Shirley, Kevin Slagle, and Xie Chen. “Universal entanglement signatures of foliated fracton phases”. In: *SciPost Physics* 6.1 (Jan. 2019). URL: <http://dx.doi.org/10.21468/SciPostPhys.6.1.015>.
- [54] Wilbur Shirley et al. “Fracton Models on General Three-Dimensional Manifolds”. In: *Physical Review X* 8.3, 031051 (July 2018), p. 031051. DOI: [10.1103/PhysRevX.8.031051](https://doi.org/10.1103/PhysRevX.8.031051). arXiv: [1712.05892](https://arxiv.org/abs/1712.05892).
- [55] Kevin Slagle, David Aasen, and Dominic Williamson. “Foliated Field Theory and String-Membrane-Net Condensation Picture of Fracton Order”. In: *SciPost Phys.* 6 (4 2019), p. 43. DOI: [10.21468/SciPostPhys.6.4.043](https://doi.org/10.21468/SciPostPhys.6.4.043). URL: <https://scipost.org/10.21468/SciPostPhys.6.4.043>.
- [56] Kevin Slagle and Yong Baek Kim. “Fracton topological order from nearest-neighbor two-spin interactions and dualities”. In: *Phys. Rev. B* 96 (16 Oct. 2017), p. 165106. DOI: [10.1103/PhysRevB.96.165106](https://doi.org/10.1103/PhysRevB.96.165106).
- [57] Kevin Slagle and Yong Baek Kim. “Quantum field theory of X-cube fracton topological order and robust degeneracy from geometry”. In: *Phys. Rev. B* 96 (19 Nov. 2017), p. 195139. DOI: [10.1103/PhysRevB.96.195139](https://doi.org/10.1103/PhysRevB.96.195139).
- [58] Kevin Slagle and Yong Baek Kim. “X-cube model on generic lattices: Fracton phases and geometric order”. In: *Phys. Rev. B* 97 (16 Apr. 2018), p. 165106. DOI: [10.1103/PhysRevB.97.165106](https://doi.org/10.1103/PhysRevB.97.165106).
- [59] Kevin Slagle, Abhinav Prem, and Michael Pretko. “Symmetric tensor gauge theories on curved spaces”. In: *Annals of Physics* 410, 167910 (Nov. 2019), p. 167910. DOI: [10.1016/j.aop.2019.167910](https://doi.org/10.1016/j.aop.2019.167910). arXiv: [1807.00827](https://arxiv.org/abs/1807.00827).

- [60] Hao Song et al. “Twisted fracton models in three dimensions”. In: *Physical Review B* 99.15 (Apr. 2019). ISSN: 2469-9969. URL: <http://dx.doi.org/10.1103/PhysRevB.99.155118>.
- [61] David T. Stephen et al. “Subsystem symmetries, quantum cellular automata, and computational phases of quantum matter”. In: (June 2018). URL: <https://arxiv.org/abs/1806.08780>.
- [62] Kevin T. Tian, Eric Samperton, and Zhenghan Wang. “Haah codes on general three-manifolds”. In: *Annals of Physics* 412 (Jan. 2020), p. 168014. ISSN: 0003-4916. DOI: [10.1016/j.aop.2019.168014](https://doi.org/10.1016/j.aop.2019.168014) URL: <http://dx.doi.org/10.1016/j.aop.2019.168014>.
- [63] Kevin T. Tian and Zhenghan Wang. “Generalized Haah Codes and Fracton Models”. In: *arXiv:1902.04543* (Feb. 2019). URL: <http://arxiv.org/abs/1902.04543>.
- [64] S. Vijay. “Isotropic Layer Construction and Phase Diagram for Fracton Topological Phases”. In: (Jan. 2017). arXiv: [1701.00762](https://arxiv.org/abs/1701.00762).
- [65] S. Vijay and L. Fu. “A Generalization of Non-Abelian Anyons in Three Dimensions”. In: (June 2017). arXiv: [1706.07070](https://arxiv.org/abs/1706.07070).
- [66] Sagar Vijay, Jeongwan Haah, and Liang Fu. “A new kind of topological quantum order: A dimensional hierarchy of quasiparticles built from stationary excitations”. In: *Phys. Rev. B* 92 (23 Dec. 2015), p. 235136. DOI: [10.1103/PhysRevB.92.235136](https://doi.org/10.1103/PhysRevB.92.235136).
- [67] Sagar Vijay, Jeongwan Haah, and Liang Fu. “Fracton topological order, generalized lattice gauge theory, and duality”. In: *Phys. Rev. B* 94 (23 Dec. 2016), p. 235157. DOI: [10.1103/PhysRevB.94.235157](https://doi.org/10.1103/PhysRevB.94.235157).
- [68] Chenjie Wang and Michael Levin. “Topological invariants for gauge theories and symmetry-protected topological phases”. In: *Phys. Rev. B* 91 (16 Apr. 2015), p. 165119. DOI: [10.1103/PhysRevB.91.165119](https://doi.org/10.1103/PhysRevB.91.165119).
- [69] Taige Wang, Wilbur Shirley, and Xie Chen. “Foliated fracton order in the Majorana checkerboard model”. In: *Physical Review B* 100.8 (Aug. 2019). ISSN: 2469-9969. URL: <http://dx.doi.org/10.1103/PhysRevB.100.085127>.
- [70] X. G. Wen and A. Zee. “Classification of Abelian quantum Hall states and matrix formulation of topological fluids”. In: *Phys. Rev. B* 46 (4 July 1992), pp. 2290–2301. DOI: [10.1103/PhysRevB.46.2290](https://doi.org/10.1103/PhysRevB.46.2290).
- [71] Xiao-Gang Wen. “A systematic construction of gapped non-liquid states”. In: (Feb. 2020). arXiv: [2002.02433](https://arxiv.org/abs/2002.02433).
- [72] Dominic J. Williamson. “Fractal symmetries: Ungauging the cubic code”. In: *Phys. Rev. B* 94 (15 Oct. 2016), p. 155128. DOI: [10.1103/PhysRevB.94.155128](https://doi.org/10.1103/PhysRevB.94.155128).

- [73] Dominic J. Williamson, Zhen Bi, and Meng Cheng. “Fractonic matter in symmetry-enriched $U(1)$ gauge theory”. In: *Physical Review B* 100.12 (Sept. 2019). ISSN: 2469-9969. URL: <http://dx.doi.org/10.1103/PhysRevB.100.125150>.
- [74] Dominic J. Williamson, Arpit Dua, and Meng Cheng. “Spurious Topological Entanglement Entropy from Subsystem Symmetries”. In: *Physical Review Letters* 122.14 (Apr. 2019). ISSN: 1079-7114. URL: <http://dx.doi.org/10.1103/PhysRevLett.122.140506>.
- [75] Han Yan. “Hyperbolic fracton model, subsystem symmetry, and holography”. In: *Physical Review B* 99.15 (Apr. 2019). ISSN: 2469-9969. URL: <http://dx.doi.org/10.1103/PhysRevB.99.155126>.
- [76] Han Yan et al. “Rank-2 $U(1)$ Spin Liquid on the Breathing Pyrochlore Lattice”. In: *Physical Review Letters* 124.12 (Mar. 2020). ISSN: 1079-7114. URL: <http://dx.doi.org/10.1103/PhysRevLett.124.127203>.
- [77] Beni Yoshida. “Exotic topological order in fractal spin liquids”. In: *Phys. Rev. B* 88 (12 Sept. 2013), p. 125122. DOI: [10.1103/PhysRevB.88.125122](http://dx.doi.org/10.1103/PhysRevB.88.125122).
- [78] Yizhi You. “Non-Abelian defects in fracton phases of matter”. In: *Physical Review B* 100.7 (Aug. 2019). ISSN: 2469-9969. URL: <http://dx.doi.org/10.1103/PhysRevB.100.075148>.
- [79] Yizhi You, Daniel Litinski, and Felix von Oppen. “Higher-order topological superconductors as generators of quantum codes”. In: *Physical Review B* 100.5 (Aug. 2019). ISSN: 2469-9969. URL: <http://dx.doi.org/10.1103/PhysRevB.100.054513>.
- [80] Yizhi You et al. “Subsystem symmetry protected topological order”. In: *Physical Review B* 98.3 (July 2018). ISSN: 2469-9969. URL: <http://dx.doi.org/10.1103/PhysRevB.98.035112>.
- [81] Yizhi You et al. “Symmetric fracton matter: Twisted and enriched”. In: *Annals of Physics* 416 (May 2020), p. 168140. ISSN: 0003-4916. URL: <http://dx.doi.org/10.1016/j.aop.2020.168140>.

STRONG PLANAR SUBSYSTEM SYMMETRY-PROTECTED TOPOLOGICAL PHASES AND THEIR DUAL FRACTON ORDERS

10.1 Introduction

Global symmetries, such as the \mathbb{Z}_2 spin-flip symmetry of the Ising model, act throughout the bulk of a system. Recently, there has been an emerging interest in symmetries that act on only *part* of a system. These include higher-form symmetries which act on deformable lower-dimensional manifolds of a system [1], as well as subsystem symmetries [2, 3, 4], which act on rigid lower-dimensional subsystems. It has also been realized that such subsystem symmetries may protect non-trivial symmetry-protected topological (SPT) phases [5, 6, 7, 8]: gapped, disordered, short-range entangled phases which cannot be adiabatically connected to the trivial disordered phase in the presence of symmetry, but can be if the symmetry is not enforced. Examples of subsystem symmetries include those which act along linear [9, 10], planar [11, 12], or even fractal [13, 14, 15, 16, 17, 18] subsystems. Such phases have been aptly named subsystem SPT (SSPT) phases, and this paper concerns their classification.

In 2+1D, such systems have gained interest due to the discovery that non-trivial SSPT phases may serve as a resource for universal measurement-based quantum computation (MBQC) [19, 20, 21, 22, 23, 24] and also due to their unusual patterns of quantum entanglement [25, 10, 26, 27, 28]. In attempting to classify 2+1D linear SSPTs, one is faced with the issue that there are uncountably infinitely many distinct phases. This is due to the presence of *weak* phases: SSPT phases which can be constructed by stacking (a process which we will define) 1+1D SPTs along the subsystems, whose nontriviality are simply a manifestation of lower dimensional physics. Ref. [10] defined an equivalence relation between phases wherein two phases that differ by stacking 1+1D SPTs belong to the same equivalence class. Phases not in the trivial equivalence class are, by definition, *strong* SSPTs. It was found that there are a small number of equivalence classes, which provided a sensible classification for

the uncountably infinite phases. In contrast, note that for 2+1D fractal SSPTs, weak phases do not exist and the number of phases is countably infinite [15]. This paper is the natural extension of Ref. [10] to planar symmetries in 3+1D (henceforth, simply 3D).

Systems with planar subsystem symmetries have also received intense interest recently due to the discovery that, under a generalized ‘gauging’ duality [11, 16, 29], they map on to long-range entangled models exhibiting *fracton* topological order [30, 31, 32, 13, 33, 34, 35, 36, 37, 38, 39, 40, 41, 42, 43, 44, 45, 46, 47, 48]. An example of such a system is the plaquette Ising model [49, 11, 50], whose paramagnetic phase is dual to the X-cube model of fracton topological order [11]. Fracton phases are characterized by a subextensive topological ground state degeneracy growing exponentially with L , and quasiparticle excitations with limited mobility. The classification of such fracton phases is an active topic of research [51, 52, 53, 54, 55, 56, 57, 58, 59]. In this paper, we focus on classification of SSPT phases which are dual to abelian fracton phases, thus also providing a useful means of categorizing such fracton phases.

The brief history of 3D planar SSPT phases begins with Ref. [12], which constructed a non-trivial 3D planar SSPT model. However, it was later discovered that its fracton dual belonged to the same foliated fracton phase as the X-cube model [60], implying that it is weak. More recently, fracton phases were constructed in Ref. [58] which possess ‘twisted’ foliated fracton orders, raising the question as to the nature of their SSPT duals. We find that these phases, too, are weak. This prompts the question: do any strong planar SSPTs exist? We answer this in the affirmative. We explicitly construct strong SSPT phases, which are dual to novel strong fracton phases with unusual braiding statistics that cannot be obtained by coupling 2D theories. In this sense these statistical interactions are “intrinsically” three-dimensional.

We will first show how to construct weak 3D planar SSPT phases via a stacking process of 2D SPTs. We then ask whether there are SSPT phases which cannot be realized by this process. We identify mechanisms by which an SSPT may be strong, leading to a classification of such phases, and construct exactly solvable, zero-correlation length models realizing these phases. In the fracton dual picture, this construction corresponds to one in which 2D topological orders are stacked on to and strongly coupled to an existing fracton model [58]. The duals of our strong SSPTs are novel fracton phases which cannot be

attained via such a procedure, also implying that they cannot be realized by a p -string condensation transition [46, 61], as we will show.

10.2 Planar subsystem symmetries

Throughout we will consider a system with degrees of freedom on each site of a cubic lattice. Each site \mathbf{r} transforms under the finite abelian on-site symmetry group G under a unitary representation $u_{\mathbf{r}}(g)$, where $g \in G$. An xy planar symmetry acting on plane z acts as $S^{xy}(z; g) = \prod_{x,y} u_{\mathbf{r}=(x,y,z)}(g)$ for $g \in G$. Similarly, we may define $S^{yz}(x; g)$ and $S^{zx}(y; g)$, which act on yz and zx planes respectively. Importantly, individual sites transform under the same on-site representation regardless of the orientation of the planar symmetry — there is therefore a redundancy: the product of all xy symmetries is identical to the product of all yz or all zx symmetries. We will refer to models which respect only one orientation of planar symmetry as 1-foliated, those with two as 2-foliated, and those with all three as 3-foliated. To construct explicit models, we choose the on-site degrees of freedom to be G -valued, $|g_{\mathbf{r}}\rangle$, which transform under the on-site symmetry as $u_{\mathbf{r}}(g) |g_{\mathbf{r}}\rangle = |gg_{\mathbf{r}}\rangle$.

10.3 Construction of weak SSPT phases

It is possible to construct non-trivial SSPT phases from known 2D global SPTs, as we will show in this section. Phases obtained in this way are ‘weak’, by definition, whose nontrivial properties are in some sense a manifestation of lower-dimensional physics. We emphasize here that we do not assume any translation invariance in our system. Hence, our definition is different (but similar in spirit) to weak crystalline SPTs with global symmetries, which are stacks of lower dimensional SPTs protected by translation symmetry.

First, we briefly review the group cohomological classification of 2D bosonic SPTs with global symmetry group G [7, 62]. For the purpose of being self-contained, we also include a more detailed review in the Supplementary Material [63]. The classification of such phases [7, 64] is given by the third cohomology group $H^3[G, U(1)]$. For simplicity, we may consider $G = (\mathbb{Z}_N)^n$, in which case an element of $H^3[G, U(1)]$ is specified by integers, p_I^i ($i \in [1, n]$), p_{II}^{ij} ($i < j$), and p_{III}^{ijk} ($i < j < k$), all modulo N , called type-I, II, and III cocycles respectively. We will specify p_I^i and p_{II}^{ij} compactly in a single symmetric $n \times n$ integer matrix \mathbf{M} with $M_{ii} = 2p_I^i$ and $M_{ij} = M_{ji} = p_{II}^{ij}$. Upon gauging the global symmetries of a 2D SPT, one obtains a topologically ordered

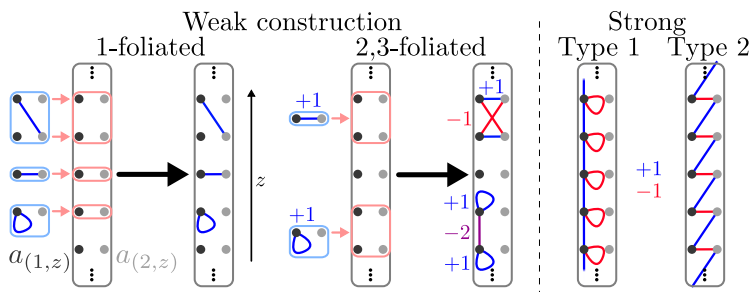


Figure 10.1: (Left) Examples of our construction of 1-foliated or weak 2 or 3-foliated models, for $G = \mathbb{Z}_N \times \mathbb{Z}_N$, in the graphical notation. 2D SPTs to be stacked, are shown in the blue boxes, and the large arrow points to the resulting SSPT after stacking. The color of the edges connecting two vertices indicate its weight modulo N . (Right) Examples of \mathbf{M} matrices that cannot be obtained by stacking 2D phases onto 2 or 3-foliated models. The Type 1 phase is only strong for even N , and Type 2 strong phases can only be realized for 2-foliated symmetries.

system with fractional quasiparticles carrying gauge charge or flux (or both). Nontrivial type-III cocycles give rise to non-abelian topological order, [65, 66] which we will not consider here. A generating set of quasiparticles are the “electric” excitations (gauge charges) $\{e_i\}$ and “magnetic” excitations (gauge fluxes) $\{m_i\}$. Each e_i has a $e^{2\pi i/N}$ braiding statistic with m_i and trivial statistics with all other generators. The elements of \mathbf{M} characterize the self and mutual statistics of gauge flux excitations [62]. In particular, the type-I cocycles give rise to a self exchange statistic $e^{\pi i M_{ii}/N^2}$ of the gauge flux m_i , and type-II cocycles lead to a mutual braiding statistic of $e^{2\pi i M_{ij}/N^2}$ between m_i and m_j . Note that these phases are only well defined modulo $e^{2\pi i/N}$, since flux is only well defined up to attachment of charge, $m_i \rightarrow m_i e_j$. Finally, we note that abelian topological orders in 2D can all be described by \mathbf{K} matrix Chern-Simons theories. [67, 68] The topological orders we have discussed have a $2n \times 2n$ \mathbf{K} matrix description with

$$\mathbf{K} = N \begin{bmatrix} -\frac{1}{N}\mathbf{M} & \mathbf{1} \\ \mathbf{1} & 0 \end{bmatrix}, \quad \mathbf{K}^{-1} = \frac{1}{N} \begin{bmatrix} 0 & \mathbf{1} \\ \mathbf{1} & \frac{1}{N}\mathbf{M} \end{bmatrix} \quad (10.1)$$

where the indices labeling quasiparticles are ordered as $\{e_1, \dots, e_n, m_1, \dots, m_n\}$. Quasiparticles are described by an integer vector ℓ in this basis, and have self-exchange statistic $e^{\pi i \ell^T \cdot \mathbf{K}^{-1} \cdot \ell}$ and mutual braiding statistics $e^{2\pi i \ell_1^T \cdot \mathbf{K}^{-1} \cdot \ell_2}$.

It is always possible to view a 3D planar SSPT as a quasi-2D system in the xy plane with a subextensively large symmetry group G^L by compactifying

the z direction. We may then proceed to compute its classification in terms of $H^3[G^L, U(1)]$, which is characterized by a subextensively large \mathbf{M} matrix. We note that it is possible to define \mathbf{M} matrices corresponding to yz or zx as well, but for reasons that will become clear we will always consider the xy symmetries only. It is useful to introduce a graphical notation for \mathbf{M} , which is used in Fig. 10.1. The α th generator of G in a plane z is denoted by a vertex $a_{i=(\alpha,z)}$. Two vertices i and j are connected by an undirected edge with weight M_{ij} , and a vertex i is connected to itself via a self-loop with weight $M_{ii}/2$, where weights are defined modulo N .

Consider the 2D global symmetry group $G_{2D} = G^K$ for an integer K . For appropriate choice of the pure phase function f_{2D} , the wavefunction $|\psi\rangle_{2D} = \sum_{\{g_{\mathbf{r}}\}} f_{2D}(\{g_{\mathbf{r}}\}) |\{g_{\mathbf{r}}\}\rangle_{2D}$ on a 2D square lattice is a zero-correlation length ground state of a commuting Hamiltonian with SPT order [63]. All phases in the group cohomology classification can be realized in this way [69, 66, 70].

Suppose we start with the trivial disordered wavefunction $|\psi_0\rangle = \sum_{\{g_{\mathbf{r}}\}} |\{g_{\mathbf{r}}\}\rangle$ on the 3D cubic lattice. We can construct a nontrivial 1-foliated SSPT by identifying each factor of G in G_{2D} in the function $f_{2D}(\{g_{\mathbf{r}}\})$ with a planar G symmetry in an arbitrary collection of planes z_1, \dots, z_K (where z_k are all within some finite range to ensure locality). The wavefunction $|\psi\rangle_{1\text{-fol}} = U |\psi_0\rangle$ with $U = \sum_{\{g_{\mathbf{r}}\}} f_{2D}(\{g_{\mathbf{r}}\}_{r_z \in \{z_k\}}) |\{g_{\mathbf{r}}\}\rangle \langle \{g_{\mathbf{r}}\}|$ is the ground state of a 1-foliated 3D SSPT, which is nontrivial only near the planes z_k . We may then repeat this procedure arbitrarily many times, each time acting on the previous state with U for different choices of f_{2D} and $\{z_k\}$. We will call this procedure “stacking” the 2D SPT $|\psi\rangle_{2D}$ onto the planes $\{z_k\}$ of a 1-foliated SSPT.

More generally, we may define a stacking operation between two SSPTs in which the two systems, with on-site symmetry representations $u_{\mathbf{r}}^{(1)}(g)$ and $u_{\mathbf{r}}^{(2)}(g)$, are placed on top of each other to create a new SSPT with on-site representation $u_{\mathbf{r}}(g) = u_{\mathbf{r}}^{(1)}(g) \otimes u_{\mathbf{r}}^{(2)}(g)$. The group structure of the standard SPT classification is realized under such a stacking operation. Stacking a 2D SPT onto a 3D SSPT can be viewed as stacking two 3D SSPTs, in which the first is only nontrivial in the vicinity of a number of planes $\{z_k\}$. We define any phase realizable by stacking 2D SPTs in this way to be weak. In the case of our 1-foliated SSPT construction, each additional stacked 2D SPT simply adds to the corresponding elements of \mathbf{M} , shown graphically in Fig. 10.1. For 1-foliated symmetries, it is thus possible to realize any \mathbf{M} by stacking 2D

SPTs; hence all phases are weak.

On the other hand, for 2- or 3-foliated models, this procedure may not work because $|\psi\rangle_{1\text{-fol}}$ is not guaranteed to be symmetric under the orthogonal planar symmetries (if it is, we can simply follow the same procedure). Instead, let us define variables $d_{\mathbf{r}} = g_{\mathbf{r}+\mathbf{z}}g_{\mathbf{r}}^{-1}$, which transform under xy planar symmetries but are invariant under all orthogonal symmetries. We may then define non-trivial SSPT wavefunctions as before, but in terms of $d_{\mathbf{r}}$ instead using the unitary

$$U = \sum_{\{g_{\mathbf{r}}\}} f_{2D}(\{d_{\mathbf{r}}\}_{r_z \in \{z_k\}}) |\{g_{\mathbf{r}}\}\rangle \langle \{g_{\mathbf{r}}\}|, \quad (10.2)$$

which is explicitly invariant under the orthogonal symmetries. However, in this case the \mathbf{M} matrix of the 2D SPT does not map directly onto that of the SSPT — instead one should view the 2D SPT as living “in between” the planes of the SSPT, at $\{z_k + 1/2\}$. To obtain the \mathbf{M} matrix of the SSPT, one can compute the appropriate type-I and II cocycles of the 2D SPT in the basis of the xy planar symmetries [63]. This process is shown in Fig. 10.1. As will be discussed in the next section, unlike for 1-foliated symmetries, there are now allowable phases which cannot be realized by stacking any number of 2D SPT.

Note that in this discussion we have implicitly ignored nontrivial SSPTs that have trivial \mathbf{M} matrices. Such phases do exist [63]. However, we conjecture that all such phases are weak (they can be realized by stacking 2D linear SSPTs [10]) and therefore irrelevant in the classification of strong phases.

10.4 General constraints and invariants

In the presence of orthogonal symmetries, there are general constraints that must be satisfied by \mathbf{M} . Conceptually, these arise due to the aforementioned redundancy: the global symmetry $S_{\text{glob}}(g) = \prod_z S^{(xy)}(z; g) = \prod_x S^{(yz)}(x; g)$. Since yz symmetries do not contribute to \mathbf{M} , the generator $S_{\text{glob}}(g)$ must therefore manifest trivially in \mathbf{M} . This leads to two types of constraints on the elements of \mathbf{M} : the global symmetry must have trivial type-II cocycle with any other symmetry and trivial type-I cocycle with itself. We prove that these constraints must hold generally [63]. Let us label the α th generator of G on the z th plane by $i = (\alpha, z)$. Then, the two constraints are expressed as

$$\sum_{z'} M_{(\alpha, z), (\beta, z')} \equiv 0 \pmod{N}, \quad \forall \alpha, z, \beta \quad (10.3)$$

and

$$\frac{1}{2} \sum_{z,z'} M_{(\alpha,z),(\alpha,z')} \equiv 0 \pmod{N}, \quad \forall \alpha \quad (10.4)$$

These constraints define a restricted subgroup of $H^3[G^L, U(1)]$ in which 2- or 3-foliated SSPTs must reside. As we will show, there are now allowed phases which cannot be realized by stacking any number of 2D SPTs — these are precisely the strong phases we are searching for. This motivates us to define two types of strong invariants, F_1 and F_2 , which cannot be changed by stacking with 2D SPTs.

10.5 Strong SSPTs: Type 1

Consider $G = \mathbb{Z}_{2N}$. Then $M_{zz'}$ is an $L \times L$ matrix. Pick an arbitrary cut that divides the system into two halves $z < z_0$ and $z \geq z_0$. Then,

$$F_1 \equiv \sum_{z < z_0} \sum_{z' \geq z_0} M_{zz'} \pmod{2} \quad (10.5)$$

is a \mathbb{Z}_2 -valued global invariant. To see why, view $M_{zz'} \pmod{2}$ as a \mathbb{Z}_2 “flux” flowing from vertex z to z' in the graphical representation. Then, Eq. 10.3 is a divergence-free constraint at each vertex. The invariant F_1 is simply the total \mathbb{Z}_2 flux flowing through a cut at z_0 . It is therefore clear that F_1 does not depend on the choice of cut z_0 , nor can it be modified by stacking a 2D SPT which amounts to adding closed flux loops locally.

10.6 Type 2

Consider $G = \mathbb{Z}_N \times \mathbb{Z}_N$, so that $M_{(\alpha,z),(\beta,z')}$ is a $2L \times 2L$ matrix. Again pick a cut z_0 . Then,

$$F_2 \equiv \sum_{z < z_0} \sum_{z' \geq z_0} (M_{(1,z),(2,z')} - M_{(2,z),(1,z')}) \pmod{N} \quad (10.6)$$

is a \mathbb{Z}_N -valued global invariant. To see how this arises, interpret $M_{(1,z),(2,z')}$ as a \mathbb{Z}_N “flux” flowing from vertex $(1, z)$ to $(2, z')$. Like before, Eq. 10.3 is a divergence-free constraint on this flux and F_2 measures the total flux flowing across a cut, which therefore does not depend on z_0 nor can it be modified by stacking with 2D SPTs.

In the Supplementary Material [63], we prove three important statements. First, that the invariant F_1 or F_2 is the same regardless of whether we consider the \mathbf{M} matrix obtained from xy symmetries or that obtained from yz

(or zx) symmetries. Secondly, 3-foliated systems must have trivial $F_2 = 0$. Thirdly, the set of F_1 and F_2 (which we also define for general G) completely classify \mathbf{M} modulo stacking with 2D SPTs. Finally, we also provide an explicit construction of a 3-foliated model which realizes a non-trivial type 1 strong phase $F_1 = 1$, and a 2-foliated model which realizes arbitrary F_1 and F_2 , thereby demonstrating the existence of such strong phases. Examples of \mathbf{M} matrices with non-trivial F_1 and F_2 are shown in Fig. 10.1 (right).

Let us define a ‘strong’ equivalence relation between SSPTs, under which two phases belong to the same equivalence class if they can be connected with one another by stacking of 2D phases (along with, of course, symmetric local unitary transformations and addition/removal of disentangled degrees of freedom transforming as an on-site linear representation of G [71]). For an arbitrary finite abelian group G , the set of equivalence classes is given by

$$C_{3\text{-fol}}[G] = \prod_i \mathbb{Z}_{\text{gcd}(2, N_i)} \quad (10.7)$$

$$C_{2\text{-fol}}[G] = \prod_i \mathbb{Z}_{\text{gcd}(2, N_i)} \times \prod_{i < j} \mathbb{Z}_{\text{gcd}(N_i, N_j)} \quad (10.8)$$

for 3-foliated and 2-foliated models respectively. The group structure is realized via the stacking operation between two SSPTs. We note that this equivalence relation can be naturally formulated in terms of planar-symmetric local unitary circuits, generalizing the definition of Ref. [10]. Indeed the unitaries U used to construct weak SSPTs are examples of such circuits.

10.7 Fracton duals

It is well known that, under a generalized gauge duality [11, 16, 29], SSPT phases map onto models of fracton topological order [12, 58]. The simplest and most well-studied fracton model is the X-cube model [11], which is obtained by gauging the planar symmetries of the plaquette Ising paramagnet, and hosts fractional quasiparticle excitations with limited mobility including immobile fractons, lineons mobile along lines, and planons mobile within planes (which are either fracton dipoles or lineon dipoles). For our discussion, we will assume that the reader has a rudimentary understanding of the X-cube fracton model and its quasiparticle excitations (see Ref. [34] for a review).

Let us begin with 3-foliated SSPTs, which are dual to ‘twisted’ X-cube fracton topological orders with fractonic charge [58]. The gauge flux $m_{(g,z)}$ of an

element g on the plane z is a planon: a composite excitation composed of a lineon anti-lineon pair on the planes $z+1/2$ and $z-1/2$, i.e. a lineon dipole. A single lineon can be regarded as a semi-infinite stack of lineon dipoles mobile in the x and y directions. For a more nuanced discussion of the mobility of such excitations, see Supplementary Material.

The constraints on the matrix \mathbf{M} have a simple interpretation in this language: the infinite stack of lineon dipoles, which belongs to the vacuum superselection sector [72], must have trivial braiding statistics with all other lineon dipoles, and a trivial exchange statistic with itself. The invariant F_1 also has a simple interpretation in this picture: the quantity $e^{2\pi i F_1/N^2}$ corresponds to the braiding (or crossing [46]) statistic of a lineon and its anti-lineon on the same plane, modulo $e^{4\pi i/N^2}$.

It is possible to construct fracton topological orders by strongly coupling intersecting stacks of topologically ordered 2D discrete gauge theories oriented along the xy , yz , and zx planes, inducing a type of transition called p -string condensation [46, 61]. More generally, these stacks of 2D gauge theories can be replaced by arbitrary 1-foliated gauge theories [58]. The twisted X-cube models that emerge from this construction are dual to weak 3-foliated SSPTs constructed via the planar-symmetric local unitaries U in Eq. 10.2. We walk through this correspondence in more detail in the Supplementary Material [63].

Equivalently, twisted X-Cube models dual to weak SSPTs may be obtained by effectively “binding” 2D anyons to existing planons in the fracton model. As an example, consider placing one layer of the doubled semion topological order (with bosonic e and semionic m) onto a plane z_0 of the X-Cube model, and condensing pairs of e and fracton dipoles in the plane z_0 . The end result is that x or y mobile lineons on plane z_0 and m become confined, but the bound state of the two remain deconfined and form the new lineon excitations. Since m is a semion, the new lineons now also inherit their semionic statistics. This procedure can be extended to general twisted quantum doubles living on multiple planes $\{z_k\}$, thereby binding more general 2D anyons to the lineons; this process is exactly dual to stacking a 2D SPT according to Eq. 10.2.

Conversely, strong 3-foliated SSPTs are dual to fracton models that cannot be realized through such a construction. This correspondence sheds light on the F_1 strong invariant — in p -string condensation, lineon crossing statistics are inherited from the self-braiding statistics of fluxes in the 1-foliated gauge

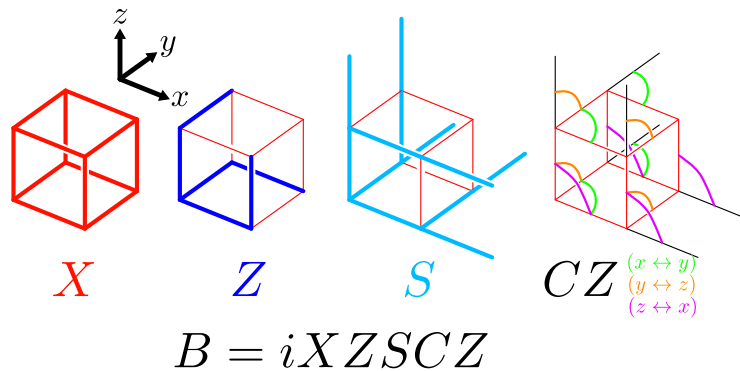


Figure 10.2: The commuting (but non-projector) Hamiltonian describing the fracton dual of the \mathbb{Z}_2 strong model is shown. Qubit degrees of freedom live on the links. The Hamiltonian is a sum over all cubes c of the term B_c , shown, which consists of Pauli X , Z , $S = \text{diag}(1, i)$, and $CZ_{12} = (-1)^{(Z_1-1)(Z_2-1)/4}$ operators between qubits on links of different orientations as shown by the colored lines. In addition, the Hamiltonian also has the usual cross terms $A_v^{\mu\nu}$ from the X-Cube which is the product of four Z operators lying in the $\mu\nu$ plane touching a vertex v . Thus, $H = -\sum_c B_c - \sum_v (A_v^{xy} + A_v^{yz} + A_v^{zx})$.

theories, and are therefore the square of a flux exchange statistic, i.e. a multiple of $e^{4\pi i/N^2}$ for $G = \mathbb{Z}_N$ with N even. In a strong phase, $F_1 = 1$ implies that this statistic is offset by $e^{2\pi i/N^2}$. The fracton dual of the Type 1 strong $G = \mathbb{Z}_2$ model [63] is an example of a novel such fracton order in which lineons satisfying a triple fusion rule have $\pm i$ mutual crossing statistic, and therefore cannot be realized via p -string condensation. A Hamiltonian realizing this phase is shown in Fig 10.2.

One can also consider the fracton duals of 2-foliated SSPTs, which are novel ‘twisted’ versions of the 2-foliated lineon-planon model introduced in Ref. [60]. Furthermore, the X-cube model may be ungauged in two different ways, by regarding either the fracton sector or the lineon sector as gauge charge. The former procedure results in a paramagnet with G -valued degrees of freedom transforming under all 3 sets of planar symmetries as before, whereas the latter yields a model with two G -valued degrees of freedom per site, the first transforming under xy and yz planar symmetries, and the second under yz and zx planar symmetries. The classification of the latter system is given by $(C_{2\text{-fol}})^2$. Thus, both Type 1 and Type 2 strong SSPTs, as well as arbitrary weak SSPTs, may be constructed. Their fracton duals are novel variants of the X-cube model whose fracton dipoles exhibit non-trivial braiding and exchange statistics.

A Type 2 strong SSPT can also be diagnosed through the statistical phases of quasiparticles of the gauged dual. Although fractons are immobile particles, we may still define a braiding statistic between two fractons by regarding a single fracton as a semi-infinite stack of fracton dipoles mobile in the xy plane. Consider a $G = \mathbb{Z}_N \times \mathbb{Z}_N$ model which has two flavors of fractons. Then, let $e^{i\theta_{ab}}$ be the statistical phase obtained by braiding two such fractons of flavors a and b on plane z_0 , where the first argument is a semi-infinite stack in the $z \rightarrow \infty$ direction, and the second argument in the $z \rightarrow -\infty$ direction. The Type 2 strong invariant is then obtained by $e^{iF_2/N} = e^{iN(\theta_{ab}-\theta_{ba})}$. This makes it clear why this strong phase with $F_2 \neq 0$ cannot be obtained by binding 2D anyons to the fractons, since braiding of 2D anyons is manifestly symmetric with respect to its two arguments.

10.8 Conclusions

We have formulated a classification of strong 3D planar SSPTs. Each phase falls into one of a finite set of equivalence classes modulo stacking with 2D phases, which we have fully enumerated. For 1-foliated systems, all SSPT phases are weak. For 2-foliated systems, there are two mechanisms by which a phase may be strong, characterized by Type 1 and Type 2 invariants. For 3-foliated systems, only Type 1 strong phases exist. Under a generalized gauge duality, our classification has a natural interpretation in terms of p -string condensation [46], and we have explicitly constructed strong SSPT models which are dual to fracton phases that cannot be realized via this mechanism. The fractional quasiparticles in these strong phases thus have novel statistical interactions which cannot be interpreted as the statistics of 2D anyonic bound states.

There are various natural extensions of our work. A relevant and open question regards the structure of entanglement in strong SSPT phases [25, 26, 27, 28, 59]. Another is the addition of non-trivial type-III cocycles, which leads to non-abelian fracton topological orders. Finally, it would be interesting to study the foliation structure of the fracton duals.

BIBLIOGRAPHY

- [1] D. Gaiotto, A. Kapustin, N. Seiberg, B. Willett, *J. High Energ. Phys.* (2015) 2015: 172.
- [2] C. D. Batista and Z. Nussinov, *Phys. Rev. B* 72, 045137 (2005).
- [3] Z. Nussinov and G. Ortiz, *Proc. Natl. Acad. Sci. USA* 106, 16944 (2009).
- [4] Z. Nussinov and G. Ortiz, *Ann. Phys.* 324, 977 (2009).
- [5] X. Chen, Z-X. Liu, and X-G. Wen, *Phys. Rev. B* 84, 235141 (2011).
- [6] X. Chen, Z-C. Gu, Z-X. Liu, and X-G. Wen, *Science* 338, 1604 (2012)
- [7] X. Chen, Z-C. Gu, Z-X. Liu, X-G. Wen, *Phys. Rev. B* 87, 155114 (2013).
- [8] T. Senthil, *Annu. Rev. Condens. Matter Phys.* 6, 299 (2015).
- [9] Y. You, T. Devakul, F.J. Burnell, S. L. Sondhi, *Phys. Rev. B* 98, 035112 (2018).
- [10] T. Devakul, D. J. Williamson, Y. You, *Phys. Rev. B* 98, 235121(2018)
- [11] S. Vijay, J. Haah, L. Fu, *Phys. Rev. B* 94, 235157 (2016).
- [12] Y. You, T. Devakul, F.J. Burnell, S. L. Sondhi, arXiv:1805.09800 (2018).
- [13] B. Yoshida, *Phys. Rev. B* 88, 125122 (2013).
- [14] T. Devakul, Y. You, F. J. Burnell, S. L. Sondhi, *SciPost Phys.* 6, 007 (2019).
- [15] T. Devakul, *Phys. Rev. B* 99, 235131 (2019).
- [16] D. J. Williamson, *Phys. Rev. B* 94, 155128 (2016).
- [17] M. E. J. Newman and C. Moore, *Phys. Rev. E* 60, 5068 (1999).
- [18] C. Castelnovo and C. Chamon, *Philos. Mag.* 92, 304 (2012).
- [19] R. Raussendorf and H. J. Briegel, *Phys. Rev. Lett.* 86, 5188 (2001).

- [20] D. V. Else, S. D. Bartlett, A. C. Doherty, *New J. Phys.* 14, 113016 (2012).
- [21] R. Raussendorf, C. Okay, D-S. Wang, D. T. Stephen, H. P. Nautrup, *Phys. Rev. Lett.* 122, 090501 (2019).
- [22] D. T. Stephen, H. P. Nautrup, J. Bermejo-Vega, J. Eisert, R. Raussendorf, *Quantum* 3, 142 (2019).
- [23] T. Devakul, D. J. Williamson, *Phys. Rev. A* 98, 022332 (2018).
- [24] A. K. Daniel, R. N. Alexander, A. Miyake, arXiv:1907.13279.
- [25] D. J. Williamson, A. Dua, M. Cheng, *Phys. Rev. Lett.* 122, 140506 (2019).
- [26] A. T. Schmitz, S-J. Huang, A. Prem, *Phys. Rev. B* 99, 205109 (2019).
- [27] D. T. Stephen, H. Dreyer, M. Iqbal, N. Schuch, *Phys. Rev. B* 100, 115112 (2019).
- [28] L. Zou and J. Haah *Phys. Rev. B* 94, 075151 (2016).
- [29] W. Shirley, K. Slagle, X. Chen, *SciPost Phys.* 6, 041 (2019).
- [30] C. Chamon, *Phys. Rev. Lett.* 94, 040402 (2005).
- [31] S. Bravyi, B. Leemhuis, B. Terhal, *Annals of Physics* 326, 839 (2011).
- [32] J. Haah, *Phys. Rev. A* 83, 042330 (2011).
- [33] S. Vijay, J. Haah, and L. Fu, *Phys. Rev. B* 92, 235136 (2015).
- [34] R. M. Nandkishore, M. Hermele, *Annual Review of Condensed Matter Physics*, 10, 295-313 (2019).
- [35] S. Pai, M. Pretko, R. M. Nandkishore, *Phys. Rev. X* 9, 021003 (2019).
- [36] M. Pretko, L. Radzihovsky, *Phys. Rev. Lett.* 120, 195301 (2018).
- [37] M. Pretko, L. Radzihovsky, *Phys. Rev. Lett.* 121, 235301 (2018).
- [38] L. Radzihovsky, M. Hermele, arXiv:1905.06951.

- [39] A. Prem, S-J. Huang, H. Song, M. Hermele, Phys. Rev. X 9, 021010 (2019).
- [40] A. Prem, D. J. Williamson, arXiv:1905.06309.
- [41] M. Pretko, Phys. Rev. B 95, 115139 (2017).
- [42] M. Pretko, Phys. Rev. B 96, 035119 (2017).
- [43] A. Prem, M. Pretko, and R. M. Nandkishore
- [44] D. Bulmash, M. Barkeshli, arXiv:1905.05771.
- [45] K. Slagle and Y. B. Kim, Phys. Rev. B 97, 165106 (2018)(2018).
- [46] H. Ma, E. Lake, X. Chen, M. Hermele, Phys. Rev. B 95, 245126 (2017).
- [47] Y. You, D. Litinski, F. von Oppen, Phys. Rev. B 100, 054513 (2019).
- [48] H. Song, A. Prem, S-J. Huang, M.A. Martin-Delgado, Phys. Rev. B 99, 155118 (2019).
- [49] D. A. Johnston, J. Phys. A 45, 405001 (2012).
- [50] C. Castelnovo, C. Chamon, and D. Sherrington, Phys. Rev. B 81, 184303 (2010)
- [51] A. Gromov, Phys. Rev. X 9, 031035 (2019).
- [52] A. Dua, I. H. Kim, M. Cheng, D. J. Williamson, arXiv:1908.08049.
- [53] S. Pai, M. Hermele, arXiv:1903.11625.
- [54] W. Shirley, K. Slagle, Z. Wang, X. Chen, Phys. Rev. X 8, 031051 (2018).
- [55] W. Shirley, K. Slagle, X. Chen, Phys. Rev. B 99, 115123 (2019).
- [56] W. Shirley, K. Slagle, X. Chen, SciPost Phys. 6, 015 (2019).
- [57] T. Wang, W. Shirley, X. Chen, Phys. Rev. B 100, 085127 (2019).
- [58] W. Shirley, K. Slagle, X. Chen, arXiv:1907.09048.

- [59] A. Dua, P. Sarkar, D. J. Williamson, M. Cheng, arXiv:1909.12304.
- [60] W. Shirley, K. Slagle, X. Chen, *Annals of Physics* 410, 167922
- [61] S. Vijay, arXiv:1701.00762.
- [62] M. Levin, Z-C. Gu, *Phys. Rev. B* 86, 115109 (2012).
- [63] See Supplementary Material.
- [64] D. V. Else, C. Nayak, *Phys. Rev. B* 90, 235137 (2014).
- [65] M. de Wild Propitius, arXiv:hep-th/9511195.
- [66] J. C. Wang, X-G. Wen, *Phys. Rev. B* 91, 035134 (2015).
- [67] X.-G. Wen, A. Zee, *Phys. Rev. B* 46, 2290 (1992).
- [68] X.-G. Wen, *Natl. Sci. Rev.* 3 (1): 68-106 (2016).
- [69] J. C. Wang, L. H. Santos and X-G. Wen, *Phys. Rev. B* 91, 195134 (2015).
- [70] J. C. Wang, Z-C. Gu, X-G. Wen, *Phys. Rev. Lett.* 114, 031601 (2015)
- [71] X. Chen, Z-C. Gu, X-G. Wen, *Phys. Rev. B* 82, 155138 (2010).
- [72] A. Kitaev, *Annals of Physics* 321 2?111 (2006)
- [73] M. Levin, X.-G. Wen, *Phys. Rev. B* 71, 045110 (2005).